The Air Stability and Operational Lifetime of Organic Photovoltaic Materials and Devices

Edward S. R. Bovill

Department of Physics and Astronomy

University of Sheffield

Thesis submitted for the degree of

Doctor of Philosophy

February 2015

Acknowledgements

I would like to take this opportunity to thank everyone who has made this work possible, both through their academic and moral support. Firstly, I would like to thank my supervisor David Lidzey for providing me with the support needed throughout the last few years. You have been a font of knowledge, and I could not have achieved this without your steady guiding hand. I would also like to thank all the members of the EPMM group and Ossila Ltd, both past and present, for all of their help and training. It has been a pleasure working with you all.

Without the unconditional love and support I have received from my amazing family this work would not have been possible. Throughout my academic career, my parents have been truly fantastic, always taking a keen interest in my work and willing to lend a hand whenever one was needed (wielding a carrot or stick, or presenting a shoulder to cry on as required). They have been there for me during the best and the worst of times, and I couldn't have wished for a more loving and nurturing environment. A big thank you to my brother Will, who always brings a big smile to my face, and drags me outside to do something active and fun whenever we get together. Long may it continue!

My friends have provided endless laughter and great memories for many years, and so thank you to Will, S-J, Ditts, Swatts, Trewin, Stuart, Milan, Elisa, Claire and Sarah.

Finally, I would like to thank my girlfriend Sharmin for being the wonderful person she is. The final years of my Ph.D. have been brightened by her presence, and her unconditional love, support and laughter have provided me with the strength to be the best I can.

Abstract

Replacing energy intensive evaporated materials with solution processed alternatives is key to allowing OPVs to be fabricated using processes such as roll-to-roll (R2R) fabrication. However, roll-to-roll fabrication is primarily an ambient processing method, and as such the materials used need to be stable in the presence of oxygen and moisture. The effects of ambient oxygen and moisture on materials utilised in OPV devices are well documented, and in almost all cases are detrimental to device performance. Therefore, identifying materials and techniques that address these difficulties are essential.

In this thesis, using a combination of spectroscopic techniques and device characterisation, it is shown that applying optimised thermal treatments can reduce the uptake of moisture in molybdenum oxide hole transport layers, and reduce the resulting negative effects on device performance. The air stability, and therefore suitability for R2R fabrication, of several polymers are investigated. PFDT2BT-8 was identified as the most stable, and was utilised to fabricate OPV devices from solution in air using a variety of materials with efficiencies > 5%. In addition, the development of lifetime testing techniques, both in a laboratory and outdoor setting, evidencing operating lifetimes of > 7 years for devices utilising ambient solution processed materials.

In conclusion, this thesis describes the development of materials and techniques to allow for the fabrication of organic photovoltaic (OPV) devices from solution under ambient conditions, having high efficiencies and long operating lifetimes.

Publications

1. Edward S. R. Bovill, Jonathan Griffin, Tao Wang, James Kingsley, Hunan Yi, Ahmed Iraqi, Alastair R. Buckley, David G. Lidzey. Air processed organic photovoltaic devices incorporating a MoOx anode buffer layer, Applied Physics Letters, **2013**, 102, 183303

2. Edward S. R. Bovill, Hunan Yi, Ahmed Iraqi, David G. Lidzey, The fabrication of polyfluorene and polycarbazole-based photovoltaic devices using an air-stable process route, Applied Physics Letters, **2014**, 105, 223302

3. Edward S. R. Bovill, Nick Scarratt, Jonathan Griffin, Hunan Yi, Ahmed Iraqi, Alastair R. Buckley, James W. Kingsley, David G. Lidzey, The role of the hole-extraction layer in determining the operational stability of a polycarbazole:fullerene bulk-heterojunction photovoltaic device, Applied Physics Letters, **2015**, 106, 073301

4. Keith T. Butler, Edward S. R. Bovill, Rachel Crespo-Ortero, David O. Scanlon, David G. Lidzey and Aron Walsh, Work function engineering of air processed hole transport layers in organic photovoltaics: understanding and controlling oxide surface hydration effects, Submitted for review to Chemistry of Materials June 2015 (first stage).

Conference Presentations

Oral Presentations:

European Optical Society Annual Meeting (EOSAM). Aberdeen, Scotland, UK, September 2012

UK semiconductors Summer Meeting 2013. Sheffield, UK, July 2013

Hybrid and Organic Photovoltaics 2014 (HOPV14). Lausanne, Switzerland, May 2014

Poster Presentations:

Materials Research Society (MRS) Spring Meeting. San Francisco, USA, April 2014

Table of Contents

Chapter 1 : Introduction 1

1.1 Thesis Summary and Motivation.. 5

1.2 References 8

Chapter 2 : Background Theory.. 11

2.0 Introduction 11

2.1 Atomic and Molecular Orbitals 12

2.2 Orbital Hybridization.. 14

2.3 Conjugation 18

2.4 Photophysics of Organic Conjugated Polymers 19

2.4.1 Exciton Formation 20

2.4.2 Exciton Diffusion and Dissociation 22

2.4.3 Charge Transport 24

2.4.4 Charge Extraction 25

2.5 Device Architecture 28

2.6 Interface Materials 32

2.6.1 PEDOT:PSS.. 32

2.6.2 Transition Metal Oxides 33

2.7 Active Layer Materials 35

2.7.1 Polymer List.. 39

2.7.2 Fullerenes.. 42

2.8 Ambient Processing.. 43

2.9 OPV Stability and Degradation 46

2.9.1 Photochemical Reactions 48

2.9.2 Trap Formation 48

2.9.3 Phase Separation 49

2.9.4 Delamination.. 49

2.9.5 Encapsulation.. 50

2.9.6 Decay Behaviour.. 51

2.10 References 53

Chapter 3 : Experimental Methods 69
3.0 Introduction 69
3.1 Fabrication Techniques 70
  3.1.1 Substrate Cleaning 71
  3.1.2 Solution Preparation 72
  3.1.3 Thin Film Deposition 73
  3.1.4 Thermal Evaporation 76
3.2 Device Fabrication 78
3.3 Device Characterization 81
  3.3.1 Device Characterization Setup 85
  3.3.2 Solar Simulator Calibration 86
  3.3.3 Aperture Mask Calibration 88
3.4 Absorbance Spectroscopy 89
3.5 Spectroscopic Ellipsometry 92
3.6 External Quantum Efficiency (EQE) 93
3.7 Laser Beam Induced Current Mapping (LBIC) 94
3.8 Electroluminescence Mapping (ELM) 95
3.9 Lifetime Testing 96
  3.9.1 Laboratory Lifetime Testing Setup 97
  3.9.2 Light Source and Spectrum 99
  3.9.3 *JV* Mismatch 101
  3.9.4 Light Uniformity 104
  3.9.5 Source-Measure Unit Comparison 105
  3.9.6 Pixel Size Variation 106
  3.9.7 Discrepancies in *JV* data 108
3.10 Outdoor Lifetime Testing 110
3.11 Lifetime Reporting 113
  3.11.1 ISOS Laboratory Weathering Testing 113
  3.11.2 ISOS Outdoor Testing 116
3.12 Conclusions 117
3.13 References 119

Chapter 4 : Air Stability of MoO$_x$ 123
4.0 Introduction 124
4.1 MoO$_x$ Films and Ambient Conditions 125
4.2 MoO$_x$ Film and Device Preparation 126
4.3 OPV Performance 127
4.3 Water Adsorption 133
4.4 Air Processing Photoactive Layers 136
4.5 Conclusions 139
4.6 References 140

Chapter 5 : Hole Transport Layer Laboratory Lifetime Study 143
5.0 Introduction 144
5.1 Hole Transport Layer Materials 145
  5.1.1 PEDOT:PSS 145
  5.1.2 Vanadium Oxide 146
5.2 Device Lifetime 147
5.3 LBIC/ELM of Aged Devices 155
5.4 Conclusions 158
5.5 References 159

Chapter 6 : Polymer Air Processing 165
6.0 Introduction 166
6.1 Polymers for Air Processing 166
6.2 Fabricating OPVs in Air 170
6.3 Photostability of Polymers 176
6.4 Effects of Extended Air Exposure 178
6.5 Conclusions 182
6.6 References 183

Chapter 7 : Outdoor Lifetime Testing..189
7.0 Introduction.. 190
7.1 Light and Temperature Variation.. 191
  7.1.2 Sunny and Cloudy Days.. 193
7.2 Temperature Effects... 196
7.3 *JV* Characteristics.. 198
7.4 OPV Device Lifetime.. 200
7.5 Conclusions.. 203
7.6 References.. 204

Chapter 8 : Solution Processed OPVs...207
8.0 Introduction.. 208
8.1 Titanium Oxide... 209
8.2 Solution Processed Devices.. 210
8.3 Conclusions.. 215
8.4 References.. 216

Chapter 9 : Conclusions..219
9.0 Conclusions of Work Undertaken.. 219
9.1 Suggestions for Further Work... 223
9.2 References.. 225

Appendix 229

Chapter 1 : Introduction

In 2013, the total power consumption of the world's population rose to 17.4 TW [1], an increase of 2.3% on 2012. At the current rate of growth, by 2030 global energy production will need to exceed 24 TW. However, as the world's population continues to grow and more countries become industrialised, the energy needs of the world's population will, in all likelihood, far exceed this figure. Currently, 87% of the world's energy is produced from burning fossil fuels (including coal, gas and oil), 4% from nuclear fuels, and only 9% from renewable sources (including hydroelectric and other technologies) [1]. There is great impetus for change in the way energy is generated due to the increased awareness of the effects of global warming and humanity's influence on the climate. Several meetings of the world's most powerful leaders have produced guidelines and protocols to curb the generation of greenhouse gasses through investment into renewable energy sources and reducing our reliance on fossil fuels, though their success is yet to be proved. Unfortunately, excluding hydroelectricity, other renewable energy technologies only accounted for 2.2% of global energy production, a small increase of 0.3% from 2012. Growth in this sector has been hampered by challenges posed by the technologies themselves and by reduced governmental investment due to global recession. However, an optimistic report predicted that it could be possible to generate all our energy needs using only renewable sources such as wind, wave and solar by 2050 if the social and political barriers to implementation are overcome [2].

The Sun is a phenomenal source of energy, with the surface of Earth irradiated with ~ 100 petajoules (10^{15} W) of energy every second [3], roughly 6000 times the current world consumption. This abundance of energy can be harvested through the use of photovoltaic panels that convert the incident light into electricity via the photoelectric effect. The solar spectrum incident on the Earth's atmosphere and the surface is shown in **Figure 1.1**, and are known as AM0 and AM1.5 respectively. The difference in the spectra arise from adjustments due to absorption in the atmosphere and to account for scattering. AM, which stands for air mass, accounts for the depth of atmosphere the light passes through, with 1 being one atmosphere depth. Many industrialised nations are located in temperate latitudes and so the sun is not directly overhead. Therefore the AM1.5 spectrum was calculated for standardisation purposes based on an analysis of solar irradiance data [4]. All standardised testing of photovoltaic devices is carried out under AM1.5 spectra at 1000 Wm^{-2} [4].

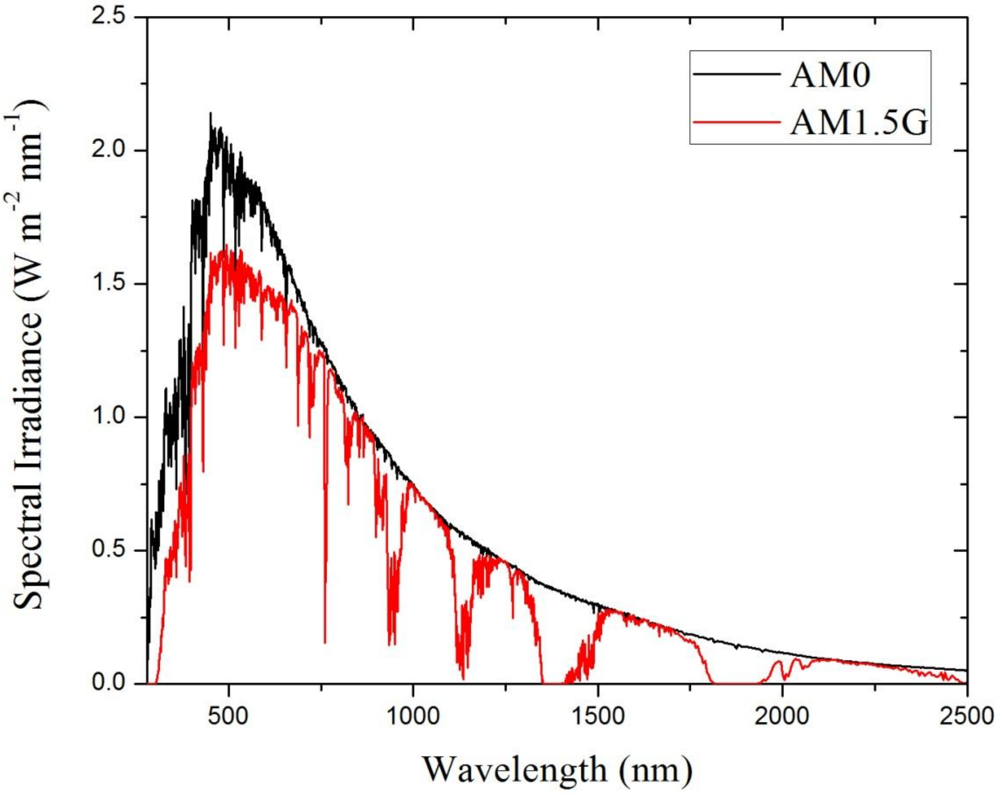

Figure 1.1 Solar spectrum incident on the Earth above the atmosphere (AM0) and on the surface at temperate latitudes (AM1.5). [4]

The majority of photovoltaic (PV) panels available today are based on silicon, a technology that has been in development for > 60 years. The efficiency of silicon PV has increased from 10% in 1955 [5] to around 25% for modern, single crystal silicon panels [6]. These high efficiencies are due to silicon's low bandgap of 1.1 eV, allowing for efficient absorption of the solar spectrum in the 400 - 800 nm region, and the material's excellent charge generation properties. However, crystalline silicon, like many inorganic semiconductors, has an indirect bandgap that necessitates thick active layers, which increases the cost of manufacture significantly.

There are many alternative material systems for photovoltaic devices, including other inorganic materials such as gallium arsenide (GaAs), indium phosphide (InP), cadmium telluride (CdTe) and various other combinations of III-V elements, with maximum efficiencies of 39.3% for a $GaInP_2$/GaAs/Ge multijunction cell [7]. However, the market for solar panels is dominated by silicon, with a > 90% share [8]. The other, more efficient and far more expensive inorganic PV technologies are reserved for specialist applications including spacecraft and satellites.

Due to the negligible running costs of solar panels during their lifetime, the only feasible way of reducing the costs to the end user, and therefore making them more attractive to both businesses and private users, is to reduce the cost of manufacture or increase operating efficiency. Unfortunately, increases in device efficiency usually mean increasing the costs, due to the necessity of using more expensive materials or more complex device architectures, such as tandem cells and concentrators. Therefore, reducing the costs of PV requires the use of cheap materials and manufacturing processes.

Another type of PV technology that addresses many of the issues with inorganic PV are organic photovoltaic devices (OPVs). These promise thin, flexible, and lightweight devices that overcome the cost of inorganic PV by being primarily composed of carbon based compounds. These compounds can be deposited from solution, allowing for use of cheap manufacturing processes, such as spray coating and roll-to-roll processing, to produce large area devices extremely rapidly. Unlike many forms of inorganic PV, which need to be fabricated onto ultra-pure crystalline substrates, OPVs can be fabricated onto amorphous substrate materials such as glass and flexible plastics such as PET [9], [10]. This not only lowers the costs of manufacture, but also the embodied energy cost of the devices themselves.

However, there are several challenges inherent in OPV technology that will need to be overcome before commercialization is possible. The optimal active layer thickness of the device if often between 50 - 100 nm due to the semiconducting materials used having high absorption co-efficients and poor charge mobility. This poses a challenge in device manufacture as dust or other impurities present during device fabrication can lead to short circuits and other defects. The charges generated on photoexcitation are strongly bound by coulombic attraction as excitons, which leads to large binding energies and was long thought to limit the potential maximum efficiency of OPVs to around 15% [11], though this has been recently revised upwards to 20 - 24% [12]. Also, the stability of OPV devices is still limited due to the oxygen and moisture sensitivity of the materials used, which requires high grade encapsulation with very low moisture and oxygen ingress rates [13]. Large scale production of OPVs is still in its infancy, but promising first steps have been made, albeit with devices of < 4% efficiency [14], [15]. Finally, the ubiquitous use of indium tin oxide (ITO) as the anode material, although also common in flat panel TVs, smart phones and other electronic devices, is also problematic due to the scarcity of indium. The current aim of the OPV community is to attain device efficiencies of 10% and operating lifetimes of 10 years, though economic assessments have shown that the technology could be competitive with silicon PV with efficiencies of only 7% and 5 years lifetime [16]. Though these goals have not yet been met, promising steps have been made towards both targets [17], [18].

1.1 Thesis Summary and Motivation

This work will investigate the materials and processes needed to manufacture OPVs from solution in an ambient atmosphere, with the aim of producing fully solution processed devices with long operating lifetimes. One of the aims of the OPV field is to develop methods and materials that allow for the production of high efficiency and stable devices using commercial deposition techniques, such as roll-to-roll printing and spray coating. Two of the requirements for these processes are that the materials can be deposited from solution in air. To this end, a variety of active layer and interlayer materials are studied, various processes developed that allow for ambient processing with little loss in efficiency, and lifetime tests are carried out using custom built systems. The structure of the thesis is as follows:

Chapter 2 gives an overview of the background theory of organic semiconductors and interface materials and their use in OPVs. The experimental techniques utilised in the fabrication and characterisation of OPV devices is covered in **Chapter 3**, as is the setup and calibration of the OPV lifetime testing systems.

Chapter 4 describes the optimisation of OPV devices utilising a molybdenum oxide (MoO_x) hole transport layer, and covers the techniques developed for reducing the negative effects of air exposure on MoO_x films. Ellipsometry was used to measure the adsorption of water into MoO_x films, and the effects of this adsorbed water were studied using OPV device characterisation. The results show that thermally annealing MoO_x films before exposure to air compacts the films and reduces the hygroscopicity by a significant degree, reducing the uptake of water into the films and decreasing the negative effects of air exposure on OPV device performance [19].

Chapter 5 addresses the effects on OPV device lifetime of changing the hole transport layer (HTL) material. Three material systems were studied; thermally evaporated MoO_x, PEDOT:PSS and solution processed vanadium oxide (V_2O_x). Lifetime tests conforming to ISOS-L-1 specifications [20] were carried out for > 600 hours, and extrapolated device lifetimes in excess of 7 years were calculated for PEDOT:PSS based devices. Several techniques, including laser beam induced current mapping (LBIC), electro luminescent mapping (ELM), external quantum efficiency (EQE) and device characterisation were used to investigate the effects of HTL material on the device lifetime and the formation of defects in the devices.

Chapter 6 looks into the effects of processing five different polymers in air compared to processing in a moisture and oxygen free environment. Four polymers similar to PCDTBT, synthesised by the Department of Chemistry at The University of Sheffield, and the high efficiency polymer PTB7 (1-Material) were studied using a standard device architecture with a PEDOT:PSS HTL. The effects of processing polymers onto PEDOT:PSS in air were studied, and the subsequent enhancement of V_{oc} investigated. Of the polymers studied, PFDT2BT-8 showed the least degradation of FF and J_{sc} when processed in air, and the resulting air processed OPV devices had a power conversion efficiency that exceeded 6.10%. [21]

Chapter 7 presents the preliminary results from a lifetime study of devices utilizing a PEDOT:PSS HTL and an PFDT2BT-8:$PC_{70}BM$ active layer in an outdoor lifetime testing system closely modelled on the ISOS-O-2 outdoor test, with data collected from August to December 2014. The effects of daily fluctuations in light intensity on *JV* characteristics were observed. It was shown that *FF* and V_{oc} are largely independent of light intensity, yet J_{sc} is extremely dependent on light intensity. T_{80} lifetimes of ~ 2500 hours were calculated, however, it was established that more data recorded over a longer period was required to remove *JV* measurement bias introduced by seasonal variation in temperature.

Chapter 8 is the final experimental chapter and presents a study of a solution processed OPV devices that utilise a PEDOT:PSS HTL, a PFDT2BT-8:$PC_{70}BM$ active layer and a TiO_x electron transport layer (ETL). The effects on device performance of processing the active layer and ETL of the devices in a nitrogen filled glovebox or in air were studied. It was found that processing the active layer in air resulted in minor losses in *FF*, commensurate with previous findings, while processing the TiO_x ETL in air resulted in a more opaque film that resulted in J_{sc} losses. Devices that were processed in the nitrogen filled glovebox had high initial *PCE*s of (6.0±0.2)%, whilst those processed in air had a reduced initial efficiency of (5.3±0.1)%.

The conclusions of this thesis are presented in **Chapter 9**. The main findings discussed are the fact that when utilising a PCDTBT based polymer system, PEDOT:PSS is the most stable HTL and can result in device lifetimes in excess of 7 years. Of the polymers studied, PFDT2BT-8 gives the highest power conversion efficiencies and is the most stable when processing in air. Finally, devices with solution processed active layers and interlayers can be fabricated in air with efficiencies in excess of 5%, which would be compatible with roll-to-roll processing techniques, an important step for scale up and commercialisation.

1.2 References

[1] "BP Statistical Review of World Energy 2014." [Online]. Available: http://www.bp.com/en/global/corporate/about-bp/energy-economics/statistical-review-of-world-energy.html.

[2] M. Z. Jacobson and M. A. Delucchi, "Providing all global energy with wind, water, and solar power, Part I: Technologies, energy resources, quantities and areas of infrastructure, and materials," *Energy Policy*, vol. 39, no. 3, pp. 1154–1169, Mar. 2011.

[3] A. Cho, "Energy's tricky tradeoffs.," *Science*, vol. 329, no. 5993, pp. 786–7, Aug. 2010.

[4] C. A. Gueymard, D. Myers, and K. Emery, "Proposed reference irradiance spectra for solar energy systems testing," *Sol. Energy*, vol. 73, no. 6, pp. 443–467, Dec. 2002.

[5] M. A. Green, "The path to 25% silicon solar cell efficiency: History of silicon cell evolution," *Prog. Photovoltaics Res. Appl.*, vol. 17, no. 3, pp. 183–189, May 2009.

[6] P. K. Nayak and D. Cahen, "Updated assessment of possibilities and limits for solar cells.," *Adv. Mater.*, vol. 26, no. 10, pp. 1622–8, Mar. 2014.

[7] R. W. Miles, G. Zoppi, and I. Forbes, "Inorganic photovoltaic cells," *Mater. Today*, vol. 10, no. 11, pp. 20–27, Nov. 2007.

[8] J. Nelson and C. J. M. Emmott, "Can solar power deliver?," *Philos. Trans. A. Math. Phys. Eng. Sci.*, vol. 371, no. 1996, p. 20120372, Aug. 2013.

[9] S. R. Dupont, M. Oliver, F. C. Krebs, and R. H. Dauskardt, “Interlayer adhesion in roll-to-roll processed flexible inverted polymer solar cells,” *Sol. Energy Mater. Sol. Cells*, vol. 97, pp. 171–175, Feb. 2012.

[10] G. Terán-Escobar, J. Pampel, J. M. Caicedo, and M. Lira-Cantú, “Low-temperature, solution-processed, layered V2O5 hydrate as the hole-transport layer for stable organic solar cells,” *Energy Environ. Sci.*, vol. 6, no. 10, p. 3088, 2013.

[11] G. Dennler, M. C. Scharber, and C. J. Brabec, “Polymer-Fullerene Bulk-Heterojunction Solar Cells,” *Adv. Mater.*, vol. 21, no. 13, pp. 1323–1338, Apr. 2009.

[12] R. A. J. Janssen and J. Nelson, “Factors limiting device efficiency in organic photovoltaics.,” *Adv. Mater.*, vol. 25, no. 13, pp. 1847–58, Apr. 2013.

[13] S. Cros, R. de Bettignies, S. Berson, S. Bailly, P. Maisse, N. Lemaitre, and S. Guillerez, “Definition of encapsulation barrier requirements: A method applied to organic solar cells,” *Sol. Energy Mater. Sol. Cells*, vol. 95, pp. S65–S69, May 2011.

[14] F. C. Krebs, S. A. Gevorgyan, and J. Alstrup, “A roll-to-roll process to flexible polymer solar cells: model studies, manufacture and operational stability studies,” *J. Mater. Chem.*, vol. 19, no. 30, p. 5442, 2009.

[15] D. Angmo, P. M. Sommeling, R. Gupta, M. Hösel, S. A. Gevorgyan, J. M. Kroon, G. U. Kulkarni, and F. C. Krebs, “Outdoor Operational Stability of Indium-Free Flexible Polymer Solar Modules Over 1 Year Studied in India, Holland, and Denmark,” *Adv. Eng. Mater.*, vol. 16, no. 8, pp. 976–987, Aug. 2014.

[16] B. Azzopardi, C. J. M. Emmott, A. Urbina, F. C. Krebs, J. Mutale, and J. Nelson, “Economic assessment of solar electricity production from organic-based photovoltaic

modules in a domestic environment," Energy & Environmental Science, vol. 4, no. 10. p. 3741, 2011.

[17] C. H. Peters, I. T. Sachs-Quintana, J. P. Kastrop, S. Beaupré, M. Leclerc, and M. D. McGehee, "High Efficiency Polymer Solar Cells with Long Operating Lifetimes," *Adv. Energy Mater.*, vol. 1, no. 4, pp. 491–494, Jul. 2011.

[18] J. You, L. Dou, K. Yoshimura, T. Kato, K. Ohya, T. Moriarty, K. Emery, C.-C. Chen, J. Gao, G. Li, and Y. Yang, "A polymer tandem solar cell with 10.6% power conversion efficiency.," *Nat. Commun.*, vol. 4, p. 1446, Jan. 2013.

[19] E. S. R. Bovill, J. Griffin, T. Wang, J. W. Kingsley, H. Yi, A. Iraqi, A. R. Buckley, and D. G. Lidzey, "Air processed organic photovoltaic devices incorporating a MoOx anode buffer layer," *Appl. Phys. Lett.*, vol. 102, no. 18, p. 183303, May 2013.

[20] M. O. Reese, S. A. Gevorgyan, M. Jørgensen, E. Bundgaard, S. R. Kurtz, D. S. Ginley, D. C. Olson, M. T. Lloyd, P. Morvillo, E. A. Katz, A. Elschner, O. Haillant, T. R. Currier, V. Shrotriya, M. Hermenau, M. Riede, K. R. Kirov, G. Trimmel, T. Rath, O. Inganäs, F. Zhang, M. Andersson, K. Tvingstedt, M. Lira-Cantu, D. Laird, C. McGuiness, S. (Jimmy) Gowrisanker, M. Pannone, M. Xiao, J. Hauch, R. Steim, D. M. DeLongchamp, R. Rösch, H. Hoppe, N. Espinosa, A. Urbina, G. Yaman-Uzunoglu, J.-B. Bonekamp, A. J. J. M. van Breemen, C. Girotto, E. Voroshazi, and F. C. Krebs, "Consensus stability testing protocols for organic photovoltaic materials and devices," *Sol. Energy Mater. Sol. Cells*, vol. 95, no. 5, pp. 1253–1267, May 2011.

[21] E. Bovill, H. Yi, A. Iraqi, and D. G. Lidzey, "The fabrication of polyfluorene and polycarbazole-based photovoltaic devices using an air-stable process route," *Appl. Phys. Lett.*, vol. 105, no. 22, p. 223302, Dec. 2014.

Chapter 2 : Background Theory

2.0 Introduction

In this chapter, the background theory behind the operation of OPV devices is covered, including the physical and electrical properties of organic semiconductors, focusing on conjugated polymers in particular. The discussion includes atomic orbitals and hybridization, as these fundamentals are key to understanding the electronic structure and semiconducting properties in these materials. The photophysics of conjugated polymers are then discussed, as are the formation of the HOMO and LUMO energy bands and charge generation, transportation and charge carrier interactions. OPV device architecture, both standard and inverted, is covered, as are the details of device characterization. The theories behind interface materials and the interactions at the interfaces found in OPV devices are reported, including a list of materials utilised in OPV devices in this thesis. Finally, the mechanisms of OPV degradation and lifetime are studied, along with the effects of ambient processing on OPV performance.

2.1 Atomic and Molecular Orbitals

Electrons present in an atom are said to be bound to the nucleus in orbitals, whose properties are determined by the uncertainty principle of quantum mechanics [1]. Therefore, unlike classical orbits of physical bodies, the orbits of electrons are clouds of probable occupation. The shape and properties of which are determined by the values of four quantum number. These are: n, the principle quantum number, the potential energy of the electron; l, the magnitude of the angular momentum of the electron; m_l, the direction of the angular momentum; and m_s, the spin direction of the electron [2]. The four quantum numbers that describe the orbits of electrons have integer values, except for m_s, the spin quantum number, which has a value of ±1/2. These numbers can be calculated using a set of inequalities outlined below.

$$1 \leq n$$

$$0 \leq l \leq n-1$$

$$-l \leq m_l \leq l$$

$$-s \leq m_s \leq s$$

These inequalities can be used to calculate the values of the quantum numbers of any given orbital, and defines its shape as well as how many electrons it contains. **Table 2.1** shows the values of the four quantum numbers for the first three orbitals in an atom. The first atomic orbital is known as the 1s shell and can be occupied by two electrons, one for each value of the spin quantum number m_s. S orbitals are characterised by values of $l = 0$ and subsequent shells, 2s, 3s, 4s etc all contain two electrons. Orbitals whose value of $l = 1$ are known as P orbitals, and are split into three types determined by their value of m_l, $2p_x$, $2p_y$, $2p_z$. Each sub-type of p orbital also contains two electrons, one for each value of the spin quantum number m_s. Each sub-type of p orbital is oriented along an orthogonal axis, hence the x, y and z

subscripts. The shape and orientation of the 2s and 2p orbitals are shown in **Figure 2.1**. Orbitals with larger values of *l*, such as D orbitals whose value of $l = 2$, are important in determining the electronic characteristics of metal oxides and are split into five sub-types determined by their value of m_l. For even larger values of *l* other orbitals exist, including the f orbitals, which are generally not present within organic materials, though are also of importance in metal oxides.

n	l	m_l	m_s	**Orbital Name**	**Total Number Of Electrons**
1	0	0	+1/2	1s	2
			- 1/2		
2	0	0	+1/2	2s	2
			- 1/2		
	1	-1	+1/2	$2p_x$	6
			- 1/2		
		0	+1/2	$2p_y$	
			- 1/2		
		1	+1/2	$2p_z$	
			- 1/2		
3	0	0	+1/2	3s	2
			- 1/2		
	1	-1	+1/2	$3p_x$	6
			- 1/2		
		0	+1/2	$3p_y$	
			- 1/2		
		1	+1/2	$3p_z$	
			- 1/2		
	2	-2	+1/2	$2d_{xy}$	10
			- 1/2		
		-1	+1/2	$2d_{xz}$	
			- 1/2		
		0	+1/2	$2d_{z^2}$	
			- 1/2		
		1	+1/2	$2d_{yz}$	
			- 1/2		
		2	+1/2	$2d_{z^2-y^2}$	
			- 1/2		

Table 2.1 Values of the quantum numbers, orbital names and total number of electrons for a given electron orbital. Only the orbitals for the first three values of *n* are shown.

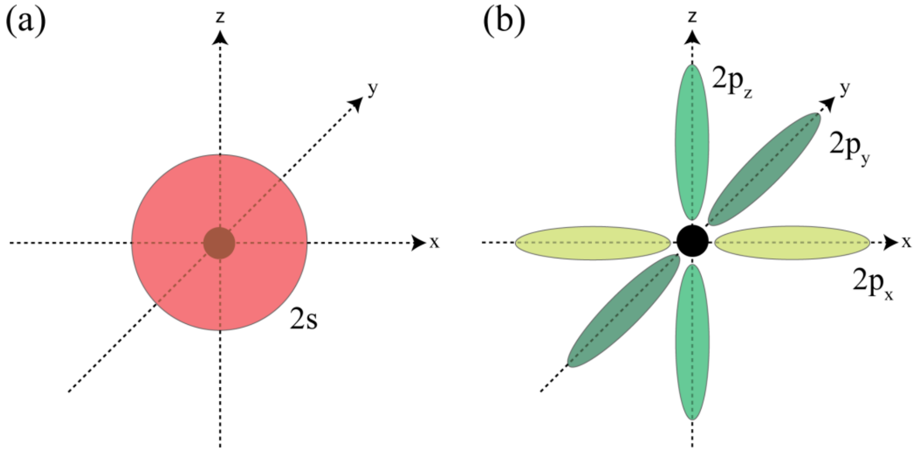

Figure 2.1 Shape and orientation of the **(a)** 2s and **(b)** 2p orbitals surrounding an atomic nucleus.

2.2 Orbital Hybridization

When two atoms are brought into close enough proximity, covalent bonds can be formed. This occurs when the electron orbitals of the two atoms overlap and form molecular orbitals, which are the combination of the overlapping original electron orbitals. For example, in hydrogen atoms, which consist of a single proton surrounded by a single electron in the 1s shell, covalent bonding occurs between two hydrogen atoms to form a diatomic hydrogen molecule, H_2. The orbitals that are formed as a result of this bonding are known as 'bonding orbitals' and are shown in **Figure 2.2**.

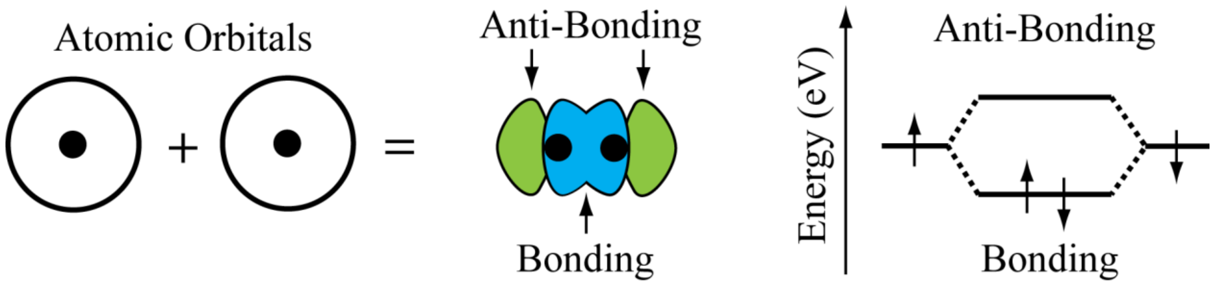

Figure 2.2 Structure and energy levels of bonding and anti-bonding orbitals for a simple two atom system.

Bonding orbitals consist of an electron cloud located between the two atoms that are covalently bonded. The energy of this bonding orbital is lower than the individual energies of the unbound electrons, as shown in **Figure 2.2**, due to the increased electron density between the atoms, which shields the repulsive force between the two nuclei, resulting in a more tightly bound molecule [3]. Anti-bonding orbitals are at a higher energy state than bonding orbitals, as electrons in this configuration do not occupy the space in between the atomic nuclei, which reduces the shielding strength of the electron cloud in between the two nuclei and results in a less stable molecule [3].

Carbon, which forms the backbone of organic semiconducting polymers, has 6 electrons with an electronic ground state of $1s^2 2s^2 2p_x^1 2p_y^1$, which results in an atom with four valence electrons that can form covalent bonds. The 1s orbital does not take part in any bonding and so will be omitted from future discussion for simplicity. In atomic carbon the 2s orbital is filled and so, according to the Pauli exclusion principle, these electrons cannot take part in covalent bonding. However, when carbon bonds with other atoms, a process called orbit hybridization takes place that allows for these electrons to take part in bonding. During orbit hybridization, one of the electrons from the 2s shell is promoted to the previously empty $2p_z$ shell, resulting in a $2s^1 2p_x^1 2p_y^1 2p_z^1$ electronic structure with four unpaired electrons. From here the s and p orbitals undergo hybridization. There are three kinds of hybridization; sp^1, sp^2 and sp^3. During sp^2 hybridization, the 2s and two of the three 2p orbitals form three new sp^2 hybrid orbitals as shown in **Figure 2.3 (a, c)**, while conserving the energy of the system **Figure 2.3 (b, d)**.

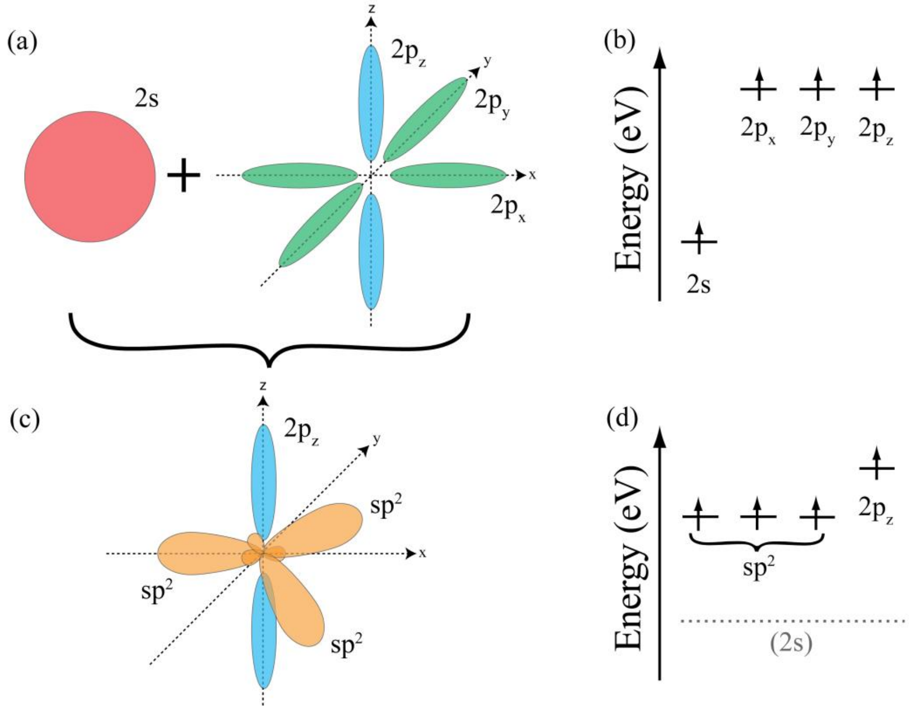

Figure 2.3 Hybridization of 1s and 2p bonds **(a)** to form sp^2 hybrid bonds **(c)**. Energy levels of the bonds pre and post hybridization are shown in **(b)** and **(d)** respectively.

Bonding between two sp^2 hybridised carbon atoms can occur in one of two ways; sigma bonding (σ) occurs when two sp^2 orbitals form a covalent bond, and pi bonding (π) occurs when the remaining unhybridised $2p_z$ orbitals overlap and form a much weaker bond that exists in a plane parallel to the σ bond. Carbon atoms that have only formed a σ bond are said to have formed a C-C single bond, as shown in **Figure 2.4 (a)**, and those that also form π bonds in addition to the σ bond are said to have formed a C=C double bond as shown in **Figure 2.4 (b)**. π bonds have a higher energy than σ bonds and sp^2 orbitals, as can be seen from **Figure 2.4 (d),** and play an important role in the semiconducting properties of conjugated polymers, as discussed later.

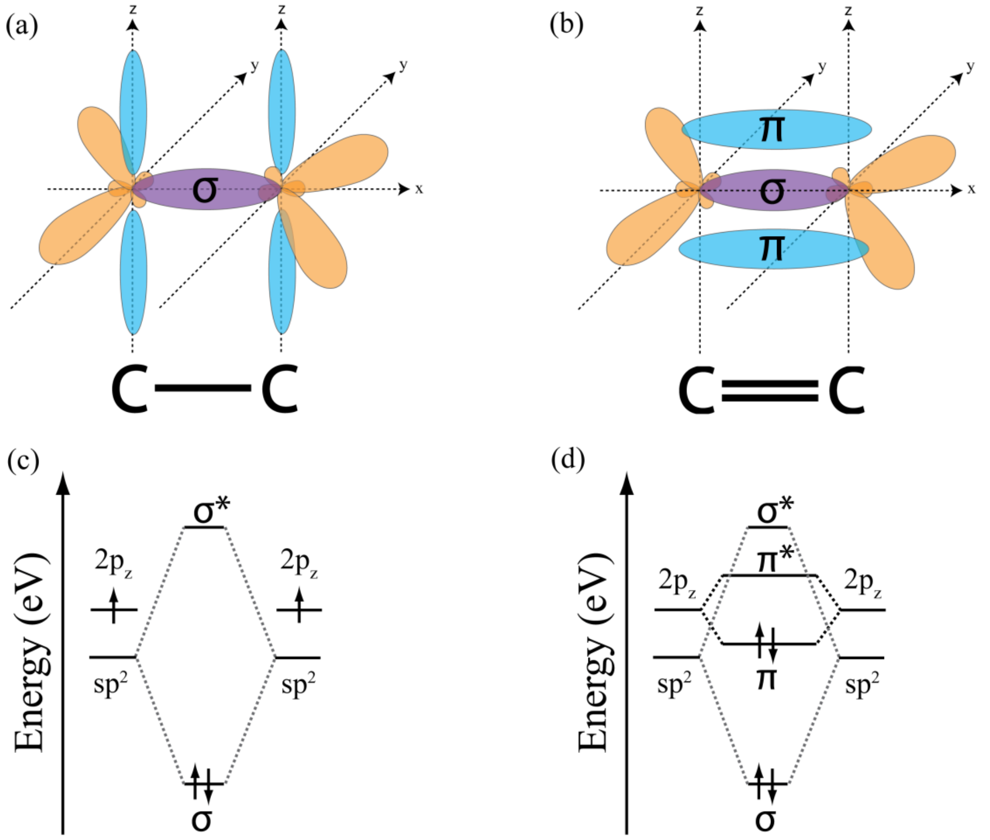

Figure 2.4 C-C single bond structure **(a)** and energy levels **(c)** and C=C double bond structure **(b)** and energy levels **(d)**.

2.3 Conjugation

Carbon-carbon chains form the backbone of many polymers, and a polymer is said to be conjugated when there are alternating single and double bonds along a carbon chain. A common example of an alternating single-double carbon bond structure is benzene, shown in **Figure 2.5**.

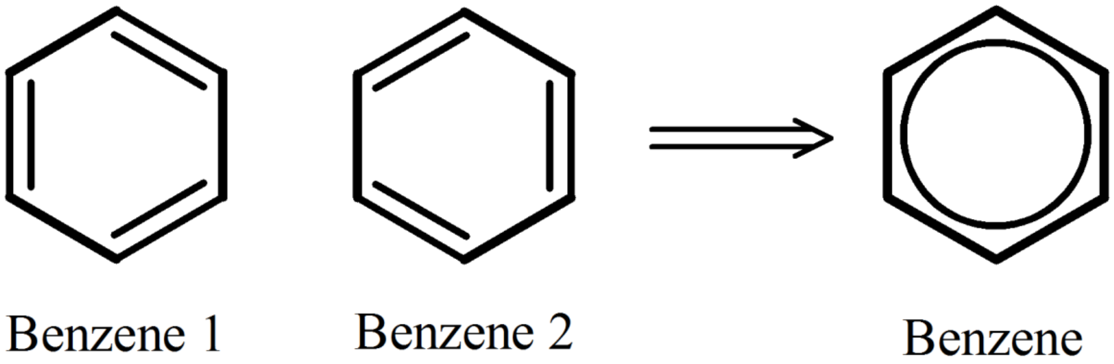

Figure 2.5 Structure of Benzene. Benzene 1 and 2 are equivalent and so the π bonds are said to be delocalised over the whole structure in the same plane above and below the ring.

Benzene is a ring of six carbon atoms that are covalently bonded with sp^2 hybridised orbitals and alternating single-double carbon bonds [3]. The positioning of the double bonds in benzene makes no difference to the material's properties and so benzene 1 and 2 are equivalent. Therefore, the alternating single and double bonds result in the weakly bound electrons in the π bonds of the double bonded carbon atoms becoming delocalised over the benzene ring as shown in **Figure 2.5**, leading to an equal probability of these electrons being found anywhere in the benzene ring .

In the polymers utilised in OPV devices, the delocalization of π bonds around conjugated bonds gives rise to the semiconducting properties of the polymers. The delocalised π bonds form the highest occupied molecular orbital (HOMO) level of the polymer, with the higher energy unoccupied π* anti-bonding orbital forming the lowest unoccupied molecular orbital (LUMO) level, as shown in **Figure 2.4 (d)**; promoting an electron from the HOMO level to the LUMO level changes the electronic structure of the molecule from bonding to anti-bonding. The HOMO and LUMO levels of semiconducting polymers can be compared to the valence and conduction bands in inorganic semiconductors, and the difference between the HOMO and LUMO energy levels is defined as the material's energy gap. These energy levels are not only affected by the individual atoms but also by the surrounding environment due to other electronic interactions. Within tightly packed amorphous films, conjugated polymer energy levels are shifted due to a property known as energetic disorder [4], [5], though this effect is reduced in more ordered and crystalline materials.

Varying the components of a conjugated polymer chain can affect the HOMO and LUMO levels of the material, which can be utilised to tune the energy gap of the material and its charge transport properties. Polymers used for OPV applications tend to have an electron 'donor' component that is electron rich, and an electron 'accepting' component that is electron poor. Changing these components, or even just individual atoms, can affect these electron rich or poor areas, resulting in modified energy levels [6]–[10].

2.4 Photophysics of Organic Conjugated Polymers

Conjugated polymers are able to absorb photons in the visible region of the solar spectrum due their energy gap, which can be engineered by making atomic or component substitutions to the polymer as covered in **2.3 Conjugation**. This process is critical to polymer design for OPV devices, as it determines the range of wavelengths that the polymer can absorb.

2.4.1 Exciton Formation

The process of photon absorption promotes an electron from the HOMO level of the polymer to the LUMO level as long as the energy of the photon equals or exceeds the energy gap between these two levels. If the energy of the photon is sufficiently high, an electron is emitted from the material due to the photoelectric effect. This process is illustrated in **Figure 2.6**, an energy level diagram based on the Franck-Condon principle. Here, the ground state, S_0, and the excited state, S_1, consist of several quantised vibrational energy levels (n), forming a ladder of states that are labelled $S_{0,n}$ and $S_{1,n}$ respectively. For conjugated polymers, the S_0 state is the HOMO level (π bonding orbital) and the excited S_1 state is the LUMO level (π anti-bonding orbital). On absorption of a photon of energy equal or greater than the energy gap, an electron is promoted from S_0 to one of the vibrational energy levels in the excited state, $S_{1,n}$ in a process known as photoexcitation. If the electron is promoted to a vibrational energy level in the excited state where $n > 0$, the electron relaxes down via an ultra fast, radiationless process to the equilibrium state, $S_{1,0}$. This excess energy results in bond vibrations along the polymer chain.

On photoexcitation, the electron is promoted to the excited state and leaves behind a hole in its ground state. The electron and hole are still bound and are known as an exciton, which has a neutral charge overall. Excitons can recombine when the electron drops from the excited state to the ground state by radiative decay, over timescales of 0.1 - 1 ns [11]. This process is known as fluorescence, and emits a photon of equal or lesser energy that the absorbed photon, depending on if any relaxation processes have taken place, as shown in **Figure 2.6**.

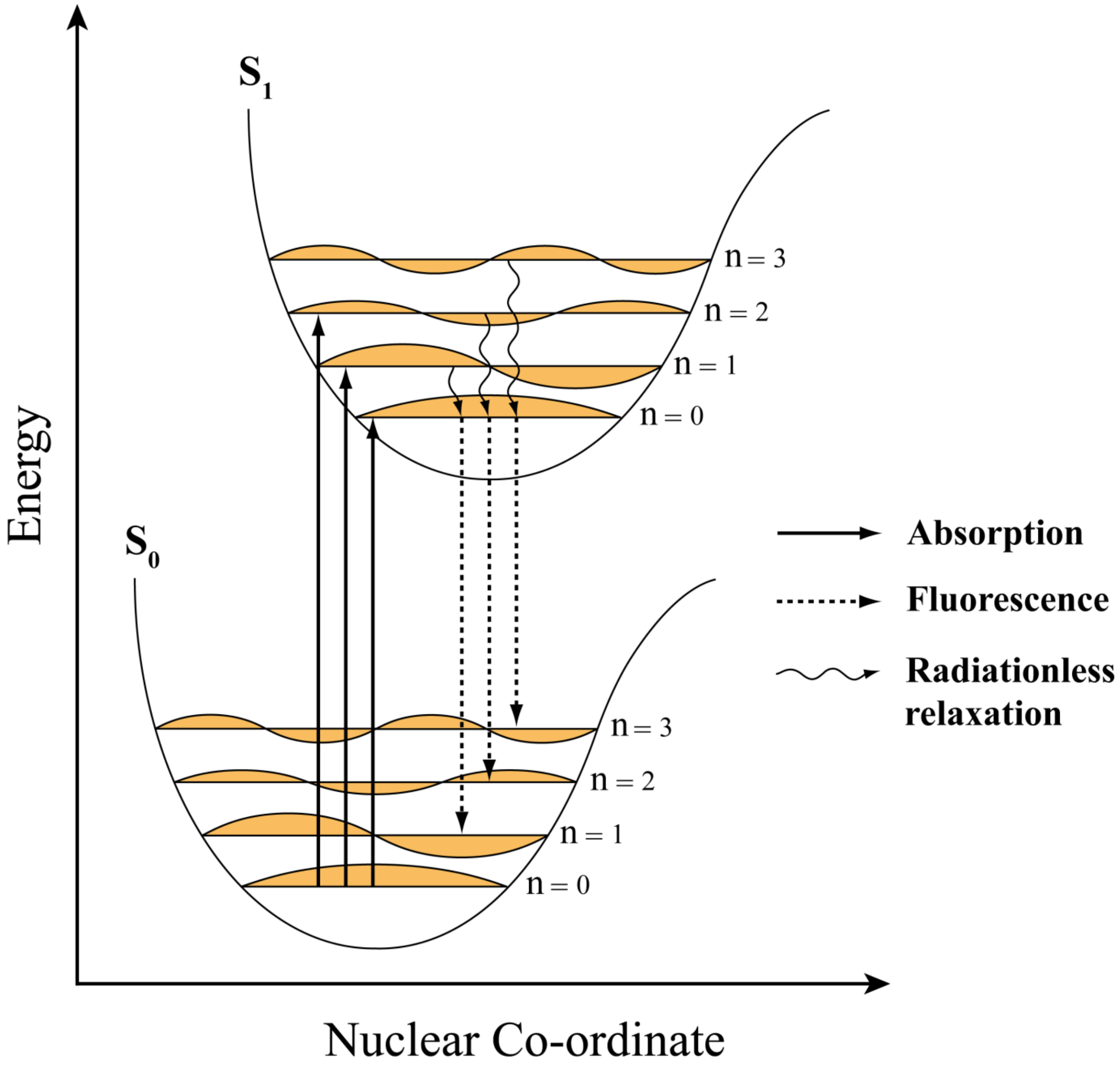

Figure 2.6 Franck-Condon energy level diagram for S_0 and S_1 energy levels with absorption, fluorescence and radiationless relaxation.

In comparison to inorganic semiconductors, conjugated polymers have a low dielectric constant, usually between 3 - 4 [12], [13], and so the charges that are generated on photoexcitation are not shielded from each other. This leads to a situation where the generated excitons are still strongly bound together by coulombic forces in a state known as an Frenkel excitons with a binding energy of ~ 0.3 eV [13]–[15].

2.4.2 Exciton Diffusion and Dissociation

Frenkel excitons cannot be dissociated thermally, as is the case for excitons in inorganic semiconductors, due to their strong binding energy. Dissociation can only occur at an interface between the conjugated polymer, henceforth referred to as the donor, and another material known as an electron acceptor [14]. However, the exciton must diffuse to this interface before recombination occurs. The efficiency of exciton diffusion is known as the diffusion co-efficient, D, and the distance an exciton can travel before recombination is known as the exciton diffusion length (L_D). The relationship between these two parameters is given in **Equation 2.1** below.

$$L_D = \sqrt{D\tau} \qquad \textbf{Equation 2.1}$$

Where τ is the photoluminescence decay lifetime of the excitons. If the average distance between the donor and acceptor interfaces are $\leq L_D$ then it is likely that the excitons will be dissociated into free charges at the interface. For conjugated polymers, the diffusion length is of the order of 10 nm [14]. If the exciton does not reach a donor-acceptor interface in time, geminate recombination occurs (where an electron and hole from the same exciton recombine), often with an associated photoluminescence. In OPV devices, this short diffusion length is overcome by the morphology of the donor-acceptor blend film, in which the two materials are intermixed at a similar length scale; a subject discussed in more detail in **2.5 Device Architecture**. The donor-acceptor blend film is also known as the 'active layer' of an OPV device.

Dissociation itself is the process by which the bound electron-hole pair (the exciton) is separated into free charge carriers. This process occurs at the interface between the conjugated polymer, the donor, and an acceptor material, providing the energy transfer is energetically favourable [14]. For this to be the case, the LUMO level of the acceptor needs to be at a higher energy than the LUMO level of the donor, and the difference between LUMO levels (ΔE) is equal to or greater than the exciton binding energy of 0.3 eV [13]–[15]. This difference in LUMO levels generates an energetic driving force which dissociates the excitons into a geminate pair (where the electron and hole originate from the same exciton), with the electron transferred to the LUMO level of the acceptor and the hole remaining in the HOMO level of the donor. This geminate pair is still bound, however, and is said to exist in a charge-transfer (CT) state. Recombination can still occur at this stage, and so the charges need to be further separated, which requires an internal electric field sufficient to break the coulomb attraction between them. This process is illustrated in **Figure 2.7**.

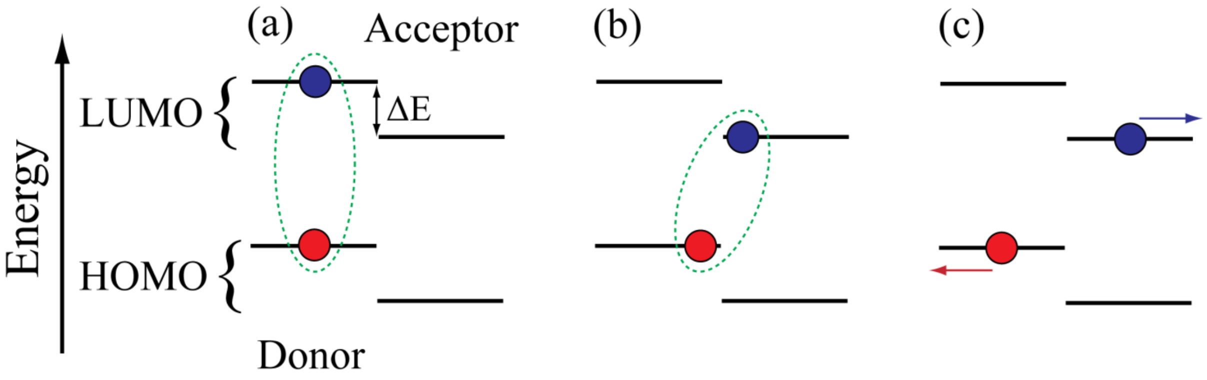

Figure 2.7 Process of exciton dissociation and charge separation at the donor-acceptor interface. **(a)** exciton diffusion to the interface, **(b)** exciton dissociation to the CT state and **(c)** exciton separation to form free charges and transport away from the interface. ΔE is the energy difference between the LUMO levels of the donor and acceptor.

2.4.3 Charge Transport

After the exciton has been dissociated, the free charges need to be transported through the donor and acceptor molecules to the electrodes for extraction. This process is facilitated by the delocalization of the HOMO and LUMO energy levels of the materials. However, energy level delocalization can only occur between states of equal energy, and so distortion in energy levels due to local effects, as discussed in **2.3 Conjugation**, results in separate localised states along the polymer chains. It is the charge transport between these localised states that determines the mobility of charge carriers in the conjugated polymers [4], and it is agreed that a hopping transport process is the dominant mechanism of charge transport through these localised states. This hopping process is dependent on both the energetic disorder of the localised states and also the distance between the hopping sites [4], [16]. Charges hop from one site to the next by tunnelling through the potential barrier separating the two sites. The barrier energy, and therefore the probability of the tunnelling taking place, is determined by differences in energy and location of the two sites. For charge carrier mobility to be improved, both of these parameters needs to be reduced as much as possible; a process that can be achieved through modifications to the chemical structure and processing conditions of the materials. Increasing conjugation length in the donor polymers, or decreasing the distance between charge transport sites between monomers, can decrease the distance between hopping sites [17], [18], and the intermolecular distance can be decreased by improving the polymer-polymer stacking in a film by improving the molecular crystallinity [19].

2.4.4 Charge Extraction

Upon exciton dissociation, separation and transport through the active layer, charge extraction may take place at the electrical contacts. This efficiency of this process is dependent on the work function (WF) of the contact materials matching the energy levels of the donor-acceptor materials, allowing for charge transport across the interface. In an ideal situation, the device electrodes should follow the rules below:

$$WF_{anode} = HOMO_{donor}$$ **Equation 2.2**

$$WF_{cathode} = LUMO_{acceptor}$$ **Equation 2.3**

Here, the WF of the anode is matched to the energy of the HOMO level of the donor for the extraction of holes, and the WF of the cathode is matched to the energy of the LUMO level of the acceptor for extraction of electrons. These interfaces, when matched in energy in such a way, are known as ohmic contacts.

However, the interfaces in OPVs are rarely so simple due to the wide variety of materials used. Metal oxides have both valence and conduction bands, and a Fermi level in the energy gap. When initially comparing materials against one another the vacuum level is aligned, as shown in **Figure 2.8**, but this depiction of energy levels only holds true when the materials are not in electrical contact with one another. When materials are brought into electrical contact, Fermi level alignment can occur under certain conditions, where the Fermi levels of the two materials equalize [20]. It is this Fermi level alignment that allows for efficient charge transfer across such interfaces.

The simplest example of Fermi level alignment is the metal-metal interface, as shown in **Figure 2.8 (a)**. In this instance, electrons flow from the metal with the highest WF to the lower WF metal. For metal-organic contacts, the Fermi levels can align in one of two ways; if the WF of the metal is equal to or lower than the upper critical Fermi level (Φ_P) level of the organic material, LUMO alignment occurs, and if the WF of the metal is equal to or higher than the lower critical Fermi level (Φ_N) of the organic material, HOMO alignment occurs, shown in **Figure 2.8 (b), (c)** respectively. If the WF of the metal is between these two values then the Fermi levels will not align and the materials will remain vacuum level aligned [21], which is detrimental to charge transport across the interface.

Energy level alignment at interfaces is critical to device performance, as poor alignment can lead to charge transfer losses due to barriers forming that inhibit extraction [22], [23]. Ohmic contacts form when there is no barrier to extraction due to well aligned energy levels, and Schottky-Mott contacts are formed when there is an energy barrier present. Charge transfer can still occur in Schottky-Mott contacts, but at the cost of device efficiency resulting from an increase in device series resistance.

In OPV devices, anode and cathode buffer layers are used to improve the energy level alignment between the active layer and the electrical contacts, and thereby improve device performance. Not only do these layers reduce the energy barrier for charge extraction and reduce charge leakage [24], [25], but they can also provide protection from ingress of oxygen and moisture into the active layer, which can cause degradation in performance (discussed in more detail in **2.9 OPV Stability and Degradation**). The buffer layer in between the active layer and the anode is known as the hole transport layer (HTL) and the buffer layer at the cathode is known as the electron transport layer (ETL). These buffer layer materials are covered in more detail in **2.6 Interface Materials**.

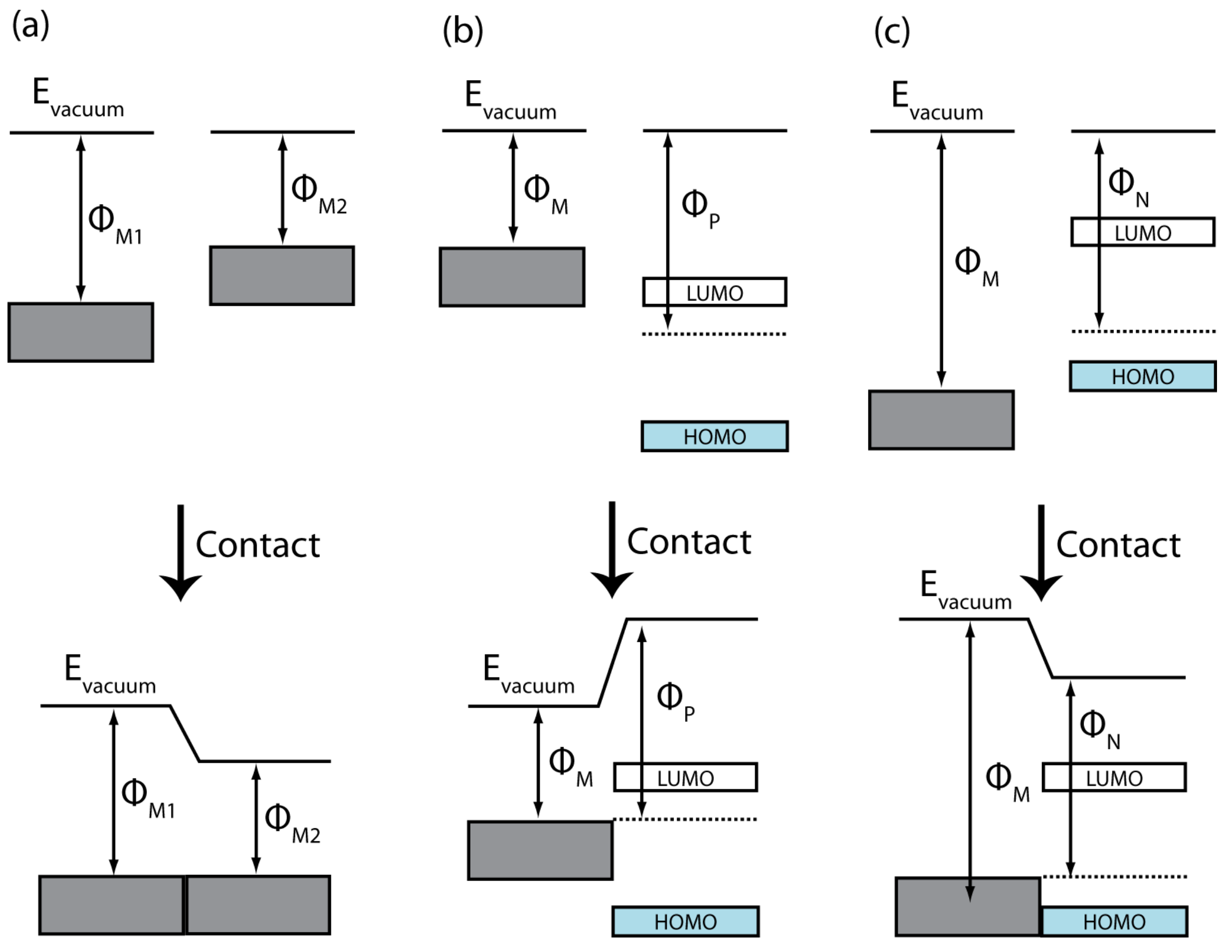

Figure 2.8 Energy level alignment pre and post contact for various interfaces. **(a)** metal-metal **(b)** metal-organic for LUMO level alignment and **(c)** metal-organic for HOMO level alignment. E_{vacuum} is the vacuum energy level, $\Phi_{M(1,2)}$ is the metal work function, Φ_P is the upper critical Fermi level and Φ_N is the lower critical Fermi level.

The alignment of energy levels on contact in an OPV device results in a built-in potential (V_{bi}) which dictates the direction of flow for charge carriers. Under open-circuit conditions, the open circuit voltage (V_{oc}) that results from the energy level alignment is determined from the energy levels of the donor and acceptor materials as in **Equation 2.4**.

$$V_{oc} = \frac{1}{e}\left(\left[E_{HOMO}^{Donor}\right] - \left[E_{LUMO}^{Acceptor}\right]\right) - 0.3V \qquad \textbf{Equation 2.4}$$

Where *E* is the energy of the corresponding energy levels of the donor and acceptor materials, *e* is the elementary charge, and 0.3 V is an empirical factor that accounts for the difference in V_{oc} and V_{bi}. This empirical factor has also been shown to be due to the binding energy of the Frenkel excitons [26]. Several other factors can affect V_{oc} in OPV devices, including recombination [27], light intensity [28], [29], charge transfer states [30] and device morphology [31], [32].

2.5 Device Architecture

OPV device architecture has evolved since its inception, when Ghosh et al. deposited an active layer of tetracene between aluminium and gold contacts in 1973 [33]. This device had an efficiency of only 10^{-4}%, but was further enhanced to 0.7% by replacing the tetracene with a merocyanine dye [34]. This single layer device was restricted in performance by a variety of factors, not least the lack of an electron accepting molecule and interfacial buffer layers.

From this single layer structure, the bilayer (or heterojunction) architecture was developed, where two materials were deposited on top of one another, which created an interface at which excitons could be dissociated. The first materials used were copper phthalocynanine (CuPc) and a perylene tetracarboxylic (PV) derivative, with an efficiency of 1% achieved in 1986 [35]. The use of indium tin oxide (ITO) as the anode contact material was also a significant advance, and this transparent conducting metal oxide is used in the majority of OPV devices to this day.

As previously mentioned in **2.4.2 Exciton Diffusion and Dissociation**, excitons in OPVs need to be dissociated within ~ 10 nm of generation before geminate recombination occurs. The bilayer structure, although it resulted in an increase in device efficiency compared to previous efforts, still resulted in significant losses due to recombination, as there was only one interface between the two materials. This problem was addressed with the introduction of the bulk heterojunction (BHJ) active layer morphology in 1995 [36], [37]. In a BHJ, the donor and acceptor materials are intimately mixed together as a result of being deposited together from the same solution, but still separated into two distinct phases, as shown in **Figure 2.9**. The arrangement of molecules within the blend film, also known as the microstructure, is dependent on several properties of the materials used. These include the molecular weight, polydispersity, the location and length of the solubilising side chains and the backbone planarity [38]. In addition to these intrinsic factors, the processing conditions can also make a significant difference to the resultant morphology of the active layer. For example, solvent choice has a crucial effect of drying rate and the length scale of the resulting phase separation between the two materials, and post deposition thermal annealing can improve the morphology after drying by causing controlled phase separation of the two materials in the BHJ. The ideal BHJ morphology has a length-scale of separation commensurate with the diffusion length of the excitons, but still have continuous phases of the two materials for the purposes of charge transport. However, the resultant microstructure may not be thermodynamically stable, and can change over time, particularly under the stresses of device operation and thermal cycling.

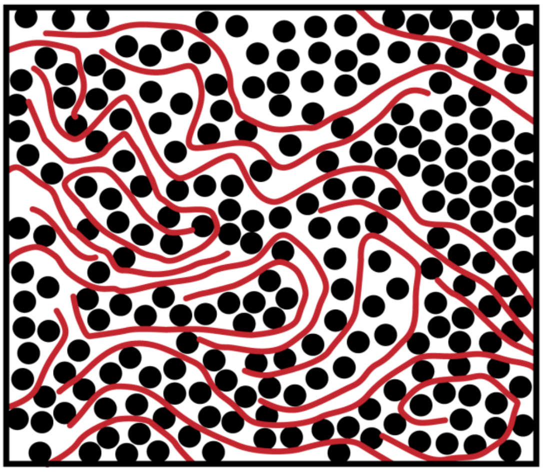

Figure 2.9 BHJ morphology. Red lines represent the donor polymer molecules and black circles represent acceptor molecules.

The standard OPV device architecture consists of several layers positioned between two electrodes, as shown in **Figure 2.10**. The anode commonly consists of ITO, and it is through this electrode that the device is illuminated, whereas the top contact is reflective and metallic, and is usually either aluminium or silver. In between these electrodes, buffer layers are incorporated to improve charge extraction by forming contacts whose energy levels are better matched to the materials in the active layer, with holes extracted at the ITO anode and electrons extracted at the metallic cathode. OPVs are fabricated onto substrates, manufactured from either glass or flexible plastics such as PET [39].

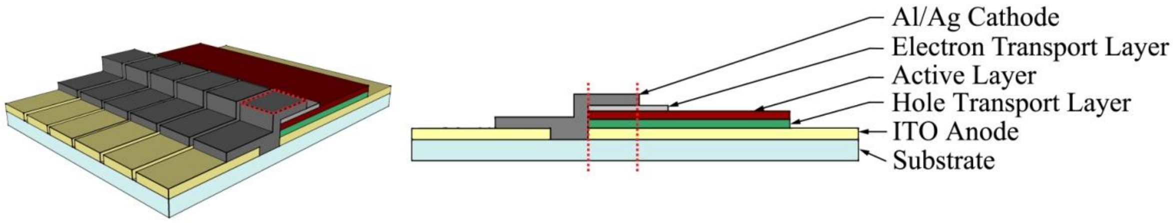

Figure 2.10 Standard architecture of OPVs as fabricated onto ITO coated substrates. Six pixels on the substrate are defined by the overlap of the electrodes and are outlined by red dotted lines.

An alternate OPV architecture has garnered much attention recently, as it offers the possibility of creating more stable devices with longer operating lifetimes [40], [41]. The so-called 'inverted' architecture utilizes ITO as a cathode and the reflective metallic contact as a cathode. This necessitates an alteration of the order of fabrication, with the electron and hole transport layers switching places as shown in **Figure 2.11**.

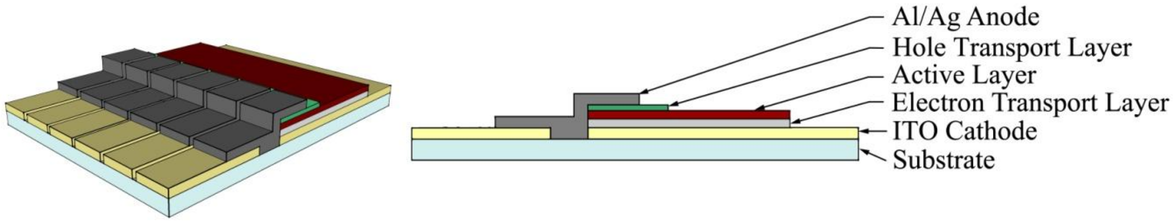

Figure 2.11 Architecture for inverted devices. ITO forms the cathode and the metallic top contact forms the anode.

2.6 Interface Materials

Interface materials play an important role in the performance of OPV devices as previously mentioned, improving the energy level alignment at the interfaces between the active layer materials and the electrical contacts. Interface materials come in two different general forms, hole transport layers (HTLs) and electron transport layers (ETLs); HTLs improve hole extraction and at the anode and ETLs improve electron extraction at the cathode. They also reduce charge leakage at the contacts by blocking unwanted charge transfer (electrons for the HTL and holes at the ETL). The following two sections cover the interface materials used in this thesis.

2.6.1 PEDOT:PSS

One of the most commonly used HTL layers is PEDOT:PSS, a mix of two polymers; the insoluble PEDOT, and PSS. With the addition of PSS, the PEDOT:PSS mixture becomes water soluble [42], and thin films can easily be processed from solution that exhibit several characteristics that are desirable for OPV interlayers: high conductivity, good film transparency and high charge carrier mobility [43]. The most commonly used PEDOT:PSS solution for OPV applications, Heraeus Clevios™ P VP AI 4083, has a ratio of 1:6 PEDOT to PSS, and a conductivity of the order of 10^{-3} Scm^{-1} [42]. PEDOT:PSS has a work function of ~ 5.2 eV [42], [44], and when used as a HTL between ITO and the active layer of OPVs, aids extraction of holes across the interface. This is achieved by planarising the surface of the ITO [45], reducing the number of shorts and inhomogeneities formed at the interface, and increasing the work function of the ITO anode; allowing energy level matching with the donor polymer in the active layer. Thin films of PEDOT:PSS are extremely hygroscopic [44], and post deposition thermal treatments are needed to remove any remaining water in the films.

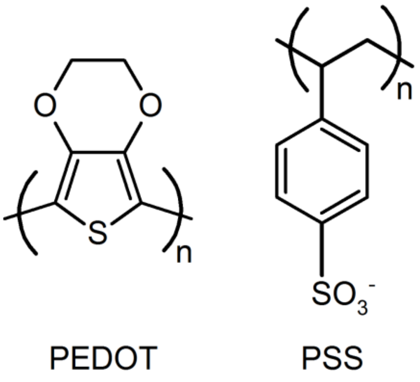

Figure 2.12 Chemical structure of PEDOT and PSS monomers. The most commonly used version of PEDOT:PSS in OPV fabrication has a blend ratio of 1:6.

2.6.2 Transition Metal Oxides

Transition metals are elements whose electronic structure and behaviour is dominated by partially filled d orbitals (which have a quantum number, *l*, of 3). Transition metal oxides (TMOs) have been studied for decades, but were only first utilised in the field of organic electronics by Tokito et al. in the late 1990's, where thin layers of molybdenum, vanadium and ruthenium oxides were used as interlayers in between the anode and organic material in organic light emitting diodes (OLEDs) [46]. This resulted in a significant increase in hole injection in the devices, and this initial work was followed by a series of papers on the use of TMOs in OLEDs and OPVs, used as both HTLs and ETLs [47]–[51].

TMOs exhibit many of the beneficial properties for OPV interlayer applications; high conductivity, high work function, good transparency (due to large energy gaps) and semiconducting properties. The position of the conduction and valence band energy levels of the TMOs used in this thesis are shown below in **Figure 2.13** in comparison to ITO, PEDOT:PSS and calcium.

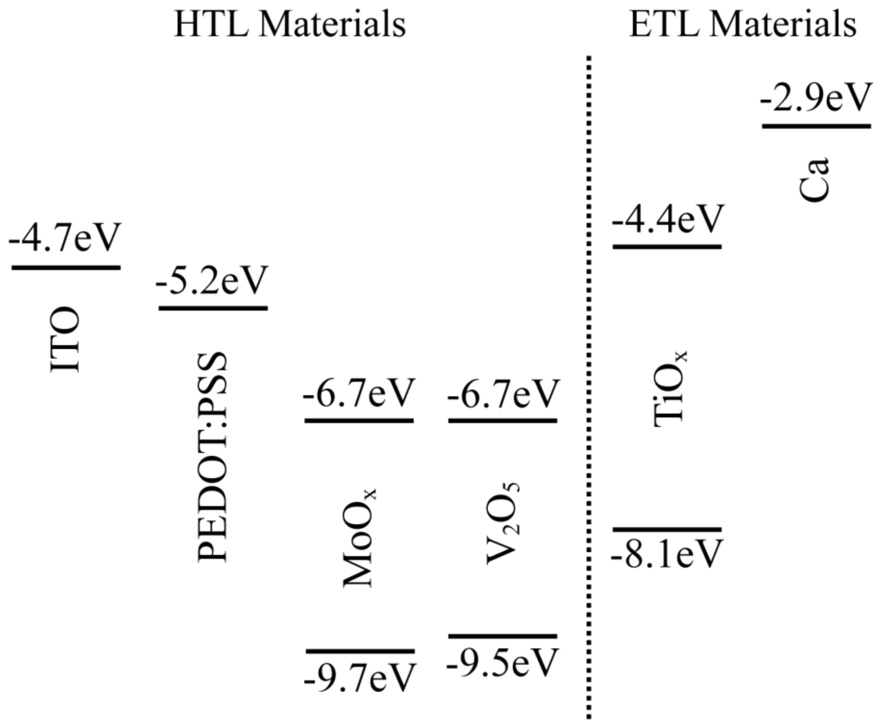

Figure 2.13 Energy levels for ITO [52], PEDOT:PSS [42], [44], MoO_x (molybdenum oxide) [53], V_2O_x (vanadium oxide) [53], TiO_x (titanium oxide) [51], and Ca (calcium). For the TMOs, the energy levels quoted are for freshly evaporated films that have not been exposed to oxygen or moisture. The materials can be grouped into two categories, HTL materials (MoO_x, V_2O_x and PEDOT:PSS) and ETL materials (TiO_x and Ca).

2.7 Active Layer Materials

Research into polymers for use in photovoltaics began in earnest in the 1970's and 1980's, fuelled by an interest in exploiting the natural organic compounds used in photosynthesis and the use of organic photoconductors in Xerographic photocopying. Initially the rather modest aims of the field were to find chemically stable materials with good optical absorption, and so the first materials to be used were merocyanine and phthalocyanine dyes [35], [54], the structures of which are shown in **Figure 2.14 (a), (b)** respectively. These materials could be deposited either by thermal evaporation or solution deposition to form thin films on conducting substrates, but only resulted in power conversion efficiencies of around 1% [35] at best.

The aspiration of the field (to achieve low cost, large area, flexible OPV modules) required the use of soluble materials that could be deposited using simple solution based methods. Polymer semiconductors were quickly earmarked as the most promising material technology; the ability to tailor the materials solubility, optical and electronic properties (including the HOMO and LUMO energy levels, and therefore the optical bandgap) closely met the demands of large scale OPV production. Although initial performance for polymer semiconductors in OPVs was rather unimpressive, the first generation of high solubility polymers such as polyphenylenevinylenes (PPV), and their derivatives, marked a milestone in OPV development. However, in pristine polymer semiconductors the charge generation efficiency was of the order of 0.1% due to the nature of the strongly bound Frenkel excitons, and the charge separation mechanism was driven largely by the presence of defects or impurities [55]. A major breakthrough in the field was made when polymer semiconductors were combined with another material having a high electron affinity, an acceptor, which allowed for charge separation of the bound excitons in the polymer at the interface between the two materials.

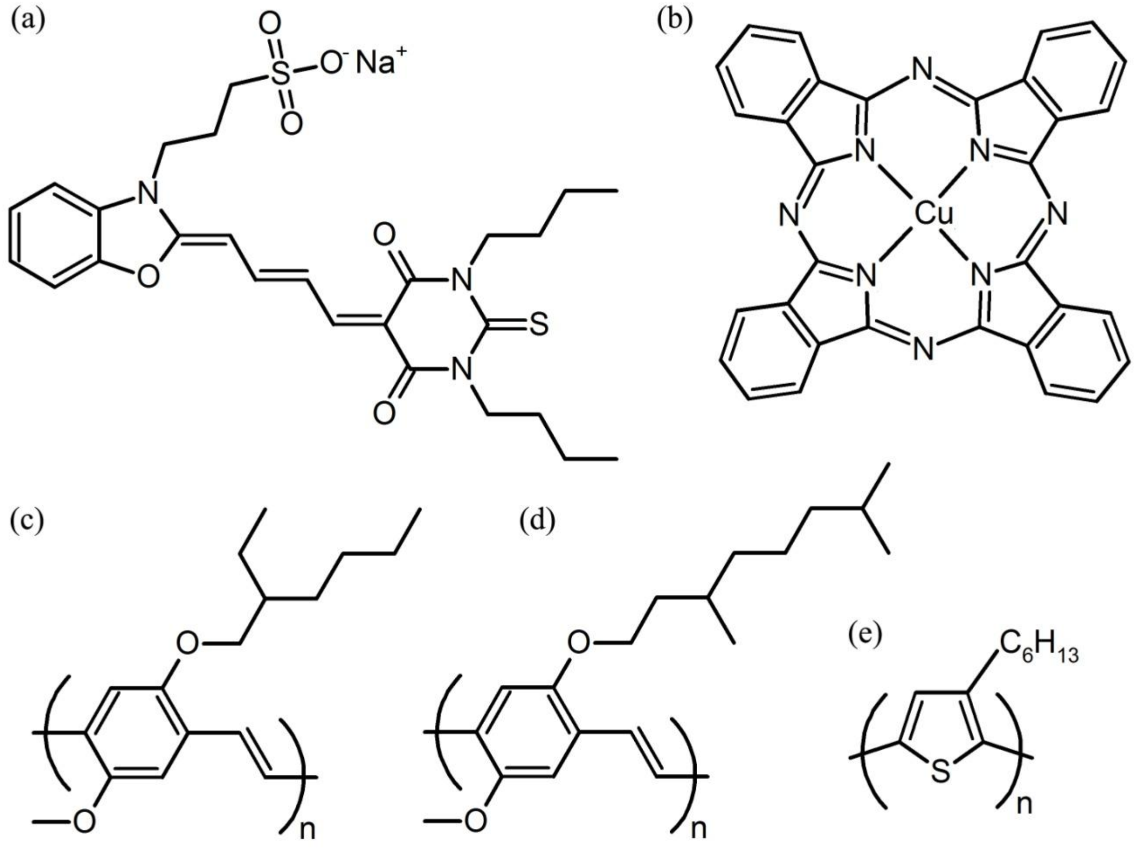

Figure 2.14 Chemical structures of the dyes **(a)** merocyanine, **(b)** phthalocyanine and the polymers **(c)** MEH-PPV, **(d)** MDMO-PPV and **(e)** P3HT.

This approach led directly to the development of the BHJ device, as the intermixing of the two materials resulted in more charge separation at interfaces throughout the active layer. The first BHJ architecture OPV devices, developed in 1995, showed efficiencies of 2.9% [37] (for monochromatic light, not the now standard AM1.5), and were based on a MEH-PPV:$PC_{60}BM$ (poly(2-methoxy-5-(2′-ethyl-hexyloxy)-1,4-phenylenevinylene):Phenyl-C61-butyric acid methyl ester) active layer. The structure of MEH-PPV is shown in **Figure 2.14 (c)**. This was also the first instance of PCBM being used as an acceptor in an OPV. Remarkably, after 17 years, PCBM is still the most widely used acceptor material in BHJ OPV devices due to its high solubility, favourable energy levels and performance, a subject that is covered in more detail in **2.7.2 Fullerenes.**

In 2001, Shaheen et al showed that the efficiency of a BHJ OPV based on another PPV derivative, MDMO-PPV (structure shown in **Figure 2.14 (d)**), and PCBM was drastically affected by the active layer morphology [56]. By optimizing the BHJ morphology of the active layer through careful choice of solvents, a device efficiency of 2.5% under AM1.5 illumination was achieved - an almost threefold increase over any previously reported device efficiencies.

Unfortunately, the relatively large bandgap of PPV type polymers, in combination with their limited charge transport mobility, led to maximum attainable efficiencies of around 3%. Considering that commercial applications require efficiencies around 10%, this limitation provided the impetus to develop the next generation of semiconducting polymers. Poly(3-hexylthiophene) (P3HT), whose structure shown in **Figure 2.14 (e)**, and other poly-alkyl-thiophenes emerged as a promising next step. P3HT was one of the first conjugated polymers studied for use in OPVs, but it was only with the discovery of the effect of post-production thermal treatments that device efficiencies of around 3.5% were reported [57]. This development led to P3HT becoming the new workhorse of OPV development, facilitated by the wide availability of the polymer from multiple manufacturers as the structure was not patented. The efficiency of P3HT:PCBM based OPV devices quickly rose to around 5% [19] due to improvements in polymer regioregularity [58] and molecular weight, optimizing the annealing temperature [19] and reducing interface losses.

However, as with the PPV based polymer systems, the limitations of P3HT were quickly discovered. P3HT has excellent absorption and charge transport properties, and as such an active layer of between 100 - 200nm absorbs most incident light and results in fill factors of around 70% [59]. Unfortunately, the energy levels of P3HT are not well suited to PCBM, and so the highest reported values for V_{oc} were around 0.66V [60].

The most recent improvements in polymer:fullerene solar cell efficiencies and stabilities have largely come from the synthesis of new polymers which have lower lying HOMO levels and smaller band gaps. A lower lying HOMO level has the twin benefit of allowing more of the energy of each photon to be harvested due to better energy alignment to PCBM [15], whilst also improving the chemical stability of the material by making oxidation more difficult. As such, there has been a recent trend in the development of polymers having a lower lying HOMO levels in the region of -5.10eV to -5.50eV, such as PCDTBT (poly[9-(heptadecan-9-yl)-9H-carbazole-2,7-diyl-alt-(4′,7′-di-2-thienyl-2′,1′,3′-benzothiadiazole)-5,5-diyl]) [61] and PTB7 (poly({4,8-bis[(2-ethylhexyl)oxy]benzo[1,2-b:4,5-b′]dithiophene-2,6-diyl}{3-fluoro-2-[(2-ethylhexyl)carbonyl]thieno[3,4-b]thiophenediyl})) [62].

One family of polymers that have attracted a lot of interest in recent years for OPV applications are the carbazole co-polymers. The most commonly studied carbazole co-polymer, PCDTBT, has achieved device efficiencies of 7.2% [63]. Several studies of this polymer have optimising the device structure [25], [50], [64]–[66] and characterised device stability and degradation pathways [61], [67], [68], with extrapolated lifetimes of up to 10 years reported [68]; all of which make it an attractive proposition for efficient, stable OPV material. The structure of PCDTBT can be altered to improve its solubility in common organic solvents such as chloroform, chlorobenzene and dichlorobenzene by the addition of an octyloxy substituent on the benzothiadiazole acceptor unit [69]. The resulting polymer has increased solubility while maintaining high device performance when blended with a $PC_{70}BM$ acceptor [69]. Extra thiophene moieties can also be added along the polymer backbone, which redshift the absorption through a reduction in the optical energy gap by increasing the intramolecular charge transfer along the polymer backbone [70]. Other substitutions can also be carried out to alter the HOMO and LUMO energy levels and bandgap of PCDTBT; the thiophene units can be replaced with selenophenes to improve the charge carrier mobility through enhanced interchain interactions [71], and the carbazole unit can be replaced with a polyfluorene unit which has enhanced thermal and chemical stability [72]–[75]. The chemical structures of these polymers and the moieties that they consist of are included **2.7.1 Polymer List**.

2.7.1 Polymer List

The following is a list of the chemical names and structures of all the polymers used within this thesis.

PCDTBT

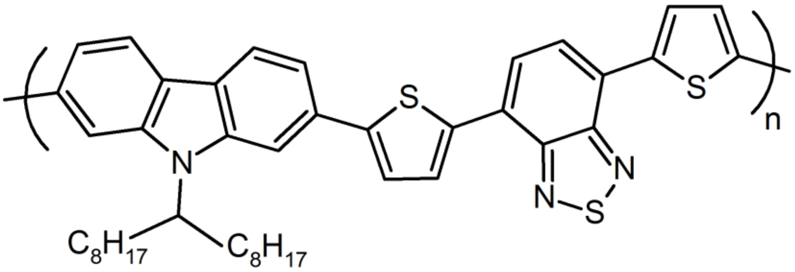

Figure 2.15 PCDTBT - Poly[N-9’-heptadecanyl-2,7-carbazole-alt-5,5-(4’,7’-di-2-thienyl-2’,1’,3’- benzothiadiazole)]

PCDTBT-8

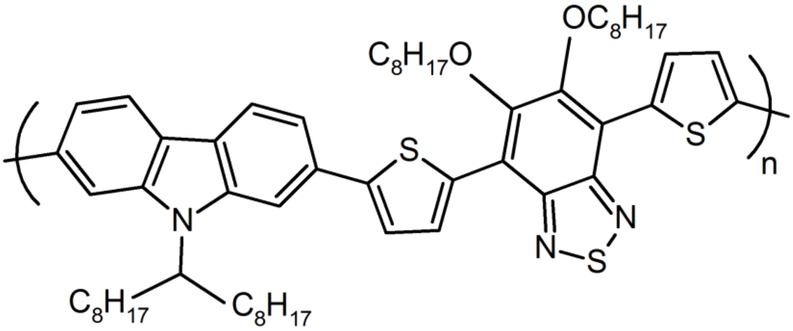

Figure 2.16 PCDTBT-8 - poly[9-(heptadecan-9-yl)-9H-carbazole-2,7-diyl-alt-(5,6-bis(octyloxy)-4,7-di(thiophen-2-yl)benzo[c][1,2,5]thiadiazole)-5,5-diyl] - the addition of an octyloxy substituent on the benzothiadiazole of PCDTBT improves the solubility of the polymer [69].

PCDSeBT-8

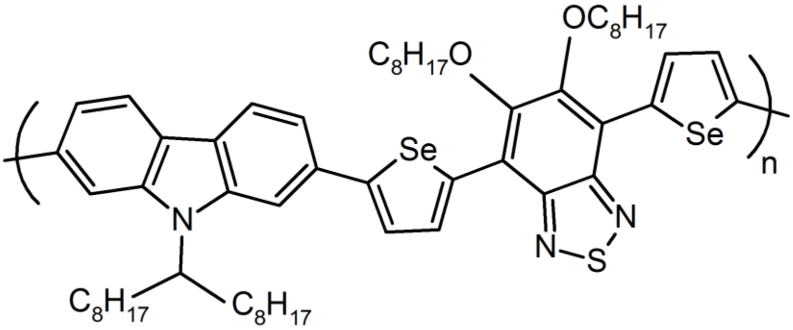

Figure 2.17 PCDSeBT-8 - (poly[9-(heptadecan-9-yl)-9H-carbazole-2,7-diyl-alt-(5,6-bis(octyloxy)-4,7-di(selenophen-2-yl)benzo[c][1,2,5]thiadiazole-5,5-diyl]). The same chemical structure as PCDTBT-8, but with the thiophenes replaced with selenophenes.

PFDT2BT-8

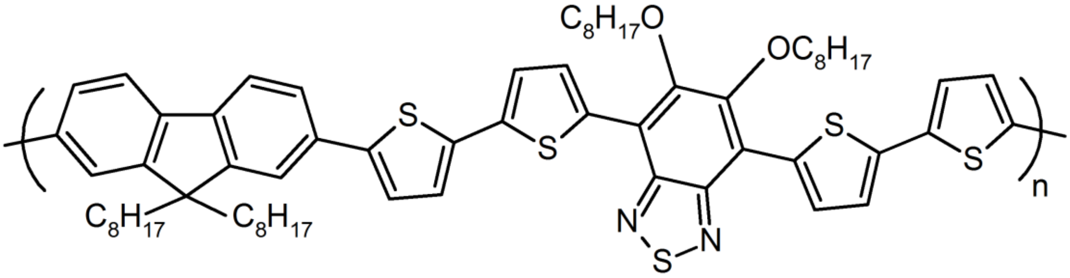

Figure 2.18 PFDT2BT-8 - (poly[9,9-dioctylfl u- orene-4,7-alt-(5,6-bis(octyloxy)-4,7-di(2,2′-bithiophen-5-yl) benzo[c][1,2,5]thiadiazole)-5,5-diyl]) - a fluorene replaces the carbazole in PCDTBT-8, with an extra thiophene on either side of the benzothiadiazole.

PTB7

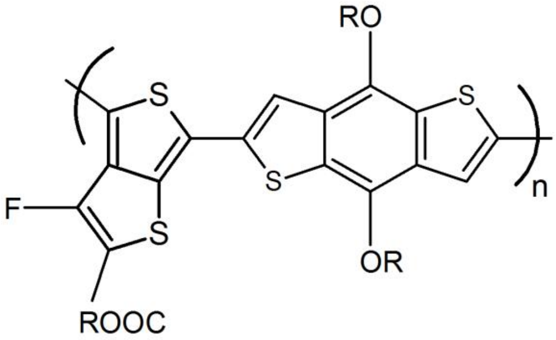

Figure 2.19 PTB7 - **(**poly({4,8-bis[(2-ethylhexyl)oxy]benzo[1,2-b:4,5-b′]dithiophene-2,6-diyl}{3-fluoro-2-[(2-ethylhexyl)carbonyl]thieno[3,4-b]thiophenediyl})). A high efficiency polymer that has achieved *PCEs* of 9.2% with an inverted device architecture [76].

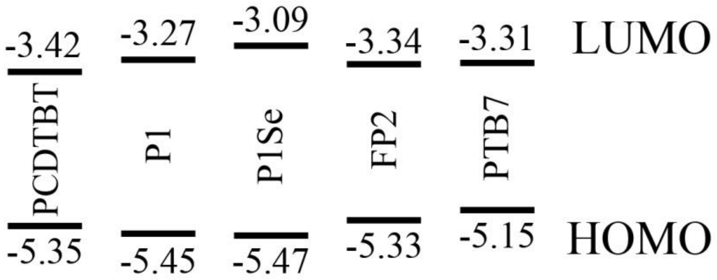

Figure 2.20 HOMO and LUMO energy levels for the above polymers. Data for PCDTBT and analogues acquired by Department of Chemistry, University of Sheffield by cyclic voltametry. Data for PTB7 from [62].

2.7.2 Fullerenes

$PC_{60}BM$ and its variants are the ubiquitous electron accepting material, found in the vast majority of OPV devices. Based on a buckminsterfullerene [77], a spherical cage of sixty carbon atoms with a solubilising methyl ester group attached, as shown in **Figure 2.21 (a)**, it offers several physical and electrical characteristics that make it a near perfect electron accepting material. When paired with organic polymers, photoinduced charge transfer from the polymer to the fullerene is extremely fast and efficient [78], and it has a very high electron mobility [79]. The LUMO level energy of $PC_{60}BM$ is - 4.3eV [25], making it an excellent match for many polymers, crucially having the required energy difference between LUMO levels of greater than 0.3 eV to allow for exciton dissociation.

Another form of PCBM that has also been used as an electron acceptor material utilises a buckminsterfullerene with 70 carbon atoms, and as such is known as $PC_{70}BM$, shown in **Figure 2.21 (b)**. Due to the lack of spherical symmetry in the C_{70} fullerene, an increase in absorption co-efficient over the visible range of the solar spectrum is observed [80]. This is beneficial to OPV devices, as although the majority of absorption is due to the polymer in OPVs, the active layer blend is often composed of a significantly larger weight fraction of PCBM to increase the number of donor-acceptor interfaces throughout the film. Therefore, the increased light absorption of $PC_{70}BM$, when compared to $PC_{60}BM$, increases the charge generation rate and leads to an enhancement of J_{sc}, and more therefore efficient devices.

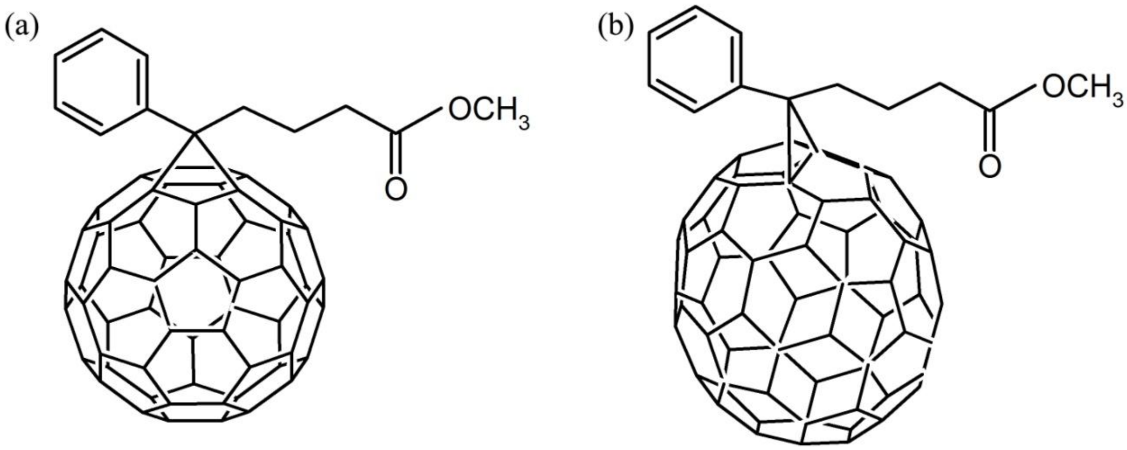

Figure 2.21 Chemical structure of the most commonly used electron acceptor materials, **(a)** $PC_{60}BM$ and **(b)** $PC_{70}BM$.

2.8 Ambient Processing

Currently, the majority of OPVs are fabricated in nitrogen atmosphere gloveboxes to exclude oxygen and moisture from the process due to their detrimental effects of device performance and long-term stability [81]–[83]. However, this is not a feasible situation for the eventual scale up of production to produce OPV devices for mass manufacturing applications, as it adds significantly to the embodied energy cost of the devices. An extra degree of complexity is added in large scale production as most results for OPVs are from small scale, laboratory produced devices, tested under extremely restrictive conditions. Laboratory devices achieve high performance through delicate and highly empirical relationships between multiple fabrication parameters such as solvent choice, drying speeds, active layer and interface materials and substrate/encapsulation materials. To scale up the fabrication process, which also involves speeding up the process, requires re-evaluating the inter-relationships between all these parameters, with added complexity due to processing in ambient conditions. Currently, attempts to scale up production of OPVs from lab to industrial scale have led to drops in *PCE* [84], [85]. Also, the solvents regularly used in OPV fabrication, such as chlorobenzene and dichlorobenzene, are extremely toxic, and would need to be replaced by less toxic alternatives in a commercial setting.

There are several reported lab investigations into ambient processing of OPVs, all of which utilize a P3HT:fullerene active layer system [83], [86], [87]. This is because the degradation mechanisms and performance of the P3HT:fullerene system are very well understood, and as such the effects of ambient processing can be separated from other device performance effects more readily.

Ambient processed devices with a P3HT:PCBM active layer exhibit lower efficiency than those processed in an inert atmosphere [87]. The loss in device performance is primarily due to a reduced *FF* as a result of oxygen doping of the active layer blend. Ambient processing decreases both hole and electron mobility, with hole transport in P3HT reduced by oxygen doping introducing trap states in the polymer, and electron mobility is reduced by a factor of ~ 2 [83]. However, it has been shown that thermal annealing treatments can successfully reduce electron and hole trap densities introduced through ambient processing [83].

The most successful fabrication technique so far, in terms of scalability, is roll-to-roll (R2R) processing. The main principles in roll-to-roll printing are so called 'wet films through contact' printing, generally used for the top and bottom electrodes, and 'wet films without contact' printing, used for solution processed layers. Wet films through contact printing is where wet films of material are transferred from a patterned roller to a substrate via direct contact, as opposed to without contact printing where there is no contact between the substrate and depositing apparatus. Multi-layer OPVs are fabricated in one continuous process onto a flexible poly(ethyleneterephthalate) (PET) sheet with a printed pattern of ITO forming the bottom electrode. Krebs et al successfully scaled up an inverted device based on a ITO/ZnO/P3HT:PCBM/PEDOT:PSS/Ag architecture from the laboratory to vacuum free R2R with little loss in cell efficiency [85]; 2.7% efficient cells for devices fabricated in a lab, and 2.3% for device fabricated using R2R techniques. The ZnO, PEDOT:PSS and active layers were deposited using normal printing techniques, the top Ag cathode was deposited using screen-printing techniques and the devices were encapsulated using an acrylic adhesive and PET foil.

Though R2R printing offers a promising method for producing OPV devices on an industrial scale, limited device efficiency due to material limitations and short device lifetimes due to insufficient encapsulation means that further developments are needed before commercialization is feasible.

2.9 OPV Stability and Degradation

Over the past decade, increased effort has been made to further the understanding of degradation mechanisms in OPVs and how this affects their operating lifetimes. Extensive studies of OPVs based on the polymer P3HT have been made [68], [88]–[90], with lifetimes of up to 3 years reported [68]. More recently, outdoor interlaboratory studies have produced devices with lifetimes in excess of 5 years [91], and laboratory studies have extrapolated device lifetimes of up to 10 years for other polymer systems [68], [92].

Much of the early work done on the lifetimes of devices was before the introduction of standardised methodologies, introduced after the publication of a consensus paper on testing protocols and the advent of the annual International Summit on OPV Stability (ISOS) [93]. These standardised methodologies have provided a framework for testing procedures and how data is reported, increasing the rigor of a variety of tests, from shelf-life to outdoor interlaboratory testing. Due to the absence of such protocols prior to ISOS, it is challenging to compare many of the published results obtained from different laboratories.

However, even though it is difficult to judge how studies from separate labs correlate, it is still possible to obtain important information from earlier work. Early on, many of the improvements in performance of OPVs came at a cost of stability, through the introduction of new device degradation pathways. Most notably, the use of reactive metal electrodes, such as calcium, and the development of interface materials such as PEDOT:PSS [94], LiF [95] and PCBM acceptors were (in some cases) found to decrease device stability. Many of these interlayers provide critical failure points within devices due to effects such as the formation of charge extraction barriers [90], physical delamination at the interface [90], [96], and the possible introduction of defect trap sites [51], [97]. However, more recently, other improvements, such as the use of active layer polymers with lower lying HOMO levels, improve device stability by making oxidation of the polymer backbone more difficult. Increased device lifetimes have also been achieved by altering the interfaces between the electrode and the organic active layer through the use of metal oxides [63], [67], [98], [99]. Whilst these metal oxides often introduce new degradation pathways themselves, it is important to obtain physically and chemically stable interfaces between the electrodes and the organic active layer.

There are many degradation paths in OPV devices, both chemical and physical, that lead to a reduction in device performance over time. Chemical reactions can occur both in the dark as well as under illumination, due to the chemical mixing of the constituent materials of the OPV, for example PEDOT:PSS etching of ITO [100]. Oxygen and moisture play an important role in device degradation, as many of the materials used in OPVs are reactive with these species; for example where Ca/Al cathodes are used, calcium or aluminium can react with oxygen, which forms insulating areas at the cathode interface, reducing charge extraction and therefore device performance [101]. Chemical reactions under illumination include photo-oxidation (in the presence of oxygen/water) and photolysis (in the absence of oxygen/moisture).

The following sections will cover the major degradation pathways present in OPVs in more detail.

2.9.1 Photochemical Reactions

As previously mentioned, organic conjugated polymers are sensitive to oxygen and moisture, and undergo chemical reactions when exposed to light in the presence of these reactive species. Photo-oxidation of a conjugated polymer results in the polymer chain undergoing scission, breaking conjugation along the backbone and leading to a loss of light absorption. Due to the loss of light absorption and the subsequent colour change of the polymer, this process is known as photobleaching. Photobleaching takes place in OPV devices whenever they are illuminated, and so excluding oxygen and moisture is vital to preventing this degradation mechanism.

2.9.2 Trap Formation

Trap formation can take two forms; either deep or shallow. Deep trap formation results from either photochemical reactions in organic materials or from metal ion diffusion from the electrodes. These deep traps cause recombination events in the active layer film, resulting in device performance loss through a reduction in V_{oc}, FF and J_{sc}.

Shallow trap formation is also due to photochemical reactions, but can also be caused by molecular reorganization, resulting in an increase in energetic disorder in the system. Shallow traps do not cause recombination, but instead trap charges and result in space-charge build up at interfaces, impacting all device operating parameters. One cause of shallow traps is annealing polymers above their glass transition temperature (T_g), which causes phase separation.

2.9.3 Phase Separation

Annealing an active layer film above the T_g of its organic materials induces phase separation. This process can cause the polymer and fullerene to separate from one another into large polymer and fullerene domains, rather than forming an intermixed state. If the size of these domains exceeds the exciton diffusion length, then losses due to recombination can reduce the device efficiency. In many cases however, the T_g of many polymer systems are in excess of 100^{o}C, and so are greater than the practical operating temperatures of OPVs.

2.9.4 Delamination

Delamination is a degradation process that can occur at any of the interfaces in the device, and is caused by thermo-mechanical stresses [102]. Delamination can result in energetic barriers forming to charge transport and extraction [90], [96], leading to complete loss of device operation in the areas that are affected. Due to the rigid substrates on which many OPV devices are fabricated, mechanical delamination is not an issue unless the devices are in physical/mechanical contact with the outside world. However, this is a cause for concern where OPVs are fabricated onto flexible substrates, where repeated bending can cause delamination if the many layers in the device do not have good adhesion, or the fabrication process itself includes repeated bending , such as in R2R.

2.9.5 Encapsulation

The lifetime of OPVs can be significantly improved by encapsulating the device, whilst also improving the mechanical stability and scratch resistance. Encapsulation protects the OPV from oxygen and moisture (two major degradation sources), and also from UV radiation. Ideally, encapsulation would seal the OPV in a glass container with an inert atmosphere to completely exclude oxygen and water as shown in **Figure 2.22**, but unfortunately this is not practical in many cases.

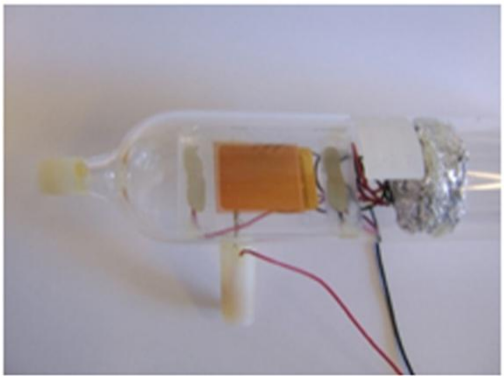

Figure 2.22 A 10 cm^2 OPV encapsulated in a glass ampoule sealed under high vacuum [103]. The electrical connections to the inside of the ampoule are made using tungsten glass seals. The sealing procedure is laborious, but the container is impervious to both oxygen and water. The white glued caps are protecting the glass seal and does not represent sealing itself. The aluminium foil is a heat shield necessary for the sealing procedure.

The most common form of encapsulation involves encasing the device between two sheets of glass, one being the device substrate, using a glue to seal the edges. Lifetimes of 5600 hours have been reached for OLEDs using this technique [104], and requirements for oxygen and moisture penetration rates are more stringent for OLEDs than OPVs [105]. Although using glass substrates and encapsulation sacrifices flexibility in the devices, glass has an extremely low transmission rate of oxygen and water, which cannot currently be matched by flexible alternatives.

Flexible encapsulation methods are of use for R2R processing. Polyethylene terephthalate (PET) was one of the first materials studied for flexible encapsulation, but the results were far from promising as the encapsulation technique itself reduced device lifetime [106]. Later studies using a R2R process also used PET substrates and encapsulated films with far more success [85], with lifetimes measured in tens of hours in air and hundreds of hours in a dry nitrogen atmosphere.

Cros et al. [105] measured the lifetimes of both standard and inverted architecture OPV devices to calculate the barrier water vapour transmission rate (WVTR) requirements for long device lifetimes. They discovered that for lifetimes of several years, the necessary WVTR of the encapsulating material must be of the order of 10^{-3} $gm^{-2}day^{-1}$ or lower. This is considerably lower than the number often quoted for OLEDs of 10^{-6} $gm^{-2}day^{-1}$ [96]. This has been correlated by results showing that lifetimes of up to 13500 hours are achievable for devices encapsulated with a triple layer of SiNx/parylene, which has a WVTR of $3x10^{-3}$ $gm^{-2}day^{-1}$ [107].

2.9.6 Decay Behaviour

The degradation of OPVs is influenced by all the mechanisms covered in this section to different degrees, determined by material choices and processing conditions. Determining the dominant sources of degradation, and minimizing or eliminating them is one of the main goals of research into OPVs.

For devices with a standard architecture, as covered in **2.5 Device Architecture**, a polymer:fullerene active layer and a metal cathode such as Ca/Al, a common *PCE* decay curve is observed as shown in **Figure 2.23**. Typically, the OPV device undergoes a period of rapid, exponential efficiency loss that is known as the burn-in period. The mechanisms that cause this burn-in period are discussed in more detail in **Chapter 5 : Hole Transport Layer Laboratory Lifetime Study**. After burn-in, a period of linear decay is often observed that can end abruptly if the encapsulation fails. The lifetime of devices is calculated from the point at which the burn-in period ends. The T_{80} lifetime is then defined by the point at which device efficiency falls to 80% of the value at the beginning of the linear decay period. The less frequently used T_{50} lifetime is similarly defined as the point at which the efficiency drops to 50% of this initial value. Various tools and methods are used to probe the causes of degradation and efficiency decay in OPV devices, and those utilised in this thesis are covered in **Chapter 3 : Experimental Methods**.

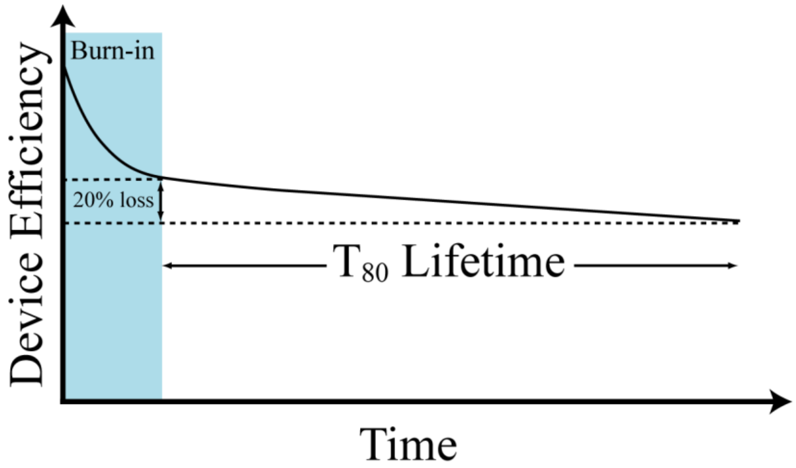

Figure 2.23 Typical decay curve for an OPV with a standard architecture. The OPV undergoes an initial rapid loss of efficiency, known as the burn-in period, and thereafter a linear period of decay is observed. The T_{80} lifetime is defined by the point at which the efficiency drops by 20% after burn-in.

2.10 References

[1] W. Heisenberg, “Uber den anschaulichen Inhalt der quantentheoretischen Kinematik und Mechanik,” *Zeitschrift fur Phys.*, vol. 43, no. 3–4, pp. 172–198, Mar. 1927.

[2] R. M. Eisberg and R. Resnick, *Quantum physics of atoms, molecules, solids, nuclei, and particles*. New York: Wiley, 1974.

[3] S. W. Jonathan Clayden, Nick Greeves, *Organic Chemistry*, 2nd ed. Oxford: Oxford University Press, 2012.

[4] N. Tessler, Y. Preezant, N. Rappaport, and Y. Roichman, “Charge Transport in Disordered Organic Materials and Its Relevance to Thin-Film Devices: A Tutorial Review,” *Adv. Mater.*, vol. 21, no. 27, pp. 2741–2761, Jul. 2009.

[5] W. R. Salaneck, R. H. Friend, and J. L. Brédas, “Electronic structure of conjugated polymers: consequences of electron–lattice coupling,” *Phys. Rep.*, vol. 319, no. 6, pp. 231–251, Oct. 1999.

[6] C. H. Woo, P. M. Beaujuge, T. W. Holcombe, O. P. Lee, and J. M. J. Fréchet, “Incorporation of furan into low band-gap polymers for efficient solar cells.,” *J. Am. Chem. Soc.*, vol. 132, no. 44, pp. 15547–9, Nov. 2010.

[7] A. Bhuwalka, J. F. Mike, M. He, J. J. Intemann, T. Nelson, M. D. Ewan, R. A. Roggers, Z. Lin, and M. Jeffries-EL, “Quaterthiophene–Benzobisazole Copolymers for Photovoltaic Cells: Effect of Heteroatom Placement and Substitution on the Optical and Electronic Properties,” *Macromolecules*, vol. 44, no. 24, pp. 9611–9617, Dec. 2011.

[8] B. Kim, H. R. Yeom, M. H. Yun, J. Y. Kim, and C. Yang, “A Selenophene Analogue of PCDTBT: Selective Fine-Tuning of LUMO to Lower of the Bandgap for Efficient Polymer Solar Cells,” *Macromolecules*, vol. 45, no. 21, pp. 8658–8664, Nov. 2012.

[9] S. Das, P. B. Pati, and S. S. Zade, “Cyclopenta[c]thiophene-Based D–A Conjugated Copolymers: Effect of Heteroatoms (S, Se, and N) of Benzazole Acceptors on the Properties of Polymers,” *Macromolecules*, vol. 45, no. 13, pp. 5410–5417, Jul. 2012.

[10] S. Beaupré, A. Pron, S. H. Drouin, A. Najari, L. G. Mercier, A. Robitaille, and M. Leclerc, “Thieno-, Furo-, and Selenopheno[3,4-c]pyrrole-4,6-dione Copolymers: Effect of the Heteroatom on the Electrooptical Properties,” *Macromolecules*, vol. 45, no. 17, pp. 6906–6914, Aug. 2012.

[11] T. M. Clarke and J. R. Durrant, “Charge photogeneration in organic solar cells.,” *Chem. Rev.*, vol. 110, no. 11, pp. 6736–67, Nov. 2010.

[12] J.-W. van der Horst, P. Bobbert, P. de Jong, M. Michels, G. Brocks, and P. Kelly, “Ab initio prediction of the electronic and optical excitations in polythiophene: Isolated chains versus bulk polymer,” *Phys. Rev. B*, vol. 61, no. 23, pp. 15817–15826, Jun. 2000.

[13] J.-L. Brédas, D. Beljonne, V. Coropceanu, and J. Cornil, “Charge-transfer and energy-transfer processes in pi-conjugated oligomers and polymers: a molecular picture.,” *Chem. Rev.*, vol. 104, no. 11, pp. 4971–5004, Nov. 2004.

[14] B. C. Thompson and J. M. J. Fréchet, “Polymer-fullerene composite solar cells.,” *Angew. Chem. Int. Ed. Engl.*, vol. 47, no. 1, pp. 58–77, Jan. 2008.

[15] M. C. Scharber, D. Mühlbacher, M. Koppe, P. Denk, C. Waldauf, A. J. Heeger, and C. J. Brabec, “Design Rules for Donors in Bulk-Heterojunction Solar Cells—Towards 10 % Energy-Conversion Efficiency,” *Adv. Mater.*, vol. 18, no. 6, pp. 789–794, Mar. 2006.

[16] H. Bässler, “Charge Transport in Disordered Organic Photoconductors a Monte Carlo Simulation Study,” *Phys. status solidi*, vol. 175, no. 1, pp. 15–56, Jan. 1993.

[17] R. J. Kline, M. D. McGehee, E. N. Kadnikova, J. Liu, and J. M. J. Fréchet, “Controlling the Field-Effect Mobility of Regioregular Polythiophene by Changing the Molecular Weight,” *Adv. Mater.*, vol. 15, no. 18, pp. 1519–1522, Sep. 2003.

[18] H. Yan, Z. Chen, Y. Zheng, C. Newman, J. R. Quinn, F. Dötz, M. Kastler, and A. Facchetti, “A high-mobility electron-transporting polymer for printed transistors.,” *Nature*, vol. 457, no. 7230, pp. 679–86, Feb. 2009.

[19] W. Ma, C. Yang, X. Gong, K. Lee, and A. J. Heeger, “Thermally Stable, Efficient Polymer Solar Cells with Nanoscale Control of the Interpenetrating Network Morphology,” *Adv. Funct. Mater.*, vol. 15, no. 10, pp. 1617–1622, Oct. 2005.

[20] J. W. M. N. Rudden, *Elements of Solid State Physics*, 2nd Editio. Chicester: John Wiley & Sons, 1993.

[21] S. Braun, W. R. Salaneck, and M. Fahlman, “Energy-Level Alignment at Organic/Metal and Organic/Organic Interfaces,” *Adv. Mater.*, vol. 21, no. 14–15, pp. 1450–1472, Apr. 2009.

[22] V. D. Mihailetchi, P. W. M. Blom, J. C. Hummelen, and M. T. Rispens, “Cathode dependence of the open-circuit voltage of polymer:fullerene bulk heterojunction solar cells,” *J. Appl. Phys.*, vol. 94, no. 10, p. 6849, 2003.

[23] D. Rauh, A. Wagenpfahl, C. Deibel, and V. Dyakonov, “Relation of open circuit voltage to charge carrier density in organic bulk heterojunction solar cells,” *Appl. Phys. Lett.*, vol. 98, no. 13, p. 133301, 2011.

[24] Z. He, C. Zhong, X. Huang, W.-Y. Wong, H. Wu, L. Chen, S. Su, and Y. Cao, “Simultaneous enhancement of open-circuit voltage, short-circuit current density, and fill factor in polymer solar cells.,” *Adv. Mater.*, vol. 23, no. 40, pp. 4636–43, Oct. 2011.

[25] S. H. Park, A. Roy, S. Beaupré, S. Cho, N. Coates, J. S. Moon, D. Moses, M. Leclerc, K. Lee, and A. J. Heeger, “Bulk heterojunction solar cells with internal quantum efficiency approaching 100%,” *Nat. Photonics*, vol. 3, no. 5, pp. 297–302, Apr. 2009.

[26] B. Rand, D. Burk, and S. Forrest, “Offset energies at organic semiconductor heterojunctions and their influence on the open-circuit voltage of thin-film solar cells,” *Phys. Rev. B*, vol. 75, no. 11, p. 115327, Mar. 2007.

[27] A. Maurano, R. Hamilton, C. G. Shuttle, A. M. Ballantyne, J. Nelson, B. O’Regan, W. Zhang, I. McCulloch, H. Azimi, M. Morana, C. J. Brabec, and J. R. Durrant, “Recombination dynamics as a key determinant of open circuit voltage in organic bulk heterojunction solar cells: A comparison of four different donor polymers,” *Adv. Mater.*, vol. 22, no. 44, pp. 4987–4992, Nov. 2010.

[28] P. Schilinsky, “Simulation of light intensity dependent current characteristics of polymer solar cells,” *J. Appl. Phys.*, vol. 95, no. 5, p. 2816, 2004.

[29] L. J. A. Koster, V. D. Mihailetchi, R. Ramaker, and P. W. M. Blom, “Light intensity dependence of open-circuit voltage of polymer:fullerene solar cells,” *Appl. Phys. Lett.*, vol. 86, no. 12, p. 123509, 2005.

[30] K. Vandewal, K. Tvingstedt, A. Gadisa, O. Inganäs, and J. V Manca, “On the origin of the open-circuit voltage of polymer-fullerene solar cells.,” *Nat. Mater.*, vol. 8, no. 11, pp. 904–9, Nov. 2009.

[31] J. Liu, Y. Shi, and Y. Yang, “Solvation-Induced Morphology Effects on the Performance of Polymer-Based Photovoltaic Devices,” *Adv. Funct. Mater.*, vol. 11, no. 6, p. 420, Dec. 2001.

[32] H. Hoppe, M. Niggemann, C. Winder, J. Kraut, R. Hiesgen, a. Hinsch, D. Meissner, and N. S. Sariciftci, “Nanoscale Morphology of Conjugated Polymer/Fullerene-Based Bulk-Heterojunction Solar Cells,” *Adv. Funct. Mater.*, vol. 14, no. 10, pp. 1005–1011, Oct. 2004.

[33] A. K. Ghosh, “Rectification, space-charge-limited current, photovoltaic and photoconductive properties of Al⁄tetracene⁄Au sandwich cell,” *J. Appl. Phys.*, vol. 44, no. 6, p. 2781, 1973.

[34] A. K. Ghosh and T. Feng, “Merocynanine organic solar cells,” *J. Appl. Phys.*, vol. 49, no. 12, p. 5982, 1978.

[35] C. W. Tang, “Two-layer organic photovoltaic cell,” *Appl. Phys. Lett.*, vol. 48, no. 2, p. 183, 1986.

[36] J. J. M. Halls, C. A. Walsh, N. C. Greenham, E. A. Marseglia, R. H. Friend, S. C. Moratti, and A. B. Holmes, “Efficient photodiodes from interpenetrating polymer networks,” *Nature*, vol. 376, no. 6540, pp. 498–500, Aug. 1995.

[37] G. Yu, J. Gao, J. C. Hummelen, F. Wudl, and A. J. Heeger, “Polymer Photovoltaic Cells: Enhanced Efficiencies via a Network of Internal Donor-Acceptor Heterojunctions,” *Science (80-.).*, vol. 270, no. 5243, pp. 1789–1791, Dec. 1995.

[38] C. J. Brabec, M. Heeney, I. McCulloch, and J. Nelson, “Influence of blend microstructure on bulk heterojunction organic photovoltaic performance.,” *Chem. Soc. Rev.*, vol. 40, no. 3, pp. 1185–1199, Mar. 2011.

[39] J. Jung, D. Kim, W. S. Shin, S.-J. Moon, C. Lee, and S. C. Yoon, “Highly Efficient Organic Photovoltaic Cells with Molybdenum Oxide Buffer Layer,” *Jpn. J. Appl. Phys.*, vol. 49, no. 5, p. 05EB05, May 2010.

[40] Y.-I. Lee, J.-H. Youn, M.-S. Ryu, J. Kim, H.-T. Moon, and J. Jang, “Highly stable inverted poly (3-hexylthiophene):methano-fullerene [6,6]-phenyl C71-butyric acid methyl ester bulk heterojunction solar cell with thin oxide nano particle layer using solution process,” *Curr. Appl. Phys.*, vol. 12, pp. e46–e48, Sep. 2012.

[41] B. Zimmermann, U. Würfel, and M. Niggemann, “Longterm stability of efficient inverted P3HT:PCBM solar cells,” *Sol. Energy Mater. Sol. Cells*, vol. 93, no. 4, pp. 491–496, Apr. 2009.

[42] A. M. Nardes, M. Kemerink, M. M. de Kok, E. Vinken, K. Maturova, and R. A. J. Janssen, “Conductivity, work function, and environmental stability of PEDOT:PSS thin films treated with sorbitol,” *Org. Electron.*, vol. 9, no. 5, pp. 727–734, Oct. 2008.

[43] Q. Wei, M. Mukaida, Y. Naitoh, and T. Ishida, "Morphological change and mobility enhancement in PEDOT:PSS by adding co-solvents.," *Adv. Mater.*, vol. 25, no. 20, pp. 2831–6, May 2013.

[44] J. Huang, P. F. Miller, J. S. Wilson, A. J. de Mello, J. C. de Mello, and D. D. C. Bradley, "Investigation of the Effects of Doping and Post-Deposition Treatments on the Conductivity, Morphology, and Work Function of Poly(3,4-ethylenedioxythiophene)/Poly(styrene sulfonate) Films," *Adv. Funct. Mater.*, vol. 15, no. 2, pp. 290–296, Feb. 2005.

[45] C. Jonda, A. B. R. Mayer, U. Stolz, A. Elschner, and A. Karbach, "Surface roughness effects and their influence on the degradation of organic light emitting devices," *J. Mater. Sci.*, vol. 35, no. 22, pp. 5645–5651, 2000.

[46] S. Tokito, K. Noda, and Y. Taga, "Metal oxides as a hole-injecting layer for an organic electroluminescent device," *J. Phys. D. Appl. Phys.*, vol. 29, no. 11, pp. 2750–2753, Nov. 1996.

[47] K. J. Reynolds, J. A. Barker, N. C. Greenham, R. H. Friend, and G. L. Frey, "Inorganic solution-processed hole-injecting and electron-blocking layers in polymer light-emitting diodes," *J. Appl. Phys.*, vol. 92, no. 12, p. 7556, 2002.

[48] F. Liu, S. Shao, X. Guo, Y. Zhao, and Z. Xie, "Efficient polymer photovoltaic cells using solution-processed MoO3 as anode buffer layer," *Sol. Energy Mater. Sol. Cells*, vol. 94, no. 5, pp. 842–845, May 2010.

[49] J. Kettle, H. Waters, M. Horie, and S.-W. Chang, “Effect of hole transporting layers on the performance of PCPDTBT : PCBM organic solar cells,” *J. Phys. D. Appl. Phys.*, vol. 45, no. 12, p. 125102, Mar. 2012.

[50] Y. Sun, J. H. Seo, C. J. Takacs, J. Seifter, and A. J. Heeger, “Inverted polymer solar cells integrated with a low-temperature-annealed sol-gel-derived ZnO film as an electron transport layer,” *Adv. Mater.*, vol. 23, no. 14, pp. 1679–1683, Apr. 2011.

[51] J. Kim, G. Kim, Y. Choi, J. Lee, S. Heum Park, and K. Lee, “Light-soaking issue in polymer solar cells: Photoinduced energy level alignment at the sol-gel processed metal oxide and indium tin oxide interface,” *J. Appl. Phys.*, vol. 111, no. 11, p. 114511, 2012.

[52] T. Gershon, “Metal oxide applications in organic-based photovoltaics,” *Mater. Sci. Technol.*, vol. 27, no. 9, pp. 1357–1371, Sep. 2011.

[53] J. Meyer, S. Hamwi, M. Kröger, W. Kowalsky, T. Riedl, and A. Kahn, “Transition metal oxides for organic electronics: energetics, device physics and applications.,” *Adv. Mater.*, vol. 24, no. 40, pp. 5408–27, Oct. 2012.

[54] G. Chamberlain, “Organic solar cells: A review,” *Sol. Cells,* vol. 8, no. 1, pp. 47–83, 1983.

[55] A. J. Campbell, D. D. C. Bradley, and D. G. Lidzey, “Space-charge limited conduction with traps in poly(phenylene vinylene) light emitting diodes,” *J. Appl. Phys.*, vol. 82, no. 12, p. 6326, 1997.

[56] S. E. Shaheen, C. J. Brabec, S. N. Sariciftci, F. Padinger, T. Fromherz, and J. C. Hummelen, “2.5% Efficient Organic Plastic Solar Cells,” *Appl. Phys. Lett.*, vol. 78, no. 6, pp. 841–843, 2001.

[57] F. Padinger, R. S. Rittberger, and N. S. Sariciftci, “Effects of Postproduction Treatment on Plastic Solar Cells,” *Adv. Funct. Mater.*, vol. 13, no. 1, pp. 85–88, 2003.

[58] Y. Kim, S. Cook, S. M. Tuladhar, S. A. Choulis, J. Nelson, J. R. Durrant, D. D. C. Bradley, M. Giles, I. McCulloch, C.-S. Ha, and M. Ree, “A strong regioregularity effect in self-organizing conjugated polymer films and high-efficiency polythiophene:fullerene solar cells,” *Nature Materials*, vol. 5, no. 3. pp. 197–203, 05-Feb-2006.

[59] M. D. Irwin, D. B. Buchholz, A. W. Hains, R. P. H. Chang, and T. J. Marks, “p-Type semiconducting nickel oxide as an efficiency-enhancing anode interfacial layer in polymer bulk-heterojunction solar cells,” *Proc. Natl. Acad. Sci.*, pp. 2–6, 2007.

[60] A. J. Moulé and K. Meerholz, “Controlling Morphology in Polymer–Fullerene Mixtures,” *Adv. Mater.*, vol. 20, no. 2, pp. 240–245, Jan. 2008.

[61] S. Cho, J. H. Seo, S. H. Park, S. Beaupré, M. Leclerc, and A. J. Heeger, “A thermally stable semiconducting polymer.,” *Adv. Mater.*, vol. 22, no. 11, pp. 1253–7, Mar. 2010.

[62] Y. Liang, Z. Xu, J. Xia, S.-T. Tsai, Y. Wu, G. Li, C. Ray, and L. Yu, “For the bright future-bulk heterojunction polymer solar cells with power conversion efficiency of 7.4%.,” *Adv. Mater.*, vol. 22, no. 20, pp. E135–8, May 2010.

[63] Y. Sun, C. J. Takacs, S. R. Cowan, J. H. Seo, X. Gong, A. Roy, and A. J. Heeger, “Efficient, air-stable bulk heterojunction polymer solar cells using MoO x as the anode interfacial layer,” *Adv. Mater.*, vol. 23, no. 19, pp. 2226–2230, May 2011.

[64] D. C. Watters, J. Kingsley, H. Yi, T. Wang, A. Iraqi, and D. Lidzey, “Optimising the efficiency of carbazole co-polymer solar-cells by control over the metal cathode electrode,” *Org. Electron.*, vol. 13, no. 8, pp. 1401–1408, Aug. 2012.

[65] T. Wang, A. J. Pearson, A. D. F. Dunbar, P. A. Staniec, D. C. Watters, H. Yi, A. J. Ryan, R. A. L. Jones, A. Iraqi, and D. G. Lidzey, “Correlating Structure with Function in Thermally Annealed PCDTBT:PC70BM Photovoltaic Blends,” *Adv. Funct. Mater.*, vol. 22, no. 7, pp. 1399–1408, Apr. 2012.

[66] J. Liu, S. Shao, G. Fang, B. Meng, Z. Xie, and L. Wang, “High-efficiency inverted polymer solar cells with transparent and work-function tunable MoO(3)-Al composite film as cathode buffer layer.,” *Adv. Mater.*, vol. 24, no. 20, pp. 2774–9, May 2012.

[67] C. H. Peters, I. T. Sachs-Quintana, W. R. Mateker, T. Heumueller, J. Rivnay, R. Noriega, Z. M. Beiley, E. T. Hoke, A. Salleo, and M. D. McGehee, “The mechanism of burn-in loss in a high efficiency polymer solar cell,” *Adv. Mater.*, vol. 24, no. 5, pp. 663–668, Feb. 2012.

[68] C. H. Peters, I. T. Sachs-Quintana, J. P. Kastrop, S. Beaupré, M. Leclerc, and M. D. McGehee, “High Efficiency Polymer Solar Cells with Long Operating Lifetimes,” *Adv. Energy Mater.*, vol. 1, no. 4, pp. 491–494, Jul. 2011.

[69] H. Yi, S. Al-Faifi, A. Iraqi, D. C. Watters, J. Kingsley, and D. G. Lidzey, “Carbazole and thienyl benzo[1,2,5]thiadiazole based polymers with improved open circuit voltages and processability for application in solar cells,” *J. Mater. Chem.*, vol. 21, no. 35, p. 13649, 2011.

[70] D. C. Watters, H. Yi, A. J. Pearson, J. Kingsley, A. Iraqi, and D. Lidzey, “Fluorene-based co-polymer with high hole mobility and device performance in bulk heterojunction organic solar cells.,” *Macromol. Rapid Commun.*, vol. 34, no. 14, pp. 1157–62, Jul. 2013.

[71] Z. Chen, H. Lemke, S. Albert-Seifried, M. Caironi, M. M. Nielsen, M. Heeney, W. Zhang, I. McCulloch, and H. Sirringhaus, “High mobility ambipolar charge transport in polyselenophene conjugated polymers.,” *Adv. Mater.*, vol. 22, no. 21, pp. 2371–5, Jun. 2010.

[72] Q. Hou, Y. Xu, W. Yang, M. Yuan, J. Peng, and Y. Cao, “Novel red-emitting fluorene-based copolymers,” *J. Mater. Chem.*, vol. 12, no. 10, pp. 2887–2892, Sep. 2002.

[73] M. Bernius, M. Inbasekaran, E. Woo, W. Wu, and L. Wujkowski, “Fluorene-based polymers-preparation and applications,” *J. Mater. Sci. Mater. Electron.*, vol. 11, no. 2, pp. 111–116, 2000.

[74] G. Klärner, J.-I. Lee, M. H. Davey, and R. D. Miller, “Exciton Migration and Trapping in Copolymers Based on Dialkylfluorenes,” *Adv. Mater.*, vol. 11, no. 2, pp. 115–119, Feb. 1999.

[75] W.-Y. Wong, “Metallated molecular materials of fluorene derivatives and their analogues,” *Coord. Chem. Rev.*, vol. 249, no. 9–10, pp. 971–997, May 2005.

[76] Z. He, C. Zhong, S. Su, M. Xu, H. Wu, and Y. Cao, “Enhanced power-conversion efficiency in polymer solar cells using an inverted device structure,” *Nat. Photonics*, vol. 6, no. 9, pp. 593–597, Aug. 2012.

[77] H. W. Kroto, J. R. Heath, S. C. O’Brien, R. F. Curl, and R. E. Smalley, “C60: Buckminsterfullerene,” *Nature*, vol. 318, no. 6042, pp. 162–163, Nov. 1985.

[78] N. S. Sariciftci, L. Smilowitz, A. J. Heeger, and F. Wudl, “Photoinduced Electron Transfer from a Conducting Polymer to Buckminsterfullerene,” *Sci.* , vol. 258 , no. 5087 , pp. 1474–1476, Nov. 1992.

[79] T. B. Singh, N. Marjanović, G. J. Matt, S. Günes, N. S. Sariciftci, A. Montaigne Ramil, A. Andreev, H. Sitter, R. Schwödiauer, and S. Bauer, “High-mobility n-channel organic field-effect transistors based on epitaxially grown C60 films,” *Org. Electron.*, vol. 6, no. 3, pp. 105–110, Jun. 2005.

[80] J. W. Arbogast and C. S. Foote, “Photophysical properties of C70,” *J. Am. Chem. Soc.*, vol. 113, no. 23, pp. 8886–8889, 1991.

[81] A. Seemann, H.-J. Egelhaaf, C. J. Brabec, and J. A. Hauch, “Influence of oxygen on semi-transparent organic solar cells with gas permeable electrodes,” *Org. Electron.*, vol. 10, no. 8, pp. 1424–1428, Dec. 2009.

[82] V. Chellappan, G. M. Ng, M. J. Tan, W.-P. Goh, and F. Zhu, “Imbalanced charge mobility in oxygen treated polythiophene/fullerene based bulk heterojunction solar cells,” *Appl. Phys. Lett.*, vol. 95, no. 26, p. 263305, 2009.

[83] C.-Y. Nam, D. Su, and C. T. Black, “High-Performance Air-Processed Polymer-Fullerene Bulk Heterojunction Solar Cells,” *Adv. Funct. Mater.*, vol. 19, no. 22, pp. 3552–3559, Nov. 2009.

[84] J.-W. Kang, Y.-J. Kang, S. Jung, M. Song, D.-G. Kim, C. Su Kim, and S. H. Kim, “Fully spray-coated inverted organic solar cells,” *Sol. Energy Mater. Sol. Cells*, vol. 103, pp. 76–79, Aug. 2012.

[85] F. C. Krebs, S. A. Gevorgyan, and J. Alstrup, “A roll-to-roll process to flexible polymer solar cells: model studies, manufacture and operational stability studies,” *J. Mater. Chem.*, vol. 19, no. 30, p. 5442, 2009.

[86] S. Wu, J. Li, Q. Tai, and F. Yan, “Investigation of High-Performance Air-Processed Poly(3-hexylthiophene)/Methanofullerene Bulk-Heterojunction Solar Cells,” *Sol. Cells*, vol. 114, no. 49, pp. 21873–21877, 2010.

[87] S. K. Hau, H.-L. Yip, H. Ma, and A. K.-Y. Jen, “High performance ambient processed inverted polymer solar cells through interfacial modification with a fullerene self-assembled monolayer,” *Appl. Phys. Lett.*, vol. 93, no. 23, p. 233304, 2008.

[88] R. De Bettignies, J. Leroy, M. Firon, and C. Sentein, “Accelerated lifetime measurements of P3HT:PCBM solar cells,” *Synth. Met.*, vol. 156, no. 7–8, pp. 510–513, Apr. 2006.

[89] J. A. Hauch, P. Schilinsky, S. A. Choulis, R. Childers, M. Biele, and C. J. Brabec, “Flexible organic P3HT:PCBM bulk-heterojunction modules with more than 1 year outdoor lifetime,” *Sol. Energy Mater. Sol. Cells*, vol. 92, no. 7, pp. 727–731, Jul. 2008.

[90] M. O. Reese, A. J. Morfa, M. S. White, N. Kopidakis, S. E. Shaheen, G. Rumbles, and D. S. Ginley, “Pathways for the degradation of organic photovoltaic P3HT:PCBM based devices,” *Sol. Energy Mater. Sol. Cells*, vol. 92, no. 7, pp. 746–752, Jul. 2008.

[91] S. A. Gevorgyan, M. V. Madsen, H. F. Dam, M. Jørgensen, C. J. Fell, K. F. Anderson, B. C. Duck, A. Mescheloff, E. A. Katz, A. Elschner, R. Roesch, H. Hoppe, M. Hermenau, M. Riede, and F. C. Krebs, “Interlaboratory outdoor stability studies of flexible roll-to-roll coated organic photovoltaic modules: Stability over 10,000h,” *Sol. Energy Mater. Sol. Cells*, vol. 116, pp. 187–196, Sep. 2013.

[92] H. Cao, W. He, Y. Mao, X. Lin, K. Ishikawa, J. H. Dickerson, and W. P. Hess, “Recent progress in degradation and stabilization of organic solar cells,” *J. Power Sources*, vol. 264, pp. 168–183, Oct. 2014.

[93] M. O. Reese, S. A. Gevorgyan, M. Jørgensen, E. Bundgaard, S. R. Kurtz, D. S. Ginley, D. C. Olson, M. T. Lloyd, P. Morvillo, E. A. Katz, A. Elschner, O. Haillant, T. R. Currier, V. Shrotriya, M. Hermenau, M. Riede, K. R. Kirov, G. Trimmel, T. Rath, O. Inganäs, F. Zhang, M. Andersson, K. Tvingstedt, M. Lira-Cantu, D. Laird, C. McGuiness, S. (Jimmy) Gowrisanker, M. Pannone, M. Xiao, J. Hauch, R. Steim, D. M. DeLongchamp, R. Rösch, H. Hoppe, N. Espinosa, A. Urbina, G. Yaman-Uzunoglu, J.-B. Bonekamp, A. J. J. M. van Breemen, C. Girotto, E. Voroshazi, and F. C. Krebs, “Consensus stability testing protocols for organic photovoltaic materials and devices,” *Sol. Energy Mater. Sol. Cells*, vol. 95, no. 5, pp. 1253–1267, May 2011.

[94] Q. Pei, G. Zuccarello, M. Ahlskog, and O. Inganäs, “Electrochromic and highly stable poly(3,4-ethylenedioxythiophene) switches between opaque blue-black and transparent sky blue,” *Polymer (Guildf).*, vol. 35, no. 7, pp. 1347–1351, Mar. 1994.

[95] L. S. Hung, C. W. Tang, and M. G. Mason, “Enhanced electron injection in organic electroluminescence devices using an Al/LiF electrode,” *Appl. Phys. Lett.*, vol. 70, no. 2, p. 152, 1997.

[96] M. Jørgensen, K. Norrman, S. A. Gevorgyan, T. Tromholt, B. Andreasen, and F. C. Krebs, “Stability of polymer solar cells.,” *Adv. Mater.*, vol. 24, no. 5, pp. 580–612, Feb. 2012.

[97] L.-M. Chen, Z. Xu, Z. Hong, and Y. Yang, “Interface investigation and engineering – achieving high performance polymer photovoltaic devices,” *J. Mater. Chem.*, vol. 20, no. 13, p. 2575, 2010.

[98] E. Voroshazi, B. Verreet, A. Buri, R. Müller, D. Di Nuzzo, and P. Heremans, “Influence of cathode oxidation via the hole extraction layer in polymer:fullerene solar cells,” *Org. Electron.*, vol. 12, no. 5, pp. 736–744, May 2011.

[99] C. Girotto, E. Voroshazi, D. Cheyns, P. Heremans, and B. P. Rand, “Solution-processed MoO_3 thin films as a hole-injection layer for organic solar cells.,” *ACS Appl. Mater. interfaces*, vol. 3, no. 9, pp. 3244–7, 2011.

[100] M. Elshobaki, J. Anderegg, and S. Chaudhary, “Efficient polymer solar cells fabricated on poly(3,4-ethylenedioxythiophene):poly(styrenesulfonate)-etched old indium tin oxide substrates.,” *ACS Appl. Mater. Interfaces*, vol. 6, no. 15, pp. 12196–202, Aug. 2014.

[101] M. T. Lloyd, D. C. Olson, P. Lu, E. Fang, D. L. Moore, M. S. White, M. O. Reese, D. S. Ginley, and J. W. P. Hsu, “Impact of contact evolution on the shelf life of organic solar cells,” *J. Mater. Chem.*, vol. 19, no. 41, p. 7638, 2009.

[102] S. R. Dupont, M. Oliver, F. C. Krebs, and R. H. Dauskardt, “Interlayer adhesion in roll-to-roll processed flexible inverted polymer solar cells,” *Sol. Energy Mater. Sol. Cells*, vol. 97, pp. 171–175, Feb. 2012.

[103] F. C. Krebs, “Encapsulation of polymer photovoltaic prototypes,” *Sol. Energy Mater. Sol. Cells*, vol. 90, no. 20, pp. 3633–3643, Dec. 2006.

[104] A. Asadpoordarvish, A. Sandström, S. Tang, J. Granström, and L. Edman, “Encapsulating light-emitting electrochemical cells for improved performance,” *Appl. Phys. Lett.*, vol. 100, no. 19, p. 193508, 2012.

[105] S. Cros, R. de Bettignies, S. Berson, S. Bailly, P. Maisse, N. Lemaitre, and S. Guillerez, “Definition of encapsulation barrier requirements: A method applied to organic solar cells,” *Sol. Energy Mater. Sol. Cells*, vol. 95, pp. S65–S69, May 2011.

[106] F. C. Krebs, J. Alstrup, H. Spanggaard, K. Larsen, and E. Kold, “Production of large-area polymer solar cells by industrial silk screen printing, lifetime considerations and lamination with polyethyleneterephthalate,” *Sol. Energy Mater. Sol. Cells*, vol. 83, no. 2–3, pp. 293–300, Jun. 2004.

[107] N. Kim, W. J. Potscavage, A. Sundaramoothi, C. Henderson, B. Kippelen, and S. Graham, “A correlation study between barrier film performance and shelf lifetime of encapsulated organic solar cells,” *Sol. Energy Mater. Sol. Cells*, vol. 101, pp. 140–146, Jun. 2012.

Chapter 3 : Experimental Methods

3.0 Introduction

In this chapter, the various techniques utilised in the fabrication of OPV devices are reported, as are the experimental techniques employed to characterise devices and determine a variety of operating parameters. Key fabrication techniques covered include substrate cleaning, solution preparation, thin film deposition, metal evaporation and encapsulation. Experimental techniques used to probe OPV device performance include current-density (*JV*) characterisation, laser beam induced current mapping (LBIC), electroluminescent mapping (ELM), absorbance spectroscopy, external quantum efficiency (EQE) and spectroscopic ellipsometry. Finally, the details of lifetime testing protocols and apparatus are covered, including set up and calibration.

3.1 Fabrication Techniques

The following is an overview of the different techniques utilised in the fabrication of OPV devices in this thesis. The majority of fabrication steps were carried out in either a nitrogen filled glovebox (< 0.1 ppm O_2, H_2O), **Figure 3.1(a)** or a Lamarflo workstation hood **Figure 3.1 (b)**.

Figure 3.1 **(a)** The nitrogen filled glovebox with key features labelled and **(b)** the Lamarflo workstation hood with key features labelled.

3.1.1 Substrate Cleaning

OPV devices were fabricated onto 20 mm x 15 mm glass substrates with a 100 nm thick pre-patterned sputtered ITO layer supplied by Ossila Ltd. The overlap of the ITO pattern and top electrical contact defines six 2 mm x 2 mm (4 mm^2) pixels on each substrate as shown in **Figure 3.2 (b)**.

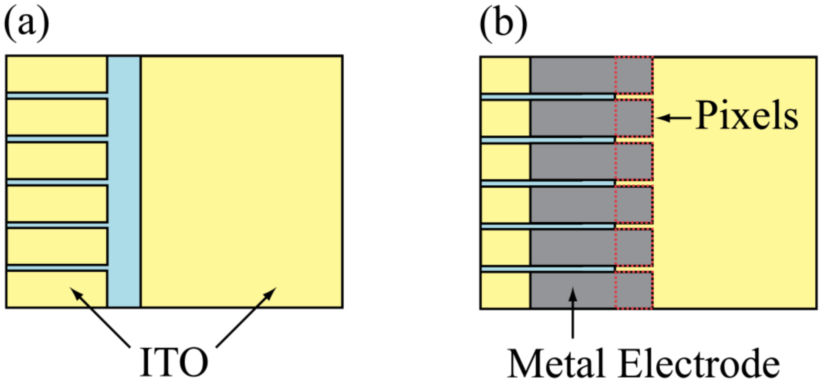

Figure 3.2 (a) Six pixel substrate design. **(b)** Pixels defined by overlap of ITO and metal electrode.

The substrates were rigorously cleaned to remove dust and dirt on the surface of the ITO, which can lead to shorts and other defects forming during device fabrication. This was done by sonicating the substrates in a hot water ultrasonic bath (70 - 80^{o}C) with Hellmanex III cleaning fluid for 10 minutes, after which they were 'dump-rinsed' twice in hot DI water. Once rinsed the substrates were sonicated for a further 10 minutes in 2-propanol (IPA) in a hot water ultrasonic bath, and dump-rinsed in hot DI water once more. The substrates were then stored in DI water until needed, for no more than an hour, at which point they were removed from the DI water and dried with a compressed nitrogen jet.

3.1.2 Solution Preparation

One of the main benefits of OPV technology is the ability to process materials from solution. This allows for the use of many different thin film deposition techniques, such as spin-coating, spray coating, ink-jet printing and R2R processing. As previously mentioned in **2.5 Device Architecture**, for the active layer of OPVs utilizing a BHJ morphology, both the donor polymer and fullerene acceptor are deposited from the same solution, which results in the interpenetrating network of phase separated materials needed for exciton dissociation and charge extraction. Solution composition can drastically affect the resulting material film, and therefore solution preparation is a key step in the deposition of thin films with the desired properties for OPV device operation.

All materials and solvents were used as received from the suppliers. Solvents, metal oxide precursors and other materials, unless otherwise stated, were sourced from Sigma-Aldrich. Donor polymers and $PC_{70}BM$ (95% purity) were provided by either the University of Sheffield (UoS) Chemistry Department or Ossila Ltd. Details of polymer source, molecular weight (M_w) and number (M_n), polydispersity index (PDI) and optimum $PC_{70}BM$ blend ratio can be found in **Table 3.1**.

Polymer solutions were prepared by dissolving dry polymer in a solvent, either chloroform ($CHCl_3$) or chlorobenzene (CB), at a concentration of 4 - 10 mgmL^{-1} depending on the solubility of the polymer. Polymer solutions were then heated at 80^{o}C for an hour with a rotating stir bar, with periodic shaking of the vial to ensure all material was fully dissolved. This solution was then cooled for 5 minutes before being added to another vial containing dry $PC_{70}BM$ to attain the desired blend ratio. The polymer:fullerene solution was then heated whilst stirring with a rotating stir bar for a further hour at 80^{o}C, before being cooled down and filtered through a polytetrafluoroethylene (PTFE) filter with a 0.45 µm pore size to remove polymer and fullerene aggregates. This process was carried out in a nitrogen filled glovebox for all studies.

Polymer	Source	M_w	M_n	PDI	$PC_{70}BM$ Blend Ratio
PCDTBT (R3CH)	UoS Chem. Dept	36,700	17,000	2.15	1:4
PCDTBT (M137)	Ossila Ltd.	42,200	19,600	2.15	1:4
PCDTBT-8	UoS Chem. Dept	78,600	32,800	2.4	1:4
PCDSeBT-8	UoS Chem. Dept	60,195	16,036	3.75	1:4
PFDT2BT-8	UoS Chem. Dept	91,600	62,400	1.47	1:4
PTB7 [1]	1-Material	97,500	-	2.1	1:1.5

Table 3.1 Polymer name, source, M_w, M_n, PDI and optimised $PC_{70}BM$ blend ratio.

3.1.3 Thin Film Deposition

Spin-coating was the method used to fabricate thin films. This is a simple and repeatable process that involves securing a substrate to a rapidly rotating disc and dispensing a solution onto its centre from above. The solution, on contact with the spinning substrate, is spread evenly over the surface by centrifugal force, with excess solution ejected off the edge. Solvent evaporation occurs while the substrate is still spinning, which results in a thin, uniform film covering the substrate. The quantity of solution used per deposition is controlled by the use of a variable volume pipette, with 20 - 50 µL of solution used per film.

The spin speed needed to attain films of a desired thickness depends on the viscosity of the solvent and the concentration of the solution, as shown in **Equation 3.1.**

$$t = \frac{c\, v(c)}{\sqrt{\omega}}$$ **Equation 3.1**

Where t is the film thickness, c is the solution concentration, $v(c)$ is the solution viscosity (which is dependent on the concentration) and ω is the spin speed.

The length of time the substrate was left to spin, such that the solvent was fully evaporated, was determined by the boiling point of the solvent; 61°C for $CHCl_3$ and 131°C for CB. For the majority of cases, 30 s was sufficient time for the solvent to evaporate and create fully dried films. Excess undried solution at the corners of the substrate was removed by the addition of a second spin stage, having a much higher spin speed (< 4000 rpm), for 10 s after the central region of the film was fully dry.

To achieve the desired film thickness, reference samples were spun onto artificial quartz coated glass slides. A trench was then scraped in the active layer using tweezers, and the depth measured using a Dektak surface profilometer. This is illustrated in **Figure 3.3** below.

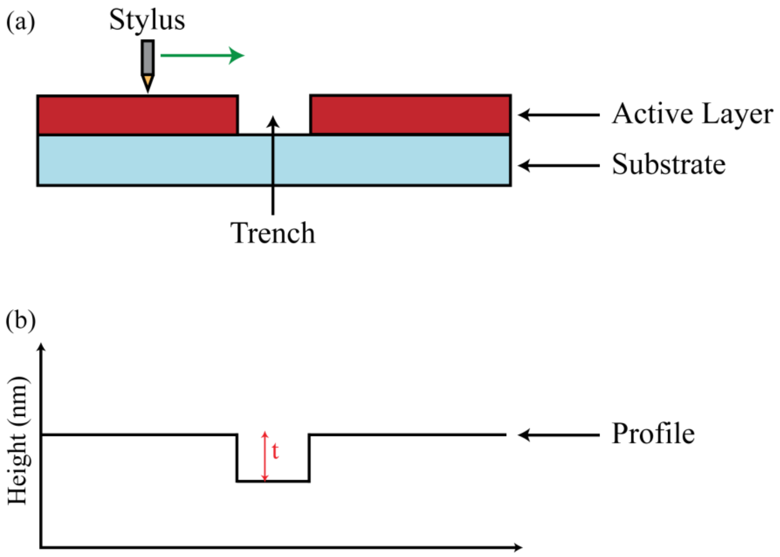

Figure 3.3 (a) Dektak stylus moving linearly across active layer surface. **(b)** Measured height profile of sample with active layer depth, *t*.

Once a reference sample had been measured, altering the spin speed of deposition allows for fine-tuning of the film thickness, as governed by **Equation 3.2**.

$$\omega_2 = \omega_r \left(\frac{t_r}{t_2}\right)^2 \qquad \textbf{Equation 3.2}$$

Where t_r is the film thickness of the reference sample created by spin speed ω_r, and t_2 is the desired film thickness created by spin speed ω_2. This relationship is dependent on the solution concentration and viscosity being kept constant.

Active layer materials were spin-coated in the glovebox for the majority of the OPVs fabricated, though in some cases deposition was carried out in air in a Lamarflo work bench.

PEDOT:PSS solutions (Heraeus Clevios™ P VP AI 4083) were filtered through a 0.45 µm polyvinylidene fluoride (PVDF) filter to remove aggregates, and were spin-coated onto cleaned ITO substrates at 6000 rpm for 30 s, to give a film thickness of 30 nm. PEDOT:PSS solutions are aqueous, and therefore could not be processed in the glovebox, so thin films were spin-coated in a Lamarflo work bench under ambient conditions. The films were then thermally annealed in air at 150^{o}C for 10 minutes prior to being transported to the glovebox, where, in some cases, they were again annealed at 150^{o}C for 10 minutes to remove any remaining moisture in the films.

Other materials, such as metal oxides, were also deposited from solution. The solution preparation details and deposition requirements for these materials are covered in the chapters in which they are utilised.

3.1.4 Thermal Evaporation

Thermal evaporation is a technique by which metal oxide interlayers and metallic top contacts can be deposited. Thermal evaporation involves two basic processes: a hot source material evaporates, and then condenses on the substrate. This is carried out in a high vacuum, such that the evaporated metal particles can travel directly to the substrate without colliding with gas molecules. The high vacuum also reduces the boiling point of the materials being evaporated, allowing for heating by electrical currents.

This process was carried out in a vacuum chamber attached to the nitrogen filled glovebox, as shown in **Figure 3.1 (a)**, to allow for substrates to be moved between the two without exposure to ambient environment. The vacuum chamber had multiple sources, and so sequential evaporations could be carried out without having to vent the chamber to atmosphere. The thickness of the material being deposited were monitored during evaporation using a calibrated quartz crystal microbalance (QCM), whose frequency changes depending on the mass deposited on its surface.

For the deposition of evaporated materials, substrates were loaded into evaporation masks which defined the area over which the material was evaporated onto the substrate, an example of which is shown in **Figure 3.4 (b)**.

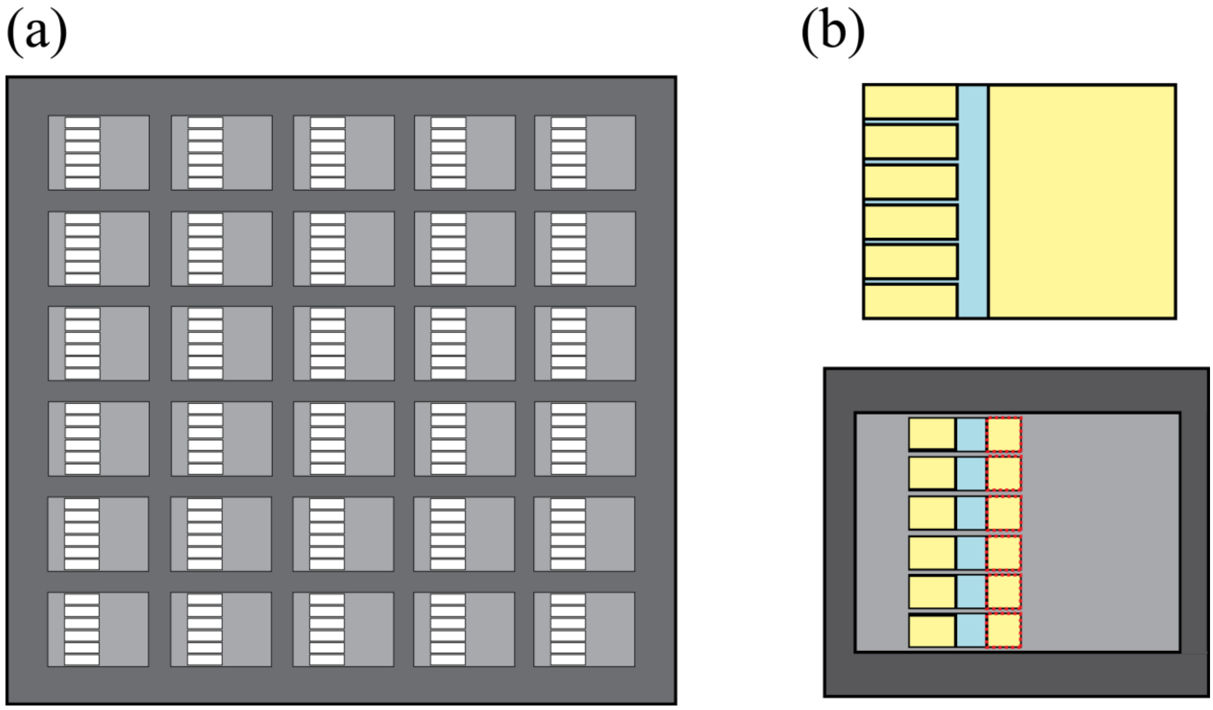

Figure 3.4 (a) Design of the top contact evaporation mask for OPVs, with space for 35 substrates. The mask consists of two 2 mm thick layers of patterned stainless steel welded together (represented by dark and light grey areas). **(b)** Shows a substrate loaded in the mask (viewed from below, through the mask), and the exposed area of substrate onto which the metal is evaporated. The pixel area is highlighted in red.

Once fully loaded with substrates, the mask was transferred to the evaporation chamber and secured on a rotating holder to allow for uniform deposition across the surface. The chamber was then pumped down to a starting pressure of $< 10^{-7}$ mbar to allow for the metal to vaporise and to remove trace gasses that could react with the materials being deposited. The chosen materials were evaporated from crucibles by passing a current through a heating coil surrounding the crucible. Depending on the material being evaporated, the optimum material deposition rate, crucible material and final film thickness varied as shown in **Table 3.2**.

Material	**Crucible Material**	**Optimised Film Thickness**	**Deposition Rate**
Molybdenum Oxide (MoO_x)	Aluminium oxide	10 - 20 nm	0.2 $Ås^{-1}$
Calcium (Ca)	Aluminium oxide	5 nm	0.4 $Ås^{-1}$
Aluminium (Al)	Boron Nitride	100 nm	1.5 $Ås^{-1}$
Silver (Ag)	Boron Nitride	100 nm	1.0 $Ås^{-1}$

Table 3.2 Evaporation parameters for the materials used for the fabrication of OPVs. 100 nm of silver or aluminium were required to form highly reflective and conductive top contacts. Optimised film thicknesses were determined from optimisation studies.

After deposition, the substrates remained in the vacuum chamber until cool, at which point the chamber was vented to atmospheric pressure and the substrates brought back into the glovebox.

3.2 Device Fabrication

Figure 3.5 (a-e) Shows the main fabrication steps for an OPV. First, patterned ITO substrates were cleaned **(a)** as covered in **3.1.1 Substrate Cleaning**, after which the first interlayer was deposited **(b)**. This formed either the HTL for standard devices or the ETL for inverted devices, and was deposited from solution by spin-coating as covered in **3.1.3 Thin Film Deposition** or by thermal evaporation as covered in **3.1.4 Thermal Evaporation**. Commonly, the HTL for standard architecture devices consists of either PEDOT:PSS, which was spin-coated from solution in air, or MoO_x, which was thermally evaporated under vacuum, though other materials were also used. The ITO contact points on either side of the substrate were wiped clean of material to allow for efficient electrical contacts.

The active layer was then deposited by spin-coating **(c)**, most often in the glovebox to prevent degradation of the polymer films, though this process was also carried out in air in a Lamarflo work bench in **Chapter 4 : Air Stability of MoOx** and **Chapter 6 : Polymer Air Processing**. Optimum active layer thicknesses of between 70 - 95 nm were achieved by varying the spin speed of deposition as covered in **3.1.3 Thin Film Deposition**. As with the first interlayer, the ITO contact points on either side of the substrate were cleaned of material to allow for efficient electrical contacts.

Next, the second interlayer was deposited **(d)**, forming the ETL for standard devices or the HTL for inverted devices. This layer was formed of 5 nm of Ca or 10 nm of titanium oxide (TiO_x). Ca was thermally evaporated using an evaporation mask, and TiO_x was processed from solution as covered in **8.1 Titanium Oxide**. For the TiO_x, the ITO contact points on either side of the substrate were cleaned of material as in previous steps.

100 nm of metal was deposited via thermal evaporation to form the top electrical contact **(e)** in the vacuum chamber at $< 10^{-7}$ mbar. This was carried out using an evaporation mask to achieve the desired cathode shape and coverage as shown in **Figure 3.4 (a)**.

Finally, devices were encapsulated using a glass cover slip and UV epoxy **(f)**, which was cured for 30 minutes under a UV lamp prior to removal from the glovebox. This encapsulation provided protection from moisture and oxygen ingress into the device, and mechanical stresses and scratches during handling. A completed device is shown in **Figure 3.6**.

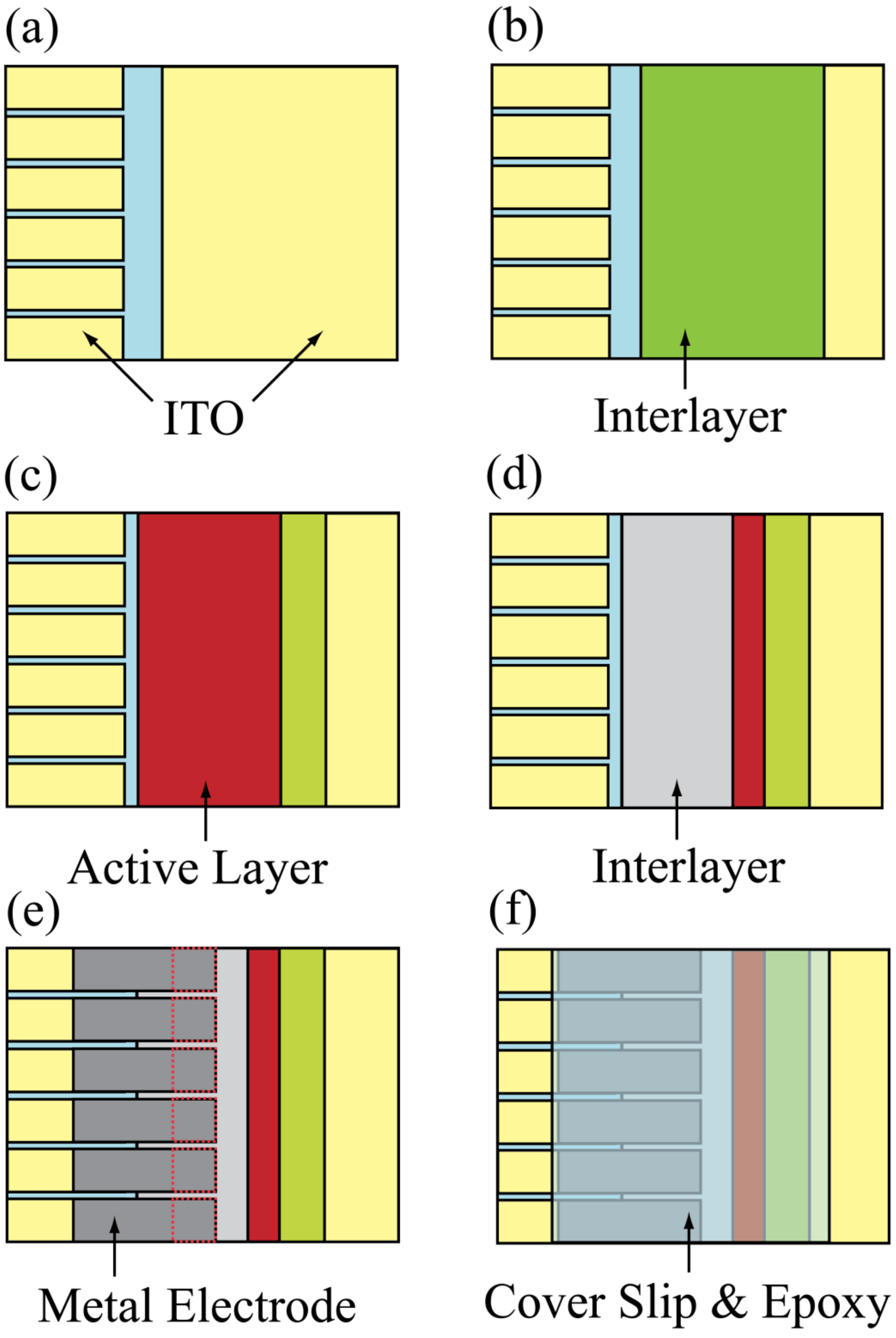

Figure 3.5 Main fabrication steps for an OPV: **(a)** ITO coated substrate after cleaning, **(b)** first interlayer deposition, **(c)** active layer deposition, **(d)** second interlayer deposition, **(e)** metal top contact evaporation with pixels highlighted in red, and **(f)** encapsulation.

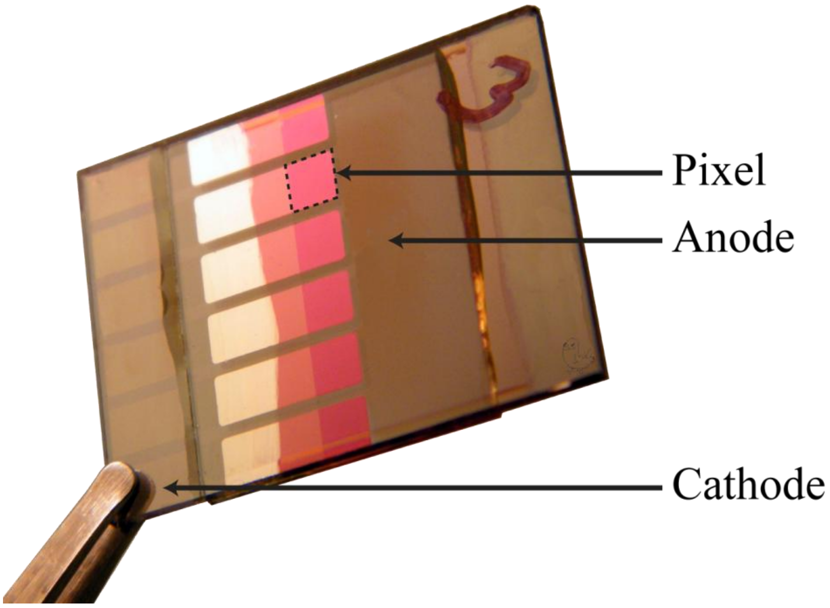

Figure 3.6 A completed 6 pixel OPV device.

3.3 Device Characterization

OPV devices were characterised by measuring a current-voltage (*IV*) curve under illumination, most often simulated AM1.5 solar spectrum as shown in **Figure 3.7**. The OPV devices were subjected to an applied voltage that swept between -1.0 and 1.0 V, and the generated current measured at 0.02 V steps. When quoting device performance, current is converted to current density to normalize the performance of the solar cell to its pixel size, resulting in a current density-voltage plot (*JV*). The properties of the materials used in the device have an effect on the generated current; including the absorption spectrum of the active layer materials, photogeneration rate, exciton diffusion, dissociation and charge extraction. The efficiency of these processes all contribute to the measured device power conversion efficiency (*PCE*).

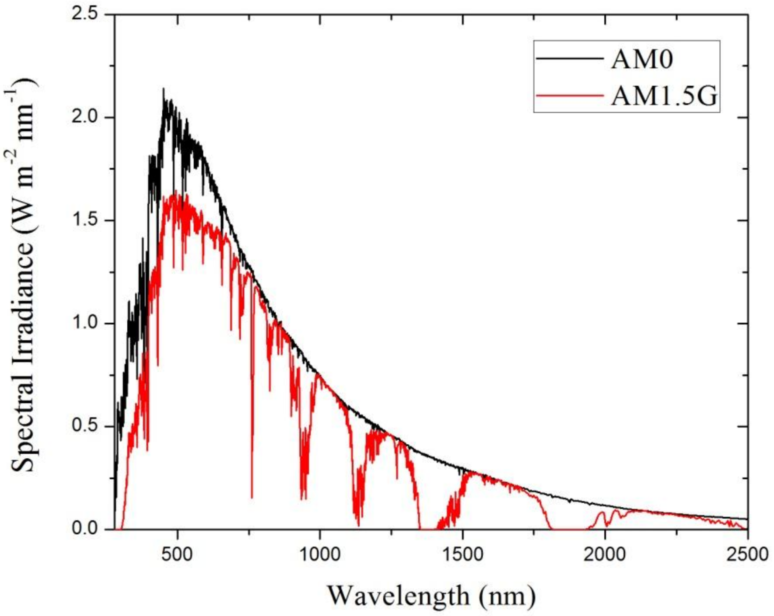

Figure 3.7 Solar spectrum incident on the Earth above the atmosphere (AM0) and on the surface at temperate latitudes (AM1.5).

A typical example of a *JV* curve for an OPV device is shown in **Figure 3.8**, with the operating parameters annotated. The device is at open circuit when $J = 0$ mAcm^{-2} and short-circuit at $V = 0$ V. The *PCE* and the fill factor (*FF*) can be calculated using **Equations 3.3** and **3.4** below.

$$PCE = \frac{P_{out}}{P_{in}} = \frac{J_{mpp}V_{mpp}}{P_{in}} = \frac{J_{sc}V_{oc}FF}{P_{in}}$$ **Equation 3.3**

$$FF = \frac{J_{mpp}V_{mpp}}{J_{sc}V_{oc}}$$ **Equation 3.4**

Where P_{in} is the incident power from the simulated AM1.5 solar spectrum, P_{out} is the output power of the device, J_{mpp} and V_{mpp} are the current density and voltage at the maximum power point (M_{pp}), V_{oc} is the open circuit voltage, J_{sc} is the short-circuit current density and *FF* is the fill factor.

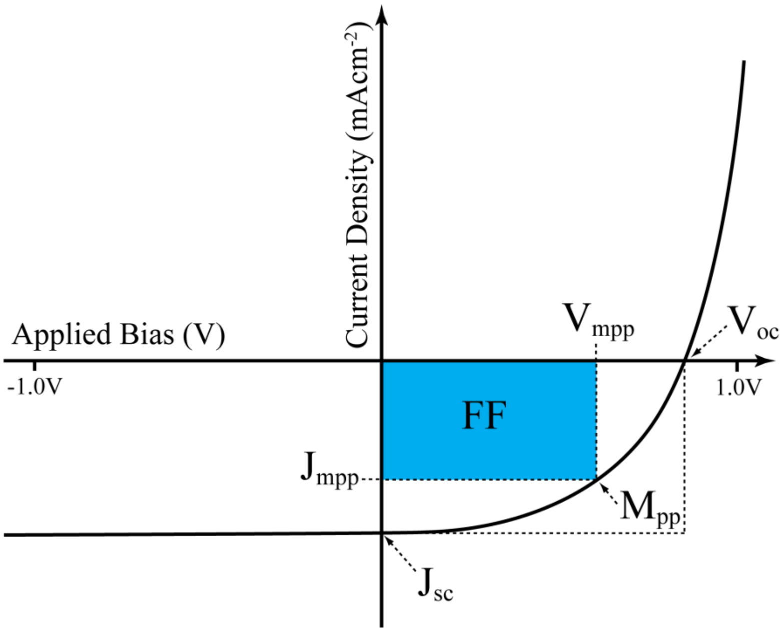

Figure 3.8 *JV* characteristics of an OPV device. The maximum power point (M_{pp}) is shown along with the other operating parameters, and the blue box represents the maximum power output of the device.

OPV devices can be approximated with an equivalent circuit as shown in **Figure 3.9**, which incorporates resistors and diodes to account for shape of the *JV* curve under illumination.

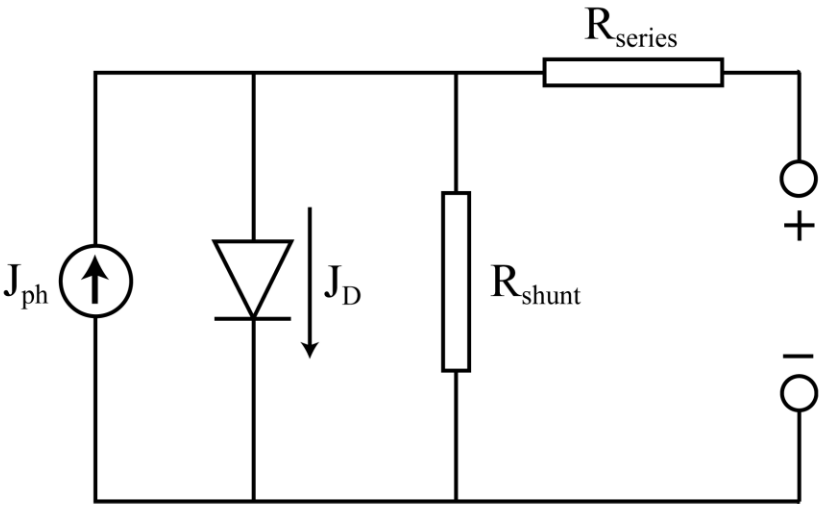

Figure 3.9 Equivalent circuit for an OPV. J_{ph} and J_D are the photocurrent and diode current as described in **Equation 3.5**.

R_{series} and R_{shunt} are known as parasitic resistances and can significantly affect the performance of an OPV device. Large values of R_{shunt} prevent current leakage in the device, and small values of R_{series} improve device performance by decreasing internal resistances in the device (originating from bulk transport, transfer of charges across interfaces and extraction at the contacts). An upper limit of values for R_{shunt} and R_{series} can be calculated from the gradient of *JV* curves at open and short circuit; with R_{shunt} primarily affecting the shape of the curve at short circuit, and R_{series} primarily affecting the shape of the curve at open circuit [2], [3]. The main impact of increasing R_{series} is to decrease the *FF* of OPV devices, though sufficiently high values can also reduce J_{sc}. Low values of R_{shunt} can also cause a decrease in *FF* by providing an alternate path for light-generated current, reducing the amount of current flowing through the device and thereby also reducing the voltage. **Equation 3.5** gives the relationship between current and voltage in an OPV, accounting for the effects of R_{series} and R_{shunt}.

$$J = J_0 \left[exp\left(\frac{e}{nkT}(V - JR_{series}) \right) - 1 \right] + \frac{V - JR_{series}}{R_{shunt}} - J_{ph} \qquad \textbf{Equation 3.5}$$

Where J is the current, J_0 is the dark current, V is the applied bias, n is the diode ideality factor, R_{series} and R_{shunt} are the series and shunt resistances and J_{ph} is the photocurrent. The diode ideality factor, n, allows for the fact that OPVs are not ideal diodes, takes a value between 1 and 2 and accounts for a variety of recombination mechanisms [4]. The diode current, J_D, is the product of J_0 and the terms in the square parentheses.

J_{sc} , J (V = 0), is the maximum attainable current that can be drawn from an OPV device under illumination. Several factors affect the J_{sc}, including the maximum amount of light that can be absorbed, which is determined by the band gap of the donor polymer. A small bandgap leads to an increase in J_{sc} due to increased absorption, but a smaller bandgap also leads to a reduction in V_{oc}. Other processes that reduce J_{sc} include recombination of charges in the active layer or at interfaces [5], and the parasitic resistances R_{shunt} and R_{series}.

The *FF* can be described as how close the electronic behaviour of an OPV is to an ideal diode. Therefore, the factors that reduce *FF* are high R_{series}, low R_{shunt} and diode ideality factors > 1. These can be overcome by reducing recombination and losses due to internal resistances [6], and decreasing the number of defects that cause shorts.

3.3.1 Device Characterization Setup

JV characteristics of OPV devices were obtained using a setup consisting of a computer controlled test board designed by Ossila Ltd, a Keithley K237 source-measure unit, and a Newport 92251A-1000 solar simulator with a calibrated AM1.5 spectrum and an output of 1000 W/m^2. The test board design is shown in **Figure 3.10**.

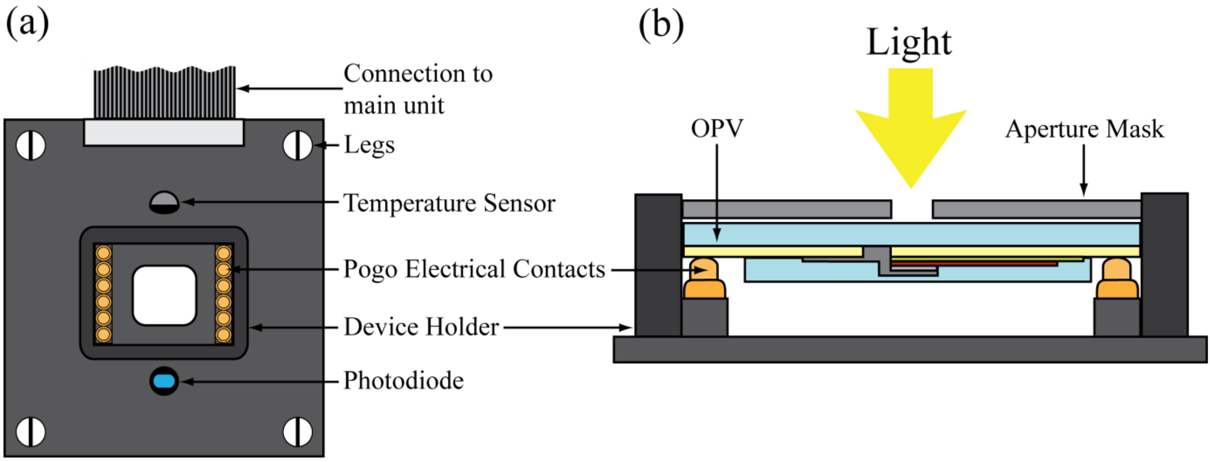

Figure 3.10 Test board used for OPV characterization. **(a)** Top view, **(b)** side view with OPV and aperture mask in place.

The test board was designed such that it would hold an OPV and an aperture mask on spring loaded pogo electrical contacts, as shown in **Figure 3.10 (b)**, uniformly illuminated from above by the solar simulator. A temperature sensor and photodiode next to the OPV allowed for monitoring of temperature and light intensity with every *JV* measurement. The test board was secured underneath the solar simulator and connected to a main circuit board that allowed for switching between the six pixels of the device for automated testing. The main circuit board was connected to the Keithley 237 source-measure unit by BNC connection, and the whole setup was controlled by a MATLAB program. This automated setup allowed for swift and repeatable device testing. The calibration of the solar simulator and aperture masks are covered in the following sections.

3.3.2 Solar Simulator Calibration

To check the calibration of the solar simulator at the University of Sheffield, the *JV* characteristics of five OPVs were measured first at Sheffield and then later at Loughborough University, whose solar simulator (CREST) had undergone rigorous calibration and testing to accurately match the AM1.5 spectrum. The five OPV devices tested at both locations had an ITO/MoO_x/PCDTBT:$PC_{70}BM$/Ca/Al standard architecture. **Table 3.3** shows the average values and standard deviation of *PCE*, *FF*, V_{oc} and J_{sc} for the five different OPV devices, omitting those pixels with gross film defects. The results were very similar, with a small relative decrease of around 3-8% in *PCE* when the devices were measured in Loughborough. The discrepancy in the two measurements could be accounted for by a spectral mismatch of the two sources, degradation of the devices during transit and under repeated testing and other differences in testing equipment.

Device	Testing Location	PCE (%)	FF	V_{oc} (V)	J_{sc} ($mAcm^{-2}$)
1	Sheffield	4.93±0.04	65.4±0.3	0.87	-8.64±0.08
	Loughborough	4.71±0.03	64.7±0.1	0.89	-8.15±0.04
2	Sheffield	4.95±0.04	65.7±0.3	0.87	-8.64±0.07
	Loughborough	4.69±0.03	65.1±0.3	0.88	-8.18±0.08
3	Sheffield	5.14±0.04	66.2±0.1	0.88	-8.82±0.06
	Loughborough	5.02±0.07	65.4±0.5	0.89	-8.6±0.2
4	Sheffield	5.01±0.04	65.5±0.3	0.88	-8.71±0.03
	Loughborough	4.62±0.06	63.4±0.8	0.89	-8.19±0.01
5	Sheffield	5.18±0.02	66.1±0.2	0.88	-8.90±0.06
	Loughborough	4.91±0.05	65.6±0.4	0.90	-8.32±0.07

Table 3.3 Operating parameters for five OPV devices tested at both Sheffield and Loughborough Universities using different solar simulators.

The *JV* curves for pixel 3 of device 1 from **Table 3.3**, as measured under the Sheffield and Loughborough solar simulators, are shown in **Figure 3.11** for comparison.

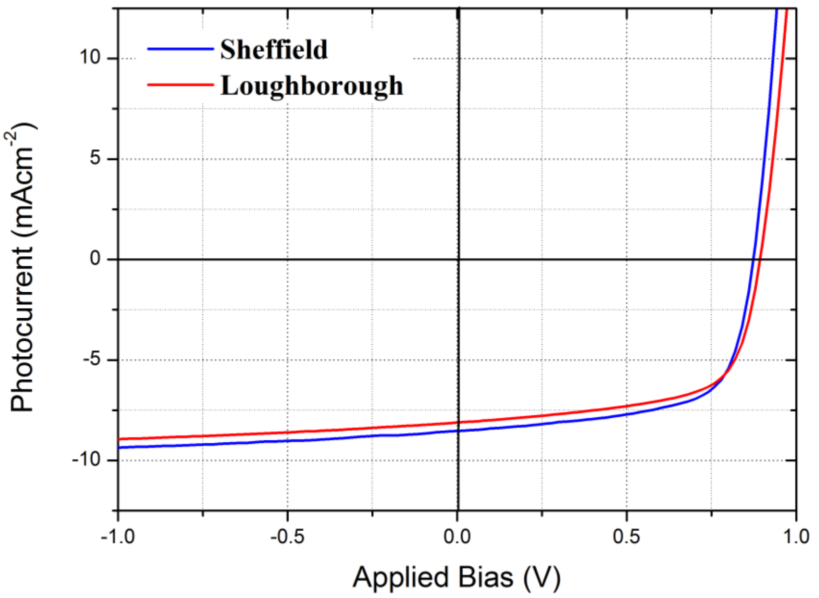

Figure 3.11 *JV* curves for the same device measured using the Sheffield and Loughborough solar simulators.

3.3.3 Aperture Mask Calibration

Devices were measured using a electrochemically etched aperture mask, the design of which is shown in **Figure 3.12 (a)**, to define an area of illumination and allow for accurate calculation of current density. The masks were etched with individual apertures for each of the six pixels, each with an area of 0.0256 cm^2. However, the manufacturing process left a roughened edge to these pixel apertures as can be seen in **Figure 3.12 (b)**. Using an optical microscope image of the pixel apertures and an eyepiece micrometer, shown in **Figure 3.12 (b), (c)** respectively, the area of the pixel apertures were calculated to be (0.0261±0.0001)cm^2, a 2% error from the value quoted by the manufacturers. This aperture calibration allowed for more accurate calculation of the current density, and subsequently *PCE*.

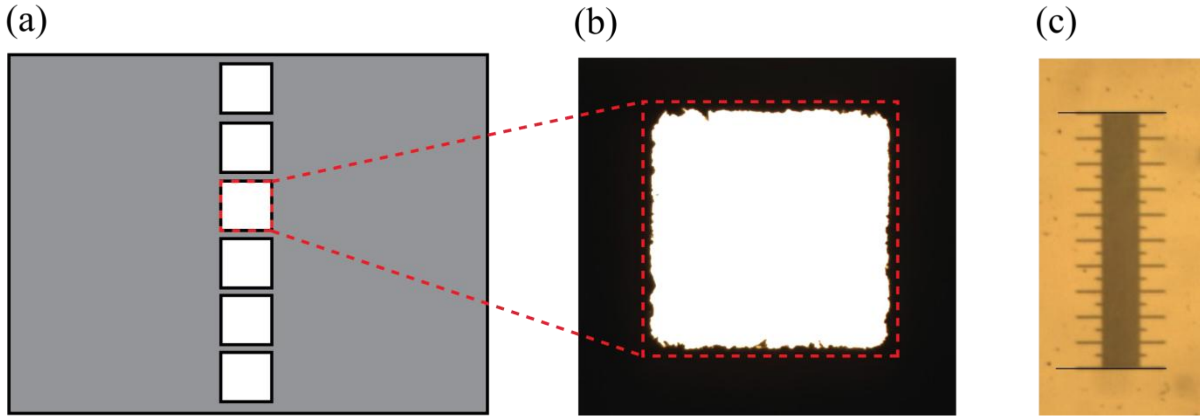

Figure 3.12 (a) Design of the aperture mask for OPV characterization, **(b)** an optical microscope image of an individual pixel aperture and **(c)** an optical microscope image of an eyepiece micrometer.

3.4 Absorbance Spectroscopy

Absorbance spectroscopy was used to measure the transmission of light at different wavelengths through a sample. This was carried out using a Jobin Yvon Horiba Fluoromax-4, the structure of which is shown in **Figure 3.13**.

A Xenon arc lamp, with an emission starting at 250 nm, was used as the light source and was housed in the first chamber of the Fluoromax. From the lamp, the light is focused using an elliptical mirror, through a quartz window, and into a Czerny-Turner monochromator. The light entering the monochromator is focused onto an entry slit, which is used to control the intensity of the light. From here, the light is collimated using a mirror and is then incident onto a blazed diffraction grating, where, upon diffraction, it is then refocused by a second mirror onto another slit and exits the monochromator. This process allows for control of the wavelength of light incident on the second slit, and is dependent on the angle of the blazed grating with respect to the second mirror. The width of the second slit can also be used to fine tune the resolution of the output spectra; the smaller the slit size the higher the resolution. As light exits the monochromator, a reference spectra is generated by focusing the light through a beam splitter onto a reference detector photodiode. The light then passes through the sample, held in a sample holder at right angles to the incident beam, and onto a second photodiode. By recording the light transmitted through the sample, it is possible to calculate the transmittance, and therefore the absorbance, of the material.

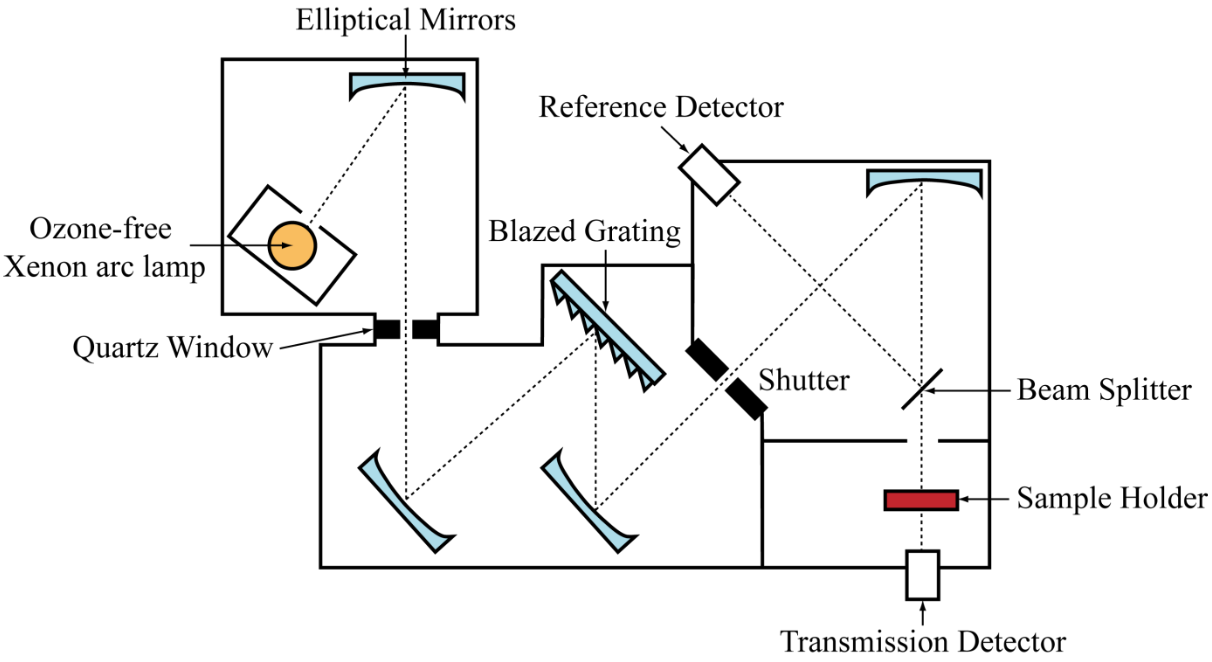

Figure 3.13 Structure of the transmission spectra section of a Jobin Yvon Horiba Fluoromax-4. The instrument is split into four parts: the light source, monochromator, reference beam detector and sample chamber with transmission detector.

The transmittance of a sample is calculated using the relationship shown in **Equation 3.6**.

$$T(\lambda) = \frac{I(\lambda)}{I_0(\lambda)} \qquad \textbf{Equation 3.6}$$

where $T(\lambda)$ is the fraction of light transmitted at wavelength λ, $I(\lambda)$ is the amount of light transmitted as measured by the sample photodiode, and $I_0(\lambda)$ is the amount of light incident on the sample as measured by the reference photodiode. The transmittance, $T(\lambda)$, includes losses due to reflections and dispersion of light at interfaces. Therefore, for the measurement of thin films deposited onto glass slides, transmission spectra of blank glass slides are taken to determine the losses due to the substrate. Calculations assumptions include that the losses due to the substrate are the same for both the reference blank glass slide and the sample to be measured.

The absorption spectrum of a sample can be calculated from the transmission using **Equation 3.7**.

$$A(\lambda) = -log_{10}\left(\frac{I(\lambda)}{I_0(\lambda)}\right) = -log_{10}(T(\lambda)) \qquad \textbf{Equation 3.7}$$

where $A(\lambda)$ is the absorption at wavelength λ.

The transmittance of thin polymer films were measured from 350 - 900 nm in 2 nm steps with a slit size of 2 nm.

3.5 Spectroscopic Ellipsometry

Spectroscopic ellipsometry is a technique that allows for the measurement of several properties of thin films, including refractive index (n), extinction coefficient (k) and thickness. This is done by measuring the change in the intensity and phase of polarised light as it is reflected from the surface of a thin film of material on a silicon substrate. These changes allow for the thickness, n and k to be modelled. A Woollam M-2000V ellipsometer was used, with a wavelength range of 370 - 1000 nm.

The optical constants of the material are calculated by characterizing the amplitude of the light parallel and perpendicular to the plane of incidence (R_p and R_s respectively). This gives the reflectance ratio, ρ, as given in **Equation 3.8**.

$$\rho = \frac{R_s}{R_p} = \tan(\psi)\exp(i\Delta)$$ **Equation 3.8**

where Ψ is the ratio of amplitudes and Δ the phase difference between the incident and reflected light.

Using Ψ and Δ, it is possible to determine the material properties using an optical model that approximates the structure of the material being measured. This technique was used in **Chapter 4 : Air Stability of MoOx** to calculate the thickness changes of MoO_x over time on adsorption of water. Data was acquired by Dr. Tao Wang.

3.6 External Quantum Efficiency (EQE)

External Quantum Efficiency (EQE) is the ratio of the number of charge carriers collected at the contacts of a solar cell per second to the number of incident photons of a given wavelength shining on the solar cell per second as in **Equation 3.9**.

$$EQE(\lambda) = \frac{electrons/second}{photons(\lambda)/second}$$ **Equation 3.9**

This gives information on the combined efficiency of several processes in the OPV, including photon absorption, charge generation, separation and transport. An EQE of 100% means that for a given wavelength, all incident photons are converted to free charges and collected at the contacts. However, due to losses at many stages due to the aforementioned processes in **2.4 Photophysics of Organic Conjugated Polymers**, OPV device EQE is < 100% for any given wavelength of light.

EQE, once measured, can be used to calculate device J_{sc} using **Equation 3.10** below.

$$J_{sc} = \sum_{\lambda} EQE \times Photon\ Flux \times e$$ **Equation 3.10**

Where the photon flux ($\gamma\ s^{-1}\ m^{-2}$) is the number of photons at a given wavelength per second per unit area, and e is the elementary charge of the electron. The values for photon flux are calculated from the AM1.5 solar spectrum. The product is summed over all wavelengths (λ) to give J_{sc} in $mAcm^{-2}$.

A Lot Oriel LSB117/5 halogen lamp was used as a light source in conjunction with a Spectral Products DK240 monochromator. A Newport 818-UV calibrated silicon photodiode was used to measure a reference spectrum of the light source, and current measurements were taken with a Keithley 237 source meter. EQE spectra were recorded over a 380 - 700 nm wavelength range, and a MATLAB program controlled the measurement process.

An OPV device was loaded vertically into a holder on a movable stage that also housed the Newport reference silicon photodiode. Focussing optics were used to focus the monochromatic light onto the reference photodiode and a reference spectrum recorded, at which point the stage was moved such that the light was focussed on one pixel of the OPV device. The EQE of the pixel was then measured for the wavelength range in 2 nm steps, and the process repeated for each pixel of the OPV device.

3.7 Laser Beam Induced Current Mapping (LBIC)

Laser beam induced current mapping (LBIC) allows for spatial characterization of the electronic properties of individual pixels in OPV devices. The images that are produced of the pixels allow for identification and localization of defects and their effects on device performance, and so this technique is often used to study OPV degradation [7], [8].

The measurement principle is based on a point by point scanning of focused monochromatic light across the surface of a pixel held under short circuit conditions. At the point of focus on the surface, absorbed photons generate current, which is extracted and measured. The device is positioned on a computer controlled x-y stage, which allows the focused light to scan over the surface, building up a current map line by line as the laser is raster-scanned across the surface. For analysis, the measured current is normalised to the incident light intensity and is then interpreted as contrast variation in the LBIC image. Light areas indicate high generated photocurrent, whereas dark areas indicate reduced photocurrent, which corresponds to a loss of local device functionality due to defects or other phenomena.

The setup used herein is as follows: A 405 nm laser diode with a power of 4 mW was focused via a 50X Mitutoyo infinity-corrected objective lens to a spot size of < 5 µm. A model SR830 lock in amplifier and a Thor Labs optical chopper were employed to generate a clear signal. A custom-made LabView computer program drove the stages and collected the data. The maps in this work covered an area of 0.06 cm^2, encompassing an entire pixel. Data was acquired by Mr. Nick Scarratt.

3.8 Electroluminescence Mapping (ELM)

Electroluminescence mapping (ELM) of OPV devices allows for mapping of defects in a completed device. The technique is based on detecting the radiative recombination of charges in the active layer of a device under forward bias with a CCD camera. Areas of relatively high luminescence indicate good charge transport characteristics, whereas areas with defects that inhibit charge transport and recombination result in a relatively low luminescence. When used in conjunction with LBIC, ELM allows for the identification and detailed mapping of defect sites in a OPV active layer films for both new and aged devices.

A light-tight box with a 16 bit Apogee Alta F-series camera with an 8.3 mega pixel silicon CCD detector with a resolution of ~ 10 µm was used as the detector. Devices were injected with a current that was equivalent to their previously measured J_{sc}, and a Keithley 2045 was used as a four wire source unit.

3.9 Lifetime Testing

In order to perform a statistically relevant and repeatable lifetime measurement of OPV devices, a robust experimental setup is required. This requires that several solar cells are tested simultaneously, and the environment of the testing chamber be monitored and controlled, including humidity, temperature and light intensity. Key device operating parameters (PCE, FF, V_{oc} and J_{sc}) should also be measured periodically during testing to monitor ageing of devices. With the publication of a consensus paper on testing protocols and the advent of the international summit on OPV stability (ISOS) [9], standardised methodologies have provided a framework for testing procedures and how data is reported, increasing the rigor of a variety of tests from shelf-life to outdoor interlaboratory testing.

During the second year of my PhD, I assembled and calibrated the laboratory lifetime testing setup used herein. This involved coding in MATLAB and SCPI to control both a Keithley source meter, and a multiplexing unit used to address several devices at once. This code is shown in the **Appendix**.

The following sections detail the design and calibration of the laboratory lifetime testing equipment used in this thesis, including a thorough comparison of all aspects of the laboratory lifetime testing system to the standard device testing system. The laboratory lifetime test setup used herein conforms to the 1st level laboratory weathering test standard, ISOS-L-1, covered in more detail in **3.11.1 ISOS Laboratory Weathering Testing**, and the outdoor lifetime test setup closely adheres to the 2nd level outdoor test standard ISOS-O-2, covered in more detail in **3.11.2 ISOS Outdoor Testing**.

3.9.1 Laboratory Lifetime Testing Setup

The lifetime testing setup was custom built with an ATLAS Suntest CPS+ as the light source and test chamber. The Suntest CPS+ consists of a large housing unit with a 1500 W air-cooled xenon lamp and coated quartz filters to approximate the solar spectrum, with options to control the temperature inside the test chamber and the irradiance in the 300 - 800 nm wavelength range. OPV devices are housed in a chamber that is fully mirror coated to achieve good irradiance uniformity over a 560 cm^2 area, and an air cooling unit that allows for temperature control from 40 - 100^{o}C.

OPV devices were characterised using a custom-made test board, which housed up to eight OPV devices, and a multiplexing unit built by Ossila Ltd. The devices were connected to SIP sockets in the test board using metal 'legs', attached to the ITO contact strips at the edge of the device substrates, as shown in **Figure 3.14**. The board also had eight silicon photodiodes and four temperature sensors installed, with which the light intensity and temperature uniformity across the board could be monitored. The test board was secured inside the Suntest CPS+ and connected to the multiplexing unit, which allowed for the 48 pixels of the eight OPV devices to be tested independently.

A Keithley 2400 source-measure unit was used to carry out IV sweeps of the devices and take readings from the photodiodes and temperature sensors at pre-determined intervals. In between *JV* measurements the OPVs were held at open circuit. The measurement process was controlled by a MATLAB program, written for purpose (**Appendix**). The whole lifetime setup is shown in **Figure 3.15**.

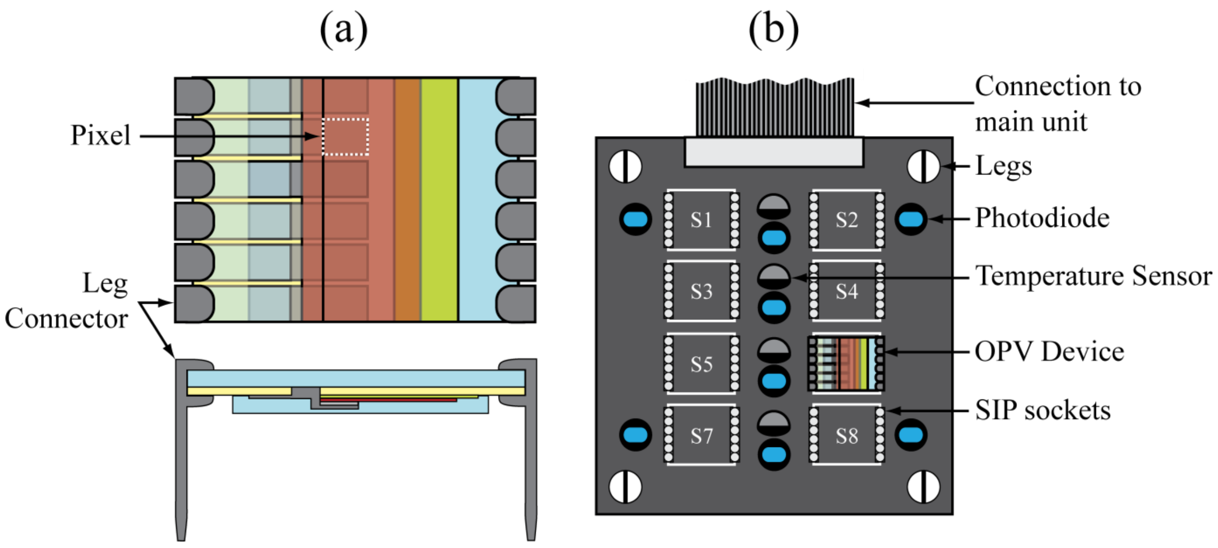

Figure 3.14 (a) OPV device with electrical connection 'legs' attached to the ITO contact strips at the edge of the substrate. **(b)** Shows the circuit board into which the OPV devices were inserted, with devices number S1, S2 etc. The test board measured 100 x 100 mm.

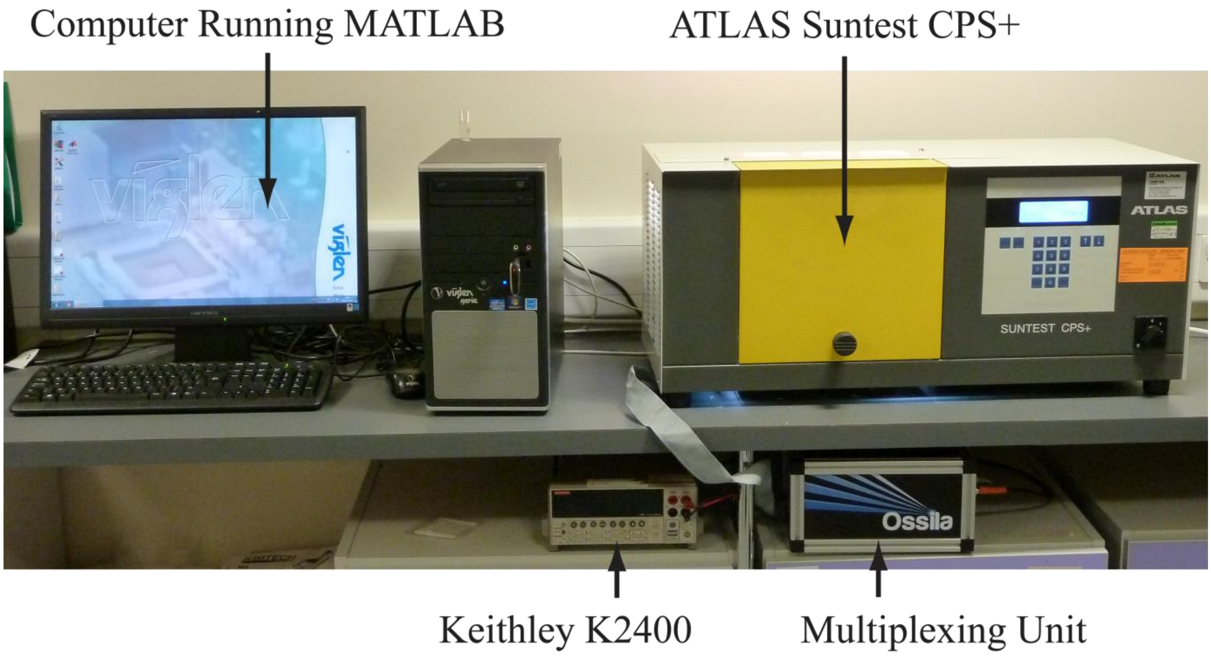

Figure 3.15 Image of the lifetime testing setup with key features labelled.

Due to the design of the test board and the reliance on reflected light to achieve 1 sun intensity, no aperture masks were used when characterizing devices in the lifetime tester. This introduced errors in measurement that are covered in more detail in **3.9.6 Pixel Size Variation**.

3.9.2 Light Source and Spectrum

The choice of light source is important for lifetime testing of OPVs, and several factors have to be taken into account: cost, lifetime, uniformity of illumination, and match to the solar spectrum. The three types of lamp that are commonly used for OPV lifetime testing are sulphur plasma, xenon arc and metal halide global lamps. All need to be fitted with daylight filters to better simulate the solar spectrum. The Suntest CPS+ system with its xenon arc lamp and appropriate daylight filters was chosen for the lifetime testing system due to its good match to the solar spectrum in the UV, visible and infrared as shown in **Figure 3.16**. The spectrum was measured using a calibrated StellarNet Inc. Blue Wave USB spectrometer, and is consistent with spectra from other xenon lamps reported in the literature [9]. It can be seen that although there is a reasonably good match to the solar spectrum between 350 - 600 nm range, the xenon bulb is less powerful in the 600 nm + range. However, as PCDTBT (the polymer used in lifetime measurements in this thesis) absorbs in the 350 - 700 nm range, this does not result in significant differences in measured photocurrent, discussed in more detail in **3.9.3 JV Mismatch**.

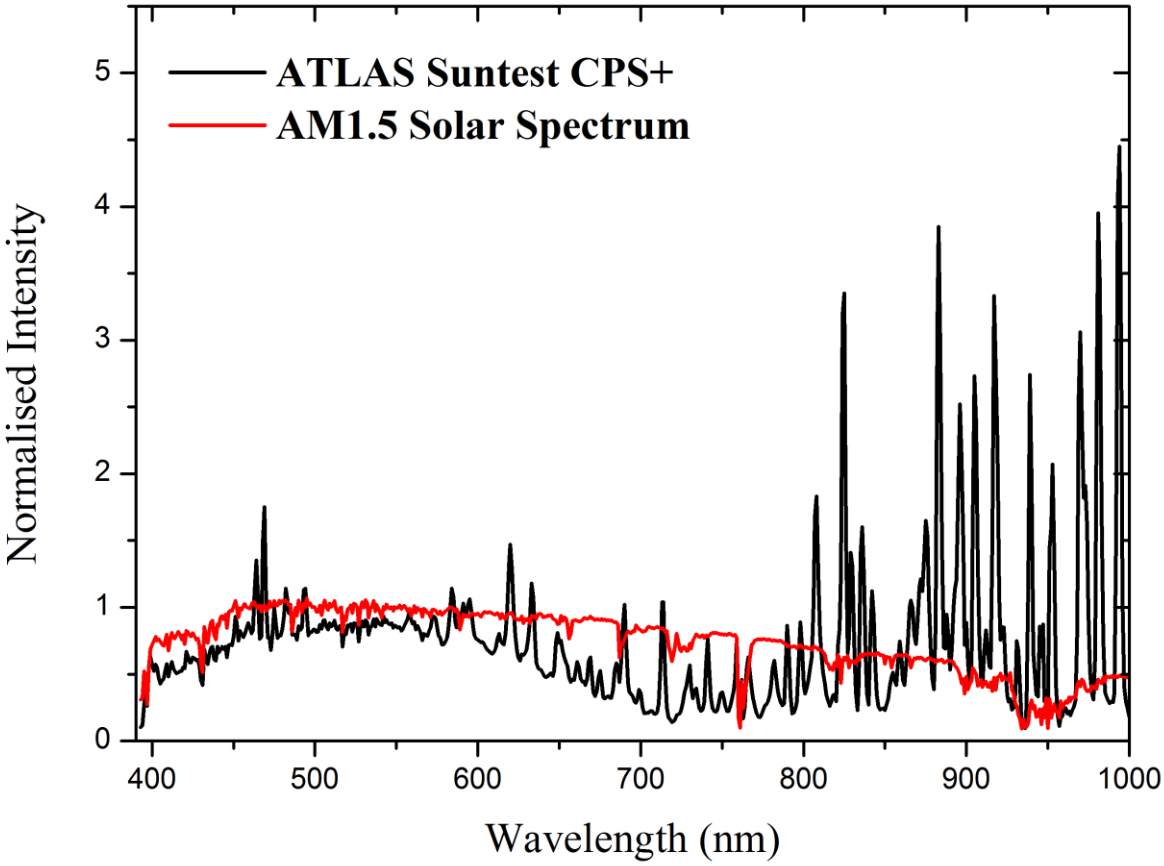

Figure 3.16 Spectra of the ATLAS Suntest CPS+ lifetime tester xenon bulb at 550 Wm^{-2} setting and the AM1.5 solar spectrum. Spectra normalised to the same total intensity in the 350 - 1000 nm range.

The Suntest CPS+ allows for irradiance to be altered from 350 Wm^{-2} to 750 Wm^{-2}, and it was found that at 550 Wm^{-2} the irradiance, including reflected light from the internal reflective walls, achieved 1 sun intensity (1000Wm^{-2}) as measured by an NREL certified silicon reference cell (Newport 91150). The system came with a computer controlled calibration tool that allowed for fine-tuning of the lamp output and temperature control, as can be seen in **Figure 3.17**. Calibration was carried out by setting the system to a specified irradiance and temperature and leaving it to run for up to an hour. During this time, both the irradiance and temperature were controlled by the Suntest CPS+, with the actual values measured by the calibration equipment every 10 seconds. The irradiance and temperature as measured by calibration equipment could then be entered into the Suntest CPS+ to correct for lamp ageing and other factors.

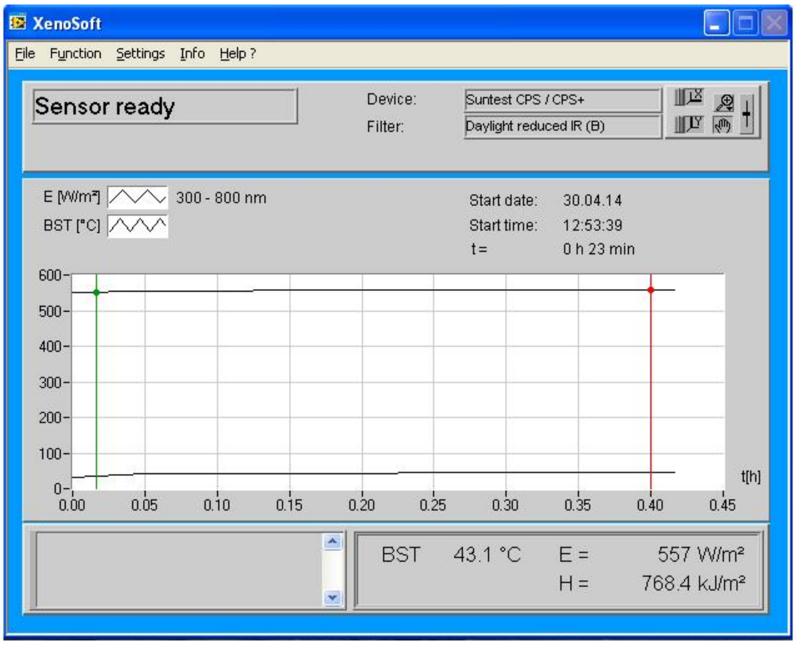

Sensor ready

Device: Suntest CPS / CPS+
Filter: Daylight reduced IR (B)

Start date: 30.04.14
Start time: 12:53:39
t = 0 h 23 min

BST 43.1 °C
E = 557 W/m²
H = 768.4 kJ/m²

Figure 3.17 XenoSoft software used to calibrate the irradiance and temperature in the Suntest CPS+ equipment.

3.9.3 *JV* Mismatch

The effect of the spectrum of the xenon bulb on device performance was calculated by loading devices in the lifetime test board and taking *JV* measurements under the Suntest CPS+ and Newport solar simulator without a pixel aperture mask. Different longpass filters were placed on top of the devices to wavelength limit the incident light and allow for the measurement of J_{sc} differences caused by differences in spectra over different wavelength bands. Longpass filters only allow light through at wavelengths longer than their stated limit, and in the case where no filters were used the UV cut-off of glass at ~ 350 nm determined the lower wavelength limit. The values for J_{sc} measured are shown in **Table 3.4**, and represents the values measured from 8 pixels over two devices with an ITO/PEDOT:PSS/PCDTBT:PC_{70}BM/Ca/Al architecture. The test was repeated for devices with a MoO_x HTL, the results of which are shown in **Table 3.5**.

PEDOT:PSS HTL

Longpass Filter	Solar Simulator J_{sc} ($mAcm^{-2}$)	Suntest CPS+ J_{sc} ($mAcm^{-2}$)	Error in J_{sc} (%)
None	-11.7±0.4	-10.6±0.2	10
400nm	-10.0±0.3	-8.8±0.2	12
455nm	-8.6±0.3	-7.5±0.2	13
495nm	-6.9±0.3	-5.7±0.2	17
550nm	-4.5±0.1	-3.4±0.1	24
590nm	-2.71±0.07	-1.87±0.06	31
645nm	-0.80±0.02	-0.50±0.01	38

Table 3.4 Short circuit current density (J_{sc}) of OPV devices utilizing a PEDOT:PSS HTL, measured using the Newport solar simulator and the ATLAS Suntest CPS+ with different longpass filters. No aperture masks were used during the measurements.

It can be seen that for both devices types there is a 10% error in measured J_{sc} when there are no filters used, with the error increasing significantly when the light is limited to above 550 nm. This corresponds well with the differences in spectra in **Figure 3.16**. However, the spectral responses of the two device types are different. This is likely due to the compositional differences of the devices, with different HTL materials and thicknesses (10 nm for MoO_x and 30 nm for PEDOT:PSS) changing the absorption profile of the devices, and resulting in the varied responses to different wavelengths of light. The devices incorporating a MoO$_x$ HTL showed a constant error of ~ 10% in J_{sc} up to 495 nm at which point the error increased linearly. In comparison, the devices incorporating a PEDOT:PSS HTL do not exhibit a constant error in J_{sc}, but show a slightly greater error at all wavelengths.

MoO$_x$ HTL

Longpass Filter	Solar Simulator J$_{sc}$ (mAcm^{-2})	Suntest CPS+ J$_{sc}$ (mAcm^{-2})	Error in J$_{sc}$ (%)
None	-9.9±0.3	-10.8±0.4	10
400nm	-7.77±0.08	-8.6±0.3	9
455nm	-6.72±0.08	-7.4±0.2	9
495nm	-5.06±0.07	-5.9±0.2	14
550nm	-3.04±0.04	-3.8±0.1	20
590nm	-1.63±0.03	-2.2±0.07	27
645nm	-0.44±0.01	-0.66±0.03	34

Table 3.5 Short circuit current density (*Jsc*) of OPV devices utilizing a MoOx HTL, measured using the Newport solar simulator and the ATLAS Suntest CPS+ with different longpass filters. No aperture masks were used during the measurements.

The effects of this error in measured J_{sc} is discussed in more detail in **3.9.7 Discrepancies in *JV* data**.

3.9.4 Light Uniformity

The light intensity variation inside the Suntest CPS+ chamber was mapped out using the calibrated NREL silicon photodiode (Newport 91150, 2 x 2 cm detector size), and is shown in **Figure 3.18**. This was carried out by first setting the irradiance to 550 Wm^{-2} and holding the temperature at ~ 40^{o}C using the air cooling system. Several readings were taken from the photodiode at fixed points, and averaged to give the values shown. The photodiode was calibrated to give readings in 'suns', 1 sun being equal to 1000 Wm^{-2} of AM1.5 light.

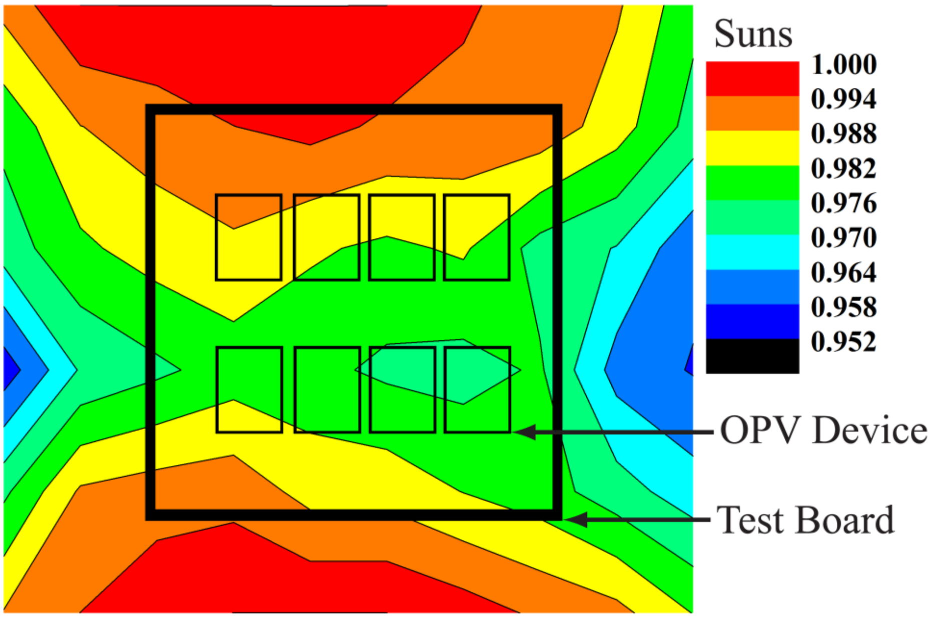

Figure 3.18 Light intensity variation inside the ATLAS Suntest CPS+ chamber as measured by a calibrated Newport 91150 photodiode. Scale is in suns. Location of lifetime test board and OPV devices are labelled.

The test board was placed in the centre of the Suntest CPS+ chamber as shown. The variation in light intensity was ~ 3% over the whole 100 x 100 mm test board and ~ 2.5% over the OPV devices. This variation is corroborated by data gathered using the photodiodes on the test board itself, shown in **Chapter 5 : Hole Transport Layer Laboratory Lifetime Study**.

3.9.5 Source-Measure Unit Comparison

The use of two different source-measure units does not introduce any errors in the measurement of *JV* characteristics, as can be seen in **Figure 3.19** below for a device with an ITO/MoO$_x$/PCDTBT:PC$_{70}$BM/Ca/Al architecture.

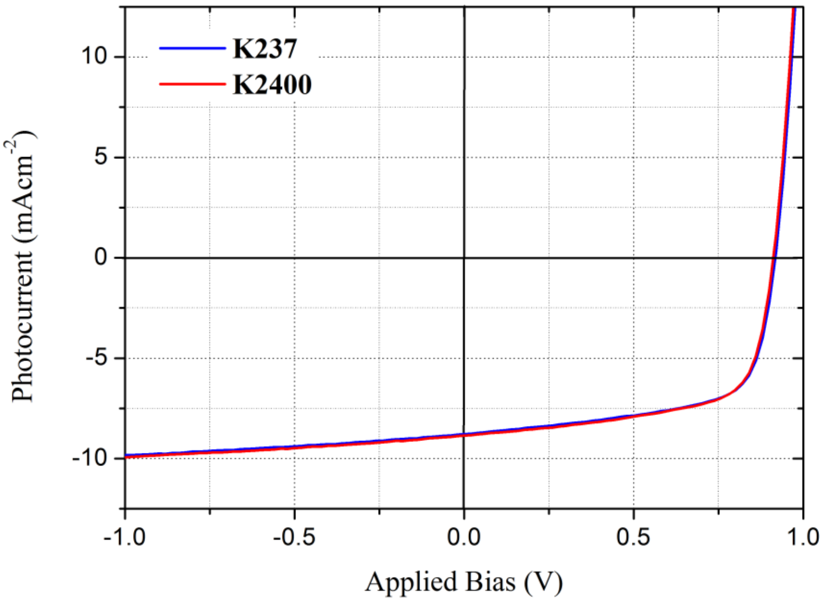

Figure 3.19 *JV* curves for the same device measured using the calibrated solar simulator and two different source-measure units, the Keithley K237 and K2400.

However, the K2400 is slower than the K237, which leads to a minimum delay between measuring any given pixel in a fully populated lifetime test board of ~10 minutes.

3.9.6 Pixel Size Variation

As previously stated, the evaporation of the top contact defines the pixel area. For the evaporation masks used, as shown in **Figure 3.4**, the size of the depression in which the substrate fits has a tolerance of 100 µm to allow for small variations in substrate size and ease of use. This means that the position of the substrates in the mask can differ by up to 200 µm in both the x and y directions. Whilst this does not have an effect on pixel size if the offset is in the y axis, it can have a significant effect on pixel size if the substrate is not perfectly central in the x direction. This is illustrated in **Figure 3.20**.

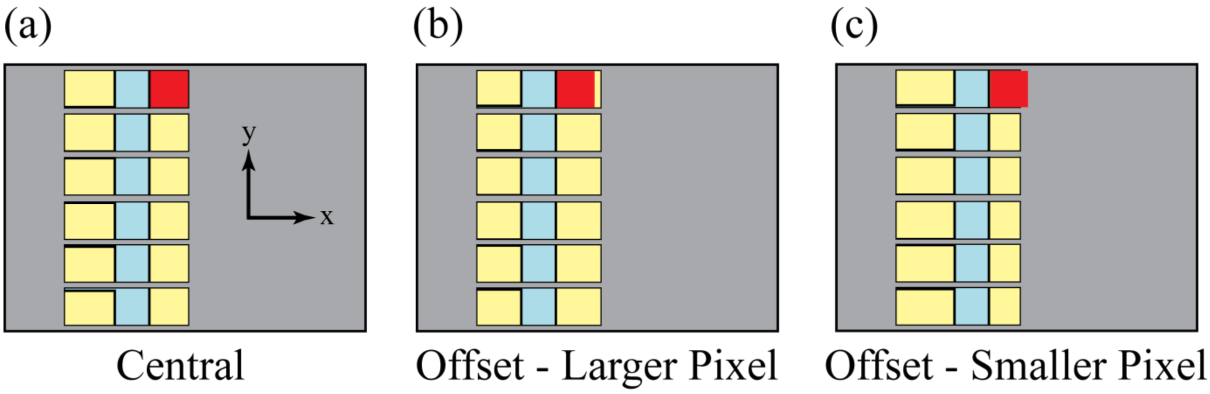

Figure 3.20 Variation in pixel size caused by misalignment of the top contact evaporation mask. The area in red is identical in size in all images. **(a)** Shows the pixel size when the substrate is perfectly aligned, **(b)** shows an x offset which increases the pixel size and **(c)** shows an x offset that decreases the pixel size.

The pixel size when the substrate and mask are perfectly aligned, as in **Figure 3.20 (a)**, is 0.04 cm^2. However, due to the 100 µm tolerance in the mask design, the actual area can be as large as 0.042 cm^2 (**Figure 3.20 (b)**) and as little as 0.038 cm^2 (**Figure 3.20 (c)**). When using an aperture mask this does not result in measurement errors, as the size of the apertures are smaller than even the minimum possible pixel size, at 0.0261 cm^2. Unfortunately, when not using an aperture mask, this inconsistency in pixel size leads to miscalculation of the J_{sc} when characterizing devices, as the MATLAB program is programmed to calculate current density based on the ideal pixel size of 0.04 cm^2, as illustrated in **Figure 3.21**. Unfortunately, a change in calculated current density 'shifts' the *JV* curve up or down the y axis, which alters the point at which it intercepts the x axis, therefore changing the calculated value for V_{oc}. Calculation of the pixel size for individual devices proved to be prohibitively time consuming and inaccurate.

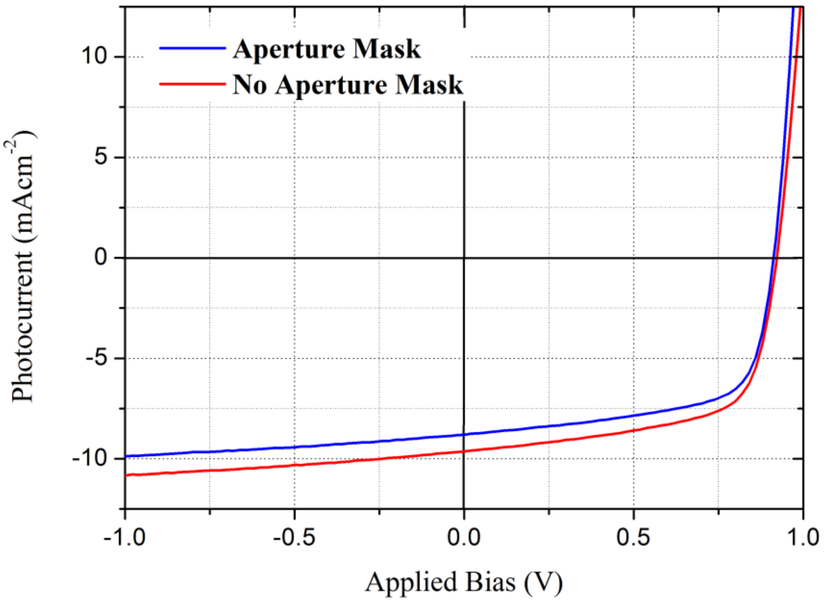

Figure 3.21 Effect of pixel size variation on *JV* characteristics. Here, the pixel size is greater than 0.04 cm^{-2} , shifting the JV curve in the -y direction, resulting in the calculated J_{sc} and V_{oc} being greater than the actual value measured when using a calibrated aperture mask.

3.9.7 Discrepancies in *JV* data

The combined effects of spectral differences between the two light sources and pixel size variation result in different measured *JV* curves when devices are tested using the lifetime tester or calibrated solar simulator. An example of this is shown in **Figure 3.22** for an OPV device with an ITO/MoO_x/PCDTBT:$PC_{70}BM$/Ca/Al architecture. Average device operating parameters are shown in **Table 3.6**.

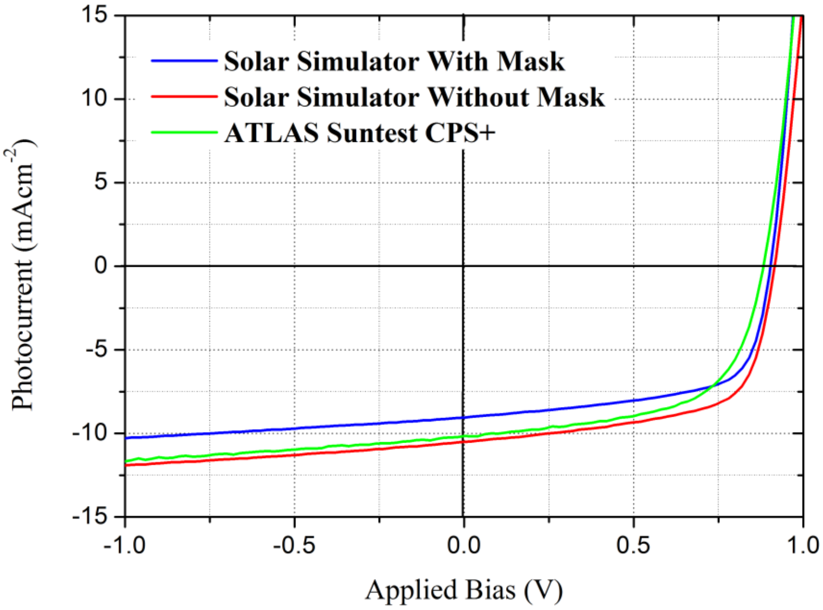

Figure 3.22 *JV* curves for the same device taken using the lifetime testing setup without an aperture mask and the solar simulator set up with and without an aperture mask.

Testing Setup	***PCE* (%)**	***FF***	**V_{oc} (V)**	**J_{sc} (mAcm^{-2})**
Solar Simulator (with mask)	5.25±0.06	64.9±0.6	0.90	-8.9±0.1
Solar Simulator (without mask)	6.10±0.07	64.1±0.3	0.92	-10.4±0.1
Lifetime Tester (without mask)	5.4±0.1	60±0.3	0.88	-10.1±0.1

Table 3.6 Average operating parameters for an OPV device tested using the solar simulator with and without an aperture mask, and the lifetime tester without an aperture mask. The values quoted for J_{sc} (and *PCE*) for measurements taken without an aperture mask are not accurate due to pixel size variation and are therefore for comparison only.

The general effect of measuring *JV* curves using the lifetime testing setup is to lower the measured *FF*, V_{oc} and J_{sc} of the devices due to the differences between the light sources, with J_{sc} also affected by pixel size variation.

The measured V_{oc} of devices is affected not only by light intensity but also by temperature [10], [11], with an increase in light intensity leading to an increase in V_{oc}, and an increase in temperature leading to a decrease in V_{oc}. As the light intensity of the Suntest CPS+ was calibrated to match that of the solar simulator, the observed loss in V_{oc} is likely due to the temperature difference of the two systems, with the Suntest CPS+ running at around 40^{o}C, compared to the solar simulator which runs at room temperature (~ 25^{o}C).

The loss in *FF* when devices are measured using the Suntest CPS+ is likely to be caused by differences in the shape of the vertical absorption profile of the device active layer under illumination at different wavelengths. OPV devices consist of several layers, each with different refractive indices and layer thicknesses on the order of the wavelength of the incident light. This layer stack forms an optical cavity, and the optical density in the layer differs for different wavelengths [12]–[14]. Varying the incident light spectrum has an effect on the generation and transport properties of carriers at different depths in the active layer due to variations in the optical density in the active layer. This has an effect on the shape of the *JV* curve, which manifests as a change in *FF* [15], [16]. As the spectrum of the xenon lamp in the Suntest CPS+ is different to that of the solar spectrum produced by the solar simulator, as shown in **3.9.2 Light Source and Spectrum**, this mechanism is likely the cause of the loss of measured *FF*.

These factors combine to give a different measured device efficiency in the lifetime testing setup when compared to that measured using the solar simulator. It has been discovered that this effect varies in magnitude depending on the device composition and architecture, due to the different layer thicknesses of the materials used leading to different absorption characteristics.

Due to this discrepancy, only *JV* data from the calibrated solar simulator is shown in results chapters, and any data collected from the lifetime tester is normalised to remove any errors introduced by the setup.

3.10 Outdoor Lifetime Testing

In addition to laboratory lifetime testing, OPV devices were also mounted in a lifetime testing setup on the roof of the Department of Physics at the University of Sheffield, England, UK. The outdoor lifetime testing setup is shown in **Figure 3.23**, and included three environmental chambers, each housing an OPV test board (with space for 8 devices) identical to that used for laboratory lifetime testing shown in **Figure 3.14 (b)**. The environmental chambers consisted of a milled aluminium block with a glass cover, sealed with an O-ring and filled with an overpressure of nitrogen to prevent air ingress into the chamber. The overpressure of nitrogen was maintained throughout the testing. A weatherproof metal case contained the electronics and the computer used to control the measurement of the *JV* characteristics of the OPV devices and monitor the temperature inside the environmental chambers. A National Instruments PXI-4132 source measure unit was used to measure the *JV* characteristics of the devices over the -1.0 to 1.0 V range in 0.02V steps every ~ 5 minutes, and a multiplexing unit was used to allow for individual measurement of the 144 pixels of the 24 devices. In between measurements, the devices were kept at open circuit as with the laboratory lifetime test.

The light intensity was monitored using a SPN1 Sunshine Pyranometer, which measured and recorded the total and diffuse irradiance at the point of each *JV* measurement. The readings from the four temperature sensors were also recorded at the point of each *JV* measurement. This allowed for the effects of both irradiance and temperature on device performance every 5 minutes to be tracked throughout the course of the experiment.

The test protocol used herein is of the outdoor testing type, and closely adheres to the second level of testing rigor, ISOS-O-2, the requirements of which are covered **3.11.2 ISOS Outdoor Testing**.

The device test chamber was mounted on a fixed platform facing south with a 30^{o} orientation to maximise incident light.

Figure 3.23 Image of the outdoor lifetime testing setup with key features labelled. Photos taken by Ellie Scott of Ossila Ltd.

3.11 Lifetime Reporting

The most widely used metric used to describe OPV device lifetime is 'T_{80} lifetime', as previously discussed in **2.9.6 Decay Behaviour**. This is defined as the period of time that elapses between the initial stabilised performance after burn-in, and the point at which 80% of this efficiency has been reached. Along with this value, the time evolution of device *JV* parameters (*PCE*, *FF*, V_{oc} and J_{sc}) give an indication of device stability. Other characterization methods, such as LBIC, ELM and absorbance spectroscopy, give valuable insight into degradation mechanisms that cause the loss in device performance.

With the advent of the annual International Summit on OPV Stability (ISOS) and the publication of a consensus paper on testing protocols [9], the reporting of OPV device stability and lifetime has been standardised. There are several tests commonly used for lifetime testing, including shelf-life, thermal cycling, outdoor and laboratory weathering testing, each with three levels of increasing rigor. The test protocol used herein for indoor testing is of the laboratory weathering type, and conforms to the first level of testing rigor, ISOS-L-1, the requirements of which are covered in the next section. The test protocol used for outdoor testing conforms closely to the ISOS-O-2 requirements.

3.11.1 ISOS Laboratory Weathering Testing

Table 3.7 shows the basic requirements for the three different levels of ISOS laboratory weathering testing. In all cases, the light source needs to match the solar spectrum as closely as possible and other parameters, such as temperature and humidity, need to be monitored or controlled.

	ISOS-L-1 (Basic)	ISOS-L-2 (Intermediate)	ISOS-L-3 (Advanced)
Light Source	Simulator	Simulator	Simulator
Temperature	Ambient	65/85^{o}C	65/85^{o}C
Relative Humidity (R.H.)	Ambient	Ambient	Near 50%
Environment Control	Light Only	Light & Temp.	Light, Temp & R.H.
Characterization Light Source	Solar Simulator	Solar Simulator	Solar Simulator
Load	M_{pp} or Open Circuit	M_{pp} or Open Circuit	M_{pp}

Table 3.7 Simplified requirements for the different levels of laboratory weathering testing [9].

The details of ISOS-L-1 testing requirements are shown in **Table 3.8**, along with the matching aspects of the lifetime setup used in this thesis. In all cases the requirements for ISOS-L-1 testing are met.

		ISOS-L-1 Requirements	Lifetime Setup
Test Setup	Light Source	Constant light source (close to AM1.5 preferable)	Yes - Constant light source - Xenon arc - close to AM1.5. See **3.9.2 Light Source and Spectrum**
	Mounting	Specimen's surface normal to light beam	Yes
	Load	Mpp tracking or Open Circuit	Yes - Open Circuit
	Temperature (temp)	Monitored, uncontrolled	Yes - Monitored, controlled
	Relative Humidity (RH)	Uncontrolled, ambient	Yes - Uncontrolled, ambient

	Irradiance Level	400-1200Wm^{-2}	Yes - 550 Wm^{-2} (~ 1000 Wm^{-2} including reflected light)
	Performance Measurement	In situ or with addition characterization step	Yes - In situ
Testing Protocol	Temp/RH	Monitor Specimen temp and RH	Yes - four temperature sensors
	Light Intensity	Monitor	Yes - eight photodiodes
	JV Characterization	Full *JV*	Yes - Full *JV*
	Minimum Measurement Interval	Daily to Weekly	Yes - every 10 minutes
Output	Time	Report Date	Yes
	Instantaneous Performance Parameters	Report *PCE, FF,* V_{oc}, J_{sc} (*JV* curves if possible)	Yes to all. *JV* curves from solar simulator quoted. See **3.9.7 Discrepancies in *JV* data**
	Stability Performance Parameters	Time evolution of *PCE, FF,* V_{oc}, J_{sc}. T_{80} calculated	Yes - to all
	Irradiance	Report irradiance level and uniformity	Yes - see **3.9.4 Light Uniformity**
	Spectrum	Report light spectrum	Yes - see **3.9.3 JV Mismatch**
	Temp/RH	Report device temp during testing and storage. Report ambient RH	Yes
	Description of Setup	Report	Yes - see **3.9.1 Laboratory Lifetime Testing Setup**

Table 3.8 Detailed requirements for ISOS-L-1 testing procedure [9] and the equivalent setup for lifetime testing used in this thesis.

3.11.2 ISOS Outdoor Testing

The details of ISOS-O-2 testing requirements are shown in **Table 3.9,** compared to the specification of the outdoor lifetime testing setup used in this thesis. The requirements for ISOS-O-2 testing are met in all cases except for the relative humidity, which instead of being ambient is close to 0%, as the environmental chamber was filled with nitrogen.

		ISOS-O-2 Requirements	**Lifetime Setup**
Test Setup	Light Source	Direct Sunlight	Yes
	Mounting	Static: Front side orientate towards equator at latitude angle	Yes - Static
	Load	MPP tracking or Open Circuit	Yes - Open Circuit
	Temperature (temp)	Ambient	Yes - Monitored
	Relative Humidity (RH)	Ambient	<u>No - 0% as under nitrogen</u>
	Performance Measurement	Outside in sunlight	Yes
Testing Protocol	Temp/RH	Monitor	Yes - Four temperature sensors
	Light Intensity	Monitor Irradiance. Calculate accumulated radiation	Yes - Pyranometer
	JV Characterization	Full JV	Yes
	Minimum Measurement Interval	Every 15 minutes - 1 hour	Yes - Every 5 minutes
Output	Location/Time	Report latitude, longitude and date	Yes: (53.380984, -1.486084) 1/8/14 - 08/12/14

	Instantaneous Performance Parameters	Report *PCE*, *FF*, V_{oc}, J_{sc} (*JV* curves if possible)	Yes
	Stability Performance Parameters	Time evolution of *PCE*, *FF*, V_{oc}, J_{sc}. T_{80} calculated	Yes
	Irradiance	Pyranometer	Yes - See **Figure 3.23**
	Temp/RH	Resistive thermal detector	Yes - average from four temperature sensors
	Description of Setup	Report	Yes - **3.10 Outdoor Lifetime Testing** and **Figure 3.23**

Table 3.9 Detailed requirements for ISOS-O-2 testing procedure [9] and the equivalent setup for outdoor lifetime testing used in this thesis.

3.12 Conclusions

The techniques and methods outlined in **3.1 Fabrication Techniques** and **3.2 Device Fabrication** are used throughout this thesis to fabricate OPV devices. Details of material processing conditions are given in chapters where they deviate from those given here.

In all chapters, OPV devices were characterised using the techniques and equipment discussed in **3.3 Device Characterization** with the calibrated Newport solar simulator and aperture mask to assure accurate measurement of device characteristics.

Spectroscopic ellipsometry, covered in **3.5 Spectroscopic Ellipsometry**, was utilised in **Chapter 4 : Air Stability of MoOx** for the measurement of the hygroscopicity of MoO_x films.

For the laboratory lifetime test of OPV devices in **Chapter 5 : Hole Transport Layer Laboratory Lifetime Study**, the lifetime test equipment detailed in **3.9 Lifetime Testing** was used. The discrepancy in *JV* characterisation between the laboratory lifetime testing system and Newport solar simulator, discussed in **3.9.7 Discrepancies in *JV* data**, are accounted for in all results.

LBIC and ELM techniques, **3.7 Laser Beam Induced Current Mapping (LBIC)** and **3.8 Electroluminescence Mapping (ELM)** respectively, were used to detect defects formed in OPV devices aged in the laboratory lifetime testing setup in **Chapter 5 : Hole Transport Layer Laboratory Lifetime Study**.

In **Chapter 6** : **Polymer Air Processing**, absorbance spectroscopy and EQE measurements, discussed in **3.4 Absorbance Spectroscopy** and **3.6 External Quantum Efficiency (EQE)** respectively, were used to investigate the effects spin-coating the active layer of OPV devices in air.

Finally, in **Chapter 7 : Outdoor Lifetime Testing**, the outdoor lifetime testing setup detailed in **3.10 Outdoor Lifetime Testing** was used to test the response of optimised OPV devices to ageing in varying illumination and thermal conditions on a rooftop in Sheffield, England, UK over the course of 4 months.

3.13 References

[1] Y. Liang, Z. Xu, J. Xia, S.-T. Tsai, Y. Wu, G. Li, C. Ray, and L. Yu, “For the bright future-bulk heterojunction polymer solar cells with power conversion efficiency of 7.4%.,” *Adv. Mater.*, vol. 22, no. 20, pp. E135–8, May 2010.

[2] J. D. Servaites, S. Yeganeh, T. J. Marks, and M. A. Ratner, “Efficiency Enhancement in Organic Photovoltaic Cells: Consequences of Optimizing Series Resistance,” *Adv. Funct. Mater.*, vol. 20, no. 1, pp. 97–104, Jan. 2010.

[3] R. A. Street, K. W. Song, and S. Cowan, “Influence of series resistance on the photocurrent analysis of organic solar cells,” *Org. Electron.*, vol. 12, no. 2, pp. 244–248, Feb. 2011.

[4] T. Kirchartz, F. Deledalle, P. S. Tuladhar, J. R. Durrant, and J. Nelson, “On the differences between dark and light ideality factor in polymer:Fullerene solar cells,” *J. Phys. Chem. Lett.*, vol. 4, no. 14, pp. 2371–2376, Jul. 2013.

[5] T. M. Clarke, A. Ballantyne, S. Shoaee, Y. W. Soon, W. Duffy, M. Heeney, I. McCulloch, J. Nelson, and J. R. Durrant, “Analysis of charge photogeneration as a key determinant of photocurrent density in polymer: fullerene solar cells.,” *Adv. Mater.*, vol. 22, no. 46, pp. 5287–91, Dec. 2010.

[6] G. F. A. Dibb, F. C. Jamieson, A. Maurano, J. Nelson, and J. R. Durrant, “Limits on the Fill Factor in Organic Photovoltaics: Distinguishing Nongeminate and Geminate Recombination Mechanisms,” *J. Phys. Chem. Lett.*, vol. 4, no. 5, pp. 803–808, Mar. 2013.

[7] J. M. Kroon, M. M. Wienk, W. J. H. Verhees, and J. C. Hummelen, “Accurate efficiency determination and stability studies of conjugated polymer/fullerene solar cells,” *Thin Solid Films*, vol. 403–404, pp. 223–228, Feb. 2002.

[8] M. T. Lloyd, C. H. Peters, A. Garcia, I. V. Kauvar, J. J. Berry, M. O. Reese, M. D. McGehee, D. S. Ginley, and D. C. Olson, “Influence of the hole-transport layer on the initial behavior and lifetime of inverted organic photovoltaics,” *Sol. Energy Mater. Sol. Cells*, vol. 95, no. 5, pp. 1382–1388, May 2011.

[9] M. O. Reese, S. A. Gevorgyan, M. Jørgensen, E. Bundgaard, S. R. Kurtz, D. S. Ginley, D. C. Olson, M. T. Lloyd, P. Morvillo, E. A. Katz, A. Elschner, O. Haillant, T. R. Currier, V. Shrotriya, M. Hermenau, M. Riede, K. R. Kirov, G. Trimmel, T. Rath, O. Inganäs, F. Zhang, M. Andersson, K. Tvingstedt, M. Lira-Cantu, D. Laird, C. McGuiness, S. (Jimmy) Gowrisanker, M. Pannone, M. Xiao, J. Hauch, R. Steim, D. M. DeLongchamp, R. Rösch, H. Hoppe, N. Espinosa, A. Urbina, G. Yaman-Uzunoglu, J.-B. Bonekamp, A. J. J. M. van Breemen, C. Girotto, E. Voroshazi, and F. C. Krebs, “Consensus stability testing protocols for organic photovoltaic materials and devices,” *Sol. Energy Mater. Sol. Cells*, vol. 95, no. 5, pp. 1253–1267, May 2011.

[10] G. Garcia-Belmonte, “Temperature dependence of open-circuit voltage in organic solar cells from generation–recombination kinetic balance,” *Sol. Energy Mater. Sol. Cells*, vol. 94, no. 12, pp. 2166–2169, Dec. 2010.

[11] A. Manor, E. A. Katz, R. Andriessen, and Y. Galagan, “Study of organic photovoltaics by localized concentrated sunlight: Towards optimization of charge collection in large-area solar cells,” *Appl. Phys. Lett.*, vol. 99, no. 17, p. 173305, 2011.

[12] J. Y. Kim, S. H. Kim, H.-H. Lee, K. Lee, W. Ma, X. Gong, and A. J. Heeger, “New Architecture for High-Efficiency Polymer Photovoltaic Cells Using Solution-Based Titanium Oxide as an Optical Spacer,” *Adv. Mater.*, vol. 18, no. 5, pp. 572–576, Mar. 2006.

[13] B. Valle, S. Loser, J. W. Hennek, V. DeGeorge, C. Klosterman, J. H. Andrews, K. D. Singer, and T. J. Marks, “Spectral aspects of cavity tuned absorption in organic photovoltaic films.,” *Opt. Express*, vol. 20 Suppl 6, no. November, pp. A954–63, Nov. 2012.

[14] X. Zhao, Z. Li, T. Zhu, B. Mi, Z. Gao, and W. Huang, “Structure optimization of organic planar heterojunction solar cells,” *J. Phys. D. Appl. Phys.*, vol. 46, no. 19, p. 195105, May 2013.

[15] J. Mescher, N. Christ, S. Kettlitz, A. Colsmann, and U. Lemmer, “Influence of the spatial photocarrier generation profile on the performance of organic solar cells,” *Appl. Phys. Lett.*, vol. 101, no. 7, p. 073301, Aug. 2012.

[16] J. D. Kotlarski and P. W. M. Blom, “Impact of unbalanced charge transport on the efficiency of normal and inverted solar cells,” *Appl. Phys. Lett.*, vol. 100, no. 1, p. 013306, 2012.

Chapter 4 : Air Stability of MoO_x

In this chapter, the optimization and air stability of OPV devices utilizing a molybdenum oxide (MoO_x) hole transport layer is reported. It is shown that on exposure to air, evaporated MoO_x HTL films adsorb water due to their hygroscopicity. Ellipsometry was used to measure the adsorption rate of water into MoOx films, and the effects of this adsorbed water on OPV device operation were studied using device characterization. It was found that the adsorbed water had a negative effect on OPV device performance, which can be mitigated with a thermal annealing process. Using spectroscopic ellipsometry, it was observed that thermally annealing MoO_x films in a glovebox before exposure to air densifies the films and reduces the hygroscopicity by a significant degree, reducing the uptake of water into the films and decreasing the negative effects of air exposure on OPV device performance [1]. Using this thermal annealing treatment on MoO_x films allowed for processing of a PCDTBT:$PC_{70}BM$ active layer in air, resulting in devices whose performance exceeded that of devices processed entirely in a glovebox.

4.0 Introduction

Recent improvements in polymer:fullerene solar cell efficiency and stability have largely come from the synthesis of new polymers that have lower lying HOMO levels and reduced energy gap. A lower lying HOMO level has the twin benefit of allowing more of the energy of each photon to be harvested due to better energy alignment to PCBM [2], while also improving the stability of the material by making oxidation more difficult. As such, there has been a recent trend for high efficiency OPVs to utilize polymers with HOMO levels in the region of -5.1 eV to -5.5 eV, including PTB7 [3] (-5.15 eV) and PCDTBT [4] (-5.5 eV). These materials contrast with more well-established polymer electron-donors such as P3HT [5] and MEH-PPV [6] that have HOMO levels of around -5.0 eV.

To utilize these materials with lower lying HOMO levels also requires the use of hole extraction contacts having a similarly low lying work-function. A variety of such interface layers have been investigated, including transition metal oxides such as MoO_x [5], WO_x [7] and VO_x [8]. In particular, MoO_x has been studied due to its low lying conduction band onset (-6.7 eV [9]) and its ease of deposition via thermal evaporation [10], sputtering [11] and solution processing [12]. When used as the hole transport layer (HTL) in an OPV device containing an organic semiconductor with a large ionisation potential, the organic semiconductor close to the MoO_x interface has been shown to become *p*-doped as a result of charge-transfer [9], with such interfaces supporting efficient hole-extraction [13]. This has resulted in OPVs utilizing a MoO_x HTL and the polymer PCDTBT achieving power conversion efficiencies of over 7% [14].

4.1 MoO_x Films and Ambient Conditions

However, whilst MoO_x can be utilized to produce high-efficiency OPV devices, it is not without problems. In particular MoO_x is susceptible to loss of oxygen during evaporation which can result in changes in stoichiometry and electronic energy levels [15]. This is illustrated in **Figure 4.1**, where after use in one thermal evaporation the colour of MoO_x source pellets changes from green/yellow to dark grey.

Figure 4.1 Colour change of MoO_x source pellets after one evaporation: **(a)** fresh pellets and **(b)** pellets after one thermal evaporation.

In certain states MoO_x is also hygroscopic, and can adsorb water to produce a hydrated crystal within a few Langmuir [16] (defined as an exposure of 10^{-6} torr in one second). It is believed that water species adsorbed into the MoO_x crystal either reside between the MoO_x clusters in the bulk of the material, changing the cluster size and, as a result, the band gap [9], or are weakly bound by Van der Walls forces on the surface [17], [18] as either H_2O or hydroxide ions [19]. Water adsorption can occur on timescales of a few tens of minutes even in a highly pure nitrogen atmosphere with water levels of less than 1 ppm [16], and almost instantaneously in air. This sensitivity suggests that understanding, and stabilizing, the oxidation and hydration state of MoO_x will be a key requirement for its use in OPV devices.

4.2 MoO_x Film and Device Preparation

MoO_x films were prepared by thermal evaporation, discussed in **3.1.4 Thermal Evaporation**. 2 - 4 mm pellets of molybdenum (VI) oxide were purchased from Testbourne Ltd and used as received. MoO_x was deposited via thermal evaporation under a vacuum of < 5E-7 mbar at a rate of 0.2 $Ås^{-1}$ using fresh molybdenum (VI) oxide pellets for each evaporation due to the change of oxidation state of the pellets as shown in **Figure 4.1**. A series of different films were prepared; films for OPV devices were deposited onto cleaned ITO coated glass substrates and had a thickness of 10 nm, whilst films for ellipsometry were deposited onto silicon wafers, which were cleaned using the same process as the OPV substrates, and had a thickness between 15 and 20 nm. The cleaning procedure is described in **3.1.1 Substrate Cleaning**.

OPV devices had a standard ITO/MoO_x/PCDTBT:$PC_{70}BM$/Ca/Al architecture, with MoO_x forming the HTL and Ca forming the ETL. The PCDTBT used was the R3CH batch, the details of which are shown in **Table 4.1**, and the $PC_{70}BM$ used was 95% pure, the other 5% being $PC_{60}BM$. Both materials were sourced from Ossila Ltd. PCDTBT:$PC_{70}BM$ active layers were deposited by spin-coating, as covered in **3.1.3 Thin Film Deposition**, in either the glovebox under inert atmosphere or in a Lamarflo workstation in air, to a thickness of 70 nm as measured by a Dektak profilometer. The calcium and aluminium top contact (sourced from Sigma-Aldrich, 99% and 99.99% purity respectively) was thermally evaporated at a pressure of < $5*10^{-7}$ mbar in the evaporation chamber to a thickness of 2.5 nm and 100 nm respectively.

In situ spectroscopic ellipsometry was used to study the uptake of moisture and the effects of thermal annealing on MoO_x, the methodology of which is discussed in **3.5 Spectroscopic Ellipsometry**.

Polymer	Source	M_w	M_n	PDI	$PC_{70}BM$ Blend Ratio
PCDTBT (R3CH)	UoS Chem. Dept	36,700	17,000	2.15	1:4

Table 4.1 Polymer name, source, M_w, M_n, PDI and optimized $PC_{70}BM$ blend ratio for the PCDTBT batch (R3CH) used in this chapter.

4.3 OPV Performance

Initially, the effects on device performance on exposing MoO_x HTL films to air was investigated. Freshly evaporated MoO_x HTL films on OPV substrates were removed from the glovebox, exposed to air for between 2 - 60 minutes, and then returned to the glovebox. The active layer and the Ca/Al top contact were deposited without any further exposure to atmosphere. OPV devices were also fabricated without exposing the MoO_x HTL films to air. The devices whose MoO_x HTLs were exposed to air are referred to as 'Air Exposed' devices, and those not exposed to air are referred to as 'Reference' devices from here on. The device operating parameters are shown in **Table 4.2**. In all cases, values quoted for device operating parameters are the average of 12 pixels across three devices, with the worst 25% of pixels removed to account for gross film defects. *JV* curves for Reference and Air Exposed devices (with 10 minute exposure time) are shown in **Figure 4.2**.

MoO_x Exposure Time (minutes)	PCE (%)	FF	V_{oc} (V)	J_{sc} ($mAcm^{-2}$)
0 (reference)	4.8±0.1	61.0±0.9	0.86	-9.0±0.2
2	3.5±0.2	48±4	0.80	-8.9±0.3
4	3.6±0.3	48±4	0.80	-9.1±0.2
10	3.7±0.2	49±4	0.80	-9.0±0.4
20	3.5±0.2	48±3	0.80	-9.1±0.2
60	3.4±0.3	48±4	0.80	-9.0±0.2

Table 4.2 Operating parameters for OPV devices where the MoO_x HTLs have been exposed to air for between 2 and 60 minutes.

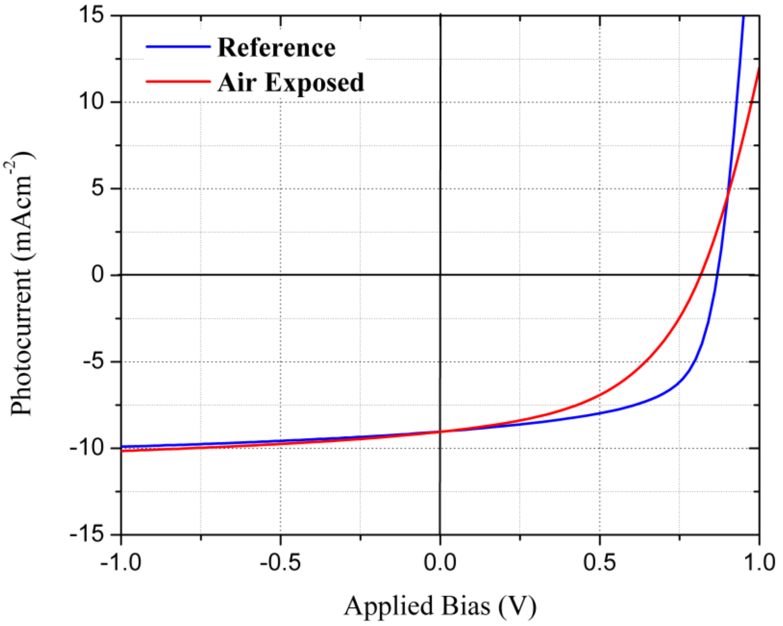

Figure 4.2 *JV* characteristics for Reference and Air Exposed OPV devices (10 minutes of air exposure).

It can be seen that exposing MoO_x HTLs to air for short periods of time, before active layer deposition in a glovebox, results in a reduction in device performance due to a loss of V_{oc} and *FF*. This reduction in *PCE* is attributed to adsorption of water into the bulk of the MoO_x film on exposure to air. Previous measurements have shown that MoO_x is hygroscopic and that its work-function is sensitive to exposure to water, and can change by up to 1.2 eV almost instantaneously on contact with moisture in the atmosphere [16]. Other studies have concluded that this results from a change in hydration state [9], with X-ray scattering used to demonstrate the presence of water molecules adsorbed within the MoO_x crystal [20]. When used with PCDTBT, the large electron-affinity of MoO_x (-6.7 eV) permits charge-transfer doping of the PCDTBT around the MoO_x-PCDTBT interface. However, the work-function of the hydrated form of MoO_x is lower lying by up to 1.2 eV [16], with such a reduction in work-function reducing *p*-type doping and thus resulting in internal charge extraction losses as confirmed by a reduction in V_{oc} and *FF* as can be seen in **Table 4.2**. It can be seen that the negative effect on device performance does not vary for air exposure times, indicating that the process of water adsorption is very fast, a result in agreement with previous studies.

To explore whether this reduction in device efficiency as a result of air exposure could be recovered, thermal annealing was used under an inert atmosphere to attempt to remove moisture from the film. The approach here is based on previous work in which it has been shown that thermal annealing at temperatures up to 120°C can modify the hydration state of thin film MoO_x, with higher temperatures altering the oxidation state [20]. To test such an approach, MoO_x HTL films were exposed to air for 5 minutes, and on return to the glovebox were thermally annealed at temperatures between 80 - 150°C for 30 minutes after exposure to air, with device operating parameters shown in **Table 4.3**. It should be noted that OPV device characteristics quoted in **Tables 4.2-4.5** represent individual batches of devices fabricated on different days. **Tables 4.5** and **4.6** show partial data from the same device batch. Slight variations in fabrication procedure can lead to differences in device characteristics even if the devices are nominally identical. Variations in J_{sc} and *FF* due to active layer blend differences are common as fresh blend solutions were prepared for each device batch, leading to minor differences in blend ratio, concentration and final film thickness.

MoO_x Annealed *After* Exposure to Air

MoO_x Annealing Temperature	PCE (%)	FF	V_{oc} (V)	J_{sc} ($mAcm^{-2}$)
Reference	4.8±0.1	60.4±0.9	0.86	-9.3±0.2
0	4.0±0.2	52±2	0.80	-9.4±0.2
80	3.9±0.1	53±1	0.80	-9.2±0.2
100	4.0±0.1	53.5±0.5	0.80	-9.4±0.2
120	4.1±0.1	55.7±0.4	0.80	-9.2±0.2
150	4.1±0.2	57±1	0.79	-9.0±0.4

Table 4.3 Operating parameters for OPV devices whose MoO_x HTLs had undergone thermal treatment in a glovebox at temperatures between 80 - 150^{o}C for 30 minutes after exposure to air. The MoO_x HTLs were not exposed to air or annealed in 'Reference' devices.

It can be seen that thermally annealing MoO_x HTL films after exposure to air results in no improvement of average *PCE* compared to 'Air Exposed' devices, regardless of the temperature at which the HTL films were annealed. It is likely that this failure to recover OPV efficiency results from incomplete removal of adsorbed water in the bulk of the films, resulting in a reduced work-function and poor charge extraction at the MoO_x-active layer interface.

The effects of applying the same thermal treatment to a MoO_x film *before* it was exposed to air (referred to as 'Annealed before Exposure') was also investigated, with the *JV* characteristics of devices shown in **Table 4.4**.

MoO_x Annealed *Before* Exposure to Air

MoO_x Annealing Temperature	PCE (%)	FF	V_{oc} (V)	J_{sc} ($mAcm^{-2}$)
Reference	5.06±0.06	62.7±0.2	0.86	-9.4±0.1
0	4.0±0.1	52±1	0.80	-9.5±0.3
80	4.6±0.2	57±2	0.85	-9.5±0.1
100	4.89±0.07	59.4±0.4	0.86	-9.57±0.06
120	4.89±0.05	59.8±0.3	0.86	-9.51±0.09
150	4.84±0.05	60.6±0.4	0.85	-9.4±0.1

Table 4.4 Operating parameters for OPV devices whose MoO_x HTLs had undergone thermal treatment in a glovebox at temperatures between 80 - 150^{o}C for 30 minutes before exposure to air for 5 minutes. The MoO_x HTLs were not exposed to air or annealed in 'Reference' devices.

Here it can be seen that thermally annealing the MoO_x HTL films *before* exposure to air (for 5 minutes) prevents the significant loss in device efficiency seen in the 'Air Exposed' devices. The reasons for this are discussed in **4.3 Water Adsorption**. For thermal treatments before or after exposure to air, 100^{o}C or 120^{o}C for 30 minutes resulted in the best performing devices. Higher temperatures (150^{o}C) resulted in losses of V_{oc}, likely due to changes in the stoichiometry of MoO_x [20]. 120^{o}C was chosen as the optimal thermal treatment temperature as it consistently gave the highest performing OPV devices over multiple device batches in addition to those shown here.

A final batch of devices was fabricated to allow for comparison between the effect of optimal thermal treatment on device performance either before or after exposure to air. As a control, the optimal thermal treatment was also applied to MoO_x films that were not subsequently exposed to the atmosphere. These devices are referred to as 'Annealed, not exposed'. The average device operating parameters are shown in **Table 4.5** and *JV* characteristics in **Figure 4.3**.

Comparative Study of Thermal Treatments				
	PCE (%)	**FF**	**V_{oc} (V)**	**J_{sc} ($mAcm^{-2}$)**
Reference	5.00 ± 0.09	58.1 ± 0.7	0.85	-10.21 ± 0.11
Annealed, not exposed (120^{o}C 30mins)	5.10 ± 0.04	58.7 ± 0.3	0.85	-10.31 ± 0.12
Air exposed (10 minutes)	4.48 ± 0.07	53.6 ± 0.8	0.80	-10.45 ± 0.09
Annealed after exposure (120^{o}C 30mins)	4.50 ± 0.07	56.2 ± 0.6	0.78	-10.29 ± 0.09
Annealed before exposure (120^{o}C 30mins)	5.06 ± 0.10	57.0 ± 0.6	0.85	-10.51 ± 0.11

Table 4.5 Operating parameters for OPV devices whose MoO_x HTLs had undergone different thermal treatments and air exposure steps.

Again, it can be seen that thermally annealing a film after air exposure results in no improvement of average *PCE*, with devices having an efficiency of (4.50 ± 0.07)% compared with Air Exposed devices (4.48 ± 0.07)%. Such a process does not recover the efficiency of the Reference devices (5.00 ± 0.09)%. However, OPVs having a MoO_x HTL annealed at 120°C for 30 minutes before exposure to air had an average *PCE* of (5.06 ± 0.10)%; an efficiency comparable to that of the Reference device (5.00 ± 0.09) and larger than that of devices that were air exposed without prior thermal treatment (4.48 ± 0.07)%. This suggests that annealing promotes a film structure that slows down the adsorption of water. The annealing process does not appear to affect the efficiency of the annealed MoO_x film that was not exposed to the atmosphere, as the efficiency of the 'Annealed, not exposed' OPV devices is (5.10 ± 0.04)%.

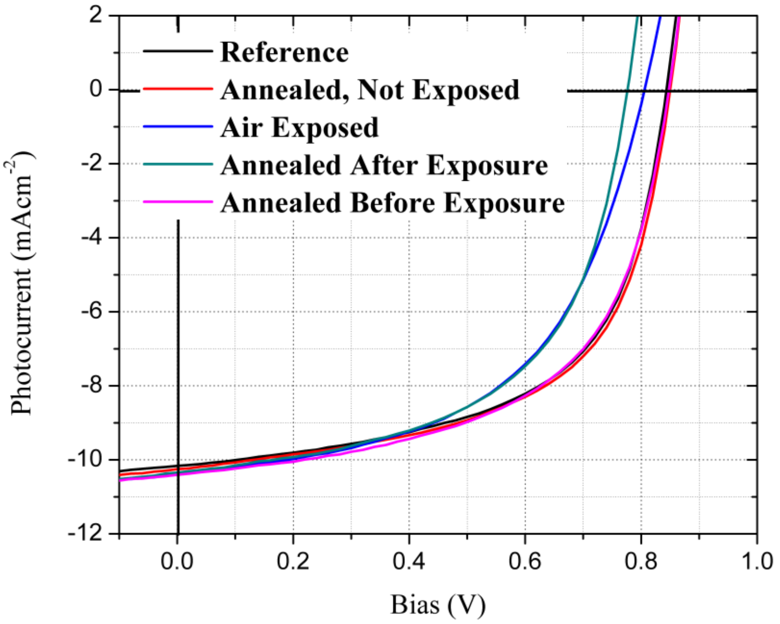

Figure 4.3 *JV* characteristics for OPV devices with varying thermal treatments and air exposure protocols for MoO_x HTLs. *JV* data from best devices from **Table 4.5**.

4.3 Water Adsorption

To test the hypothesis that thermal treatment of MoO_x films before exposure to air slows down the adsorption of water, spectroscopic ellipsometry was used to explore the rate at which MoO_x films undergo swelling as they are exposed to air. Here, two nominally identical 20 nm thick MoO_x films were deposited on to silicon wafers, with one film initially thermally annealed at 120°C for 30 minutes in the glovebox and the other left unannealed. The results of this experiment are shown in **Figure 4.4**, where the % change in film thickness as a function of exposure time is shown. It can be seen that the unannealed MoO_x film undergoes an increase in thickness of around 1.30% over the course of the experiment, while the film that was initially thermally annealed undergoes a much smaller increase in thickness (around 0.18%). This process has a time constant of 10s of minutes, and is significantly longer that reported elsewhere on the basis of in-situ XPS data [16]. However the ellipsometry measurements probe the bulk of the film rather than being sensitive to the properties of the surface alone, which is likely to undergo much faster changes. The findings demonstrate a correlation between the uptake of moisture by a MoO_x film and reduced device efficiency, and confirm the speculation that thermal annealing suppresses the uptake of moisture, thereby resulting in a smaller change in work-function and thus improved device performance.

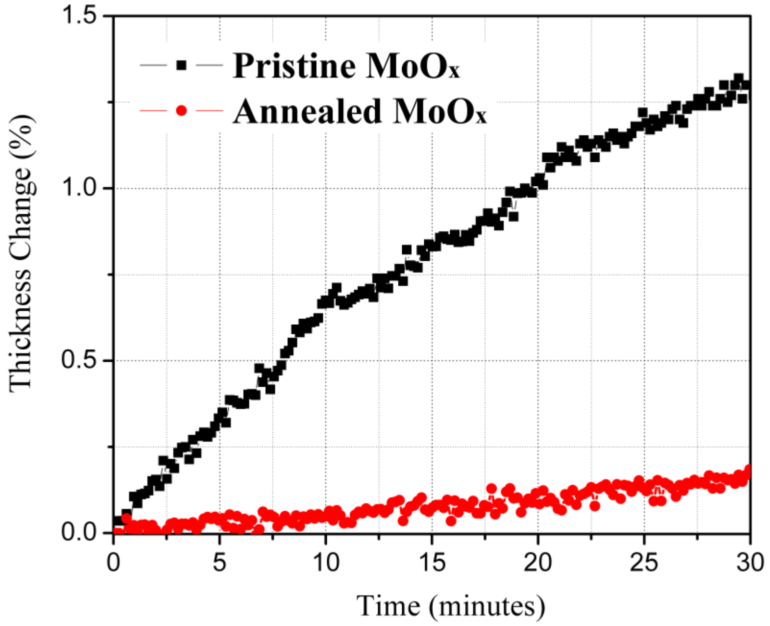

Figure 4.4 % thickness change over time for annealed and unannealed MoO_x films exposed to air.

The thermal annealing process results in a densification of the MoO_x film, thereby reducing its porosity and limiting its ability to adsorb moisture, with such a densification process resulting from thermal annealing previously observed in other metal-oxide films [17]. Ellipsometry was again used to measure changes in the thickness of a pristine MoO_x film as it was annealed at 120°C for 30 minutes in a nitrogen atmosphere and then returned to room temperature. The results of which are shown in **Figure 4.5**. The initial increase in thickness is due to thermal expansion, but on return to room-temperature the thickness of the MoO_x film was reduced by 0.19%, suggesting an increase in density of the same order. This increase in film density most likely results from a reduction of the volume of voids between grains in the MoO_x crystal, thereby reducing its ability to adsorb water. This increased density and reduction in voids between MoO_x crystals results in the reduced hygroscopicity of the thermally annealed MoO_x film on exposure to air in **Figure 4.4**.

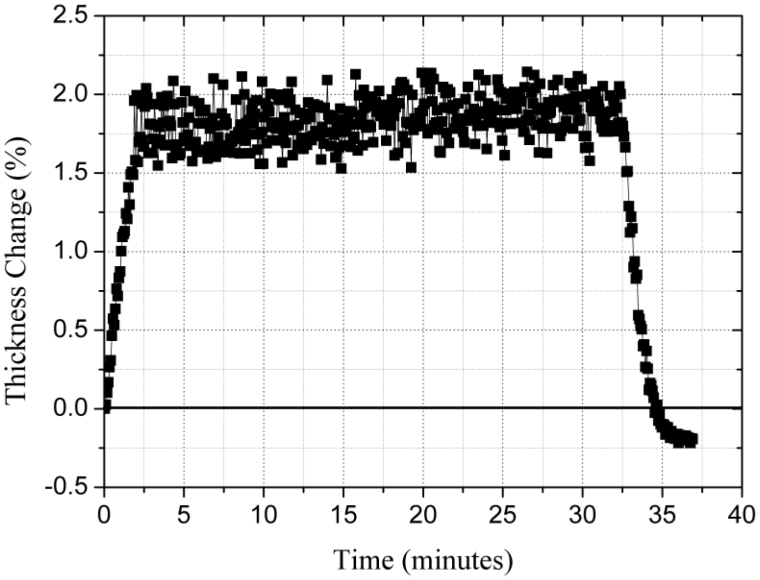

Figure 4.5 % film thickness change for a MoO_x film thermally annealed for 30 minutes at 120°C in a nitrogen atmosphere before being returned to room temperature.

The effects of water adsorption and thermal annealing on MoO_x energy levels were studied with the use of x-ray photoelectron spectroscopy (XPS) and ultra-violet photoelectron spectroscopy (UPS) techniques. XPS confirmed the presence of O-H (water) bonds within MoO_x films that had been exposed to air, with fewer bonds present in those that had been thermally annealed. A shift in the MoO_x HOMO level between samples was also measured by UPS. However, due to the nature of the equipment used, there was no opportunity to measured a pristine sample of MoO_x that had not been exposed to air as the samples were loaded into the equipment in an ambient atmosphere. Therefore, with no reference with which to compare the results to, no strong conclusions could be drawn, and the results have been left out of this thesis.

4.4 Air Processing Photoactive Layers

It is possible to use this enhanced stability of MoO_x to air exposure on thermal annealing to explore the processing of the active semiconductor under ambient conditions. OPV devices were fabricated in which the PCDTBT:$PC_{70}BM$ blend was spin-coated in air under a Lamarflo workstation before being returned to the glovebox for cathode evaporation and encapsulation. Here, the active layer was deposited on untreated MoO_x films and on MoO_x films that had been thermally annealed in a glove-box at 120°C for 30 minutes prior to exposure to air. Such devices are identified as ‘Air processed’ and ‘Annealed, air processed’. The *JV* curves of the devices are shown in **Figure 4.6**, with device operating parameters summarized in **Table 4.6**.

Air Processed Devices				
	PCE (%)	**FF**	**V_{oc} (V)**	**J_{sc} ($mAcm^{-2}$)**
Reference	5.00 ± 0.09	58.1 ± 0.7	0.85	-10.21 ± 0.11
Annealed, not exposed (120°C 30mins)	5.10 ± 0.04	58.7 ± 0.3	0.85	-10.31 ± 0.12
Air processed	4.98 ± 0.12	57.7 ± 1.2	0.85	-10.12 ± 0.09
Annealed, air processed (120°C 30mins)	5.26 ± 0.04	60.2 ± 0.4	0.86	-10.17 ± 0.06

Table 4.6 OPV operating parameters for devices with air processed active layers. Devices fabricated in the same batch as those in **Table 4.5**.

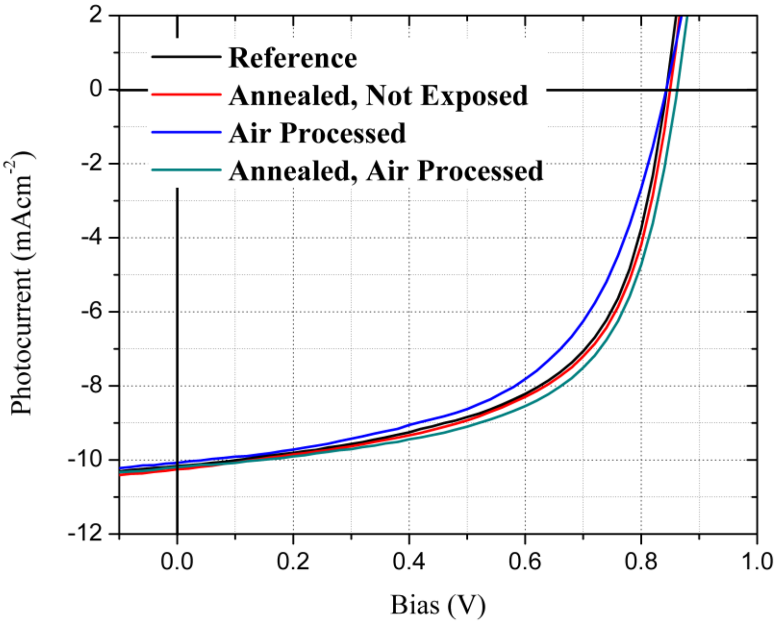

Figure 4.6 *JV* characteristics for OPV devices with air processed active layers.

Devices processed in air on MoO_x films that were not initially thermally annealed (4.98 ± 0.12)% had efficiencies comparable to the Reference devices, and devices in which the MoO_x film was initially thermally annealed before air exposure, with the PCDTBT film then deposited in air had a slightly higher average efficiency (5.26 ± 0.04)% (with one device having an efficiency of 5.36%) compared to devices that were thermally annealed and then processed in the glovebox (5.10 ± 0.04)%. This small, but surprising, improvement in efficiency results from improved V_{oc} and *FF*, indicating that spin-coating the active layer in air onto thermally annealed MoO_x films is apparently beneficial to charge extraction at the polymer-MoO_x interface.

We speculate that this improvement in device efficiency does not result from changes in the active organic layer, as no apparent changes are detected in J_{sc}. Rather, the improvement derives from the presence of a thin layer of a water species on the surface of the MoO_x film. Such a surface-bound layer is apparently not detrimental to device efficiency (as opposed to water adsorbed within the MoO_x film that reduces the work-function), as it will result in the formation of a dipole, due to the charged nature of the water species chemically bound to the surface [18], [21].

This dipole layer may then promote charge extraction, resulting in improved device efficiency as seen in 'Air Processed' and 'Annealed, Air Processed' devices via an improved V_{oc} and *FF*. This improvement is not seen in devices in which the active layer was deposited in the glove box, as the weakly bound water species on the surface of air exposed MoO_x films are likely to be partially removed in the vacuum load-lock on re-entry to the glovebox. Therefore, the devices in which the active layer was spun in air show an improvement over devices prepared in the glovebox as water species are still present on the surface of the MoO_x when the active layer is deposited. It is possible that the active layer 'locks in' the water dipole layer, preventing its removal on re-entry to the glovebox. In 'Air processed' devices, in which the active layer was deposited in air on a MoO_x film that was not initially annealed, water is still adsorbed into the bulk of the film, resulting in less efficient devices than the 'Annealed, air processed' devices. However, due to the presence of a water dipole layer between the MoO_x film and the active layer, the device efficiency is still greater than the 'Air exposed' devices.

4.5 Conclusions

In summary, the effects on OPV device performance of exposure of MoO_x HTLs to air has been studied, and thermal treatments to stabilize the MoO_x film developed. As MoO_x films are hygroscopic, spectroscopic ellipsometry measurements have shown that air exposure results in a swelling of the MoO_x on adsorption of water that is detrimental to device efficiency. However by applying an initial thermal anneal to the MoO_x film, this uptake of water can be suppressed; a process that results from film densification. This result is then used to fabricate OPV devices based on a blend of PCDTBT:$PC_{70}BM$, with the active semiconductor layer spin cast in air. Such air-processed devices had an average value for *PCE* of (5.26 ± 0.04)%; a value significantly larger than that of devices in which no thermal anneal process was applied that were fabricated inside a nitrogen-filled glovebox (5.00 ± 0.09)%. This promising result suggests that the active layers of a polymer photovoltaic device can be fabricated using an air-based processing route; a result that may be of significant benefit in the development of a low cost, high volume manufacturing process.

4.6 References

[1] E. S. R. Bovill, J. Griffin, T. Wang, J. W. Kingsley, H. Yi, A. Iraqi, A. R. Buckley, and D. G. Lidzey, “Air processed organic photovoltaic devices incorporating a MoOx anode buffer layer,” *Appl. Phys. Lett.*, vol. 102, no. 18, p. 183303, May 2013.

[2] M. C. Scharber, D. Mühlbacher, M. Koppe, P. Denk, C. Waldauf, A. J. Heeger, and C. J. Brabec, “Design Rules for Donors in Bulk-Heterojunction Solar Cells—Towards 10 % Energy-Conversion Efficiency,” *Adv. Mater.*, vol. 18, no. 6, pp. 789–794, Mar. 2006.

[3] Y. Liang, Z. Xu, J. Xia, S.-T. Tsai, Y. Wu, G. Li, C. Ray, and L. Yu, “For the bright future-bulk heterojunction polymer solar cells with power conversion efficiency of 7.4%.,” *Adv. Mater.*, vol. 22, no. 20, pp. E135–8, May 2010.

[4] S. Cho, J. H. Seo, S. H. Park, S. Beaupré, M. Leclerc, and A. J. Heeger, “A thermally stable semiconducting polymer.,” *Adv. Mater.*, vol. 22, no. 11, pp. 1253–7, Mar. 2010.

[5] C.-Y. Nam, D. Su, and C. T. Black, “High-Performance Air-Processed Polymer-Fullerene Bulk Heterojunction Solar Cells,” *Adv. Funct. Mater.*, vol. 19, no. 22, pp. 3552–3559, Nov. 2009.

[6] A. L. Holt, J. M. Leger, and S. A. Carter, “Electrochemical and optical characterization of p- and n-doped poly[2-methoxy-5-(2-ethylhexyloxy)-1,4-phenylenevinylene].,” *J. Chem. Phys.*, vol. 123, no. 4, p. 044704, Jul. 2005.

[7] M. Vasilopoulou, L. C. Palilis, D. G. Georgiadou, P. Argitis, S. Kennou, I. Kostis, G. Papadimitropoulos, N. A. Stathopoulos, A. A. Iliadis, N. Konofaos, D. Davazoglou, and L.

Sygellou, “Tungsten oxides as interfacial layers for improved performance in hybrid optoelectronic devices,” *Thin Solid Films*, vol. 519, no. 17, pp. 5748–5753, Jun. 2011.

[8] G. Li, C.-W. Chu, V. Shrotriya, J. Huang, and Y. Yang, “Efficient inverted polymer solar cells,” *Appl. Phys. Lett.*, vol. 88, no. 25, p. 253503, 2006.

[9] M. C. Gwinner, R. D. Pietro, Y. Vaynzof, K. J. Greenberg, P. K. H. Ho, R. H. Friend, and H. Sirringhaus, “Doping of organic semiconductors using molybdenum trioxide: A quantitative time-dependent electrical and spectroscopic study,” *Adv. Funct. Mater.*, vol. 21, no. 8, pp. 1432–1441, Apr. 2011.

[10] N. Miyata, T. Suzuki, and R. Ohyama, “Physical properties of evaporated molybdenum oxide films,” *Thin Solid Films*, vol. 281–282, pp. 218–222, Aug. 1996.

[11] C. V. Ramana, V. V. Atuchin, V. G. Kesler, V. A. Kochubey, L. D. Pokrovsky, V. Shutthanandan, U. Becker, and R. C. Ewing, “Growth and surface characterization of sputter-deposited molybdenum oxide thin films,” *Appl. Surf. Sci.*, vol. 253, no. 12, pp. 5368–5374, Apr. 2007.

[12] S. R. Hammond, J. Meyer, N. E. Widjonarko, P. F. Ndione, A. K. Sigdel, A. Garcia, A. Miedaner, M. T. Lloyd, A. Kahn, D. S. Ginley, J. J. Berry, and D. C. Olson, “Low-temperature, solution-processed molybdenum oxide hole-collection layer for organic photovoltaics,” *J. Mater. Chem.*, vol. 22, no. 7, p. 3249, 2012.

[13] J. Meyer, S. Hamwi, M. Kröger, W. Kowalsky, T. Riedl, and A. Kahn, “Transition metal oxides for organic electronics: energetics, device physics and applications.,” *Adv. Mater.*, vol. 24, no. 40, pp. 5408–27, Oct. 2012.

[14] Y. Sun, C. J. Takacs, S. R. Cowan, J. H. Seo, X. Gong, A. Roy, and A. J. Heeger, “Efficient, air-stable bulk heterojunction polymer solar cells using MoO x as the anode interfacial layer,” *Adv. Mater.*, vol. 23, no. 19, pp. 2226–2230, May 2011.

[15] A. Siokou, G. Leftheriotis, S. Papaefthimiou, and P. Yianoulis, “Effect of the tungsten and molybdenum oxidation states on the thermal coloration of amorphous WO3 and MoO3 films,” *Surf. Sci.*, vol. 482–485, pp. 294–299, Jun. 2001.

[16] I. Irfan, A. James Turinske, Z. Bao, and Y. Gao, “Work function recovery of air exposed molybdenum oxide thin films,” *Appl. Phys. Lett.*, vol. 101, no. 9, p. 093305, 2012.

[17] T. He and J. Yao, “Photochromism of molybdenum oxide,” *J. Photochem. Photobiol. C Photochem. Rev.*, vol. 4, no. 2, pp. 125–143, Oct. 2003.

[18] X. Yin, H. Han, and A. Miyamoto, “Structure and adsorption properties of MoO 3 : insights from periodic density functional calculations,” *J. Mol. Model.*, vol. 5, pp. 207–215, 2001.

[19] K. T. Butler, E. Bovill, R. Crespo-Ortero, D. O. Scanlon, D. Lidzey, and A. Walsh, “Work function engineering of air processed hole transport layers in organic photovoltaics: Understanding and controlling oxide surface hydration effects,” 2014.

[20] A. Kuzmin and J. Purans, “Dehydration of the molybdenum trioxide hydrates MoO 3 · n H 2 O: in situ x-ray absorption spectroscopy study at the Mo K edge,” *J. Phys. Condens. Matter*, vol. 12, no. 9, pp. 1959–1970, Mar. 2000.

[21] R. Steim, F. R. Kogler, and C. J. Brabec, “Interface materials for organic solar cells,” *J. Mater. Chem.*, vol. 20, no. 13, p. 2499, 2010.

Chapter 5 : Hole Transport Layer Laboratory Lifetime Study

In the previous chapter, details were given regarding the air stability of MoO_x and its suitability as a hole transport layer (HTL) in OPV devices. In this chapter, the fabrication and optimization of OPV devices utilizing a PCDTBT:$PC_{70}BM$ active layer and three different HTL materials, MoO_x, PEDOT:PSS and vanadium oxide (V_2O_x), is presented, with all devices having initial *PCEs* in excess of 5%. A detailed lifetime study was then carried out on the devices for 620 hours in the laboratory lifetime testing system, with *JV* characterization, LBIC and ELM used to investigate device degradation and image defects present in the devices on ageing. It was found that a PEDOT:PSS HTL afforded devices the highest degree of stability, with T_{80} lifetimes extrapolated to 14,500 hours (~ 7 years). LBIC and ELM images clearly show a reduced density of defects in the devices with a PEDOT:PSS HTL when compared to MoO_x and V_2O_x on ageing. The lifetime study carried out here in conforms to the ISOS-L-1 standards as covered in **3.11.1 ISOS Laboratory Weathering Testing**.

5.0 Introduction

Much work on OPV degradation processes have studied devices based on the material poly(3-hexylthiophene) (P3HT) [1]–[4], with lifetimes of up to 3 years reported [4]. More recently, outdoor interlaboratory studies have produced devices based on P3HT having extrapolated lifetimes in excess of 5 years [5], with laboratory studies demonstrating extrapolated device lifetimes of up to 10 years in OPVs based on polymer system PCDTBT:$PC_{70}BM$ [4], [6].

To improve OPV stability and lifetime, most work thus far has focused on understanding degradation processes within the polymer:fullerene active semiconductor layer. However several studies now report the effect of changing other interlayers in a device [7]–[10], although this work is almost exclusively based on OPVs based on the polymer (P3HT). The polymer P3HT has been largely superseded by new generations of low energy-gap donor-acceptor polymers that have significantly enhanced *PCE*, in particular the polymer PCDTBT. Studies on PCDTBT have explored device stability and degradation pathways [4], [9], [11] and have concluded that polycarbazole polymers have a high degree of photostability [12], as shown in **Chapter 6 : Polymer Air Processing**, and can be used to create devices having extended operational lifetimes [4]. The comparatively high degree of stability afforded by PCDTBT thus presents an opportunity to test the effect of a variety of different hole transport layer (HTL) materials and determine their relative role in contributing to device stability. To this end, OPV devices have been fabricated using a PCDTBT:$PC_{70}BM$ OPV (PCDTBT M137 batch from Ossila Ltd) active layer that utilize a range of different hole-transporting layers including PEDOT:PSS, MoO_x and V_2O_x. Device *PCE* was recorded under simulated solar radiation over a period of 620 hours, and it was found that a PEDOT:PSS HTL afforded devices the highest degree of stability, with T_{80} lifetimes extrapolated to 14,500 hours.

5.1 Hole Transport Layer Materials

The devices fabricated for this study were based on the standard device architecture of ITO/HTL/PCDTBT:$PC_{70}BM$/Ca/Al, in which the hole transport layer was either composed of MoO_x, PEDOT:PSS or V_2O_x. 10 nm MoO_x HTL films were prepared as in **Chapter 4 : Air Stability of MoOx** and were left unannealed.

5.1.1 PEDOT:PSS

PEDOT:PSS is a material that has been widely explored as a hole-transporting layer as it combines several characteristics that are desirable for OPV applications, including high conductivity and good film transparency [13]. When used as an interlayer between ITO and the active layer of an OPV, PEDOT:PSS aids extraction of charges across the interface and planarizes the surface of ITO [14], reducing the number of shorts and inhomogeneities formed at the interface. It also increases the work function of the ITO anode, permitting energy level matching with the donor polymer in the active layer. Thin films of PEDOT:PSS are however extremely hygroscopic [15], and post deposition thermal treatments are needed to remove any remaining water in the films, the effects of which are discussed in more detail in **Chapter 6 : Polymer Air Processing**.

The PEDOT:PSS solution used herein (Heraeus Clevios™ P VP AI 4083), had a ratio of 1:6 PEDOT to PSS and was filtered through a 0.45 µm PVDF filter to remove any aggregates before use. To fabricate PEDOT:PSS HTLs, the PEDOT:PSS solution was spin-coated onto cleaned ITO coated substrates at 6000 rpm for 30 s in air to form a ~ 30 nm thick film, and then annealed on a hot plate in air for 10 minutes at 150°C, following which they were transferred to the glovebox.

5.1.2 Vanadium Oxide

Vanadium Oxide is a transition metal oxide that has been extensively used as a hole transport layer in OPVs. It can be deposited by thermal evaporation [16] and a variety of solution processes [17]–[20], and has a work function of 5.6 eV [17], making it well matched for hole extraction from polymers having deep HOMO levels such as PCDTBT.

A facile synthetic process was used to form uniform thin layers of V_2O_x from solution [17]. The precursor used was vanadium oxytriisopropoxide [$OV(OCH(CH_3)_2)_3$], the structure of which is shown in **Figure 5.1**. The vanadium oxytriisopropoxide precursor was sourced from Sigma-Aldrich and used as received.

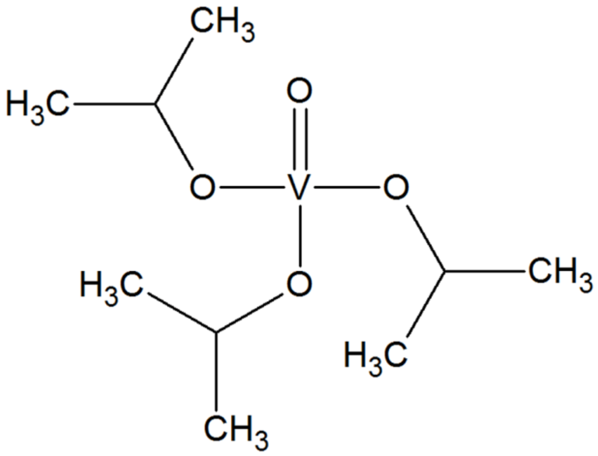

Figure 5.1 Chemical structure of vanadium oxytriisopropoxide, $OV(OCH(CH_3)_2)_3$.

V_2O_x HTL films were spin-coated in air to allow for hydrolysis of the vanadium oxytriisopropoxide precursor, the chemical reaction of which is shown in **Equations 5.1** and **5.2**.

$$2.OV(OCH(CH_3)_2)_3 + 6.H_2O \longrightarrow 6.C_3H_7OH + VO_4H_3$$ **Equation 5.1**

$$2.VO_4H_3 \longrightarrow V_2O_x + 3.H_2O$$ **Equation 5.2**

For **Equation 5.1**, in the presence of water vapour, H^+ cations cleave the alkyl chain ($CH(CH_3)$) in the vanadium oxytriisopropoxide precursor and bind to the singly bound oxygen on the vanadium oxide, forming VO_4H_3, whilst OH^- anions bind to the alkyl chain and produce isopropanol (C_3H_7OH), which evaporates. In **Equation 5.2**, the vanadium intermediary molecules (VO_4H_3) react together, releasing water, and form vanadium oxide (V_2O_x).

The vanadium oxide precursor solution was spin-coated at 3500 rpm to form films ~ 5 nm thick, which were left in air for 45 minutes to allow for the hydrolysis process to undergo completion and form an amorphous and extremely smooth V_2O_x layer. No annealing steps were necessary.

5.2 Device Lifetime

In all cases, OPV devices were fabricated, characterized and placed in the lifetime tester on the same day. The devices were tested for a total of 620 hours under constant illumination, during which time they were periodically removed for other brief tests including *JV* measurements under the Newport solar simulator. This was done due to the spectral mismatch between the calibrated Newport solar simulator and the Suntest system as detailed in **3.9.2 Light Source and Spectrum**. Due to this discrepancy, all device metrics quoted here (*PCE, FF*, V_{oc}, J_{sc} and T_{80}) were determined from *JV* scans measured using the calibrated Newport solar simulator, with data recorded using the ATLAS is included to highlight general trends in device metrics as they undergo aging.

The light intensity and temperature inside the test chamber, as measured by the photodiodes and temperature sensors on the test board, are shown in **Figure 5.2**. It can be seen that the light intensity was extremely stable over the course of the experiment. However, the temperature fluctuated in a regular pattern that followed the room's occupancy during a working week as a result of the building's heating and air-conditioning systems. At the weekend, when the room was not in use, the temperature readings were steady (for example, at the beginning of the test). This led to an daily increase in the temperature inside the test chamber of ~ 3°C. Regardless of this, the measured values for light intensity and temperature stayed within accepted variance as stipulated by the ISOS-L-1 test protocol for the duration of the test.

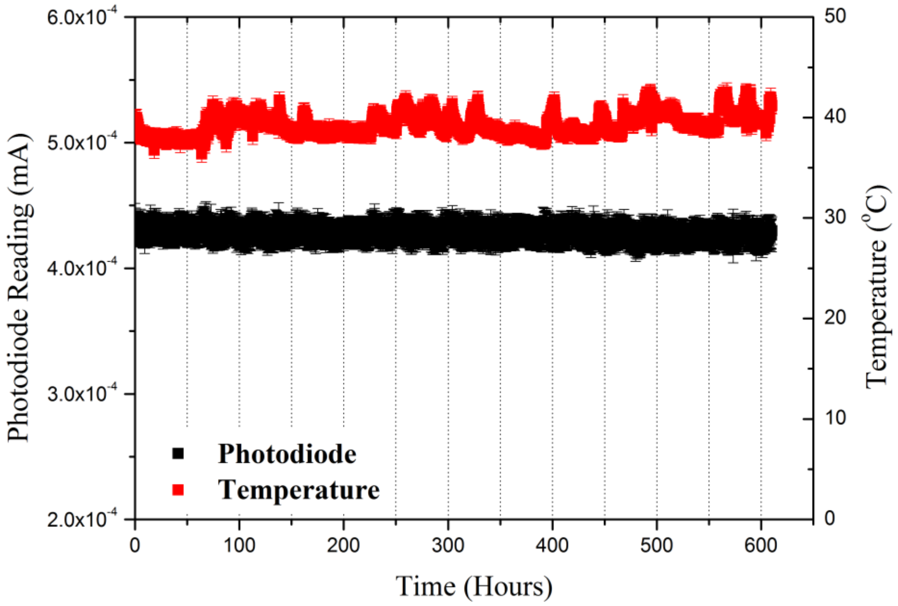

Figure 5.2 Mean values for temperature and light intensity as measured by the temperature sensors and photodiodes on the lifetime test board. Error bars represent standard deviation around the mean.

In **Figure 5.3**, the average values of *PCE*, *FF*, V_{oc} and J_{sc}, determined from the different devices are shown as a function of irradiation time in the Suntest chamber. Here, data is normalized to their initial values, with the data shown representing the average values for the pixels determined every 10 minutes. J_{sc} and *PCE* are corrected to account for intensity fluctuations in the Suntest xenon lamp, which varied by less than ± 5% over the course of the experiment.

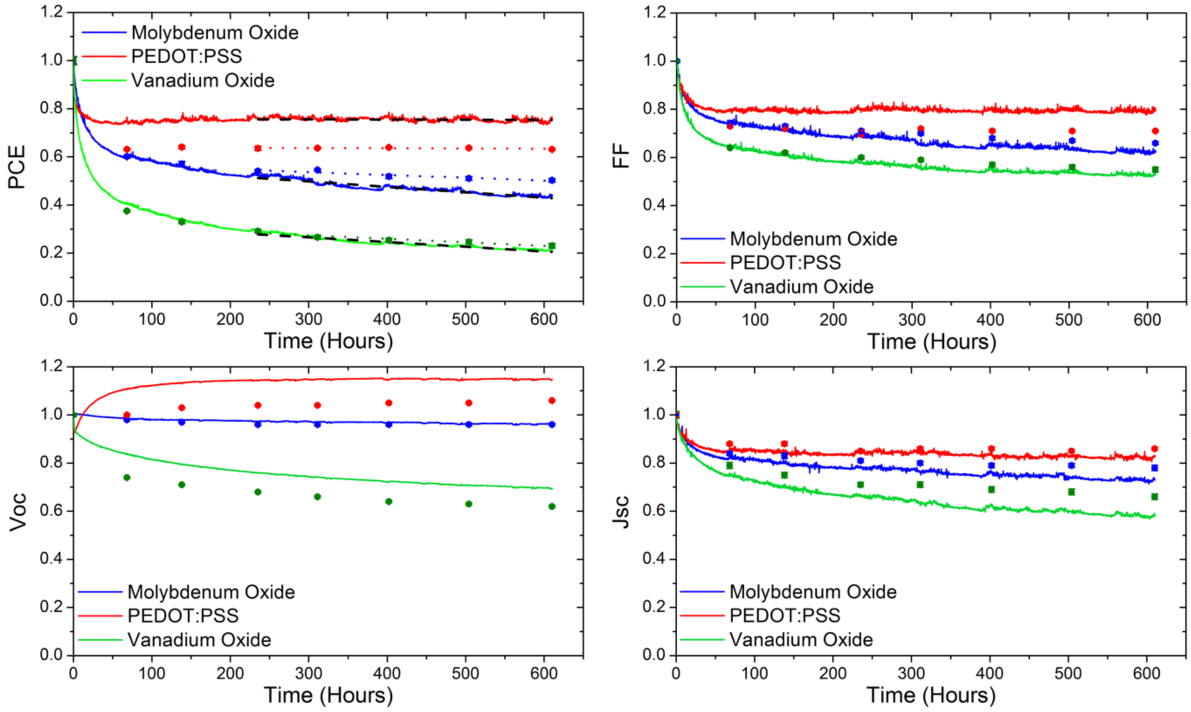

Figure 5.3 shows *PCE*, V_{oc}, J_{sc} and *FF* for devices utilising the different HTL materials as a function of irradiation time under the ATLAS solar simulator. All data is normalised to its initial value determined at $t = 0$. In each part, data is plotted as measured every 10 minutes using the ATLAS solar simulator (solid lines) and every 3 days using the calibrated Newport solar simulator (circular data points). The decay in *PCE* (determined using both types of solar simulator) is fitted to a straight line (dashed line or dotted line) for times beyond the burn-in period ($t > 250$ hours). This linear fit to the PCE is used to determine the T_{80} decay lifetime.

All devices undergo a burn in phase that lasts for ~ 250 hours, in which the *FF* and J_{sc} decrease at an exponential rate, after which the decay follows a linear trend. In **Table 5.1** the average values of *PCE*, peak EQE, *FF*, V_{oc} and J_{sc} (and their uncertainties) are shown for all devices before and after lifetime testing with corresponding *JV* and EQE curves shown in **Figure 5.4** and **Figure 5.5** respectively. A linear-fit to the *PCE* data (after the burn-in period) was used to determine the T_{80} lifetime of the devices using the data from the ATLAS and Newport solar simulators (plotted using coloured dashed lines).

The initial burn-in that is observed in all devices (see **Figure 5.3**) is believed to originate from photochemical reactions in the PCDTBT:PC$_{70}$BM blend that adversely affect its charge transport properties [4], [9], [11], [21]. The EQE spectra recorded before and after irradiation (see **Figure 5.5 (a)** and **(b)** respectively), indicate a general reduction in quantum efficiency without any change in spectral shape; a result consistent with a degree of photooxidation (note that there is a systematic error in EQE measurement of ~ 10% but results agree with J_{sc} within experimental error). Here, photochemical reactions in PCDTBT result in an increase in the density of sub-bandgap and trap states that lead to a reduction in hole mobility [9]. Other work has demonstrated that the inclusion of PCBM in the blend film slows down the rate of photo-oxidation by quenching the excited state, however oxidation of the fullerene itself can lead to a reduction in carrier mobility by inducing deep trap states inside the PCBM domains [21]. The formation of trap states saturates over time, which results in an end to the burn-in phase and subsequent linear decay [9].

		PCE (%)	Peak EQE (%)	FF	V_{oc} (V)	J_{sc} ($mAcm^{-2}$)
Molybdenum Oxide (MoO_x)	Initial	5.19±0.07	54.7±0.1	64.6±0.7	0.91	-8.9±0.1
	Final	2.7±0.1	47.4±0.2	43.9±0.9	0.87	-7.0±0.2
PEDOT:PSS	Initial	5.6±0.2	63.7±0.2	65.9±0.9	0.85	-9.9±0.2
	Final	3.4±0.2	56.6±0.3	46±1	0.89	-8.3±0.4
Vanadium Oxide (V_2O_x)	Initial	5.2±0.2	58.4±0.1	65±1	0.85	-9.4±0.1
	Final	1.18±0.04	43.7±0.1	36.8±0.8	0.51	-6.3±0.1

Table 5.1 Average values for *PCE*, *FF*, V_{oc} and J_{sc} were calculated from 12 pixels across two substrates, as measured using the Newport solar simulator, where the worst 25% of pixels were discarded due to film defects. The error quoted on all measurements is based on the standard deviation around the mean.

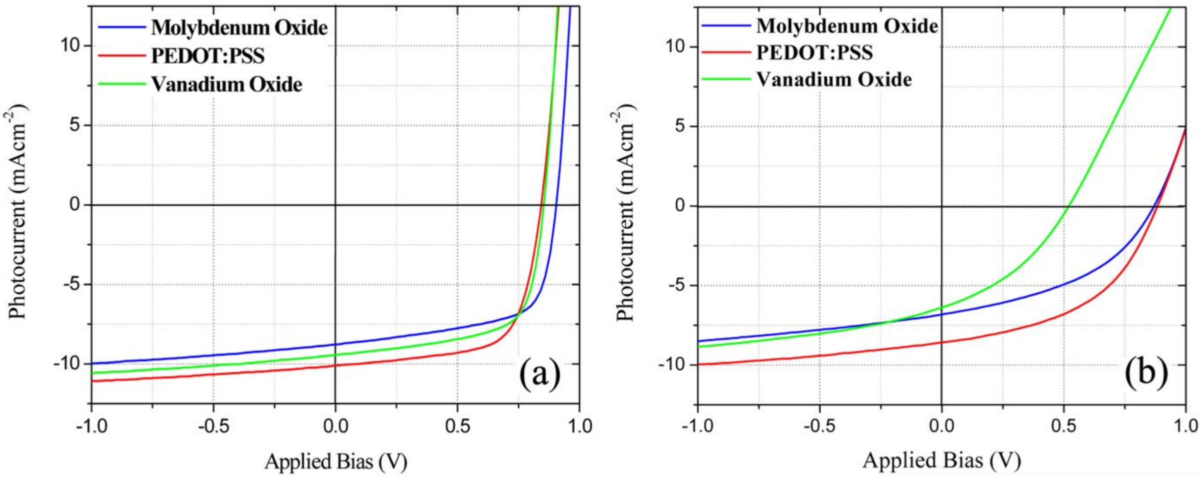

Figure 5.4 Part **(a)** shows initial *JV* characteristics for devices, with part **(b)** showing device *JV* characteristics after 620 hours of lifetime testing.

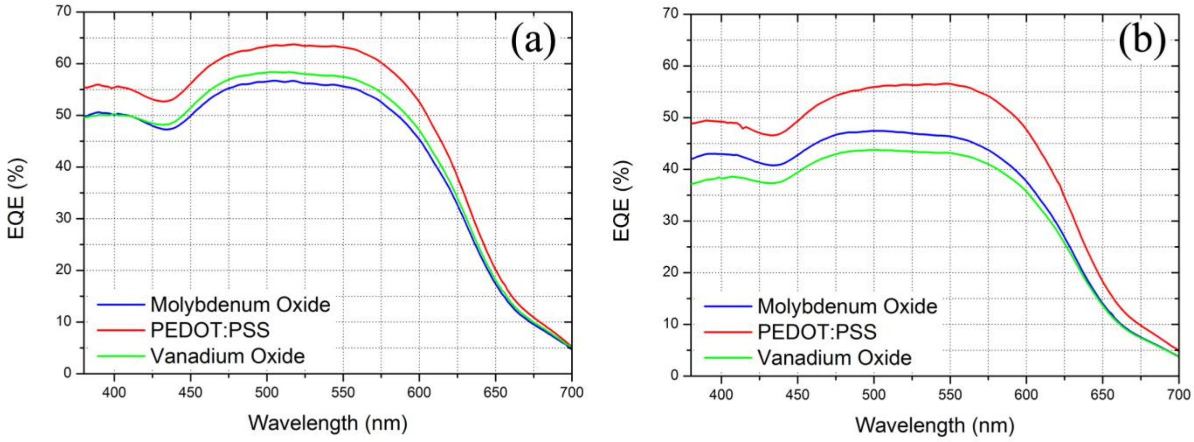

Figure 5.5 Part **(a)** shows initial EQE for devices, with part **(b)** showing device EQE after 620 hours of lifetime testing.

It can be seen in **Figure 5.3** that that devices utilizing a PEDOT:PSS HTL underwent a rapid, initial burn in phase that was dominated by a reduction in *FF* and J_{sc} that then stabilized after 60 hours. Significantly, the V_{oc} of such devices also underwent an initial and rapid reduction (over a period 5 hours) but then recovered and stabilized over a period of 200 hours to a value that was some 15 mV higher than the initial V_{oc}. This is speculated to result from charge transfer from the PEDOT:PSS to the active layer [22], [23]; a process that alters the work function of the PEDOT:PSS surface and thus facilitates charge transfer. Note that the PEDOT:PSS used here is known to be acidic (pH ~ 2 [24], [25]), and has been shown to react with the ITO anode [26]–[28], resulting in degradation of device efficiency. It is possible that the use of different grades of PEDOT:PSS having a more neutral pH may well reduce the observed drop in efficiency during the initial burn-in period.

It was found that the *PCE, FF*, J_{sc}, and V_{oc} of devices based on MoO_x or V_2O_x HTLs degraded at a significantly faster rate than that of the PEDEOT:PSS based devices, both during the burn-in period and in the subsequent linear decay phase. In MoO_x HTL devices, the overall reduction in PCE is dominated by the reduction in *FF* and J_{sc}, with the V_{oc} only undergoing a relatively small reduction (by 4%) over 620 hours. In contrast, in V_2O_x HTL devices, the V_{oc} reduced by 40% over the 620 hours of testing. This reduction was also accompanied by significant reductions in *PCE*, *FF* and J_{sc} as can be seen in **Table 5.1** resulting in the largest loss in device *PCE*. However, the vanadium oxytriisopropoxide precursor is a Lewis acid, and has been shown to damage conjugated polymers, resulting in the formation of main-chain defects and trap states and a reduction in device *PCE* [29]. It is speculated therefore that residues of the precursor material in the HTL film, along with other organic by-products of the hydrolysis process, may be the cause of such device degradation in this instance. This suggests that the use of V_2O_x HTLs prepared by this synthetic process would be problematic for practical applications. The use of other techniques to deposit V_2O_x layers [20], [29]–[31] may address this issue.

The values for *PCE* after the burn-in period, the relative loss in the *PCE* after 250 and 620 hours, and calculated T_{80} lifetimes are shown in **Table 5.2**.

	PCE after burn-in (250hrs)	**PCE Loss over burn-in (250hrs)**	**PCE Loss over 620 hours**	**T_{80} (hours) Newport**	**T_{80} (hours) ATLAS**
Molybdenum Oxide (MoO_x)	2.9±0.1%	44±3%	48±3%	1000 (0.5 years)	650 (0.3 years)
PEDOT:PSS Annealed	3.4±0.4%	39±6%	39±5%	14500 (7.2 years)	20000 (10 years)
Vanadium Oxide (V_2O_x)	1.5±0.1%	72±4%	77±4%	350 (0.2 years)	236 (0.1 years)

Table 5.2 *PCE* loss on burn in and over the full 620 hrs of testing with calculated T_{80} lifetimes determined using the Newport solar simulator data and the ATLAS Suntest CPS+ data. All *PCE* values and losses were calculated using data from the Newport solar simulator.

The average lifetime for devices using a PEDOT:PSS HTL was calculated to be 14,500 hours from data acquired from the Newport solar simulator. If other possible catastrophic device degradation processes are eliminated (e.g. sudden failure of the device encapsulation), the recorded lifetime is equivalent to 7.2 years of practical operation, assuming an operational device would receive 5.5 hours of $1000Wm^{-2}$ irradiation per day [4]. For MoO_x, however the device T_{80} lifetime was found to be 1000 hours (equivalent to 6 months operation); a value reduced to 350 hours (63 days) for the V_2O_x HTL devices. It is important to emphasise that lifetime figures that have been determined here are for devices aged indoors under the ISOS-L-1 specification [32], as outdoor testing results in thermal cycling and light intensity variations, as discussed in more detail in **Chapter 7 : Outdoor Lifetime Testing**.

T_{80} lifetimes as calculated from data acquired from the ATLAS system are different from those as calculated using data from the Newport solar simulator, due to the spectral mismatch of the two light sources and its effect on measured device operating parameters. However, in all cases the lifetimes as calculated from the different light sources are of a similar magnitude.

It is clear, therefore, that the rate of degradation of all device metrics is a significant function of the nature of the HTL materials; a result that suggests that degradation in the active layer cannot completely account for the observed degradation of device performance. Rather, the changes in FF, J_{sc}, and V_{oc} that are observed during both burn-in and subsequent linear decay must also result from the formation of additional trap states at the interface between the active layer and the hole transport layers, due to generation of structural and compositional defects [11]. Additional processes are likely to be also active at the interface between the active layer and the device cathode however the relative importance of such a process cannot be determined from these experiments.

In contrast to previous work [7], [8], [10], the PEDOT:PSS HTL affords devices the highest stability. This is believed to be mainly due to the use of PCDTBT as opposed to P3HT as the donor polymer in the devices, though the use of encapsulation also plays a role. PCDTBT has been shown to be stable in the presence of water and oxygen even under elevated temperatures [9], which PEDOT:PSS, which is known to be highly hygroscopic [33], tends to introduce into devices during processing, whereas P3HT is highly sensitive to such ingress [7], [34]. Other studies have also shown that devices based on PCDTBT:$PC_{70}BM$ using a PEDOT:PSS hole transport layer have achieved similar device lifetimes [4], though with no comparison to other hole transport layer materials. The cause of device degradation in devices utilising the different hole transport layers will require further investigation.

5.3 LBIC/ELM of Aged Devices

After testing in the laboratory lifetime setup for 620 hours, both LBIC and ELM images were taken of several pixels of the devices, as shown in **Figure 5.6**. The methods by which the images were acquired are described in **3.7 Laser Beam Induced Current Mapping (LBIC)** and **3.8 Electroluminescence Mapping (ELM).** It was not possible to also obtain these images prior to testing due to time restrictions, and as such the formation of defects on ageing devices cannot be studied. However, the density of defects shown in the LBIC and ELM images can be compared between device types.

For LBIC images, the colour scale is shown in **Figure 5.6**, with high generated current indicated by dark blue, and low current indicated by red. ELM images are shown in greyscale, with lighter areas indicating higher electroluminescence and black areas indicating little or no electroluminescence. The colour scale is identical for all three LBIC images and the edges of the pixels can clearly be seen in all images.

It can be seen that defects that affect the charge transport in the active layer films are found in all device types. From the LBIC images, the defects are correlated with a reduction in charge generation efficiency, and correspond to areas of little or no electroluminescence in the matching ELM image. The degradation of the V_2O_x devices was so severe that it was impossible to obtain an ELM image for comparison to the LBIC image.

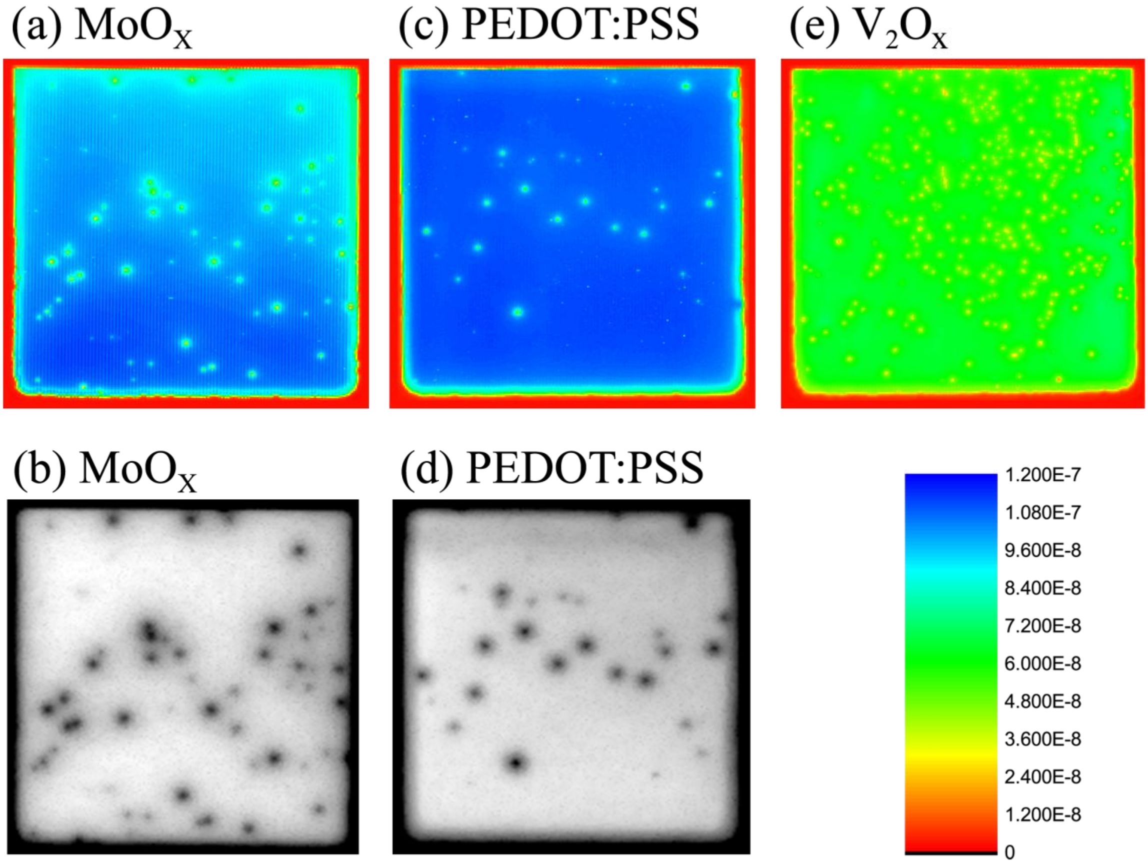

Figure 5.6 Parts **(a)** and **(b)** show LBIC and ELM images for a MoO_x device respectively, parts **(c)** and **(d)** show LBIC and ELM images for a PEDOT:PSS device respectively, and part **(e)** shows an LBIC image for a V_2O_x device. A colour scale for the LBIC images is shown in the bottom right.

From previous studies, it has been shown that V_2O_x layers formed from an oxytriisopropoxide precursor and hydrolysis process contain a large number of nano-scopic voids in the film as a result of solvent evaporation during film formation [17]. These voids in the film, along with the residual precursor or other organic products of hydrolysation, appear to lead to extensive defect formation in the active layer of the device, as can be seen in the LBIC images in **Figure 5.6 (e)**. These defects lead to a drastic reduction in charge generation in the film around the defect sites. The LBIC image for the V_2O_x device also shows that the charge generation in the bulk of the film has decreased significantly when compared to the other HTL devices, which correlates with the relatively large loss in J_{sc} on ageing as seen in **Figure 5.3**.

The devices with a MoO_x HTL also showed a significant number of defects with a large area of effect, as can be seen in **Figure 5.6 (a,b)**. It is suspected that these originate from structural defects in the evaporated MoO_x film acting as formation sites for charge trap states and photochemical reactions in the active layer.

LBIC and ELM measurements also reveal defects in the PEDOT:PSS devices, as seen in **Figure 5.6 (c,d)**, but in comparison to the other device types they are fewer in number. This, in combination with the degradation characteristics seen in **Figure 5.3**, indicate that the interface between the PEDOT:PSS and the active layer is more stable than MoO_x and V_2O_x.

5.4 Conclusions

These experiments demonstrate that the rate of degradation of the device metrics is a significant function of the nature of the HTL material; a result that confirms that degradation in the active layer does not completely account for the observed reduction in device performance. Rather, the changes in FF, J_{sc}, and V_{oc} that are observed during both burn-in and subsequent linear decay must also result from the formation of additional trap states at the interface between the active layer and the hole transport layers, due to generation of structural and electronic defects [11], as shown in both LBIC and ELM images of the devices after ageing.

It has been shown that OPV devices utilising a PEDOT:PSS HTL have a higher stability than comparable devices using a MoO_x or V_2O_x HTLs, with extrapolated T_{80} lifetimes for devices utilising a PEDOT:PSS HTL being 14,500 hours. Such lifetimes are in good accord with the results of previous studies [4]. Other work [7], [8], [10] however has suggested that OPVs having a PEDOT:PSS HTLs have relatively poor operational stability. However, this apparent contradiction likely results from the differing sensitivity of the donor-polymer to trapped moisture, as previous studies explored OPVs based on the polymer P3HT; a material known to be sensitive to the presence of moisture that is likely introduced into the device by the highly hygroscopic PEDOT:PSS [33]. In contrast, however, PCDTBT is more stable to the presence of water and oxygen even under elevated temperatures [9], and thus the effect of trapped moisture within the PEDOT:PSS appears less problematic, an effect covered in more detail in **Chapter 6 : Polymer Air Processing**.

5.5 References

[1] R. De Bettignies, J. Leroy, M. Firon, and C. Sentein, “Accelerated lifetime measurements of P3HT:PCBM solar cells,” *Synth. Met.*, vol. 156, no. 7–8, pp. 510–513, Apr. 2006.

[2] J. A. Hauch, P. Schilinsky, S. A. Choulis, R. Childers, M. Biele, and C. J. Brabec, “Flexible organic P3HT:PCBM bulk-heterojunction modules with more than 1 year outdoor lifetime,” *Sol. Energy Mater. Sol. Cells*, vol. 92, no. 7, pp. 727–731, Jul. 2008.

[3] M. O. Reese, A. J. Morfa, M. S. White, N. Kopidakis, S. E. Shaheen, G. Rumbles, and D. S. Ginley, “Pathways for the degradation of organic photovoltaic P3HT:PCBM based devices,” *Sol. Energy Mater. Sol. Cells*, vol. 92, no. 7, pp. 746–752, Jul. 2008.

[4] C. H. Peters, I. T. Sachs-Quintana, J. P. Kastrop, S. Beaupré, M. Leclerc, and M. D. McGehee, “High Efficiency Polymer Solar Cells with Long Operating Lifetimes,” *Adv. Energy Mater.*, vol. 1, no. 4, pp. 491–494, Jul. 2011.

[5] S. A. Gevorgyan, M. V. Madsen, H. F. Dam, M. Jørgensen, C. J. Fell, K. F. Anderson, B. C. Duck, A. Mescheloff, E. A. Katz, A. Elschner, R. Roesch, H. Hoppe, M. Hermenau, M. Riede, and F. C. Krebs, “Interlaboratory outdoor stability studies of flexible roll-to-roll coated organic photovoltaic modules: Stability over 10,000h,” *Sol. Energy Mater. Sol. Cells*, vol. 116, pp. 187–196, Sep. 2013.

[6] H. Cao, W. He, Y. Mao, X. Lin, K. Ishikawa, J. H. Dickerson, and W. P. Hess, “Recent progress in degradation and stabilization of organic solar cells,” *J. Power Sources*, vol. 264, pp. 168–183, Oct. 2014.

[7] E. Voroshazi, B. Verreet, A. Buri, R. Müller, D. Di Nuzzo, and P. Heremans, “Influence of cathode oxidation via the hole extraction layer in polymer:fullerene solar cells,” *Org. Electron.*, vol. 12, no. 5, pp. 736–744, May 2011.

[8] C. Girotto, E. Voroshazi, D. Cheyns, P. Heremans, and B. P. Rand, “Solution-processed MoO_3 thin films as a hole-injection layer for organic solar cells.,” *ACS Appl. Mater. interfaces*, vol. 3, no. 9, pp. 3244–7, 2011.

[9] C. H. Peters, I. T. Sachs-Quintana, W. R. Mateker, T. Heumueller, J. Rivnay, R. Noriega, Z. M. Beiley, E. T. Hoke, A. Salleo, and M. D. McGehee, “The mechanism of burn-in loss in a high efficiency polymer solar cell,” *Adv. Mater.*, vol. 24, no. 5, pp. 663–668, Feb. 2012.

[10] Y. Sun, C. J. Takacs, S. R. Cowan, J. H. Seo, X. Gong, A. Roy, and A. J. Heeger, “Efficient, air-stable bulk heterojunction polymer solar cells using MoO x as the anode interfacial layer,” *Adv. Mater.*, vol. 23, no. 19, pp. 2226–2230, May 2011.

[11] E. Voroshazi, I. Cardinaletti, T. Conard, and B. P. Rand, “Light-Induced Degradation of Polymer:Fullerene Photovoltaic Devices: An Intrinsic or Material-Dependent Failure Mechanism?,” *Adv. Energy Mater.*, Aug. 2014.

[12] E. Bovill, H. Yi, A. Iraqi, and D. G. Lidzey, “The fabrication of polyfluorene and polycarbazole-based photovoltaic devices using an air-stable process route,” *Appl. Phys. Lett.*, vol. 105, no. 22, p. 223302, Dec. 2014.

[13] Q. Wei, M. Mukaida, Y. Naitoh, and T. Ishida, “Morphological change and mobility enhancement in PEDOT:PSS by adding co-solvents.,” *Adv. Mater.*, vol. 25, no. 20, pp. 2831–6, May 2013.

[14] C. Jonda, A. B. R. Mayer, U. Stolz, A. Elschner, and A. Karbach, “Surface roughness effects and their influence on the degradation of organic light emitting devices,” *J. Mater. Sci.*, vol. 35, no. 22, pp. 5645–5651, 2000.

[15] J. Huang, P. F. Miller, J. S. Wilson, A. J. de Mello, J. C. de Mello, and D. D. C. Bradley, “Investigation of the Effects of Doping and Post-Deposition Treatments on the Conductivity, Morphology, and Work Function of Poly(3,4-ethylenedioxythiophene)/Poly(styrene sulfonate) Films,” *Adv. Funct. Mater.*, vol. 15, no. 2, pp. 290–296, Feb. 2005.

[16] I. Hancox, L. a. Rochford, D. Clare, P. Sullivan, and T. S. Jones, “Utilizing n-type vanadium oxide films as hole-extracting layers for small molecule organic photovoltaics,” *Appl. Phys. Lett.*, vol. 99, no. 1, p. 013304, 2011.

[17] K. Zilberberg, S. Trost, H. Schmidt, and T. Riedl, “Solution Processed Vanadium Pentoxide as Charge Extraction Layer for Organic Solar Cells,” *Adv. Energy Mater.*, vol. 1, no. 3, pp. 377–381, May 2011.

[18] Y.-M. Chang and J.-M. Ding, “High efficiency inverted polymer solar cells with the sol–gel derived vanadium oxide interlayer,” *Thin Solid Films*, vol. 520, no. 16, pp. 5400–5404, Jun. 2012.

[19] G. Terán-Escobar, J. Pampel, J. M. Caicedo, and M. Lira-Cantú, “Low-temperature, solution-processed, layered V2O5 hydrate as the hole-transport layer for stable organic solar cells,” *Energy Environ. Sci.*, vol. 6, no. 10, p. 3088, 2013.

[20] Z. Tan, W. Zhang, C. Cui, Y. Ding, D. Qian, Q. Xu, L. Li, S. Li, and Y. Li, “Solution-processed vanadium oxide as a hole collection layer on an ITO electrode for high-

performance polymer solar cells.," *Phys. Chem. Chem. Phys.*, vol. 14, no. 42, pp. 14589–95, Nov. 2012.

[21] M. O. Reese, A. M. Nardes, B. L. Rupert, R. E. Larsen, D. C. Olson, M. T. Lloyd, S. E. Shaheen, D. S. Ginley, G. Rumbles, and N. Kopidakis, "Photoinduced Degradation of Polymer and Polymer-Fullerene Active Layers: Experiment and Theory," *Adv. Funct. Mater.*, vol. 20, no. 20, pp. 3476–3483, Oct. 2010.

[22] C. Perlov, W. Jackson, C. Taussig, S. Mo, and S. R. Forrest, "A polymer / semiconductor write-once read-many-times memory," vol. 426, no. November, pp. 2–5, 2003.

[23] R. A. Nawrocki, E. M. Galiger, D. P. Ostrowski, B. A. Bailey, X. Jiang, R. M. Voyles, N. Kopidakis, D. C. Olson, and S. E. Shaheen, "An inverted, organic WORM device based on PEDOT:PSS with very low turn-on voltage," *Org. Electron.*, vol. 15, no. 8, pp. 1791–1798, Aug. 2014.

[24] M. Kuş and S. Okur, "Electrical characterization of PEDOT:PSS beyond humidity saturation," *Sensors Actuators B Chem.*, vol. 143, no. 1, pp. 177–181, Dec. 2009.

[25] J. Ouyang, C. Chu, F. Chen, Q. Xu, and Y. Yang, "Polymer Optoelectronic Devices with High-Conductivity Poly(3,4-Ethylenedioxythiophene) Anodes," *J. Macromol. Sci. Part A*, vol. 41, no. 12, pp. 1497–1511, Dec. 2004.

[26] T. P. Nguyen and S. A. de Vos, "An investigation into the effect of chemical and thermal treatments on the structural changes of poly(3,4-ethylenedioxythiophene)/polystyrenesulfonate and consequences on its use on indium tin oxide substrates," *Appl. Surf. Sci.*, vol. 221, no. 1–4, pp. 330–339, 2004.

[27] K. W. Wong, H. L. Yip, Y. Luo, K. Y. Wong, W. M. Lau, K. H. Low, H. F. Chow, Z. Q. Gao, W. L. Yeung, and C. C. Chang, “Blocking reactions between indium-tin oxide and poly (3,4-ethylene dioxythiophene):poly(styrene sulphonate) with a self-assembly monolayer,” *Appl. Phys. Lett.*, vol. 80, no. 15, 2002.

[28] M. P. de Jong, L. J. van IJzendoorn, and M. J. A. de Voigt, “Stability of the interface between indium-tin-oxide and poly(3,4-ethylenedioxythiophene)/poly(styrenesulfonate) in polymer light-emitting diodes,” *Appl. Phys. Lett.*, vol. 77, no. 14, p. 2255, 2000.

[29] K. Zilberberg, S. Trost, J. Meyer, A. Kahn, A. Behrendt, D. Lützenkirchen-Hecht, R. Frahm, and T. Riedl, “Inverted Organic Solar Cells with Sol-Gel Processed High Work-Function Vanadium Oxide Hole-Extraction Layers,” *Adv. Funct. Mater.*, vol. 21, no. 24, pp. 4776–4783, Dec. 2011.

[30] J.-S. Huang, C.-Y. Chou, M.-Y. Liu, K.-H. Tsai, W.-H. Lin, and C.-F. Lin, “Solution-processed vanadium oxide as an anode interlayer for inverted polymer solar cells hybridized with ZnO nanorods,” *Org. Electron.*, vol. 10, no. 6, pp. 1060–1065, Sep. 2009.

[31] F. Xie, W. C. H. Choy, C. Wang, X. Li, S. Zhang, and J. Hou, “Low-temperature solution-processed hydrogen molybdenum and vanadium bronzes for an efficient hole-transport layer in organic electronics.,” *Adv. Mater.*, vol. 25, no. 14, pp. 2051–5, Apr. 2013.

[32] M. O. Reese, S. A. Gevorgyan, M. Jørgensen, E. Bundgaard, S. R. Kurtz, D. S. Ginley, D. C. Olson, M. T. Lloyd, P. Morvillo, E. A. Katz, A. Elschner, O. Haillant, T. R. Currier, V. Shrotriya, M. Hermenau, M. Riede, K. R. Kirov, G. Trimmel, T. Rath, O. Inganäs, F. Zhang, M. Andersson, K. Tvingstedt, M. Lira-Cantu, D. Laird, C. McGuiness, S. (Jimmy) Gowrisanker, M. Pannone, M. Xiao, J. Hauch, R. Steim, D. M. DeLongchamp, R. Rösch, H.

Hoppe, N. Espinosa, A. Urbina, G. Yaman-Uzunoglu, J.-B. Bonekamp, A. J. J. M. van Breemen, C. Girotto, E. Voroshazi, and F. C. Krebs, “Consensus stability testing protocols for organic photovoltaic materials and devices,” *Sol. Energy Mater. Sol. Cells*, vol. 95, no. 5, pp. 1253–1267, May 2011.

[33] A. M. Nardes, M. Kemerink, M. M. de Kok, E. Vinken, K. Maturova, and R. A. J. Janssen, “Conductivity, work function, and environmental stability of PEDOT:PSS thin films treated with sorbitol,” *Org. Electron.*, vol. 9, no. 5, pp. 727–734, Oct. 2008.

[34] J. Schafferhans, A. Baumann, A. Wagenpfahl, C. Deibel, and V. Dyakonov, “Oxygen doping of P3HT:PCBM blends: Influence on trap states, charge carrier mobility and solar cell performance,” *Org. Electron.*, vol. 11, no. 10, pp. 1693–1700, Oct. 2010.

Chapter 6 : Polymer Air Processing

In this chapter, a comparative study based on the fabrication of polymer:fullerene photovoltaic devices incorporating carbazole, fluorene and a PTB based co-polymer is presented. The effects on efficiency and performance of spin coating the polymer:fullerene active layer in the glovebox or in air are investigated using device characterisation. It is shown that OPV devices based on carbazole and fluorene based materials have very similar power conversion efficiency when processed under both air and nitrogen. Absorption measurements recorded after light-soaking suggest that PCDTBT and PFDT2BT-8 have comparatively enhanced photostability. Devices based on the PTB co-polymer however have reduced efficiency when processed in air. [1]

6.0 Introduction

The air-stability of the conjugated polymer used in an OPV is likely to contribute to the ultimate operational stability of the device, as a reduction in device efficiency is known to occur on oxidation of the polymer [2]–[4]. The polymer poly(3-hexylthiophene) [P3HT] is one of the most commonly used in OPV devices. However it is known to be susceptible to oxidation in air [2], [3], [5], whilst other interlayer materials have also been shown to be affected by air exposure [6], requiring them to be processed in a nitrogen atmosphere in order to achieve maximum performance in a device. The ubiquitous acceptor material, PCBM, has also been shown to be unstable in air; exhibiting a reduction in charge mobility on exposure to atmospheric conditions [7]. It is, however, desirable to manufacture OPV devices in air, as this may reduce the capital investment required to develop the necessary production infrastructure. Indeed, many new polymers for OPV applications have lower lying HOMO levels (highest occupied molecular orbitals) which both promote efficient charge transfer to PCBM [8] and reduces their oxidation-rate in air.

6.1 Polymers for Air Processing

One family of polymers that has attracted significant interest for OPV applications are the carbazole co-polymers. The most commonly studied carbazole co-polymer is PCDTBT which has a HOMO level of -5.5 eV [9] and in optimized devices [10]–[14] has demonstrated a *PCE* of 7.2% [15]. Here, a number of studies have characterized device stability and degradation pathways [4], [16], [17], with extrapolated lifetimes of up to 10 years now reported [16]. Other studies have explored the chemical modification of PCDTBT, and have attached octyloxy substituents to the benzothiadiazole acceptor unit in order to improve its solubility in common organic solvents such as chloroform, chlorobenzene and dichlorobenzene [18]. The resulting polymer has been shown to have increased solubility while maintaining high device performance when blended with a $PC_{70}BM$ acceptor [18]. Additional thiophene moieties have also been incorporated along the polymer backbone, which have been shown to reduce the absorption band-gap by increasing the intramolecular charge transfer along the polymer backbone [19]. Other work has explored the replacement of the thiophene moieties in PCDTBT with selenophene to improve the charge carrier mobility through enhanced interchain interactions [20], and the replacement of the carbazole moiety with fluorene to enhance the thermal and chemical stability of the polymer [21]–[24].

While such polymers show promising photovoltaic performance, their stability under an air-based processing-route has not yet been studied in detail. Indeed, the majority of studies investigating such materials have generally explored the fabrication of devices in a nitrogen glovebox [11], [12], [25]. Here this issue is addressed, and it is shown that both carbazole and fluorene based OPV devices can be fabricated in air with little loss in efficiency compared to similar devices prepared in a glovebox. It is also demonstrated that such materials are comparatively stable when exposed in air to optical radiation (an AM1.5 solar simulator), similarly suggesting a high level of photostability. This promising result suggests that there may be significant scope to simplify an OPV manufacture process using air-based printing and processing techniques.

To explore the effect of air-processing, five polymers were explored; namely PCDTBT (M137 batch from Ossila Ltd), PCDTBT-8, PCDSeBT-8, PFDT2BT-8 and PTB7. The chemical structure of each of the polymers is shown in **Figure 6.1 (a)**. The PCDTBT, PCDTBT-8, PCDSeBT-8 and PFDT2BT-8 were synthesized using previously published routes [18], [19], [26] and their M_w, M_n and PDI are shown in **Table 6.1**. The PTB7 was purchased from 1-Material and was used without further purification. The polymer PCDTBT-8 is a derivative of PCDTBT, with the addition of octyloxy substituents on the benzothiadiazole (BT) acceptor improving the solubility of the polymer [18]. The polymer PCDSeBT-8 also has octyloxy side-chain attached to the BT acceptor, however the thiophene moieties along the backbone have been replaced with selenophene. For PFDT2BT-8, the carbazole moiety is replaced by a fluorene, with two thiophene moieties either side of the BT acceptor. We have also included PTB7 in our studies as it has been shown to produce devices having high efficiencies, although it is known to be unstable in air [27]. The HOMO and LUMO energy levels of the five polymers as determined by cyclic voltametry are shown in **Figure 6.1 (b)** [18], [19], [26], [28]. **Figure 6.2** shows pure polymer films spin-coated onto blank glass substrates for colour comparison.

Polymer	Source	M_w	M_n	PDI
PCDTBT (M137)	Ossila Ltd.	42,200	19,600	2.15
PCDTBT-8	UoS Chem. Dept	78,600	32,800	2.4
PCDSeBT-8	UoS Chem. Dept	60,195	16,036	3.75
PFDT2BT-8	UoS Chem. Dept	91,600	62,400	1.47
PTB7 [28]	1-Material	97,500	-	2.1

Table 6.1 Polymer name, source, molecular weight (M_w), molecular number (M_n) and polydispersity index (PDI).

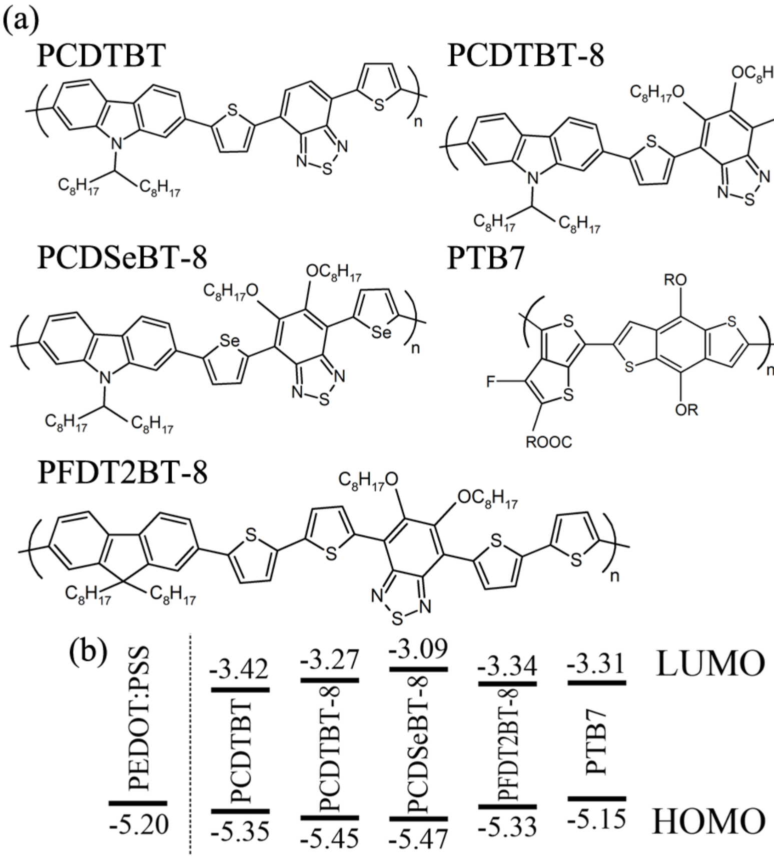

Figure 6.1 (a) Chemical structures of PCDTBT, PCDTBT-8, PCDSeBT-8, PFDT2BT-8 and PTB7. **(b)** HOMO and LUMO levels of polymers and PEDOT:PSS as determined using cyclic voltametry.

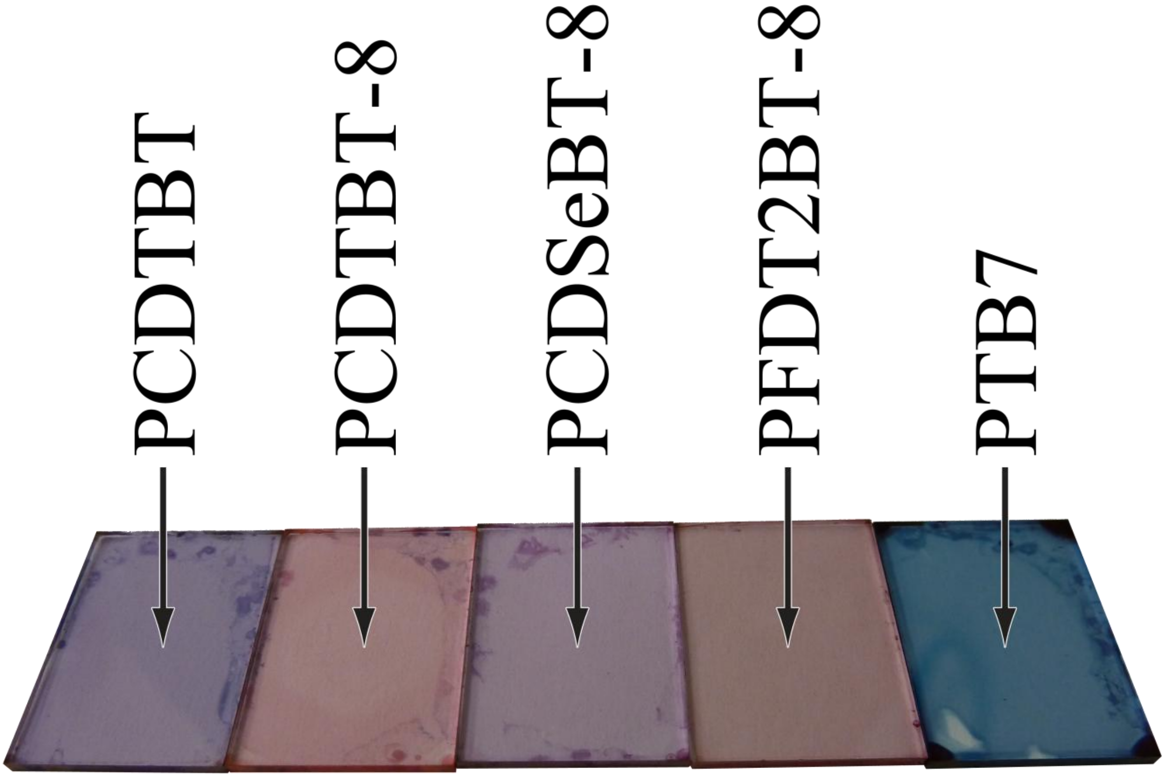

Figure 6.2 Pure polymer films spin-coated onto blank glass substrates for colour comparison.

6.2 Fabricating OPVs in Air

For each polymer:fullerene blend, six OPV devices were fabricated: three whose active layers were deposited in the glovebox and three under ambient conditions in a Lamarflo workstation. OPV devices were based on a standard device architecture of ITO/PEDOT:PSS(30 nm)/active-layer(70-95 nm)/Ca(5 nm)/Al(100 nm). In each case, the active layer was composed of a polymer:$PC_{70}BM$ blend, with the solvent, material concentration, blend ratio and film thickness (as determined by detailed optimization studies) recorded in **Table 6.2**. PEDOT:PSS was chosen as the HTL material due to its ease of deposition and stability in completed OPV devices as demonstrated in **Chapter 5 : Hole Transport Layer Laboratory Lifetime Study**.

Polymer	Solvent	Blend Ratio with $PC_{70}BM$	Total Concentration (mg/mL)	Optimized Film Thickness (nm)
PCDTBT	CB	1:4	25	70
PCDTBT-8	CB	1:4	25	70
PCDSeBT-8	CB	1:4	25	70
PFDT2BT-8	$CHCl_3$	1:4	20	70
PTB7	CB:DIO (97/3%)	1:1.5	25	95

Table 6.2 Optimised processing conditions for PCDTBT, PCDTBT-8, PCDSeBT-8, PFDT2BT-8 and PTB7.

The OPV devices were fabricated using methods discussed in **Chapter 3 : Experimental Methods**. The addition of the high boiling point solvent additive DIO in the PTB7 polymer:fullerene solution resulted in an unusually long spin-coating time of 120 s, after which the film had to be vacuum dried for 10 minutes before it was fully dry. The addition of 3% by volume DIO into the PTB7 solution results in improved film morphology and device performance [28]. Other materials only required a standard 30s spin-coating time with no extra drying steps.

Device characteristics are shown in **Table 6.3**, and JV curves in **Figure 6.3** for devices whose active layers were deposited in the glovebox (GB) **(a)** or in air in the Lamarflo workstation (Air) **(b)**. In each case, the device operating parameters quoted represent an average recorded from 12 pixels defined on three separate substrates in which the worst 25% of pixels had been omitted to account for pixels in which there was a defect. The errors quoted are defined by the standard deviation about the mean.

Polymer	PCE (%)	FF	V_{oc} (V)	J_{sc} ($mAcm^{-2}$)
PCDTBT (GB)	5.4±0.1	64.9±0.7	0.87	-9.6±0.1
(Air)	5.4±0.1	63.3±0.5	0.91	-9.3±0.1
PCDTBT-8 (GB)	3.44±0.05	46.0±0.3	0.81	-9.3±0.1
(Air)	3.82±0.08	44.6±0.5	0.95	-9.0±0.1
PCDSeBT-8 (GB)	3.56±0.04	46.6±0.5	0.81	-9.5±0.1
(Air)	3.77±0.08	44.5±0.7	0.91	-9.2±0.1
PFDT2BT-8 (GB)	5.64±0.07	63±1	0.89	-10.1±0.1
(Air)	6.1±0.1	63.6±0.6	0.92	-10.3±0.1
PTB7 (GB)	5.5±0.1	59±1	0.74	-12.7±0.2
(Air)	4.8±0.2	56.2±0.9	0.70	-11.9±0.2

Table 6.3 Operating parameters for devices incorporating five different polymers, processed either in the nitrogen filled glovebox (GB) or in air.

It can be seen that on processing PCDTBT, PCDTBT-8, PCDSeBT-8, and PFDT2BT-8 based devices in air, there is an enhancement in V_{oc} by between 30 to 140 mV. We attribute this increase in V_{oc} to a very rapid hydration of the PEDOT:PSS hole extraction layer that occurs in air; a process that results in an increase in its work-function. Previous work has shown that the exposure of PEDOT:PSS to moist air can result in an increase in its conductivity [29], [30], and also the formation of a thin layer of water at the film surface (bound to the positively charged PSS ionomers) that increases charge conduction across the interface [6], [30]. This hydration effect is known to be accelerated in PEDOT:PSS films having a high PSS concentration [29], [31] as is the case for the 1:6 PEDOT:PSS material used here [32].

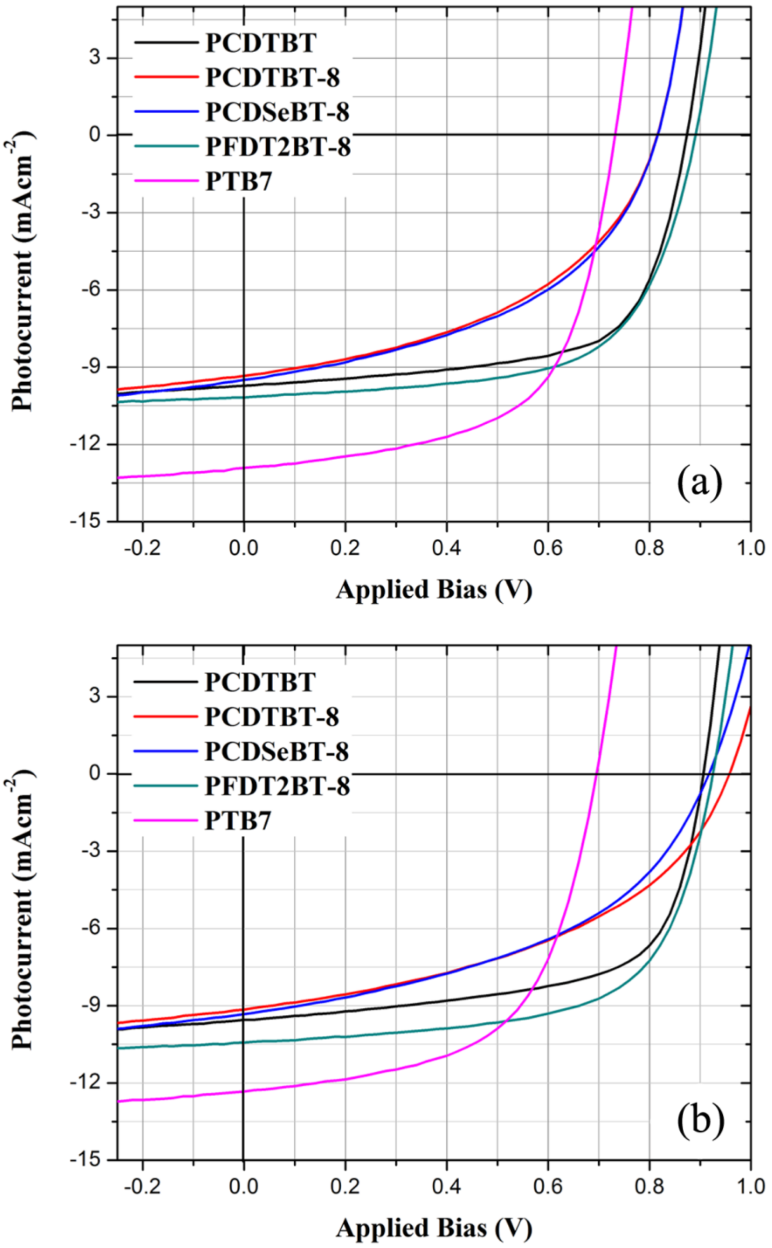

Figure 6.3 Part **(a)** shows JV characteristics for devices processed in a nitrogen-filled glovebox, with part **(b)** showing device characteristics when processed in air.

Thus, we propose that the enhancement of V_{oc} that we observe results from the presence of a water layer at the PEDOT:PSS film surface that increases its work function; a conclusion in accord with previous findings using other hole-extraction layers [6]. Notably, the increase in V_{oc} is largest for the PCDTBT-8 and PCDSeBT-8 based devices, being 140 mV and 100 mV respectively. We believe this occurs as a direct result of the deeper HOMO levels of these polymers (-5.45eV for PCDTBT-8 and -5.47eV for PCDSeBT-8). Here, hole transfer to "dehydrated" PEDOT:PSS (HOMO at -5.2 eV), is less efficient, resulting in a relatively low value of V_{oc} (0.81 V) when these devices are processed under nitrogen. When however the devices are processed in air, the increased work function of "hydrated" PEDOT:PSS results in more efficient charge extraction and an increase in V_{oc}. In contrast, PCDTBT and PFDT2BT-8 have a HOMO level that is already close to that of "dehydrated" PEDOT:PSS (-5.35, -5.33 and -5.2 eV respectively) and thus the gain in V_{oc} on processing devices in air is relatively limited as hole extraction is already relatively efficient. There does not however appear to be a gain in V_{oc} when processing PTB7 OPV devices in air. Here, the HOMO level of the PTB7 is smaller than that of "dehydrated" PEDOT:PSS (-5.15 and -5.20 eV respectively). On exposure to moisture, the increase in PEDOT:PSS work-function is likely to further impede the extraction of holes.

For all the polymers studied (with the exception of PFDT2BT-8), both the J_{sc} and the *FF* are reduced when the active layer blend is deposited in air. This correlates with an overall reduction in the EQE of the devices that were processed in air as can be seen in **Figure 6.4**, measured using the equipment described in **3.6 External Quantum Efficiency (EQE)**. Notably however, the J_{sc} and EQE of PFDT2BT-8 based devices do not appear to be significantly affected by such air exposure.

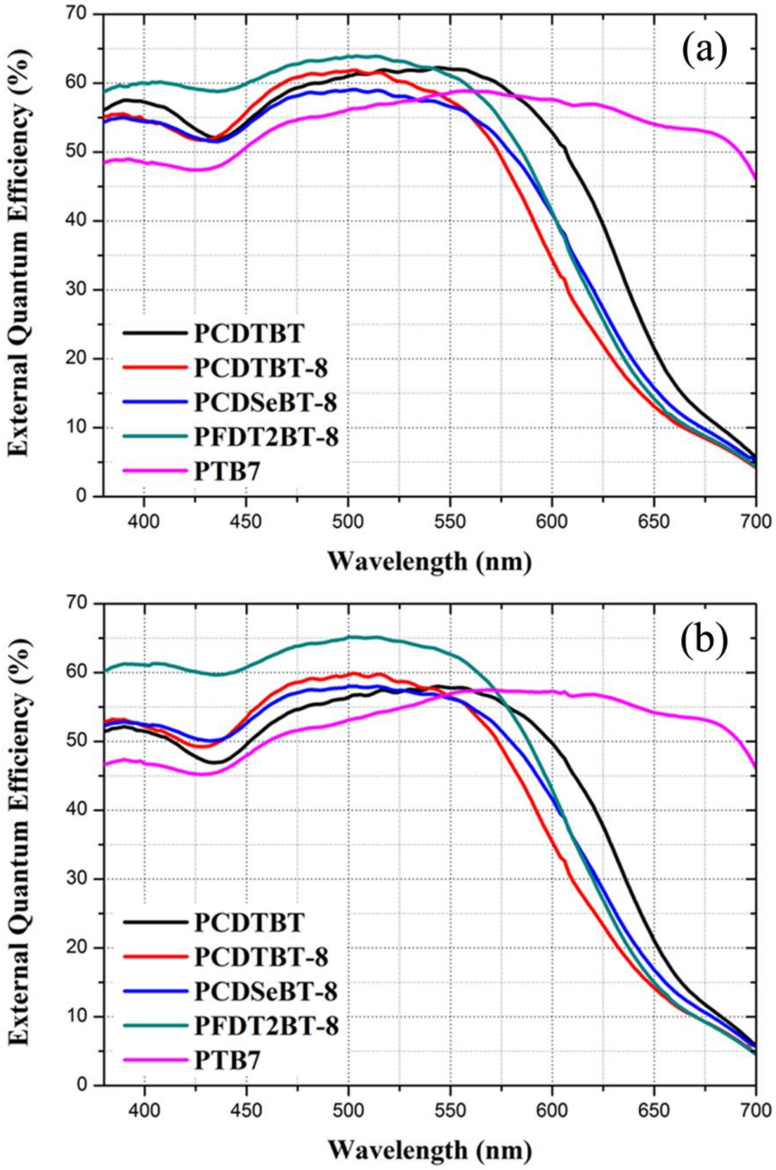

Figure 6.4 Part **(a)** shows the EQE of devices processed in a nitrogen-filled glovebox, with part **(b)** showing EQE of devices when processed in air.

It is hypothesized that reductions in J_{sc} and FF result from the generation of trap states resulting from light-induced oxidation that reduces charge-carrier mobility [33]. This effect is particularly pronounced for PTB7-based devices; a finding in accord with previous work showing that PTB7 is rapidly oxidized on exposure in air [27]. Notably however, the reduction in FF and J_{sc} observed in the PCDTBT-8 and PCDSeBT-8 based devices is counterbalanced by the large increase in V_{oc}, resulting in an overall increase in *PCE* on processing in air. For PCDTBT, the smaller gain in V_{oc} is balanced by a comparable reduction in *FF* and J_{sc}, resulting in devices processed under nitrogen and air having similar values of *PCE*. For PTB7, the combined effects of a reduction in V_{oc} due to energy level misalignment at the PEDOT:PSS interface and a reduction of *FF* and J_{sc} due to oxidation when processed in air results in a significant reduction in *PCE*. Of the five polymers explored, PFDT2BT-8 alone does not undergo a reduction in any of the device metrics, resulting in a higher *PCE* for air-processed devices.

6.3 Photostability of Polymers

To explore whether any degradation in efficiency of OPVs fabricated in air could be correlated with the rate at which the polymer underwent optically induced oxidation, freshly-spun, un-encapsulated polymer films on quartz substrates were exposed for various times to light from a solar simulator in air (for 10, 20, 40, 80 and 160 minutes). The optical transmission of the exposed films was then recorded using a Horiba Fluormax-4 spectrophotometer as described in **3.4 Absorbance Spectroscopy**.

To further understand the relative air stability of the different polymers, the changes in their ability to harvest light as they are deliberately photo-oxidized was studied. This is shown in **Figure 6.5 (a)** and **(b)**, where the normalized absorption spectra of the polymer films both before, and after exposure for 160 minutes to simulated AM1.5 radiation is plotted. In **Figure 6.5 (c)**, the relative absorption of each polymer film (integrated over the wavelength range λ = 350 to 900 nm) as a function of time during the light exposure, with data normalized to the absorption determined at $t = 0$ is shown. It was found that the absorption maxima of each of the polymers undergoes a blue shift on extended light exposure which is attributed to a reduction in electronic-conjugation as a result of oxidation of the polymer backbone [33]. This spectral shift is most pronounced for PTB7, with the absorption maxima undergoing a blue-shift of ~ 70 nm; a value significantly larger than that of the other polymers whose absorption blue-shift is limited to around 10 nm.

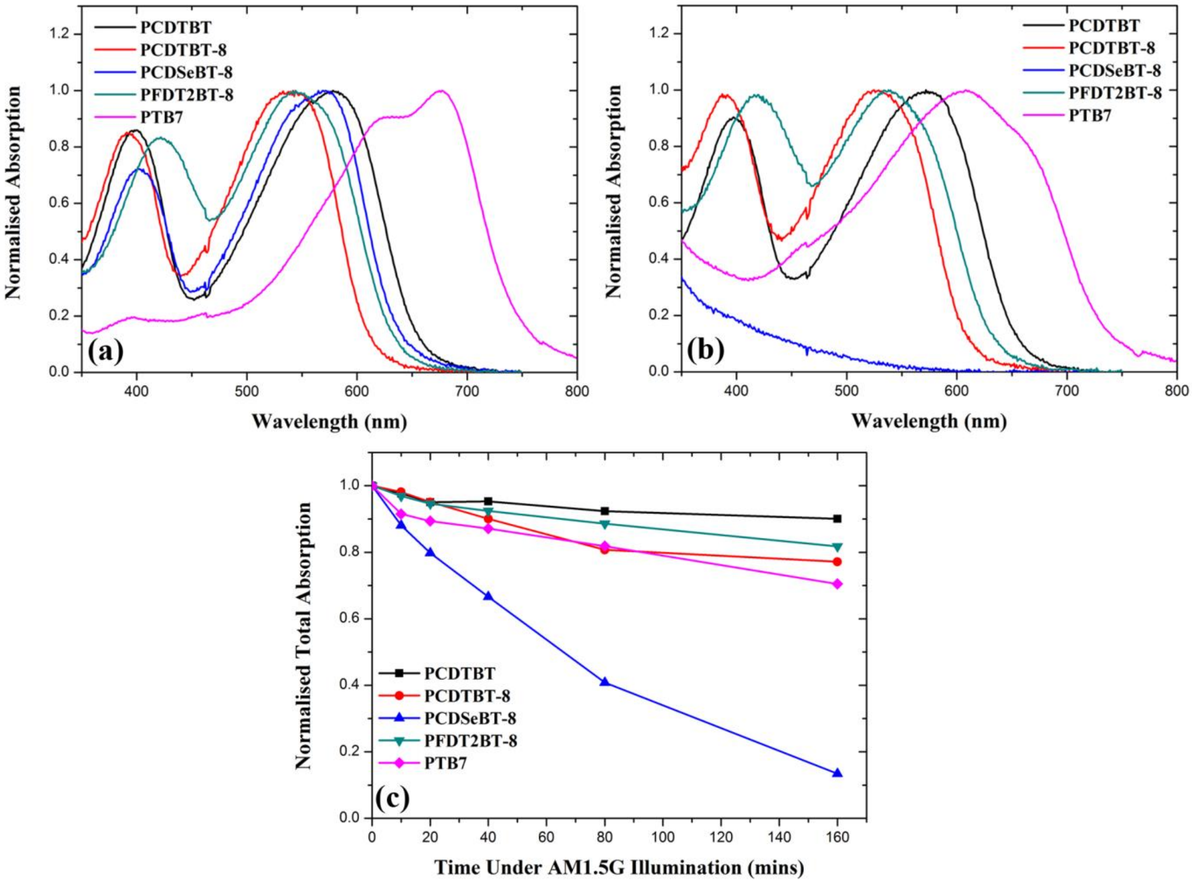

Figure 6.5 Part **(a)** shows the normalized absorption spectra for the unexposed polymers. Part **(b)** shows normalized absorption spectra for the same (un-encapsulated) materials after exposure to light from an AM1.5 solar simulator in air for 160 min. The data shown in part (c) plots the integrated absorption of the polymer films (normalized to their initial values) as a function of light-exposure time in air. Spectra in parts **(a)** and **(b)** are normalised such that the spectral maximum is equal to 1.

In **Figure 6.5 (c)**, it can be seen in that over a relatively short timescale concurrent with spin-coating in air (< 10 minutes), PCDTBT, PCDTBT-8 and PFDT2BT-8 undergo a small (2 - 3%) but similar reduction in their total absorbance. Notably however, both PTB7 and PCDSeBT-8 photo-bleach more rapidly, with the absorbance being reduced by 7 and 11% respectively. At the end of the experiment (160 minutes of illumination), the PCDSeBT-8 sample had become almost totally bleached, thus suggesting it has a poor photostability that is attributed to the substitution of the thiophene moieties with selenophene. Of all the polymers explored, PCDTBT undergoes the smallest degree of bleaching over the experiment, indicating it has the highest degree of photostability. Its polyfluorene analogue PFDT2BT-8 also demonstrates a similar (but slightly reduced) photostability.

6.4 Effects of Extended Air Exposure

To explore the effects of extended air exposure of active layer films on device performance, OPV devices were fabricated with the same architecture and processing methods as previously used in this chapter. However, once the active layer had been deposited the partially completed devices were left in air under ambient conditions for up to 30 minutes. For reference, devices were also processed in the glovebox and were not exposed to air at any point during their fabrication. Two polymers were used for this study, PFDT2BT-8 and PTB7. PFDT2BT-8 was chosen as it was the only polymer studied that did not exhibit a reduction in operating parameters on processing in air, and PTB7 was chosen for comparison due to its poor air stability. The average operating parameters for PFDT2BT-8 devices are shown in **Table 6.4** and *JV* curves in **Figure 6.6**. Devices with 0 mins exposure time were processed in the glovebox with no exposure to air at any point during fabrication.

PFDT2BT-8:$PC_{70}BM$ Devices

Air Exposure Time (mins)	PCE (%)	FF	V_{oc} (V)	J_{sc} ($mAcm^{-2}$)
0 (reference)	5.59±0.07	64.3±0.6	0.88	-9.92±0.03
1	5.69±0.09	63.5±0.5	0.90	-10.03±0.05
2	5.5±0.1	62±2	0.90	-9.94±0.08
5	5.4±0.2	61±2	0.90	-9.87±0.09
10	5.1±0.1	58±1	0.90	-9.7±0.1
20	5.05±0.09	57.8±0.9	0.90	-9.76±0.04
30	4.6±0.2	53±2	0.90	-9.54±0.09

Table 6.4 Operating parameters for devices with a PFDT2BT-8:$PC_{70}BM$ active layer with different air exposure times.

It can be seen that for devices utilizing a PFDT2BT-8:$PC_{70}BM$ active layer, exposure to air for up to 5 minutes does not (within error) result in any loss in device performance. On deposition in air, an increase in V_{oc} is seen, due to the hydration of the PEDOT:PSS HTL as discussed in **6.2 Fabricating OPVs in Air**. No significant loss in *FF* or J_{sc} is seen until after 5 minutes of exposure to air, a time-scale commensurate processes such as R2R, indicating that PFDT2BT-8 is a promising polymer for such manufacturing processes. No loss of V_{oc} is observed, even when devices were exposed to air for 30 minutes, indicating that the interface between the active layer and PEDOT:PSS HTL is stable over these timescales.

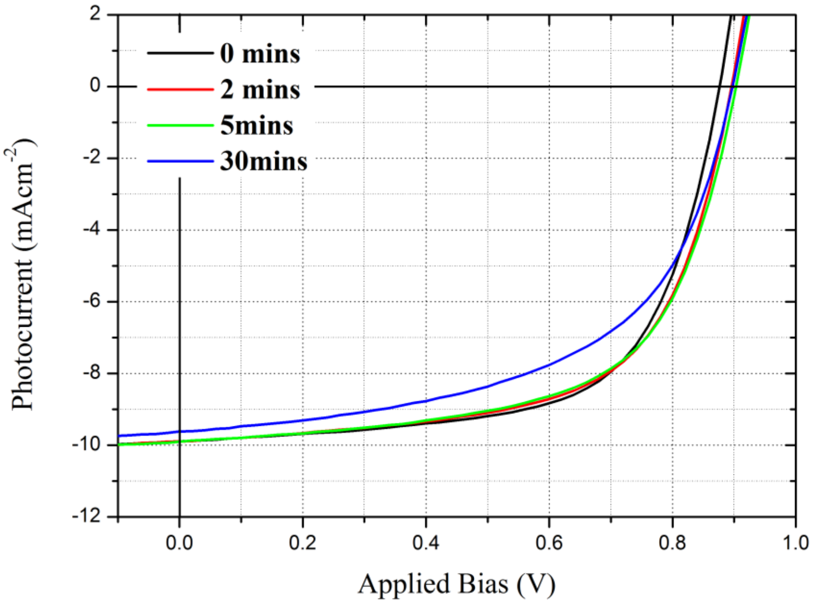

Figure 6.6 *JV* characteristics for devices with a PFDT2BT-8:PC$_{70}$BM active layer exposed to air for 0, 2, 5 and 30 minutes.

The average operating parameters for PTB7 devices are shown in **Table 6.5** and *JV* curves in **Figure 6.7**. It can be seen that on processing in air, there is an immediate reduction in all device operating parameters. On deposition in air, a decrease in V_{oc} is seen, due to hydration of the PEDOT:PSS HTL and the resulting energy mismatch between the HOMO level of the polymer and PEDOT:PSS. Oxidation of the polymer backbone on exposure to air results in a decrease in charge-carrier mobility and a reduction in *FF* and J_{sc}. Whilst there is little change in *FF* after the initial decrease on exposure to air, J_{sc} undergoes a steady reduction with increased air exposure time as a result of photo-oxidation.

PTB7:PC_{70}BM Devices

Air Exposure Time (mins)	PCE (%)	FF	V_{oc} (V)	J_{sc} ($mAcm^{-2}$)
0 (reference)	5.64±0.08	60.0±0.5	0.72	-13.06±0.06
1	3.4±0.1	48±1	0.69	-10.31±0.3
2	3.09±0.07	45±1	0.69	-9.98±0.07
5	2.6±0.1	44±1	0.66	-9.63±0.04
10	2.7±0.2	42±2	0.66	-9.6±0.4
20	2.67±0.06	43.5±0.5	0.66	-9.3±0.1
30	2.39±0.06	44.7±0.5	0.66	-8.1±0.1

Table 6.5 Operating parameters for devices with a PTB7:PC_{70}BM active layer with different air exposure times.

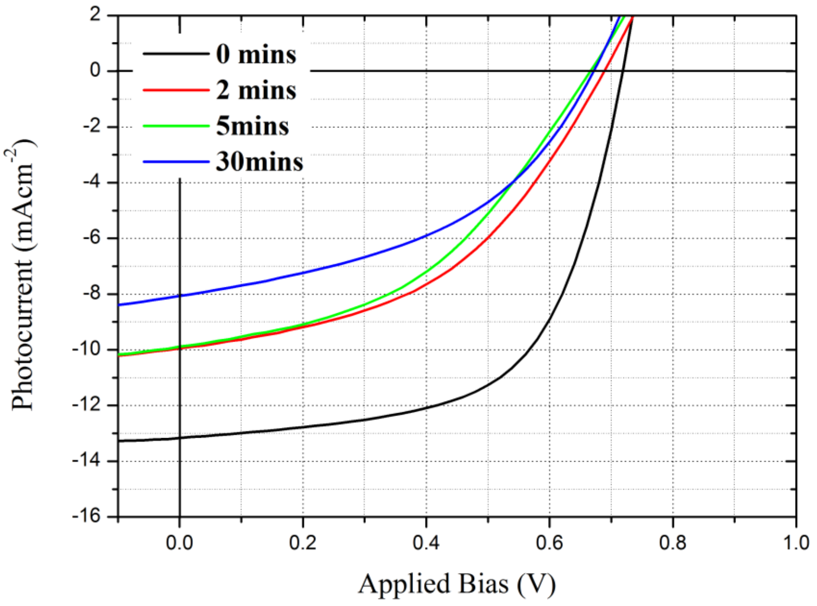

Figure 6.7 *JV* characteristics for devices with a PTB7:PC_{70}BM active layer exposed to air for 0, 2, 5 and 30 minutes.

6.5 Conclusions

It was found that carbazole and fluorene based conjugated polymers have a relatively high degree of photostability that permit them to be processed (in a polymer:fullerene blend) into the active layer of a photovoltaic device in air with little loss in *PCE*. Indeed, in some cases, devices processed in air have enhanced efficiency compared with comparable devices processed under nitrogen; an affect that is attributed to changes in the work function of the underlying PEDOT:PSS anode. PFDT2BT-8:$PC_{70}BM$ active layers have been shown to be stable in air for up to 5 minutes with little loss in device performance. This timeframe is commensurate with processing timeframes for scale up processes such as R2R printing, indicating that PFDT2BT-8 is a promising polymer for such manufacturing processes. It will be interesting to determine whether the photostability of conjugated polymers measured under optical irradiation in air can be directly correlated with their operational stability when processed into an OPV device, as this technique could be used as a rapid and efficient screening tool to identify new polymers for device applications.

6.6 References

[1] E. Bovill, H. Yi, A. Iraqi, and D. G. Lidzey, “The fabrication of polyfluorene and polycarbazole-based photovoltaic devices using an air-stable process route,” *Appl. Phys. Lett.*, vol. 105, no. 22, p. 223302, Dec. 2014.

[2] V. Chellappan, G. M. Ng, M. J. Tan, W.-P. Goh, and F. Zhu, “Imbalanced charge mobility in oxygen treated polythiophene/fullerene based bulk heterojunction solar cells,” *Appl. Phys. Lett.*, vol. 95, no. 26, p. 263305, 2009.

[3] A. Seemann, H.-J. Egelhaaf, C. J. Brabec, and J. A. Hauch, “Influence of oxygen on semi-transparent organic solar cells with gas permeable electrodes,” *Org. Electron.*, vol. 10, no. 8, pp. 1424–1428, Dec. 2009.

[4] C. H. Peters, I. T. Sachs-Quintana, W. R. Mateker, T. Heumueller, J. Rivnay, R. Noriega, Z. M. Beiley, E. T. Hoke, A. Salleo, and M. D. McGehee, “The mechanism of burn-in loss in a high efficiency polymer solar cell,” *Adv. Mater.*, vol. 24, no. 5, pp. 663–668, Feb. 2012.

[5] F. C. Krebs and K. Norrman, “Analysis of the Failure Mechanism for a Stable Organic Photovoltaic During 10 000 h of Testing,” no. September, pp. 697–712, 2007.

[6] E. S. R. Bovill, J. Griffin, T. Wang, J. W. Kingsley, H. Yi, A. Iraqi, A. R. Buckley, and D. G. Lidzey, “Air processed organic photovoltaic devices incorporating a MoOx anode buffer layer,” *Appl. Phys. Lett.*, vol. 102, no. 18, p. 183303, May 2013.

[7] J. M. Ball, R. K. M. Bouwer, F. B. Kooistra, J. M. Frost, Y. Qi, E. B. Domingo, J. Smith, D. M. De Leeuw, J. C. Hummelen, J. Nelson, A. Kahn, N. Stingelin, D. D. C. Bradley,

and T. D. Anthopoulos, “Soluble fullerene derivatives: The effect of electronic structure on transistor performance and air stability,” *J. Appl. Phys.*, vol. 110, no. 2011, 2011.

[8] M. C. Scharber, D. Mühlbacher, M. Koppe, P. Denk, C. Waldauf, A. J. Heeger, and C. J. Brabec, “Design Rules for Donors in Bulk-Heterojunction Solar Cells—Towards 10 % Energy-Conversion Efficiency,” *Adv. Mater.*, vol. 18, no. 6, pp. 789–794, Mar. 2006.

[9] N. Blouin, A. Michaud, and M. Leclerc, “A Low-Bandgap Poly(2,7-Carbazole) Derivative for Use in High-Performance Solar Cells,” *Adv. Mater.*, vol. 19, no. 17, pp. 2295–2300, Sep. 2007.

[10] D. C. Watters, J. Kingsley, H. Yi, T. Wang, A. Iraqi, and D. Lidzey, “Optimising the efficiency of carbazole co-polymer solar-cells by control over the metal cathode electrode,” *Org. Electron.*, vol. 13, no. 8, pp. 1401–1408, Aug. 2012.

[11] T. Wang, A. J. Pearson, A. D. F. Dunbar, P. A. Staniec, D. C. Watters, H. Yi, A. J. Ryan, R. A. L. Jones, A. Iraqi, and D. G. Lidzey, “Correlating Structure with Function in Thermally Annealed PCDTBT:PC70BM Photovoltaic Blends,” *Adv. Funct. Mater.*, vol. 22, no. 7, pp. 1399–1408, Apr. 2012.

[12] S. H. Park, A. Roy, S. Beaupré, S. Cho, N. Coates, J. S. Moon, D. Moses, M. Leclerc, K. Lee, and A. J. Heeger, “Bulk heterojunction solar cells with internal quantum efficiency approaching 100%,” *Nat. Photonics*, vol. 3, no. 5, pp. 297–302, Apr. 2009.

[13] J. Liu, S. Shao, G. Fang, B. Meng, Z. Xie, and L. Wang, “High-efficiency inverted polymer solar cells with transparent and work-function tunable MoO(3)-Al composite film as cathode buffer layer.,” *Adv. Mater.*, vol. 24, no. 20, pp. 2774–9, May 2012.

[14] Y. Sun, J. H. Seo, C. J. Takacs, J. Seifter, and A. J. Heeger, “Inverted polymer solar cells integrated with a low-temperature-annealed sol-gel-derived ZnO film as an electron transport layer,” *Adv. Mater.*, vol. 23, no. 14, pp. 1679–1683, Apr. 2011.

[15] Y. Sun, C. J. Takacs, S. R. Cowan, J. H. Seo, X. Gong, A. Roy, and A. J. Heeger, “Efficient, air-stable bulk heterojunction polymer solar cells using MoO x as the anode interfacial layer,” *Adv. Mater.*, vol. 23, no. 19, pp. 2226–2230, May 2011.

[16] C. H. Peters, I. T. Sachs-Quintana, J. P. Kastrop, S. Beaupré, M. Leclerc, and M. D. McGehee, “High Efficiency Polymer Solar Cells with Long Operating Lifetimes,” *Adv. Energy Mater.*, vol. 1, no. 4, pp. 491–494, Jul. 2011.

[17] S. Cho, J. H. Seo, S. H. Park, S. Beaupré, M. Leclerc, and A. J. Heeger, “A thermally stable semiconducting polymer.,” *Adv. Mater.*, vol. 22, no. 11, pp. 1253–7, Mar. 2010.

[18] H. Yi, S. Al-Faifi, A. Iraqi, D. C. Watters, J. Kingsley, and D. G. Lidzey, “Carbazole and thienyl benzo[1,2,5]thiadiazole based polymers with improved open circuit voltages and processability for application in solar cells,” *J. Mater. Chem.*, vol. 21, no. 35, p. 13649, 2011.

[19] D. C. Watters, H. Yi, A. J. Pearson, J. Kingsley, A. Iraqi, and D. Lidzey, “Fluorene-based co-polymer with high hole mobility and device performance in bulk heterojunction organic solar cells.,” *Macromol. Rapid Commun.*, vol. 34, no. 14, pp. 1157–62, Jul. 2013.

[20] Z. Chen, H. Lemke, S. Albert-Seifried, M. Caironi, M. M. Nielsen, M. Heeney, W. Zhang, I. McCulloch, and H. Sirringhaus, “High mobility ambipolar charge transport in polyselenophene conjugated polymers.,” *Adv. Mater.*, vol. 22, no. 21, pp. 2371–5, Jun. 2010.

[21] Q. Hou, Y. Xu, W. Yang, M. Yuan, J. Peng, and Y. Cao, “Novel red-emitting fluorene-based copolymers,” *J. Mater. Chem.*, vol. 12, no. 10, pp. 2887–2892, Sep. 2002.

[22] M. Bernius, M. Inbasekaran, E. Woo, W. Wu, and L. Wujkowski, “Fluorene-based polymers-preparation and applications,” *J. Mater. Sci. Mater. Electron.*, vol. 11, no. 2, pp. 111–116, 2000.

[23] G. Klärner, J.-I. Lee, M. H. Davey, and R. D. Miller, “Exciton Migration and Trapping in Copolymers Based on Dialkylfluorenes,” *Adv. Mater.*, vol. 11, no. 2, pp. 115–119, Feb. 1999.

[24] W.-Y. Wong, “Metallated molecular materials of fluorene derivatives and their analogues,” *Coord. Chem. Rev.*, vol. 249, no. 9–10, pp. 971–997, May 2005.

[25] S. Alem, T.-Y. Chu, S. C. Tse, S. Wakim, J. Lu, R. Movileanu, Y. Tao, F. Bélanger, D. Désilets, S. Beaupré, M. Leclerc, S. Rodman, D. Waller, and R. Gaudiana, “Effect of mixed solvents on PCDTBT:PC70BM based solar cells,” *Org. Electron.*, vol. 12, no. 11, pp. 1788–1793, Nov. 2011.

[26] A. A. B. Alghamdi, D. C. Watters, H. Yi, S. Al-Faifi, M. S. Almeataq, D. Coles, J. Kingsley, D. G. Lidzey, and A. Iraqi, “Selenophene vs. thiophene in benzothiadiazole-based low energy gap donor–acceptor polymers for photovoltaic applications,” *J. Mater. Chem. A*, vol. 1, no. 16, p. 5165, 2013.

[27] Y. W. Soon, H. Cho, J. Low, H. Bronstein, I. McCulloch, and J. R. Durrant, “Correlating triplet yield, singlet oxygen generation and photochemical stability in polymer/fullerene blend films.,” *Chem. Commun. (Camb).*, vol. 49, no. 13, pp. 1291–3, Feb. 2013.

[28] Y. Liang, Z. Xu, J. Xia, S.-T. Tsai, Y. Wu, G. Li, C. Ray, and L. Yu, “For the bright future-bulk heterojunction polymer solar cells with power conversion efficiency of 7.4%.,” *Adv. Mater.*, vol. 22, no. 20, pp. E135–8, May 2010.

[29] A. M. Nardes, M. Kemerink, M. M. de Kok, E. Vinken, K. Maturova, and R. A. J. Janssen, “Conductivity, work function, and environmental stability of PEDOT:PSS thin films treated with sorbitol,” *Org. Electron.*, vol. 9, no. 5, pp. 727–734, Oct. 2008.

[30] M. Kuş and S. Okur, “Electrical characterization of PEDOT:PSS beyond humidity saturation,” *Sensors Actuators B Chem.*, vol. 143, no. 1, pp. 177–181, Dec. 2009.

[31] J. Huang, P. F. Miller, J. S. Wilson, A. J. de Mello, J. C. de Mello, and D. D. C. Bradley, “Investigation of the Effects of Doping and Post-Deposition Treatments on the Conductivity, Morphology, and Work Function of Poly(3,4-ethylenedioxythiophene)/Poly(styrene sulfonate) Films,” *Adv. Funct. Mater.*, vol. 15, no. 2, pp. 290–296, Feb. 2005.

[32] “PEDOT:PSS - Heraeus Clevios^{TM} P VP Al 4083.” [Online]. Available: http://www.heraeus-clevios.com/en/_technik/productdetail_1034017.aspx?psMarketId=1286&psApplicationId=.

[33] E. T. Hoke, I. T. Sachs-Quintana, M. T. Lloyd, I. Kauvar, W. R. Mateker, A. M. Nardes, C. H. Peters, N. Kopidakis, and M. D. McGehee, “The Role of Electron Affinity in Determining Whether Fullerenes Catalyze or Inhibit Photooxidation of Polymers for Solar Cells,” *Adv. Energy Mater.*, vol. 2, no. 11, pp. 1351–1357, Nov. 2012.

Chapter 7 : Outdoor Lifetime Testing

In **Chapter 5 : Hole Transport Layer Laboratory Lifetime Study**, the operational lifetimes of OPV devices utilising a PCDTBT:$PC_{70}BM$ active layer and three different hole transport layers were investigated using a laboratory lifetime testing setup. From this test, it was shown that PEDOT:PSS resulted in devices having the longest extrapolated T_{80} lifetimes of ~ 7.2 years. In **Chapter 6** : **Polymer Air Processing**, it was shown that devices with a PFDT2BT-8:$PC_{70}BM$ active layer had the highest *PCE* of all the polymers tested and were extremely stable when processed in air. Utilising these materials, devices with an ITO/PEDOT:PSS/PFDT2BT-8:$PC_{70}BM$/Ca/Al architecture were fabricated and installed in an outdoor testing setup, as described in **3.10 Outdoor Lifetime Testing**, on the roof of the Department of Physics at the University of Sheffield, England, UK, for a period of four months. It was shown that daily and seasonal light intensity and temperature variation has a significant effect on measured J_{sc}, *FF*, V_{oc} and *PCE*, and the calculation of device T_{80} lifetime.

7.0 Introduction

In comparison to laboratory testing of OPV devices, outdoor testing is more representative of the real-world conditions that commercial devices would experience during their operational lifetime. However, only a few such studies have been carried out so far [1]–[5], almost all with a P3HT:PCBM active layer blend on flexible PET substrates, with T_{80} lifetimes of up to 10,000 hours calculated for the best performing devices [1]. Outdoor testing of OPV devices introduces many challenges that are not present in laboratory testing. The increased humidity and the presence of precipitation in outdoor environments (especially in temperate countries) stresses the encapsulation of OPV devices, and is often the cause of catastrophic device failure [1]. Daily thermal cycling also introduces degradation mechanisms and efficiency measurement issues, discussed in more detail in **7.2 Temperature Effects**.

Here, four devices based on an ITO/PEDOT:PSS/PFDT2BT-8:$PC_{70}BM$/Ca/Al architecture were tested under conditions closely modelled on the ISOS-O-2 specifications [6], outlined in **3.11.2 ISOS Outdoor Testing**. The outdoor testing setup used did not expose the OPV devices to atmospheric conditions, but enclosed them in an environmental chamber filled with an overpressure of nitrogen at close to 0% humidity. This was to exclude extrinsic degradation processes, such as water and oxygen ingress, and allow for study of intrinsic degradation processes under outdoor conditions. The data presented here is for the first four months of an ongoing study.

7.1 Light and Temperature Variation

The devices were tested from 1/8/14 to 8/12/14, with a break in measurements from 11/9/14 to 17/9/14 due to technical issues with the system, though the devices were left in the test setup during this period. As a result, the devices were exposed to one of the hottest periods of the year (with daily temperatures at times reaching 30^{o}C) and the beginning of winter where the average daily temperatures were far lower. Due to the enclosed nature of the environmental chambers, this meant that on hot, sunny days the temperature inside the chamber reached a maximum of 80^{o}C, and during December the temperature of the devices dropped to a minimum of ~ 10^{o}C, resulting in a 70^{o}C variation in device temperature during measurement. The total light intensity as measured by the pyranometer and the daily average temperature as measured inside the environmental chamber housing the devices is shown in **Figure 7.1**.

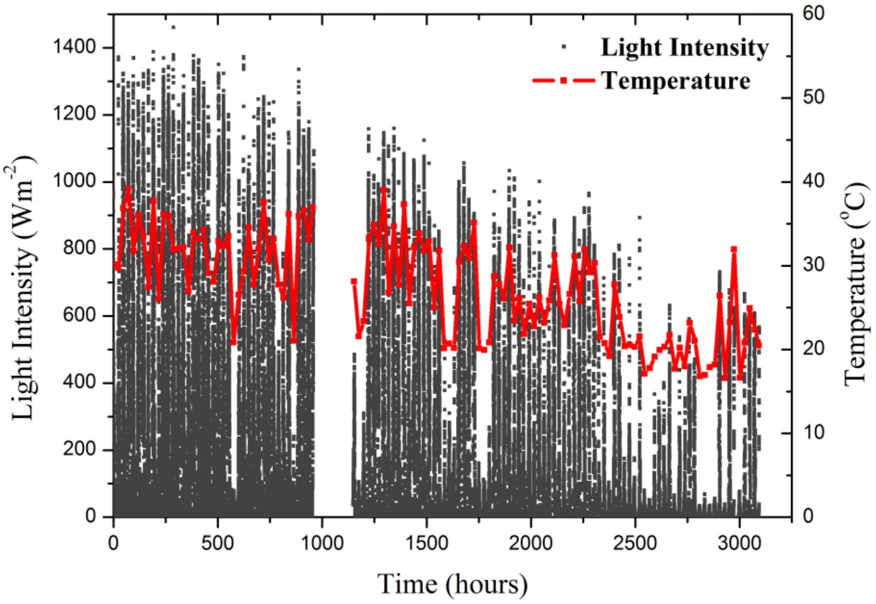

Figure 7.1 Total light intensity (Wm^{-2}) as measured by the pyranometer every minute, and average daily temperature (^{o}C) over the 4 month outdoor lifetime test. Gap in data is due to a one week shut down of the equipment due to technical issues.

It can be seen that the daily peak light intensity decreases from August to December, with a reduction in daily peak light intensity of ~ 40% over the course of the experiment. Also, the number of hours of daylight changed over the course of the experiment, with ~ 15 hours of daylight in August and only ~ 8 hours in December. For this reason, it is recommended that for outdoor testing, device characteristics are plotted as a function of accumulated energy rather than as a function of time (as with laboratory tests where the light intensity is constant) [6]. Accumulated energy can be calculated by integrating the measured light intensity with time. This was done for each pixel of the four devices and then averaged, the results of which are shown in **Figure 7.2**. To account for the week where the system was shut down, but the devices were still exposed to daylight on the roof, the accumulated energy was assumed to be the average of the week immediately previous to shut down and the week immediately after shut down. The accumulated energy is plotted in units of Jm^{-2} to account for uncertainly in the size of the pixels as discussed in **3.9.6 Pixel Size Variation**.

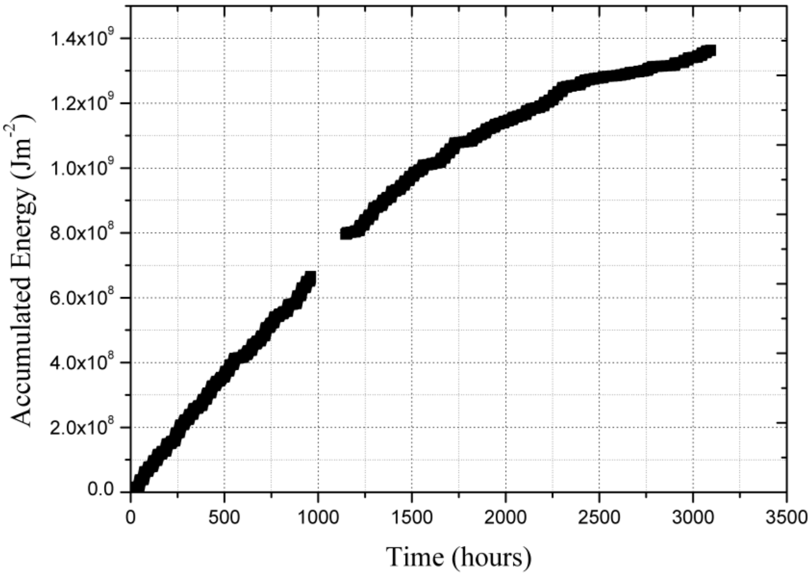

Figure 7.2 Accumulated energy for devices (Jm^{-2}) over the 4 month outdoor lifetime test. Gap in data is due to a one week shut down of the equipment due to technical issues.

It can be seen that initially the accumulated radiation is relatively linear until ~ 1000 hours (10/09/14), at which point the daily accumulated radiation decreases at the onset of autumn, and subsequently winter, as the days become shorter and the maximum daily light intensity is lower as seen in **Figure 7.1**. The total accumulated energy of the devices in the outdoor testing setup was 1.37×10^9 Jm^{-2}, equivalent to 381 hours in the laboratory lifetime tester under constant illumination conditions at 1000 Wm^{-2}.

7.1.2 Sunny and Cloudy Days

The response of OPV devices is highly dependent on the incident light intensity [7], [8], and as such the daily and seasonal varying light intensity shown in **Figure 7.1** results in fluctuations in device operating parameters over time, independent of device degradation. In **Figure 7.3** device *PCE*, *FF*, V_{oc} and J_{sc} are plotted for a cloudy and sunny day in August 2014 (2nd and 3rd respectively). *PCE* is calculated in all instances using the recorded values of *FF*, V_{oc}, J_{sc} and the total light intensity from the pyranometer, using **Equation 3.3**.

It can be seen that for both the sunny and cloudy days, *PCE*, V_{oc} and *FF* are largely independent of light intensity, except at very low light levels where there are inconsistencies with the measurement of V_{oc} and *FF*. In comparison, J_{sc} is linearly dependent on light intensity [8], as shown in **Figure 7.4** for data from the sunny day (3/8/14) (not accounting for temperature effects). However, the temperature of the devices has an effect on their measured *PCE*, as covered in more detail in **7.2 Temperature Effects**.

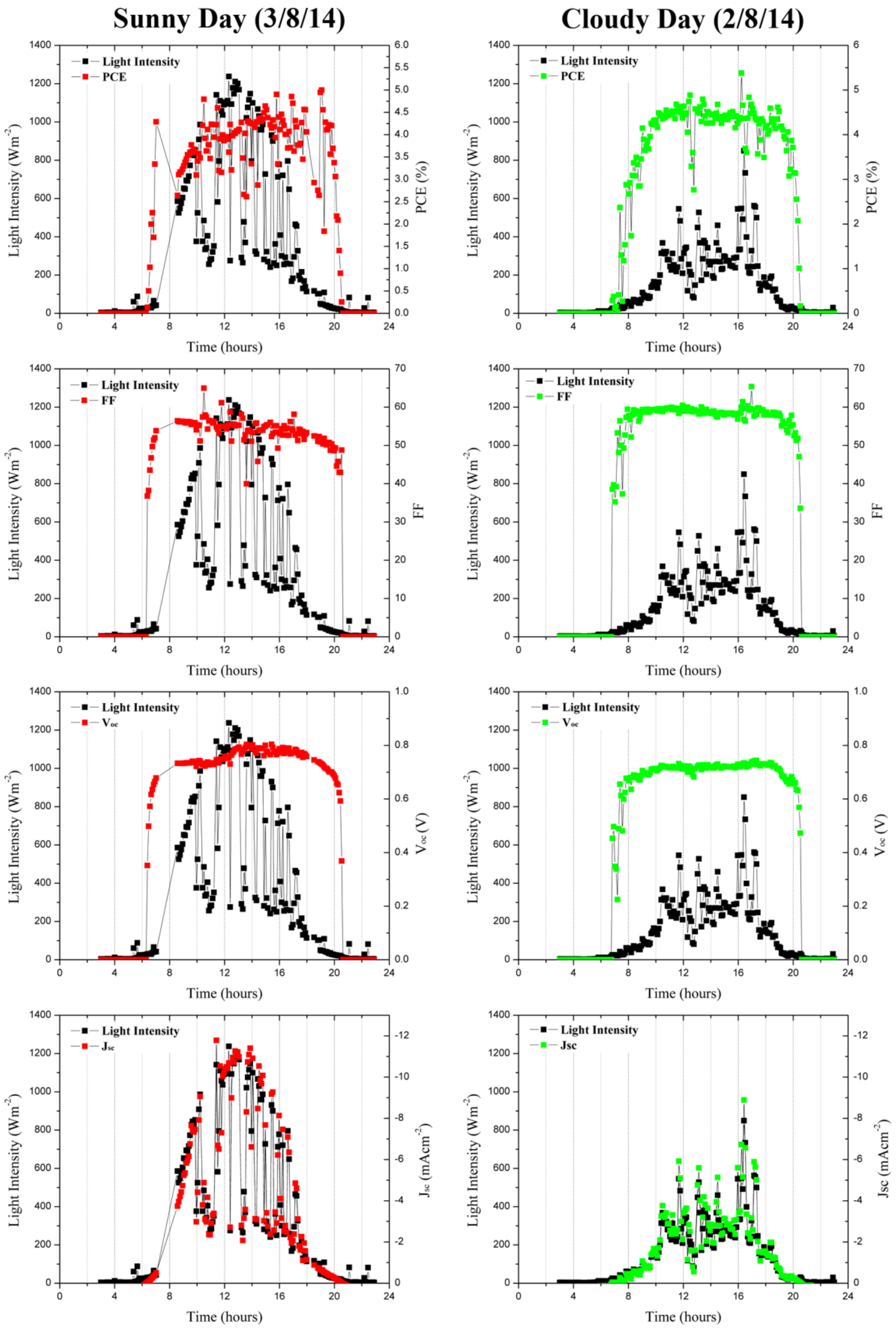

Figure 7.3 Variation in *PCE*, *FF*, V_{oc} and J_{sc} for devices over the course of a cloudy day and a sunny day in August 2014 (2nd and 3rd respectively).

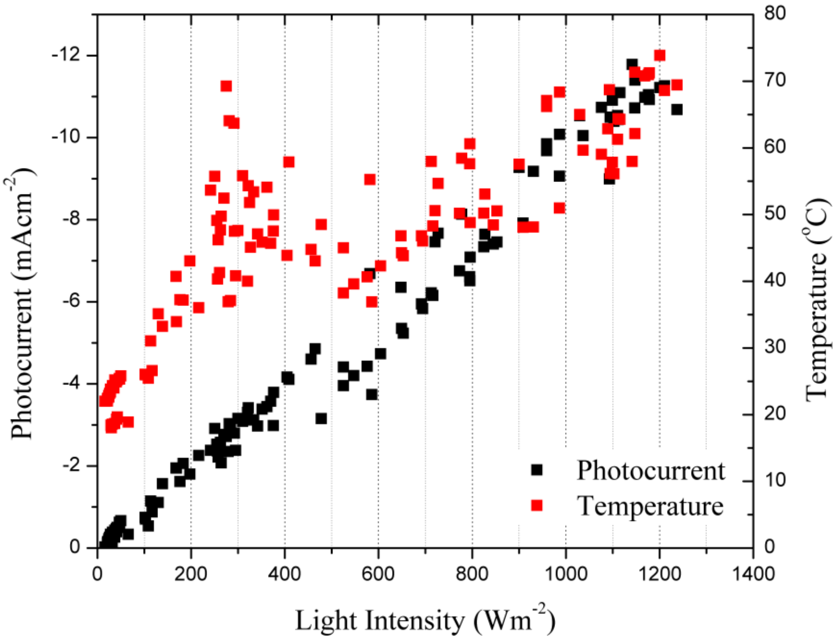

Figure 7.4 J_{sc} and Temperature as a function of light intensity for a sunny day (3/8/14).

As the maximum and average daily light intensity decreases over the course of the experiment from August to December 2014, as shown in **Figure 7.1**, the relative independence of the calculated *PCE, FF* and V_{oc} of the devices from light intensity means that it is possible to be confident in the values given in **7.4 OPV Device Lifetime** over the course of the experiment.

The analysis of the degradation of device operating parameters is studied at three different light intensity levels, 1000 Wm^{-2} (high), 500 Wm^{-2} (medium) and 250 Wm^{-2} (low) with a 5% margin of error in each case to increase the sample population. These intensity values were chosen to account for days where the maximum light intensity did not reach 1 Sun (1000W m^{-2}), which is the case for the latter half of the experiment, as can be seen from **Figure 7.1**.

7.2 Temperature Effects

A major issue with outdoor testing of OPVs is thermal cycling over the course of every day, especially for the setup used here due to the enclosed nature of the environmental chamber and the resulting high internal temperatures. High temperatures can cause thermal annealing of active layer materials in the device [9], and induce mechanical stresses due to different thermal expansion coefficients of the materials, which can lead to delamination at interfaces and device failure. Indeed, thermal cycling and its effects on OPV devices is such an important factor when calculating the real-world stability of OPV devices that it is the subject of its own ISOS testing protocol, ISOS-T [6]. Device temperatures for the 2nd August (cloudy day) and 3rd August (sunny day) days are shown in **Figure 7.5**.

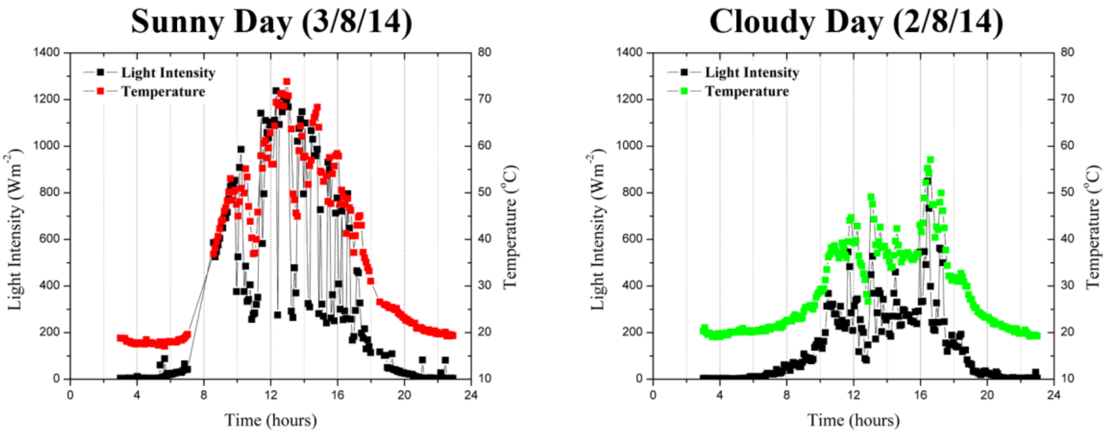

Figure 7.5 Variation in temperature for devices over the course of a cloudy day and a sunny day in August 2014 (2nd and 3rd respectively).

It can be seen that the temperature is highly dependent on light intensity due to the enclosed nature of the environmental chamber housing the OPV devices. For the sunny day shown here, the maximum temperature reached was 73.9°C with an average temperature of 36.5°C, and on the cloudy day the maximum temperature reached was 57.1^{o}C with an average temperature of 29.0^{o}C.

At temperatures below their glass transition temperature (T_g), polymers such as PFDT2BT-8 undergo thermal annealing. This has been shown to improve device performance in PCDTBT (a polymer that is similar in structure) by improving charge mobility in the polymer film [9], [10]. However, thermal annealing above the T_g can also induce phase separation of the materials in the active layer, resulting in a non-ideal morphology and a reduction in device performance. The T_g of PFDT2BT-8 has been shown to be ~ 70^{o}C [11].

In addition to this, device FF, V_{oc} and J_{sc} are affected by device temperature. Indeed, it has been shown that with increasing temperature, the V_{oc} of devices decreases, while the J_{sc} and FF increase [7], [8], [12].

The effects of thermal annealing during testing due to high chamber temperatures is extremely difficult to ascertain in this instance, as the devices were not removed from the environmental chamber for testing under the Newport solar simulator. However, the effects of average daily temperature on FF, V_{oc}, J_{sc}, and therefore PCE, are more easily explored.

The average daily temperature at high, medium and low light intensity are shown in **Figure 7.6**. It can be seen for all three light intensity levels the average temperature falls by 15 - 20^{o}C over the course of the experiment from August to December 2014. This likely introduces a temperature bias to the data shown, due to the aforementioned effects on FF, V_{oc}, J_{sc}, and therefore PCE. In other studies, it was calculated that temperature had an effect on the J_{sc} of OPVs of between 0.7 - 3.3 %/K [1], [12]. The effects this has on the measured JV characteristics of the devices under test here are discussed in more detail in **7.4 OPV Device Lifetime**.

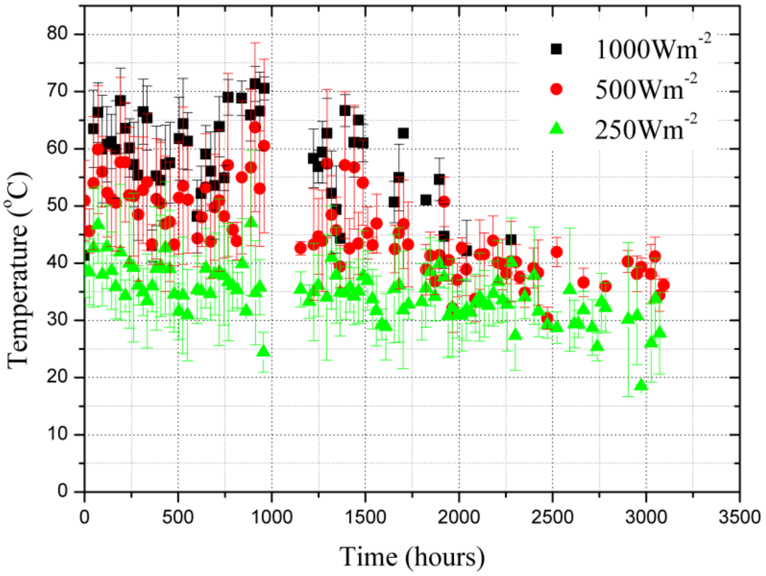

Figure 7.6 Average daily temperature recorded for three different light intensity levels; 1000 Wm^{-2}, 500 Wm^{-2} and 250 Wm^{-2}.

7.3 *JV* Characteristics

The four devices were based on the ITO/PEDOT:PSS/PFDT2BT-8:PC$_{70}$BM/Ca/Al architecture optimised in previous chapters. 30 nm thick PEDOT:PSS films were spin-coated and annealed in air, and 70 nm thick PFDT2BT-8:PC$_{70}$BM active layer films were spin-coated in the glovebox. The devices were fabricated, tested under the Newport solar simulator and placed in the rooftop testing setup on the same day. The average initial operating parameters for the four devices, as measured by the Newport solar simulator, are shown **Table 7.1**, and an average *JV* curve is shown in **Figure 7.7**. The data represents 16 pixels across four substrates where the worst 25% of pixels have been removed to account for gross film defects. The error quoted on all measurements is based on the standard deviation around the mean.

Device Type	**PCE (%)**	**FF**	**V_{oc} (V)**	**J_{sc} (mAcm^{-2})**
PEDOT:PSS **PFDT2BT-8**	5.4±0.1	63.0±0.8	0.83	-10.3±0.1

Table 7.1 Numerical average of initial device operating parameters as measured by the Newport solar simulator for the four devices in the rooftop testing setup.

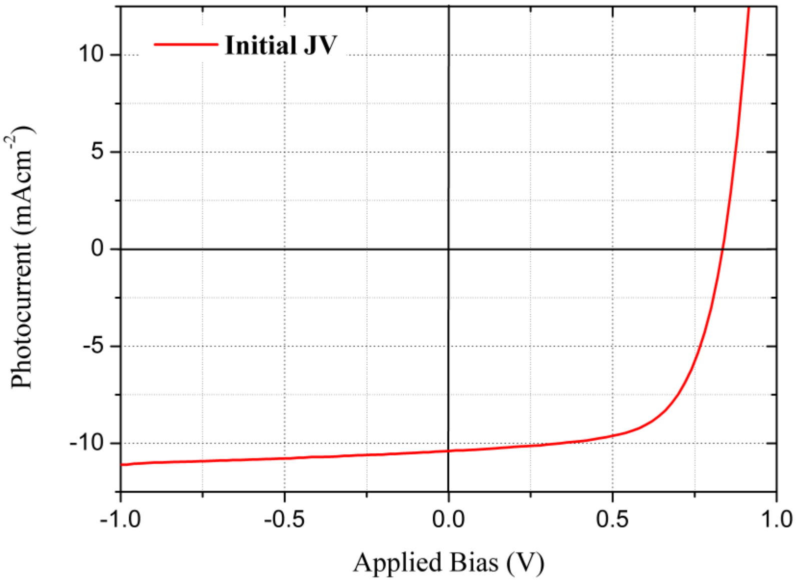

Figure 7.7 Numerically averaged initial *JV* curve for devices in the rooftop testing setup, averaged over all devices. Measured under the Newport solar simulator at 1000 Wm^{-2}.

7.4 OPV Device Lifetime

Daily average device operating parameters for the four devices in the rooftop testing system, with error bars representing standard deviation of the data, are shown in **Figure 7.8**.

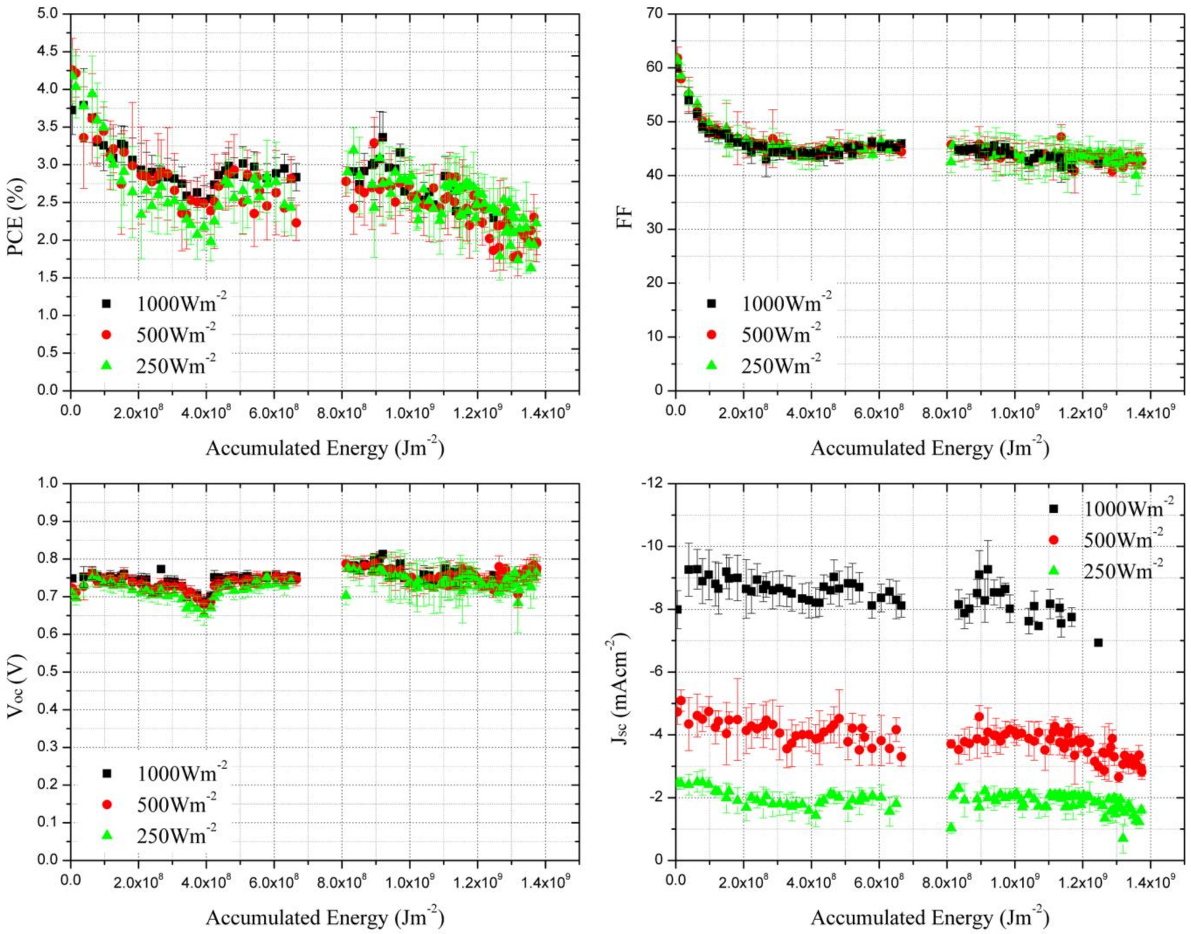

Figure 7.8 Average device operating parameters for four devices in the rooftop testing system as a function of accumulated energy (Jm^{-2}). Each data point represents the average and standard deviation from one day of testing

It can be seen that as with the device tested in the laboratory (see **5.2 Device Lifetime**), a large initial decrease in FF and J_{sc} is observed on burn-in (taken to end after 3.5×10^8 Jm^{-2} / 500 hours / 21 days), which then approaches a linear decay. V_{oc} remains relatively constant throughout, with an initial small decrease followed by recovery to a value higher than the starting V_{oc}. The behaviour of V_{oc} is believed to be due to a change in surface work function of PEDOT:PSS at the active layer interface on repeated charge transfer [13], [14].

After 1.25×10^{9} Jm^{-2} (4/11/14) the maximum light intensity did not reach 1000 Wm^{-2}, and so there are no data points for this light intensity level beyond this point.

Table 7.2 shows numerically averaged device operating parameters for all devices at ~ 500 Wm^{-2} at the start of the test on 1/8/14, and the end of the test, 8/12/14. **Figure 7.9** shows the corresponding *JV* curves. Comparative *JV* data at 1000 Wm^{-2} cannot be shown for the end of the test due to a lack of data at that light intensity.

	Light Intensity (Wm^{-2})	**Temperature (^{0}C)**	**PCE (%)**	**FF**	**V_{oc} (V)**	**J_{sc} ($mAcm^{-2}$)**
Initial (1/8/14)	499±13	54.7±0.4	4.77±0.05	63.8±0.6	0.73	-5.1±0.2
Final (8/12/14)	493±2	35.39±0.05	2.12±0.03	43.7±01	0.80	-2.97±0.03

Table 7.2 Initial and final average device operating parameters, light intensity and temperature for all devices.

Over the course of the test there is a loss of *PCE* of 56%, and the devices have a T_{80} lifetime of the order of 2500 hours (calculated using *PCE* data at 500 Wm^{-2} and 250 Wm^{-2} after the 18/9/14 (8×10^{8} Jm^{-2}) at which point the decay become relatively linear). This data seems to indicate that the devices are degrading far more quickly than the devices tested under laboratory conditions in **Chapter 5 : Hole Transport Layer Laboratory Lifetime Study**, which had a lifetime of 14500 hours. However, as the J_{sc}, V_{oc} and *FF* are all affected by temperature at which the measurement was taken, this introduces a large margin of error in the measurements of device characteristics over time. For this reason, any calculated T_{80}

lifetime is complicated by such large temperature variations. Therefore, it will be necessary to collect more data for the devices over a longer period of time, preferably a whole year, to allow for comparison of data taken at similar temperatures and light intensities as in previous studies, permitting a more accurate estimation of device lifetime to be made.

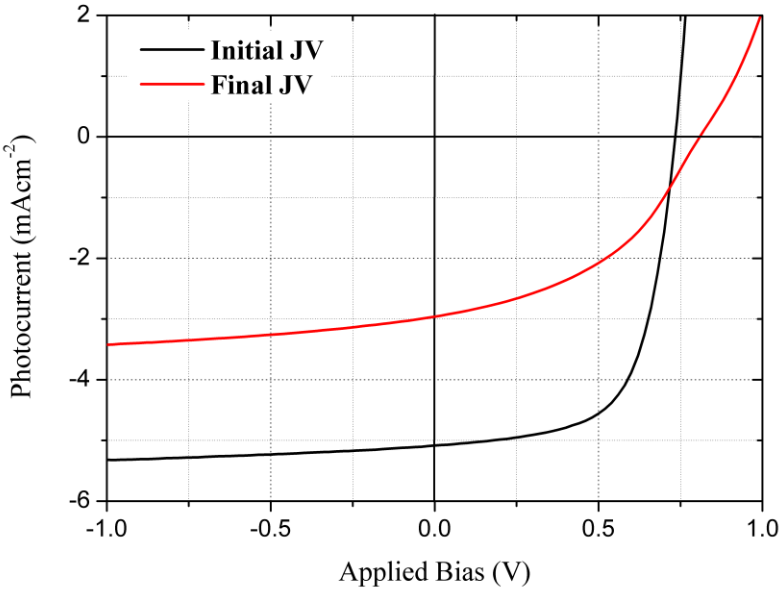

Figure 7.9 Average initial and final *JV* curves for all devices as measured at a light intensity of ~ 500 Wm^{-2}.

7.5 Conclusions

In summary, initial and preliminary measurements of the stability and degradation of OPV devices when tested outdoors under conditions closely modelled on the ISOS-O-2 test have been made. The effects of daily and seasonal light intensity and temperature variation on device performance are investigated, and have been shown to have a marked effect on the measurement of device *JV* characteristics. The effects of daily fluctuations in light intensity on *JV* characteristics have been observed, and it was shown that *FF* and V_{oc} are largely independent, though J_{sc} is extremely dependent on light intensity. T_{80} lifetimes of ~ 2500 hours are calculated, however, more data over a longer period is required to remove *JV* measurement bias introduced by seasonal variations in temperature. The test is currently ongoing, with plans to extend it up to one year to acquire the necessary data to make an accurate calculation of device T_{80} lifetime.

7.6 References

[1] S. A. Gevorgyan, M. V. Madsen, H. F. Dam, M. Jørgensen, C. J. Fell, K. F. Anderson, B. C. Duck, A. Mescheloff, E. A. Katz, A. Elschner, R. Roesch, H. Hoppe, M. Hermenau, M. Riede, and F. C. Krebs, "Interlaboratory outdoor stability studies of flexible roll-to-roll coated organic photovoltaic modules: Stability over 10,000h," *Sol. Energy Mater. Sol. Cells*, vol. 116, pp. 187–196, Sep. 2013.

[2] D. Angmo, P. M. Sommeling, R. Gupta, M. Hösel, S. A. Gevorgyan, J. M. Kroon, G. U. Kulkarni, and F. C. Krebs, "Outdoor Operational Stability of Indium-Free Flexible Polymer Solar Modules Over 1 Year Studied in India, Holland, and Denmark," *Adv. Eng. Mater.*, vol. 16, no. 8, pp. 976–987, Aug. 2014.

[3] J. A. Hauch, P. Schilinsky, S. A. Choulis, R. Childers, M. Biele, and C. J. Brabec, "Flexible organic P3HT:PCBM bulk-heterojunction modules with more than 1 year outdoor lifetime," *Sol. Energy Mater. Sol. Cells*, vol. 92, no. 7, pp. 727–731, Jul. 2008.

[4] R. R. Søndergaard, T. Makris, P. Lianos, A. Manor, E. A. Katz, W. Gong, S. M. Tuladhar, J. Nelson, R. Tuomi, P. Sommeling, S. C. Veenstra, A. Rivaton, A. Dupuis, G. Teran-Escobar, M. Lira-Cantu, S. B. Sapkota, B. Zimmermann, U. Würfel, A. Matzarakis, and F. C. Krebs, "The use of polyurethane as encapsulating method for polymer solar cells—An inter laboratory study on outdoor stability in 8 countries," *Sol. Energy Mater. Sol. Cells*, vol. 99, pp. 292–300, Apr. 2012.

[5] M. V. Madsen, S. A. Gevorgyan, R. Pacios, J. Ajuria, I. Etxebarria, J. Kettle, N. D. Bristow, M. Neophytou, S. A. Choulis, L. Stolz Roman, T. Yohannes, A. Cester, P. Cheng, X. Zhan, J. Wu, Z. Xie, W. C. Tu, J. H. He, C. J. Fell, K. Anderson, M. Hermenau, D.

Bartesaghi, L. Jan Anton Koster, F. Machui, I. González-Valls, M. Lira-Cantu, P. P. Khlyabich, B. C. Thompson, R. Gupta, K. Shanmugam, G. U. Kulkarni, Y. Galagan, A. Urbina, J. Abad, R. Roesch, H. Hoppe, P. Morvillo, E. Bobeico, E. Panaitescu, L. Menon, Q. Luo, Z. Wu, C. Ma, A. Hambarian, V. Melikyan, M. Hambsch, P. L. Burn, P. Meredith, T. Rath, S. Dunst, G. Trimmel, G. Bardizza, H. Müllejans, A. E. Goryachev, R. K. Misra, E. a. Katz, K. Takagi, S. Magaino, H. Saito, D. Aoki, P. M. Sommeling, J. M. Kroon, T. Vangerven, J. Manca, J. Kesters, W. Maes, O. D. Bobkova, V. a. Trukhanov, D. Y. Paraschuk, F. A. Castro, J. Blakesley, S. M. Tuladhar, J. Alexander Röhr, J. Nelson, J. Xia, E. A. Parlak, T. A. Tumay, H. J. Egelhaaf, D. M. Tanenbaum, G. Mae Ferguson, R. Carpenter, H. Chen, B. Zimmermann, L. Hirsch, G. Wantz, Z. Sun, P. Singh, C. Bapat, T. Offermans, and F. C. Krebs, “Worldwide outdoor round robin study of organic photovoltaic devices and modules,” *Sol. Energy Mater. Sol. Cells*, vol. 130, pp. 281–290, Nov. 2014.

[6] M. O. Reese, S. A. Gevorgyan, M. Jørgensen, E. Bundgaard, S. R. Kurtz, D. S. Ginley, D. C. Olson, M. T. Lloyd, P. Morvillo, E. A. Katz, A. Elschner, O. Haillant, T. R. Currier, V. Shrotriya, M. Hermenau, M. Riede, K. R. Kirov, G. Trimmel, T. Rath, O. Inganäs, F. Zhang, M. Andersson, K. Tvingstedt, M. Lira-Cantu, D. Laird, C. McGuiness, S. (Jimmy) Gowrisanker, M. Pannone, M. Xiao, J. Hauch, R. Steim, D. M. DeLongchamp, R. Rösch, H. Hoppe, N. Espinosa, A. Urbina, G. Yaman-Uzunoglu, J.-B. Bonekamp, A. J. J. M. van Breemen, C. Girotto, E. Voroshazi, and F. C. Krebs, “Consensus stability testing protocols for organic photovoltaic materials and devices,” *Sol. Energy Mater. Sol. Cells*, vol. 95, no. 5, pp. 1253–1267, May 2011.

[7] G. Garcia-Belmonte, “Temperature dependence of open-circuit voltage in organic solar cells from generation–recombination kinetic balance,” *Sol. Energy Mater. Sol. Cells*, vol. 94, no. 12, pp. 2166–2169, Dec. 2010.

[8] I. Riedel, J. Parisi, V. Dyakonov, L. Lutsen, D. Vanderzande, and J. C. Hummelen, “Effect of Temperature and Illumination on the Electrical Characteristics of Polymer–Fullerene Bulk-Heterojunction Solar Cells,” *Adv. Funct. Mater.*, vol. 14, no. 1, pp. 38–44, Jan. 2004.

[9] S. Cho, J. H. Seo, S. H. Park, S. Beaupré, M. Leclerc, and A. J. Heeger, “A thermally stable semiconducting polymer.,” *Adv. Mater.*, vol. 22, no. 11, pp. 1253–7, Mar. 2010.

[10] H. Yi, S. Al-Faifi, A. Iraqi, D. C. Watters, J. Kingsley, and D. G. Lidzey, “Carbazole and thienyl benzo[1,2,5]thiadiazole based polymers with improved open circuit voltages and processability for application in solar cells,” *J. Mater. Chem.*, vol. 21, no. 35, p. 13649, 2011.

[11] D. C. Watters, H. Yi, A. J. Pearson, J. Kingsley, A. Iraqi, and D. Lidzey, “Fluorene-based co-polymer with high hole mobility and device performance in bulk heterojunction organic solar cells.,” *Macromol. Rapid Commun.*, vol. 34, no. 14, pp. 1157–62, 2013.

[12] E. a. Katz, D. Faiman, S. M. Tuladhar, J. M. Kroon, M. M. Wienk, T. Fromherz, F. Padinger, C. J. Brabec, and N. S. Sariciftci, “Temperature dependence for the photovoltaic device parameters of polymer-fullerene solar cells under operating conditions,” *J. Appl. Phys.*, vol. 90, no. 10, p. 5343, 2001.

[13] C. Perlov, W. Jackson, C. Taussig, S. Mo, and S. R. Forrest, “A polymer / semiconductor write-once read-many-times memory,” vol. 426, no. November, pp. 2–5, 2003.

[14] R. A. Nawrocki, E. M. Galiger, D. P. Ostrowski, B. A. Bailey, X. Jiang, R. M. Voyles, N. Kopidakis, D. C. Olson, and S. E. Shaheen, “An inverted, organic WORM device based on PEDOT:PSS with very low turn-on voltage,” *Org. Electron.*, vol. 15, no. 8, pp. 1791–1798, Aug. 2014.

Chapter 8 : Solution Processed OPVs

In **Chapter 5 : Hole Transport Layer Laboratory Lifetime Study**, it was shown that utilising a PEDOT:PSS HTL resulted in devices having the highest device operational stability, and in **Chapter 6 : Polymer Air Processing** a PFDT2BT-8:$PC_{70}BM$ active layer was shown to have the highest *PCE* of all the polymers tested, and was extremely stable when processed in air. In this chapter, these materials were used, in addition to a solution processed titanium dioxide (TiO_x) electron transport layer (ETL), to fabricate OPV devices with an ITO/PEDOT:PSS/PFDT2BT-8:$PC_{70}BM/TiO_x$/Al architecture whose HTL, active layer and ETL were all processed in air from solution, having a maximum *PCE* of 5.35%.

8.0 Introduction

The electron transport layer (ETL) of OPV devices facilitates the transfer of electrons from the active layer to the anode as shown in **2.4.4 Charge Extraction**. A number of materials have been used as ETLs, including calcium, zinc oxide (ZnO) [1]–[3], caesium carbonate (CS_2CO_3) [4], [5], poly[(9,9-bis(3′-(N,N-dimethylamino)propyl)-2,7-fluorene)-alt-2,7-(9,9-dioctylfluorene)] (PFN) [6] and titanium oxide (TiO_x) [7]–[9].

All of the materials listed above (with the exception of calcium) can be processed from solution, allowing for manufacturing methods such as R2R processing and other large area solution based deposition techniques to scale up the production of OPVs. In addition, the replacement of calcium in OPV devices, which is highly reactive when exposed to water and oxygen, and is a known cause of OPV device degradation [10], promises an improvement in device lifetime.

Titanium oxide is a promising material for use in ETLs, as evidenced by its use as an electron acceptor and transport material in dye-sensitized cells [11]–[13], and has been shown to improve device efficiency for both standard and inverted device architectures in OPV devices [9]. Typically, in dye-sensitized solar cells, crystalline TiO_x is used, which requires high annealing temperatures ($T > 450^{o}C$) to form. However, these processing conditions are incompatible with OPV devices, as the polymer:$PC_{70}BM$ active layer cannot survive such high temperatures. Here, amorphous TiO_x ETL films were fabricated using a facile, solution based process with no annealing steps, for use in devices with an ITO/PEDOT:PSS/PFDT2BT-8:$PC_{70}BM/TiO_x$/Al architecture.

8.1 Titanium Oxide

Titanium Oxide (TiO_x) is a transition metal oxide that has been used as an electron transport layer and an optical spacer in OPVs [7]–[9]. It is commonly deposited from solution from a precursor of titanium isopropoxide, the structure of which is shown in **Figure 8.1.** This is then hydrolysed to form amorphous TiO_x. This process is very similar to the formation of vanadium oxide by hydrolysis, detailed in **5.1.2 Vanadium Oxide**.

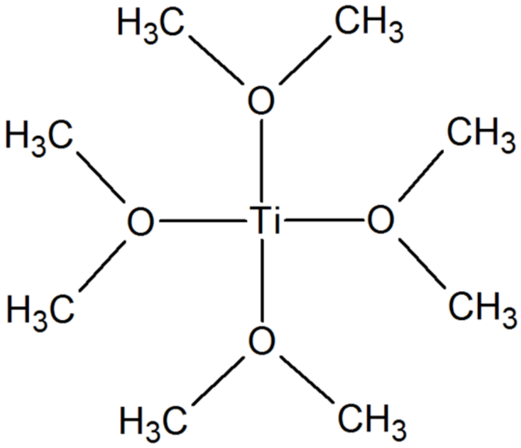

Figure 8.1 Chemical structure of titanium isopropoxide, $Ti[OCH(CH_3)_2]_4$.

The titanium isopropoxide precursor was purchased from Sigma-Aldrich and diluted in the organic solvent isopropyl alcohol (IPA, 99.999% pure) at a concentration of 10 $mgmL^{-1}$. Solution preparation was carried out in the glovebox to avoid hydrolysis of the precursor before spin-coating of the film, which occurs almost instantaneously in air, the chemical reaction of which is shown in **Equations 8.1** and **8.2**.

$$Ti[OCH(CH_3)_2]_4 + 4.H_2O \longrightarrow 4.C_3H_7OH + Ti(OH)_4 \qquad \textbf{Equation 8.1}$$

$$Ti(OH)_4 \longrightarrow TiO_2 + 2.H_2O \qquad \textbf{Equation 8.2}$$

In **Equation 8.1**, in the presence of water vapour, H^+ cations cleave the alkyl chain ($CH(CH_3)$) in the titanium isopropoxide precursor and bind to the singly bound oxygen on the titanium oxide, forming $Ti(OH)_4$. OH^- anions bind to the alkyl chain and produce isopropanol (C_3H_7OH), which evaporates. In **Equation 8.2**, the titanium intermediary molecules ($Ti(OH)_4$) react together, releasing water and form titanium oxide (TiO_2). However, due to the amorphous nature of the film, the oxidation state is likely to be less than TiO_2, and therefore the material will henceforth be referred to as TiO_x.

The titanium oxide precursor solution was spin-coated at 2000 rpm to form ~ 20 nm thick films as measured by a profilometer. These were left in air for 5 minutes to allow for the hydrolysis process to complete fully and form an amorphous and extremely smooth TiO_x layer. The films were not annealed, as it was found to result in devices having lower efficiency.

8.2 Solution Processed Devices

The development of methods and materials that allow high efficiency and stable devices to be fabricated using commercial deposition techniques, such as R2R printing and spray coating, is a key target for OPV manufacture. Vacuum deposition of materials is less attractive for commercial production of OPVs as the process is very energy intensive [14], and thus solution based processes offer distinct advantages. The most successful demonstration of this technology to date was carried out by Krebs et al [15]. Multi-layer OPVs based on an inverted

ITO/ZnO/P3HT:PCBM/PEDOT:PSS/Ag architecture were fabricated in one continuous process onto a flexible poly(ethyleneterephthalate) (PET) sheet, with all layers deposited using solution based techniques, and efficiencies of 2.3% achieved

Here, OPV devices were fabricated whose HTL, active layer, and ETL were all spin-coated from solution with the architecture: ITO/PEDOT:PSS(30nm)/PFDT2BT-8:$PC_{70}BM$(70nm)/TiO_x(20nm)/Al(100nm). The ITO anode was deposited by sputtering, and the aluminium top cathode thermally evaporated, as no solution based deposition methods were available. The devices were fabricated in both the glovebox and in air in the Lamarflo work station, and several types of devices were fabricated to isolate the effects on device performance of spin-coating the different layers in air. The active layers and TiO_x ETLs were either spin coated in air or in the glovebox, resulting in four device types: 'Fully Glovebox Processed', 'Active Layer Glovebox, TiO_x Air', 'Active Layer Air, TiO_x Glovebox' and 'Fully Air Processed'. In all cases the active layer and TiO_x layer for each device were spun sequentially, with a 30s spin time for each layer and with no delay in between depositions. This was done to minimize the air exposure of the active layer for air processed devices, and to emulate the fast deposition times that would be used in a commercial environment. Due to the orthogonal nature of the solvents used, there were no issues with films being re-dissolved by subsequent depositions. For all devices, the PEDOT:PSS HTL was spin-coated and then only annealed in air.

Average device operating parameters are shown in **Table 8.1** and *JV* curves in **Figure 8.2**. The data represents 12 pixels across three substrates where the worst 25% of pixels have been removed to account for gross film defect. The error quoted on all measurements is based on the standard deviation around the mean.

Device Type	PCE (%)	FF	V_{oc} (V)	J_{sc} ($mAcm^{-2}$)
Fully Glovebox Processed	6.0±0.2	63±2	0.91	-10.5±0.1
Active Layer Glovebox, TiO_x Air	5.7±0.2	64±1	0.91	-9.7±0.1
Active Layer Air, TiO_x Glovebox	5.9±0.2	62±1	0.91	-10.5±0.1
Fully Air Processed	5.3±0.1	60±1	0.91	-9.7±0.2

Table 8.1 Operating parameters for OPV devices whose active layers and TiO_x ETLs were spin-coated either in air or under nitrogen in the glovebox.

It can be seen that devices that were fully processed in the glovebox showed the highest device performance, with an average PCE of (6.0±0.2)% and a maximum PCE of 6.25%. On deposition of the active layer in air in "Active Layer Air, TiO_x Glovebox' devices achieved a PCE of (5.9±0.2)%, within error of the 'Fully Glovebox Processed' devices.

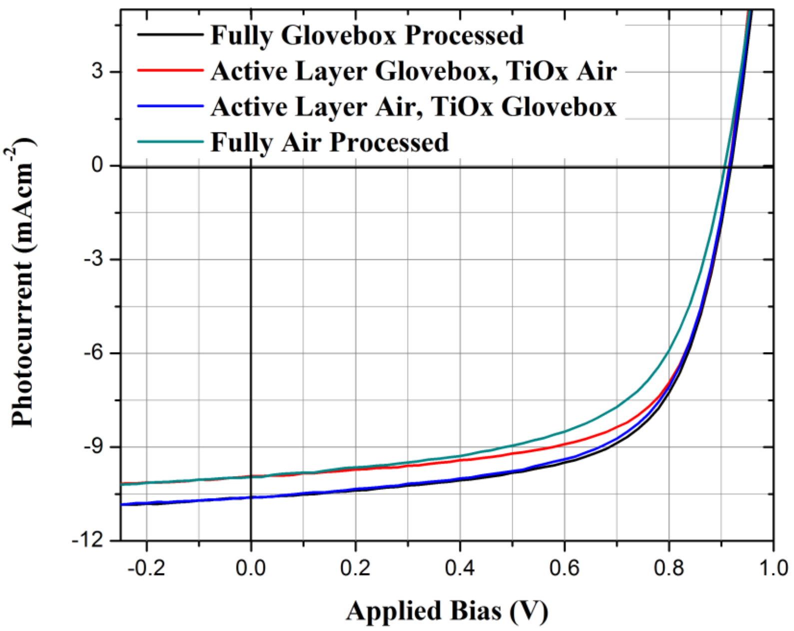

Figure 8.2 *JV* curves for 'Fully Glovebox Processed', 'Active Layer Glovebox, TiO_x Air', 'Active Layer Air, TiO_x Glovebox' and 'Fully Air Processed' OPV devices.

On spin-coating the TiO_x in air a reduction in J_{sc} is seen for both the 'Fully Air Processed' and the 'Active Layer Glovebox, TiO_x Air' devices. This is believed to be due to the extremely fast hydrolysation of the TiO_x in air. When the TiO_x precursor solution is spin-coated in the glovebox it forms a extremely smooth and clear film, which becomes translucent and white on exposure to air as the film hydrolyses and forms amorphous TiO_x. However, when the TiO_x precursor solution is spin-coated in air, the hydrolysation process occurs whilst the film is still drying, and the resulting film is far more opaque and white in colour. This appears to reduce the J_{sc} of the devices by altering the light absorption characteristics of the devices.

For the 'Fully Air Processed' devices, spin-coating both the active layer and the TiO_x ETL in air results in losses in J_{sc} due to the increased opacity of the TiO_x. The resulting devices have an average PCE of (5.3±0.1)%, a *PCE* loss of 12% compared to 'Fully Glovebox Processed' devices. This is a very promising result that shows that high efficiency devices can be processed in air from solution based materials with only a moderate loss in overall efficiency compared to glovebox processed devices.

For OPV devices utilising this architecture to be completely solution processed, both the ITO and metallic electrodes, which are currently deposited via sputtering and thermal evaporation processes respectively, need to be replaced with solution processed alternatives.

The deposition of ITO is a costly process, both due to the scarcity of indium and the energy intensive nature of sputtering techniques, and thermal evaporation of metallic electrodes has been shown to account for ~ 30% of energy input in the fabrication of OPV devices [14]. Solution processed alternatives to ITO include high conductivity PEDOT:PSS [16] and silver nanowires [17], with life-cycle analyses of these materials showing a potential reduction in module costs of up to 17% [18]. Screen printing [15], [19] and stamp-transfer [20] have been used to successfully replace thermal evaporation for top metal contacts in R2R manufacture.

Inclusion of these materials and processes in the devices fabricated in this chapter could yield high efficiency, low cost and air processable OPV modules compatible with R2R manufacturing processes. However, the effects of these materials and processes on device lifetime are as yet unknown.

8.3 Conclusions

In summary, the optimisation of a solution processed OPV device that utilised a PEDOT:PSS HTL, a PFDT2BT-8:$PC_{70}BM$ active layer and a TiO_x ETL has been explored. The effects on device performance of processing the active layer and ETL of the devices in a nitrogen filled glovebox or in air were studied. It was found that processing the active layer in air resulted in minor losses in FF, commensurate with previous findings, and processing the TiO_x ETL in air resulted in a more opaque film that resulted in J_{sc} losses. Devices that were processed in the glovebox had high initial PCEs of (6.0±0.2)%, whilst those processed in air had a reduced initial efficiency of (5.3±0.1)%.

8.4 References

[1] T. Yang, W. Cai, D. Qin, E. Wang, L. Lan, X. Gong, J. Peng, and Y. Cao, "Solution-Processed Zinc Oxide Thin Film as a Buffer Layer for Polymer Solar Cells with an Inverted Device Structure," *J. Phys. Chem. C*, vol. 114, no. 14, pp. 6849–6853, 2010.

[2] S. K. Hau, H.-L. Yip, N. S. Baek, J. Zou, K. O'Malley, and A. K.-Y. Jen, "Air-stable inverted flexible polymer solar cells using zinc oxide nanoparticles as an electron selective layer," *Appl. Phys. Lett.*, vol. 92, no. 25, p. 253301, 2008.

[3] Z. Liang, Q. Zhang, O. Wiranwetchayan, J. Xi, Z. Yang, K. Park, C. Li, and G. Cao, "Effects of the Morphology of a ZnO Buffer Layer on the Photovoltaic Performance of Inverted Polymer Solar Cells," *Adv. Funct. Mater.*, vol. 22, no. 10, pp. 2194–2201, May 2012.

[4] G. Li, C.-W. Chu, V. Shrotriya, J. Huang, and Y. Yang, "Efficient inverted polymer solar cells," *Appl. Phys. Lett.*, vol. 88, no. 25, p. 253503, 2006.

[5] H.-H. Liao, L.-M. Chen, Z. Xu, G. Li, and Y. Yang, "Highly efficient inverted polymer solar cell by low temperature annealing of Cs[sub 2]CO[sub 3] interlayer," *Appl. Phys. Lett.*, vol. 92, no. 17, p. 173303, 2008.

[6] Z. He, C. Zhong, S. Su, M. Xu, H. Wu, and Y. Cao, "Enhanced power-conversion efficiency in polymer solar cells using an inverted device structure," *Nat. Photonics*, vol. 6, no. 9, pp. 593–597, Aug. 2012.

[7] S. Chambon, E. Destouesse, B. Pavageau, L. Hirsch, and G. Wantz, "Towards an understanding of light activation processes in titanium oxide based inverted organic solar cells," *J. Appl. Phys.*, vol. 112, no. 9, p. 094503, 2012.

[8] C. Waldauf, M. Morana, P. Denk, P. Schilinsky, K. Coakley, S. a. Choulis, and C. J. Brabec, “Highly efficient inverted organic photovoltaics using solution based titanium oxide as electron selective contact,” *Appl. Phys. Lett.*, vol. 89, no. 23, p. 233517, 2006.

[9] J. Y. Kim, S. H. Kim, H.-H. Lee, K. Lee, W. Ma, X. Gong, and A. J. Heeger, “New Architecture for High-Efficiency Polymer Photovoltaic Cells Using Solution-Based Titanium Oxide as an Optical Spacer,” *Adv. Mater.*, vol. 18, no. 5, pp. 572–576, Mar. 2006.

[10] M. T. Lloyd, D. C. Olson, P. Lu, E. Fang, D. L. Moore, M. S. White, M. O. Reese, D. S. Ginley, and J. W. P. Hsu, “Impact of contact evolution on the shelf life of organic solar cells,” *J. Mater. Chem.*, vol. 19, no. 41, p. 7638, 2009.

[11] B. O’Regan and M. Gratzel, “A low-cost, high-efficiency solar cell based on dye-sensitized colloidal TiO2 films,” *Nature*, vol. 353, no. 6346, pp. 737–740, Oct. 1991.

[12] U. Bach, D. Lupo, P. Comte, J. E. Moser, F. Weissortel, J. Salbeck, H. Spreitzer, and M. Gratzel, “Solid-state dye-sensitized mesoporous TiO2 solar cells with high photon-to-electron conversion efficiencies,” *Nature*, vol. 395, no. 6702, pp. 583–585, Oct. 1998.

[13] J. R. Durrant, J. Nelson, and D. R. Klug, “Functionalising nanocrystalline TiO2 films: dye sensitised solar cells and optical biosensors,” *Materials Science and Technology*, vol. 16, no. December. pp. 1345–1348, 2000.

[14] R. García-Valverde, J. a. Cherni, and A. Urbina, “Life cycle analysis of organic photovoltaic technologies,” *Prog. Photovoltaics Res. Appl.*, vol. 18, no. April, pp. 535–538, 2010.

[15] F. C. Krebs, S. A. Gevorgyan, and J. Alstrup, “A roll-to-roll process to flexible polymer solar cells: model studies, manufacture and operational stability studies,” *J. Mater. Chem.*, vol. 19, no. 30, p. 5442, 2009.

[16] S. I. Na, B. K. Yu, S. S. Kim, D. Vak, T. S. Kim, J. S. Yeo, and D. Y. Kim, “Fully spray-coated ITO-free organic solar cells for low-cost power generation,” *Sol. Energy Mater. Sol. Cells*, vol. 94, no. 8, pp. 1333–1337, 2010.

[17] D.-S. Leem, A. Edwards, M. Faist, J. Nelson, D. D. C. Bradley, and J. C. de Mello, “Efficient organic solar cells with solution-processed silver nanowire electrodes.,” *Adv. Mater.*, vol. 23, no. 38, pp. 4371–5, Oct. 2011.

[18] C. J. M. Emmott, A. Urbina, and J. Nelson, “Environmental and economic assessment of ITO-free electrodes for organic solar cells,” *Sol. Energy Mater. Sol. Cells*, vol. 97, pp. 14–21, Feb. 2012.

[19] D. Angmo, T. T. Larsen-olsen, and F. C. Krebs, “Roll-to-roll fabrication of polymer solar cells As the performance in terms of power conversion efficiency and operational,” *Mater. Today*, vol. 15, no. 1, pp. 36–49, 2012.

[20] X. Wang, T. Ishwara, W. Gong, M. Campoy-Quiles, J. Nelson, and D. D. C. Bradley, “High-performance metal-free solar cells using stamp transfer printed vapor phase polymerized poly(3,4-ethylenedioxythiophene) top anodes,” *Adv. Funct. Mater.*, vol. 22, pp. 1454–1460, 2012.

Chapter 9 : Conclusions

9.0 Conclusions of Work Undertaken

The development of R2R processing of organic photovoltaics has opened up the possibility of commercial scale production, with printing speeds of several kilometres an hour possible using existing technology. Unlike many forms of inorganic PV, which need to be fabricated onto ultra-pure crystalline substrates, OPVs can be fabricated onto amorphous substrate materials, including flexible plastics such as PET [1], [2]. This not only lowers the costs of manufacture, but also the embodied energy cost of the devices themselves.

However, although the printing technology is available, and several pilot R2R studies have produced promising results [3], [4], there are several challenges inherent in OPV technology that will need to be overcome before commercialization is possible. Low efficiencies and operating lifetimes, in comparison to the more established inorganic photovoltaic technologies, are issues that can only partially be compensated for by lower manufacturing costs and embodied energy.

Improvements in initial device efficiencies have been achieved with the introduction of a new generation of donor polymers, such as PCDTBT, with low lying HOMO levels [5]. Studies have explored PCDTBT device stability and degradation pathways [6]–[8] and have concluded that polycarbazole polymers have a high degree of photostability [9], and can be used to create devices having extended operational lifetimes [6]. However, the stability of OPV devices is limited by the oxygen and moisture sensitivity of the materials used. To overcome this, oxygen and moisture free manufacturing environments such as gloveboxes, and high-grade encapsulation systems with very low moisture and oxygen ingress rates are often used. Unfortunately, these manufacturing processes are expensive and energy intensive, and alternatives need to be found to allow for OPV technology to be financially competitive with silicon PV.

Throughout this work, the overarching theme was the study of OPV materials with the aim of processing in air with little or no reduction in initial efficiency and operating lifetime. Both active layer materials and interlayer materials were studied in detail, with the aim of identifying materials that are air stable and result in high efficiency devices with long operating lifetimes.

In **Chapter 4**, the effects on OPV device performance of exposure of MoO_x HTLs to air was studied. Ellipsometry measurements showed that air exposure resulted in a swelling of the MoO_x films on adsorption of water that was detrimental to device efficiency. However by applying an initial thermal anneal to the MoO_x film, this uptake of water could be partially suppressed; a process that was shown to result from film densification. This result was then used to fabricate OPV devices based on a blend of PCDTBT:$PC_{70}BM$, with the active semiconductor layer spin cast in air. Such air-processed devices had an average value for *PCE* that was significantly larger than that of devices that were fabricated inside a nitrogen-filled glovebox. This promising result suggested that the active layers of a polymer photovoltaic device could be fabricated using an air-based processing route. These results were used in later chapters to investigate the air stability of various donor polymers and the operational lifetime of devices with different HTLs.

Chapter 5 presented a study of the operational lifetime of OPV devices utilising three different HTL materials; MoO_x, PEDOT:PSS and V_2O_x. The OPV devices were tested using a laboratory weathering test conforming to the ISOS-L-1 testing standards [10] for 620 hours of constant illumination. It was shown that OPV devices utilising a PEDOT:PSS HTL had higher stability than comparable devices using a MoO_x or V_2O_x HTLs, with extrapolated T_{80} lifetimes for devices utilising a PEDOT:PSS HTL being 14,500 hours (comparable to 7.2 years of outdoor use). These experiments demonstrated that the rate of degradation of the device metrics is a significant function of the nature of the HTL material; a result that confirms that degradation in the active layer does not completely account for the observed reduction in device performance. Rather, the changes in FF, J_{sc}, and V_{oc} that were observed during both burn-in and subsequent linear decay must also result from the formation of additional trap states at the interface between the active layer and the hole transport layers, due to generation of structural and electronic defects [7], as shown in both LBIC and ELM images of the devices after ageing. The identification of PEDOT:PSS as a stable HTL material was key to the work in the following chapters.

In **Chapter 6**, five donor polymer materials were used to study the effects of air processing on initial device efficiency. The results suggest that carbazole and fluorene based conjugated polymers have a relatively high degree of photostability that permit them to be processed (in a polymer:fullerene blend) into the active layer of a photovoltaic device in air with little loss in *PCE*. Indeed, in some cases, devices processed in air had an enhanced efficiency compared with comparable devices processed under nitrogen; an affect that was attributed to changes in the work function of the underlying PEDOT:PSS anode. It was hypothesised however that the absorption of a small quantity of water by the PEDOT:PSS anode may result in reduced operational stability of devices over extended time periods. In addition, PFDT2BT-8:$PC_{70}BM$ active layers were shown to be stable in air for up to 5 minutes during the device run with little loss in device performance. This timeframe is commensurate with processing timeframes for R2R processing, indicating that PFDT2BT-8 is a promising polymer for such manufacturing processes.

In **Chapter 7**, the stability and degradation of OPV devices when tested outdoors under conditions closely modelled on the ISOS-O-2 outdoor test were studied. The effects of daily and seasonal light intensity and temperature variation on device performance were investigated, and were shown to have a marked effect on the measurement of device *JV* characteristics. The effects of daily fluctuations in light intensity on *JV* characteristics were observed, and it was shown that *FF* and V_{oc} are largely independent, though J_{sc} is extremely dependent on light intensity. T_{80} lifetimes of ~ 2500 hours were calculated, however, it is clear that more data recorded over a longer period is required to remove *JV* measurement bias introduced by seasonal variation in temperature.

In the final results section of this thesis, **Chapter 8**, the optimisation of a solution processed OPV device that utilised a PEDOT:PSS HTL, a PFDT2BT-8:$PC_{70}BM$ active layer and a TiO_x ETL was explored. The effects on device performance of processing the active layer and ETL of the devices in the glovebox or in air were studied. It was found that processing the active layer in air resulted in minor losses in *FF*, commensurate with previous findings, with processing the TiO_x ETL in air resulting in a more opaque film that resulted in J_{sc} losses. Devices that were processed in the glovebox had high initial *PCE*s of (6.0±0.2)%, whilst those processed in air had a reduced initial efficiency of (5.3±0.1)%. This promising result suggests that it is possible to achieve high initial efficiencies for OPV devices whose active layers and interlayers have been processed from solution in air - a key requirement for R2R processing.

9.1 Suggestions for Further Work

The work presented in this thesis provides some insight into the suitability of several commonly used OPV materials to be processed in air into devices having long operating lifetimes. However, additional work is required to further the understanding of the mechanisms of some of the effects observed.

In **Chapter 4**, the effects of thermal annealing treatments and air exposure on MoO_x were discussed. Obtaining valid XPS and UPS results would also shed light on the mechanism that causes the change in device performance, and how adsorbed moisture affects the structure, stoichiometry, and energy levels of MoO_x. Performing lifetime tests on OPV devices whose MoO_x HTLs had undergone different thermal treatments and air exposure protocols would shed light on the effects of air exposure and adsorbed moisture on device lifetime. Other forms of MoO_x would also benefit from study, as several solution based processing methods have been developed for this material [11]–[14], which would be more compatible with commercial fabrication processes.

For the lifetime study reported in **Chapters 5**, the degradation processes caused by the different HTL materials warrant a detailed investigation to identify the underlying mechanisms. This could be achieved by characterisation using LBIC and ELM imaging both before, during and after lifetime testing. Other techniques, such as FIB/TEM cross sections of devices could be used to identify and track the formation of defects. The understanding and minimising the causes of device degradation is imperative for the development of commercially viable devices with long operating lifetimes.

In **Chapter 6**, identifying the mechanism by which the polymers are oxygen doped under illumination would allow for the design of new polymers specifically designed to be air stable and appropriate for use in R2R fabrication.

The ongoing outdoor lifetime study detailed in **Chapter 7** is planned to continue until August 2015, at which point it will be possible to extrapolate device lifetime without complicating temperature effects. Outdoor studies are key to the understanding the real world stability of OPVs, as our measurements using conventional solar simulators indicate that additional degradation pathways result from fluctuations in temperature and light intensity.

A natural progression of the research presented in this thesis is the development of fully air and solution processed devices. In **Chapter 8**, devices whose HTL, ETL and active layer were all solution processed in air were fabricated and achieved a high *PCE* of > 5%. However, the use of an isopropoxide precursor for the TiO_x is likely to be a cause of device stability issues, due to the action of the precursor material on the active layer causing damage and leading to device degradation [15]. A detailed lifetime study of these devices is needed to identify the sensitivity of the polymer to the precursor material, and if appropriate identify other synthetic techniques to produce TiO_x ETL layers that do not impact on device stability. In addition to this, the development of solution processed anode and cathode materials is needed to allow for devices to be processed entirely from solution, and therefore be compatible with R2R (a result demonstrated in other studies [3], [16] using screen printing techniques). Preliminary experiments were carried out investigating a solution processable aluminium nano-particle suspension deposited by spray coating. However, the solvents used in the suspension were not compatible with the underlying materials, and dissolved the entire structure.

9.2 References

[1] S. R. Dupont, M. Oliver, F. C. Krebs, and R. H. Dauskardt, “Interlayer adhesion in roll-to-roll processed flexible inverted polymer solar cells,” *Sol. Energy Mater. Sol. Cells*, vol. 97, pp. 171–175, Feb. 2012.

[2] G. Terán-Escobar, J. Pampel, J. M. Caicedo, and M. Lira-Cantú, “Low-temperature, solution-processed, layered V2O5 hydrate as the hole-transport layer for stable organic solar cells,” *Energy Environ. Sci.*, vol. 6, no. 10, p. 3088, 2013.

[3] F. C. Krebs, S. A. Gevorgyan, and J. Alstrup, “A roll-to-roll process to flexible polymer solar cells: model studies, manufacture and operational stability studies,” *J. Mater. Chem.*, vol. 19, no. 30, p. 5442, 2009.

[4] D. Angmo, P. M. Sommeling, R. Gupta, M. Hösel, S. A. Gevorgyan, J. M. Kroon, G. U. Kulkarni, and F. C. Krebs, “Outdoor Operational Stability of Indium-Free Flexible Polymer Solar Modules Over 1 Year Studied in India, Holland, and Denmark,” *Adv. Eng. Mater.*, vol. 16, no. 8, pp. 976–987, Aug. 2014.

[5] N. Blouin, A. Michaud, and M. Leclerc, “A Low-Bandgap Poly(2,7-Carbazole) Derivative for Use in High-Performance Solar Cells,” *Adv. Mater.*, vol. 19, no. 17, pp. 2295–2300, Sep. 2007.

[6] C. H. Peters, I. T. Sachs-Quintana, J. P. Kastrop, S. Beaupré, M. Leclerc, and M. D. McGehee, “High Efficiency Polymer Solar Cells with Long Operating Lifetimes,” *Adv. Energy Mater.*, vol. 1, no. 4, pp. 491–494, Jul. 2011.

[7] E. Voroshazi, I. Cardinaletti, T. Conard, and B. P. Rand, “Light-Induced Degradation of Polymer:Fullerene Photovoltaic Devices: An Intrinsic or Material-Dependent Failure Mechanism?,” *Adv. Energy Mater.*, Aug. 2014.

[8] C. H. Peters, I. T. Sachs-Quintana, W. R. Mateker, T. Heumueller, J. Rivnay, R. Noriega, Z. M. Beiley, E. T. Hoke, A. Salleo, and M. D. McGehee, “The mechanism of burn-in loss in a high efficiency polymer solar cell,” *Adv. Mater.*, vol. 24, no. 5, pp. 663–668, Feb. 2012.

[9] E. Bovill, H. Yi, A. Iraqi, and D. G. Lidzey, “The fabrication of polyfluorene and polycarbazole-based photovoltaic devices using an air-stable process route,” *Appl. Phys. Lett.*, vol. 105, no. 22, p. 223302, Dec. 2014.

[10] M. O. Reese, S. A. Gevorgyan, M. Jørgensen, E. Bundgaard, S. R. Kurtz, D. S. Ginley, D. C. Olson, M. T. Lloyd, P. Morvillo, E. A. Katz, A. Elschner, O. Haillant, T. R. Currier, V. Shrotriya, M. Hermenau, M. Riede, K. R. Kirov, G. Trimmel, T. Rath, O. Inganäs, F. Zhang, M. Andersson, K. Tvingstedt, M. Lira-Cantu, D. Laird, C. McGuiness, S. (Jimmy) Gowrisanker, M. Pannone, M. Xiao, J. Hauch, R. Steim, D. M. DeLongchamp, R. Rösch, H. Hoppe, N. Espinosa, A. Urbina, G. Yaman-Uzunoglu, J.-B. Bonekamp, A. J. J. M. van Breemen, C. Girotto, E. Voroshazi, and F. C. Krebs, “Consensus stability testing protocols for organic photovoltaic materials and devices,” *Sol. Energy Mater. Sol. Cells*, vol. 95, no. 5, pp. 1253–1267, May 2011.

[11] T. Stubhan, T. Ameri, M. Salinas, J. Krantz, F. Machui, M. Halik, and C. J. Brabec, “High shunt resistance in polymer solar cells comprising a MoO[sub 3] hole extraction layer processed from nanoparticle suspension,” *Appl. Phys. Lett.*, vol. 98, no. 25, p. 253308, 2011.

[12] C. Girotto, E. Voroshazi, D. Cheyns, P. Heremans, and B. P. Rand, “Solution-processed MoO_3 thin films as a hole-injection layer for organic solar cells.,” *ACS Appl. Mater. interfaces*, vol. 3, no. 9, pp. 3244–7, 2011.

[13] F. Liu, S. Shao, X. Guo, Y. Zhao, and Z. Xie, “Efficient polymer photovoltaic cells using solution-processed MoO3 as anode buffer layer,” *Sol. Energy Mater. Sol. Cells*, vol. 94, no. 5, pp. 842–845, May 2010.

[14] S. Murase and Y. Yang, “Solution processed MoO3 interfacial layer for organic photovoltaics prepared by a facile synthesis method.,” *Adv. Mater.*, vol. 24, no. 18, pp. 2459–62, May 2012.

[15] K. Zilberberg, S. Trost, J. Meyer, A. Kahn, A. Behrendt, D. Lützenkirchen-Hecht, R. Frahm, and T. Riedl, “Inverted Organic Solar Cells with Sol-Gel Processed High Work-Function Vanadium Oxide Hole-Extraction Layers,” *Adv. Funct. Mater.*, vol. 21, no. 24, pp. 4776–4783, Dec. 2011.

[16] S. A. Gevorgyan, M. V. Madsen, H. F. Dam, M. Jørgensen, C. J. Fell, K. F. Anderson, B. C. Duck, A. Mescheloff, E. A. Katz, A. Elschner, R. Roesch, H. Hoppe, M. Hermenau, M. Riede, and F. C. Krebs, “Interlaboratory outdoor stability studies of flexible roll-to-roll coated organic photovoltaic modules: Stability over 10,000h,” *Sol. Energy Mater. Sol. Cells*, vol. 116, pp. 187–196, Sep. 2013.

Appendix

MATLAB Code for Laboratory Lifetime Testing System

```
close all
clear all
clear global
clc

%%%%%%%%%%%%%%%%%%%%%%%%%%%%%%%%%%%%%%%%%%%%%%%%%%%%%%%%%%%%%%%%%%%%%%%%%%
%user variables
%%%%%%%%%%%%%%%%%%%%%%%%%%%%%%%%%%%%%%%%%%%%%%%%%%%%%%%%%%%%%%%%%%%%%%%%%%

batch='OPV140611';
base_directory='C:\Users\Lifetime Tester PC\Desktop\Users\Ed\Thesis Calibration\6 LT LT Board K2400 Left Wall LT Computer';

%Set number of repeats (through all devices) and delay between repeats (s)
%NOTE: Measurement takes ~120s per device (normal accuracy) ~1000s for all
%8, including the time it takes to take PD and Temp measurements.
%e.g. measuring 8 devices, 30min delay between measurements = 800s delay
repeats=1;               %repeated measurements of all devices that are being tested
delay_between_repeats=0;    %in seconds
delay_between_devices=0;    %in seconds

start_device=1; %Device number to start testing (populate board from this number)
end_device=8;   %Device number to stop testing at(populate board up to this number)

start_pixel=1;  %Program will start testing from this pixel
end_pixel=6;    %and finish with this pixel (1-6 only)

%New sytle substrates (single anode, pixellated cathode)
%device_area=0.02606;   %cm^2 - New substrate, 6 pixel 'legless' version with mask. APETURE MASK #2!
device_area=0.0400;   %cm^2 - New substrate, 6 pixel 'legless' version without mask

%Old style substrates (single cathode, pixellated cathode)
%device_area=0.0212; %cm^2 0.0212 for standard 6 pixel with aperature mask
%device_area=0.048; %cm^2 - for standard 6 pixel without apeture mask (0.048 = corrected area, 0.045 = original area)
%device_area=0.0400;   %cm^2 - New substrate, 6 pixel 'legless' version without mask

%Device architecture.
%For Pixellated Cathode Substrate (new style) Board use 1 for normal and 0 for inverted
%For Pixellated Anode Substrate (old style) Board use 0 for normal and 1 for inverted
inverted1=1;
inverted2=1;
inverted3=1;
```

```
inverted4=1;
inverted5=1;
inverted6=1;
inverted7=1;
inverted8=1;

%Device state in between measurements.
%NOTE: Only pixels selected below will be shorted
%0 = Open circuit
%1 = Short Circuit

Device1=0;
Device2=0;
Device3=0;
Device4=0;
Device5=0;
Device6=0;
Device7=0;
Device8=0;

%Pixel state in between measurements (will be the same for all devices that are shorted)
%0 = Open circuit
%1 = Short Circuit

Pixel1=0;
Pixel2=0;
Pixel3=0;
Pixel4=0;
Pixel5=0;
Pixel6=0;


high_accuracy=0; %use if you want high accuracy measurements (will take between 2x and 10x
longer)
%this will put the K2400 on autorange, increase the settle time and GPIB timeout

%Dev Number for USB Board

%dev_number='Dev1';
dev_number='LTE';
%dev_number='LTE';
%%%%%%%%%%%%%%%%%%%%%%%%%%%%%%%%%%%%%%%%%%%%%%%%%%%%%%%%%%%%%%%%%%%%%%%%%%%%%%%%%%%
%%%%%%%%%%%%%%%%%%%%%%%%%%%%%%%%%%%%%%%%%%%%%%%%%%%%%%%%%%%%%%%%%%%%%%%%%%%%%%%%%%%
%%%%%%%%%%%%%%%%%%%%%%%%%%%%%%%%%%%%%%%%%%%%%%%%%%%%%%%%%%%%%%%%%%%%%%%%%%%%%%%%%%%
%%%%%%%%%%%%%%%%%%MATLAB SCRIPT BELOW - DO NOT  EDIT%%%%%%%%%%%%%%%%%%%%%%
%%%%%%%%%%%%%%%%%%%%%%%%%%%%%%%%%%%%%%%%%%%%%%%%%%%%%%%%%%%%%%%%%%%%%%%%%%%%%%%%%%%
%%%%%%%%%%%%%%%%%%%%%%%%%%%%%%%%%%%%%%%%%%%%%%%%%%%%%%%%%%%%%%%%%%%%%%%%%%%%%%%%%%%
%%%%%%%%%%%%%%%%%%%%%%%%%%%%%%%%%%%%%%%%%%%%%%%%%%%%%%%%%%%%%%%%%%%%%%%%%%%%%%%%%%%
%%%%%%%%%%%%%%%%%%%%%%%%%%%%%%%%%%%%%%%%%%%%%%%%%%%%%%%%%%%%%%%%%%%%%%%%%%%%%%%%%%%


%set up the inverter array for either normal or inverted operation
inverter=1;
inverted_array=[inverted1,inverted2,inverted3,inverted4,inverted5,inverted6,inverted7,inverted
8];

%%%%%%%%%%%%%%%%%%%%%%%%%%%%%%%%%%%%%%%%%%%%%%%%%%%%%%%%%%%%%%%%%%%%%%%%%%%%%%%%%%%
%Create Sub Directories for devices 1-8, Photodiodes and Thermometers
```

```
%%%%%%%%%%%%%%%%%%%%%%%%%%%%%%%%%%%%%%%%%%%%%%%%%%%%%%%%%%%%%%%%%%%%%%%%%%

for device=1:8

    sub_directory=[base_directory,'\D', num2str(device)];
    if exist(sub_directory,'dir')~=7
        mkdir(sub_directory);
        display(['making directory ', sub_directory]);
    else
        display('directory already exists');
    end

end

sub_directory=[base_directory,'\PD'];
if exist(sub_directory,'dir')~=7
    mkdir(sub_directory);
    display(['making directory ', sub_directory]);
else
    display('directory already exists');
end

sub_directory=[base_directory,'\T'];
if exist(sub_directory,'dir')~=7
    mkdir(sub_directory);
    display(['making directory ', sub_directory]);
else
    display('directory already exists');
end

%%%%%%%%%%%%%%%%%%%%%%%%%%%%%%%%%%%%%%%%%%%%%%%%%%%%%%%%%%%%%%%%%%%%%%%%%%
%Initialise USB Interface and set all values to 0
%%%%%%%%%%%%%%%%%%%%%%%%%%%%%%%%%%%%%%%%%%%%%%%%%%%%%%%%%%%%%%%%%%%%%%%%%%

[USB6501, USB6501_outputs]=Initialise_USB6501(dev_number);

%%%%%%%%%%%%%%%%%%%%%%%%%%%%%%%%%%%%%%%%%%%%%%%%%%%%%%%%%%%%%%%%%%%%%%%%%%
%Set up Keithley Interface
%%%%%%%%%%%%%%%%%%%%%%%%%%%%%%%%%%%%%%%%%%%%%%%%%%%%%%%%%%%%%%%%%%%%%%%%%%

K2400_GPIB_address=10; % Keithley 2400 GPIB Address
initial_settle_time=0.25;

if high_accuracy==1;
    %Set very long timeout as measurements are slow
    GPIB_timeout=300;%seconds
    %set long settle time
    settle_time=0.2;%seconds
else
    %set normal timeout
    GPIB_timeout=300;%seconds
    %set normal settle time
    settle_time=0.02;%seconds
end


%Create the GPIB object for talking to the K2400
K2400 = gpib('ni',0,K2400_GPIB_address);
```

```
%set the interface mode
set(K2400,'EOSMode','read&write');
%set the end of line characters
set(K2400,'EOSCharCode','LF');
%set timeout
set(K2400,'Timeout',GPIB_timeout);

set(K2400, 'InputBufferSize', 20000);
set(K2400, 'OutputBufferSize', 20000);

%open the interface
fopen(K2400);

%Restore GPIB defaults
fprintf(K2400,':*RST')
%Clear buffer
fprintf(K2400,':TRAC:CLE')




%%%%%%%%%%%%%%%%%%%%%%%%%%%%%%%%%%%%%%%%%%%%%%%%%%%%%%%%%%%%%%%%%%%%%%%%%%
%%%%%%%%%%%%%%%%%%%%%%%%%%%%%%%%%%%%%%%%%%%%%%%%%%%%%%%%%%%%%%%%%%%%%%%%%%
%initiate all the data arrays to the correct size. This is not in general
%necessary with matlab but it does mean that we can run 1 individual pixel and the data
%formatting for the output to file remains the same which is useful.

Efficiency(6)=0;
FF(6)=0;
Jsc(6)=0;
Voc(6)=0;
max_power(6)=0;
Vmpp(6)=0;
Jmpp(6)=0;
PD(8)=0;
T(4)=0;
current_density(101,6)=0;


tic



for repeat=1:repeats


    disp('********************************')
    disp('********************************')
    disp(['Repeat ', num2str(repeat), ' of ', num2str(repeats)] );

    %%%%%%%%%%%%%%%%%%%%%%%%%%%%%%%%%%%%%%%%%%%%%%%%%%%%%%%%%%%%%%%%%%%%%%%%%%
    % Photodiode and Thermometer Measurements
    %%%%%%%%%%%%%%%%%%%%%%%%%%%%%%%%%%%%%%%%%%%%%%%%%%%%%%%%%%%%%%%%%%%%%%%%%%

    % Restore GPIB defaults
    fprintf(K2400,':*RST')
    %Clear buffer
    fprintf(K2400,':TRAC:CLE')
```

```
%SET SOURCE MODE, RANGE and COMPLIANCE
%set source mode (voltage)
fprintf(K2400, ':SOUR:FUNC VOLT')
%set voltage range
fprintf(K2400, ':SOUR:VOLT:RANG 20')
%set current compliance level (mA)
fprintf(K2400, ':SENS:CURR:PROT 10E-3')


%SET MEASUREMENT MODE, RANGE
%set measurement mode (current)
fprintf(K2400, ':SENS:FUNC "CURR"')
%set current measurement range
fprintf(K2400, ':SENS:CURR:RANG 10E-3')
%set to current read only
fprintf(K2400, ':FORM:ELEM CURR')

%%%%%%%%%%%%%%%%%%%%%%%%%%%%%%%%%%%%%%%%%%%%%%%%%%%%%%%%%%%%%%%%%%%%%%%%%%%
%Photodiode Measurement
%%%%%%%%%%%%%%%%%%%%%%%%%%%%%%%%%%%%%%%%%%%%%%%%%%%%%%%%%%%%%%%%%%%%%%%%%%%

for photodiode=1:8

if photodiode==1
USB6501_outputs(9)=1;
elseif photodiode==2
USB6501_outputs(10)=1;
elseif photodiode==3
USB6501_outputs(11)=1;
elseif photodiode==4
USB6501_outputs(12)=1;
elseif photodiode==5
USB6501_outputs(13)=1;
elseif photodiode==6
USB6501_outputs(14)=1;
elseif photodiode==7
USB6501_outputs(15)=1;
elseif photodiode==8
USB6501_outputs(16)=1;
end

USB6501_outputs(1)=1;
putvalue(USB6501,USB6501_outputs);

%allow current to settle  and take current reading
pause(initial_settle_time);

%Set Voltage output value (0V)
fprintf(K2400, ':SOUR:VOLT:LEV 0')
%turn output on
fprintf(K2400, ':OUTP ON')
%trigger reading
fprintf(K2400, ':READ?')

%Pause to allow measurement to take place
%pause (0.25)
```

```
    %read it off the GPIB
    raw_data = fscanf(K2400);

%     %turn output off
%     fprintf(K2400, ':OUTP OFF')

    %turn the text into an array of numbers
    processed_data = sscanf(raw_data,'%g,');
    %and pick off the measurement we want
    PD(photodiode) = processed_data;

    disp(['Reference photodiode ',num2str(photodiode),' current=' num2str(PD(photodiode))  ]);

    USB6501_outputs=logical([0  0  0  0  0  0  0  0  0  0  0  0  0  0  0  0  0  0  0  0  0  0
0  0]);
    putvalue(USB6501,USB6501_outputs);


    end

    %write photodiode measurements to file
    directory=[base_directory,'\PD'];
    fid=fopen([directory,'\PD.csv'],'a');
    fprintf(fid,'PD,%g,%g,%g,%g,%g,%g,%g,%g,%g\n',toc,PD);
    fclose(fid);


    %%%%%%%%%%%%%%%%%%%%%%%%%%%%%%%%%%%%%%%%%%%%%%%%%%%%%%%%%%%%%%%%%%%%%%%%%%%%
    %Thermometer Measurement
    %%%%%%%%%%%%%%%%%%%%%%%%%%%%%%%%%%%%%%%%%%%%%%%%%%%%%%%%%%%%%%%%%%%%%%%%%%%%

    for temp=1:4

    if temp==1
    USB6501_outputs(9)=1;
    elseif temp==2
    USB6501_outputs(10)=1;
    elseif temp==3
    USB6501_outputs(11)=1;
    elseif temp==4
    USB6501_outputs(12)=1;
    end

    USB6501_outputs(8)=1;
    putvalue(USB6501,USB6501_outputs);

    %allow current to settle  and take current reading
    pause(initial_settle_time);

    %Set Voltage output value (0V)
    fprintf(K2400, ':SOUR:VOLT:LEV 0')
%     %turn output on
%     fprintf(K2400, ':OUTP ON')
    %trigger reading
    fprintf(K2400, ':READ?')

    %Pause to allow measurement to take place
    %pause (0.25)
```

```
    %read it off the GPIB
    raw_data = fscanf(K2400);


%     %turn output off
%     fprintf(K2400, ':OUTP OFF')

    %turn the text into an array of numbers
    processed_data = sscanf(raw_data,'%g,');
    %and pick off the measurement we want
    T(temp) = -273.15 -(1E9/227)*processed_data ;

    disp(['Temperature ', num2str(temp), ' =', num2str(T(temp))  ]);

    USB6501_outputs=logical([0  0  0  0  0  0  0  0  0  0  0  0  0  0  0  0  0  0  0  0  0  0
0  0]);
    putvalue(USB6501,USB6501_outputs);

    end

    %write thermometer measurements to file
    directory=[base_directory,'\T'];
    fid=fopen([directory,'\T.csv'],'a');
    fprintf(fid,'T,%g,%g,%g,%g,%g\n',toc,T);
    fclose(fid);

    %%%%%%%%%%%%%%%%%%%%%%%%%%%%%%%%%%%%%%%%%%%%%%%%%%%%%%%%%%%%%%%%%%%%%%%%%%
    %Set up Keithley for JV measurement
    %%%%%%%%%%%%%%%%%%%%%%%%%%%%%%%%%%%%%%%%%%%%%%%%%%%%%%%%%%%%%%%%%%%%%%%%%%
    % Restore GPIB defaults
    fprintf(K2400,':*RST')
    %Clear and set up buffer
    fprintf(K2400,':TRAC:CLE')
    %set up buffer size
    fprintf(K2400,':TRAC:POIN 101')
    %turn off concurrent functions
    fprintf(K2400,':SENS:FUNC:CONC ON')
    %set up source mode (voltage)
    fprintf(K2400,':SOUR:FUNC VOLT')
    %set measurement mode (current)
    fprintf(K2400,':SENS:FUNC "CURR"')
    %set current limit
    fprintf(K2400,':SENS:CURR:PROT 10E-3')
    fprintf(K2400,':SENS:CURR:RANG:AUTO OFF')
    %Set NPLC
    fprintf(K2400,':SENS:CURR:NPLC 1');
    %set voltage start
    fprintf(K2400,':SOUR:VOLT:START -1')
    %set voltage stop
    fprintf(K2400,':SOUR:VOLT:STOP 1.0')
    %set voltage step
    fprintf(K2400,':SOUR:VOLT:STEP 0.02')
    fprintf(K2400,':SOUR:CLE:AUTO ON')
    %set voltage sweep
    fprintf(K2400,':SOUR:VOLT:MODE SWE')
    %set fixed range on source
    fprintf(K2400,':SOUR:SWE:RANG FIX')
```

```
    %set sweep type (linear)
    fprintf(K2400,':SOUR:SWE:SPAC LIN')
    %trigger count (=number of sweep points = stop-start/step +1)
    fprintf(K2400,':TRIG:COUNT 101')
    fprintf(K2400,':TRIG:DEL 0')
    %set source delay
    fprintf(K2400,':SOUR:DEL 0.1')


for device=start_device:end_device

    %Set the Inverter for inverted or normal devices
    inverter=1;
    if inverted_array(device)==1;
        inverter=-1;
    end




    %clears figure in between devices
    clf;

    disp('********************************')
    disp('********************************')
    disp(['Testing Device #', num2str(device), ' of ', num2str([end_device-start_device+1])]
);
    t=clock;
    time_string=[num2str(t(1)),'.',num2str(t(2)),'.',num2str(t(3)),'
',num2str(t(4)),'.',num2str(t(5)),'.',num2str(round(t(6)))];

    directory=[base_directory,'\D', num2str(device)];
    file_name=[time_string,' ',num2str(batch),'-', 'Device', num2str(device), ' Repeat',
num2str(repeat),];
    file_path=[directory,'\',file_name,'.csv'];


    %turn off everything for safety reasons
    USB6501_outputs=logical([0  0  0  0  0  0  0  0  0  0  0  0  0  0  0  0  0  0  0  0  0  0
0  0]);
    putvalue(USB6501,USB6501_outputs);


    if device==1
    USB6501_outputs(9)=1;
    elseif device==2
    USB6501_outputs(10)=1;
    elseif device==3
    USB6501_outputs(11)=1;
    elseif device==4
    USB6501_outputs(12)=1;
    elseif device==5
    USB6501_outputs(13)=1;
    elseif device==6
    USB6501_outputs(14)=1;
    elseif device==7
    USB6501_outputs(15)=1;
    elseif device==8
```

```
    USB6501_outputs(16)=1;
    end



        for pixel= start_pixel:end_pixel

            %Clear buffer
            fprintf(K2400,':DATA:CLE')
            %enable buffer
            fprintf(K2400,':TRAC:FEED:CONT NEXT')

            %debugging point 2
            %disp(['DP2', ' Rep=',num2str(repeat),' Dev=',num2str(repeat),'
Pix=',num2str(pixel), ' Inverter=', num2str(inverter)]);

            if pixel==1;
            USB6501_outputs(2)=1;
            elseif pixel==2
            USB6501_outputs(3)=1;
            elseif pixel==3
            USB6501_outputs(4)=1;
            elseif pixel==4
            USB6501_outputs(5)=1;
            elseif pixel==5
            USB6501_outputs(6)=1;
            elseif pixel==6
            USB6501_outputs(7)=1;
            end

            %Switch on pixel by sending value to board
            putvalue(USB6501,USB6501_outputs);
            pause(0.5);

            %Display: Device X Pixel X on
            disp(['********************************'])
            disp(['Device ',num2str(device),' Pixel ',num2str(pixel),' on'])

            %Pause if necessary
            pause(initial_settle_time);

            %Initiate readings
            fprintf(K2400,':INIT')

            disp('Reading Currents')

            %Pause to allow measurement to take place ~7s
            %pause (7)


            %Recall data from buffer (voltage,current,time,resistance,?)
            fprintf(K2400,':TRAC:DATA?');
            %Turn huge data string into numbers
            raw_data=str2num(fscanf(K2400));

            %Pick out data we want
            voltage=inverter * raw_data(1:5:505)';
            current=inverter * raw_data(2:5:505)';
```

```
%flip data if inverter=-1 to make sure Voc is correctly calculated
if inverter==-1;
    voltage=flipud(voltage);
    current=flipud(current);
end

current_density(:,pixel)=1000*current/device_area;

%Switch off pixel
USB6501_outputs(pixel+1)=0;
putvalue(USB6501,USB6501_outputs);

disp('Plotting')
plot(voltage,current_density(:,pixel)); grid on; hold on;

disp('Calculating key parameters')
%calculate key parameters
power=abs(voltage.*current); %Watts
%find key parameters
max_power(pixel)=0;
max_power_data_point=1;
Jsc(pixel)=0;
Voc(pixel)=0;


for i=1:1:101
    if voltage(i)==0;
        Jsc(pixel)=current_density(i,pixel);
    end
    if  voltage(i) > 0  && current(i) <= 0 && i<101
        Voc(pixel)=   voltage(i)  +  (0-current(i)) * (voltage(i+1)-voltage(i)) /
(current(i+1)-current(i)) ;
        if power(i)>=max_power(pixel);
            max_power_data_point=i;
            max_power(pixel)=power(i);
        end
    end
end

Vmpp(pixel)=voltage(max_power_data_point);
Jmpp(pixel)=current_density(max_power_data_point,pixel);

%disp(['Vmpp=',num2str(Vmpp(pixel))]);
%disp(['Jmpp=',num2str(Jmpp(pixel))]);
%calculate efficiency from the maximum output power divided by the input
%power of the device area times the solar power density
%(1000 watts/m^2 = 0.1 %W/cm^2)
%x100 to turn into percent
Efficiency(pixel)=100*max_power(pixel)/(device_area*0.1);
FF(pixel)=100*Vmpp(pixel)*Jmpp(pixel)/(Voc(pixel)*Jsc(pixel));

disp(['PCE=',num2str(Efficiency(pixel)),'  Jsc=',num2str(Jsc(pixel)),'
Voc=',num2str(Voc(pixel)),'  FF=',num2str(FF(pixel))]);



%%%%%%%%%%%%%%%%%%%%%%%%%%%%%%%%%%%%%%%%%%%%%%%%%%%%%
```

```
            %write JV data to file for this device in the device subdirectory


            %write data file for this device
            fid=fopen(file_path,'w');
            fprintf(fid,'Bias,J(pixel 1),J(pixel 2),J(pixel 3),J(pixel 4),J(pixel 5),J(pixel
6)\n');
            fprintf(fid,'V,mA/cm^2,mA/cm^2,mA/cm^2,mA/cm^2,mA/cm^2,mA/cm^2\n');
            fprintf(fid,'%g,%g,%g,%g,%g,%g,%g\n', [voltage ,current_density].');

            fprintf(fid,'\n\n');
            fprintf(fid,'Parameter,Pixel 1,Pixel 2,Pixel 3,Pixel 4,Pixel 5,Pixel 6\n');
            fprintf(fid,'Voc (V),%g,%g,%g,%g,%g,%g\n',Voc);
            fprintf(fid,'Jsc (mA/cm^2),%g,%g,%g,%g,%g,%g\n',Jsc);
            fprintf(fid,'FF (%%),%g,%g,%g,%g,%g,%g\n',FF);
            fprintf(fid,'Vmpp (V),%g,%g,%g,%g,%g,%g\n',Vmpp);
            fprintf(fid,'Jmpp (mA/cm^2),%g,%g,%g,%g,%g,%g\n',Jmpp);
            fprintf(fid,'Efficiency (%%),%g,%g,%g,%g,%g,%g\n',Efficiency);

            fprintf(fid,'\n\n');
            fprintf(fid,'\nDevice Area,%g,cm^2',device_area);
            fprintf(fid,'\nsettle_time,%g,seconds',settle_time);

            fclose(fid);

            %disable buffer - needs to be done so the buffer can be
            %cleared before the next reading is taken.
            fprintf(K2400,':TRAC:FEED:CONT NEV')

        end

        %Append data to summary files for this device in the device subdirectory

        %for Voc
        fid=fopen([directory,'\Voc.csv'],'a');

fprintf(fid,'%s,%s,%s,%g,%g,%g,%g,%g,%g,%g\n',time_string,batch,['D',num2str(device)],toc,Voc)
;
        fclose(fid);

        %for Jsc
        fid=fopen([directory,'\Jsc.csv'],'a');

fprintf(fid,'%s,%s,%s,%g,%g,%g,%g,%g,%g,%g\n',time_string,batch,['D',num2str(device)],toc,Jsc)
;
        fclose(fid);

        %for FF
        fid=fopen([directory,'\FF.csv'],'a');

fprintf(fid,'%s,%s,%s,%g,%g,%g,%g,%g,%g,%g\n',time_string,batch,['D',num2str(device)],toc,FF);
        fclose(fid);

        %for PCE
        fid=fopen([directory,'\PCE.csv'],'a');

fprintf(fid,'%s,%s,%s,%g,%g,%g,%g,%g,%g,%g\n',time_string,batch,['D',num2str(device)],toc,Effi
ciency);
```

```
        fclose(fid);

        %for Vmpp
        fid=fopen([directory,'\VMPP.csv'],'a');

fprintf(fid,'%s,%s,%s,%g,%g,%g,%g,%g,%g,%g\n',time_string,batch,['D',num2str(device)],toc,Vmpp
);
        fclose(fid);

        %for Jmpp
        fid=fopen([directory,'\JMPP.csv'],'a');

fprintf(fid,'%s,%s,%s,%g,%g,%g,%g,%g,%g,%g\n',time_string,batch,['D',num2str(device)],toc,Jmpp
);
        fclose(fid);

       pause(delay_between_devices);

end

%%%%%%%%%%%%%%%%%%%%%%%%%%%%%%%%%%%%%%%%%%%%%%%%%%%%%%%%%%%%%%%%%%%%%%%%%%%
%Set devices in open or short circuit after measurements
%%%%%%%%%%%%%%%%%%%%%%%%%%%%%%%%%%%%%%%%%%%%%%%%%%%%%%%%%%%%%%%%%%%%%%%%%%%

USB6501_outputs=logical([0  Pixel1  Pixel2  Pixel3  Pixel4  Pixel5  Pixel6  0  Device1
Device2  Device3  Device4  Device5  Device6  Device7  Device8  1  0  0  0  0  0  0]);
putvalue(USB6501,USB6501_outputs);




pause(delay_between_repeats);

end

%turn everything off
USB6501_outputs=logical([0  0  0  0  0  0  0  0  0  0  0  0  0  0  0  0  0  0  0  0  0  0  0
0]);
putvalue(USB6501,USB6501_outputs);

%turn output off
fprintf(K2400, ':OUTP OFF')

%close down instruments

% Restore GPIB defaults
fprintf(K2400,':*RST')
fprintf(K2400,':*CLS ')
fprintf(K2400,':*SRE 0');

delete(USB6501); clear USB6501;

%delete GPIB objects
fclose(K2400);delete(K2400);clear K2400;
```